

# **Development of Improved Rheometric Tools and their Application on the Non-Newtonian Rheology of Polymeric Fluids**

Zur Erlangung des akademischen Grades  
**Doktor der Ingenieurwissenschaften**  
der Fakultät für Maschinenbau  
Karlsruher Institut für Technologie (KIT)

genehmigte  
**Dissertation**

von

Dipl.-Ing. Ingo F. C. Naue  
aus  
Langen (Hessen)

*Tag der mündlichen Prüfung:* 12.07.2013

*Hauptreferent:* Prof. Dr. Ing. Peter Elsner

*Korreferent:* Prof. Dr. rer. nat. Manfred Wilhelm

*"Data! Data! Data! ... I can't make bricks without clay."*

Sherlock Holmes in "The adventure of the copper beaks"<sup>1</sup>

I dedicate this thesis to my parents Ursula and Helmut  
Naue, to my teacher Steffen G. Fröhlich and to  
Prof. Kolumban Hutter.



# Contents

<b>Zusammenfassung</b>	<b>ix</b>
<b>Abstract</b>	<b>xi</b>
<b>Nomenclature</b>	<b>xiii</b>
<b>1. Introduction</b>	<b>1</b>
1.1. Thesis Outline . . . . .	6
<b>2. Data Acquisition, Data Analysis and Material Properties</b>	<b>9</b>
2.1. Mathematical Methods for Data Analysis . . . . .	9
2.1.1. Fourier Series . . . . .	10
2.1.2. Fourier Transform . . . . .	11
2.1.3. Discrete Fourier Transform . . . . .	13
2.1.4. Window Functions . . . . .	15
2.1.5. Autocorrelation Function . . . . .	19
2.1.6. Discrete Autocorrelation Function . . . . .	20
2.2. Introduction to Data Acquisition . . . . .	22
2.3. Mechanical Models for Ideal Materials . . . . .	26
2.3.1. Basic Ideas About Mechanical Bodies . . . . .	26
2.3.2. The Stress Tensor . . . . .	29
2.3.3. Rheological Models . . . . .	32
2.4. Polymers . . . . .	36
2.4.1. Introduction to the Structure of Polymeric Materials .	36
2.4.2. Materials of Investigation . . . . .	42
<b>3. Rotational Rheology</b>	<b>45</b>
3.1. Detection of Normal Forces under Oscillatory Shear . . . . .	47

3.2.	The Rotational Shear Rheometer . . . . .	48
3.2.1.	Oscillatory Shear . . . . .	50
3.2.2.	Time-Temperature-Superposition (TTS) . . . . .	54
3.2.3.	Polymer Melts under Oscillatory Shear . . . . .	56
3.3.	Fourier Transform Rheology (FT-R) . . . . .	58
3.4.	An Improved Normal Force Geometry . . . . .	60
3.4.1.	Data Acquisition for the Rotational Rheometer . . . . .	61
3.5.	Experimental Set-up for the Oscillatory Shear Experiments . . . . .	61
3.6.	Analysing the Data from the Oscillatory Shear Experiments . . . . .	66
3.7.	Validation of the Normal Force Geometry . . . . .	70
3.8.	Non-linear Parameters from the FT-Measurement . . . . .	73
3.9.	Comparison of the Results of the Non-linear Behaviour of PS and PE Samples . . . . .	76
3.10.	Summary and Conclusions for the NoForGe . . . . .	81
<b>4.</b>	<b>Detection of Mechanical Instabilities in the Capillary Rheometer and the Extruder</b> . . . . .	<b>83</b>
4.1.	Detection of Melt Flow Instabilities on the Extruder . . . . .	84
4.2.	Melt Flow Instabilities . . . . .	85
4.3.	Experimental Set-up for the Capillary Rheometer . . . . .	90
4.4.	Experimental Set-up for the Extrusion . . . . .	93
4.4.1.	The First Generation Sharkskin Die (SSD-1) . . . . .	94
4.4.2.	The Second Generation Sharkskin Die (SSD-2) . . . . .	99
4.4.3.	Data Acquisition . . . . .	100
4.4.4.	Mathematical Treatment of the Pressure Raw Data . . . . .	101
4.4.5.	Analysing the Pressure Fluctuations of Melt Flow In- stabilities with the Sharkskin Die . . . . .	104
4.4.6.	Optical Analysis of the Extrudate . . . . .	112
4.4.6.1.	Comparison of the Optical Analysis of the Extrudate and the Analysis of the Time-dependent Pressure Fluctuations . . . . .	127
4.4.7.	Experimental Conditions for the Experiments with the Extruder . . . . .	129
4.5.	Pressure Fluctuations Determined during the Extrusion of Polymer Melts . . . . .	130
4.5.1.	Identification of the Melt Flow Instabilities Inside the Extruder Die . . . . .	132

---

4.5.2.	Observing the Development of the Melt Flow Instabilities in the Extruder . . . . .	134
4.5.3.	Using the ACF to Analyse the Time-dependent Pressure Fluctuations from the Sharkskin Die on the Extruder . . . . .	136
4.5.4.	Comparison Between Optical Analysis and Pressure Based Analysis of the Melt Flow Instabilities . . . . .	137
4.5.5.	Noise Reduction for Automated Detection of the Melt Flow Instabilities . . . . .	148
4.6.	Summary and Conclusions for the Extruder . . . . .	149
<b>5.</b>	<b>Improving the CaBER with a Measurement of the Axial Force</b>	<b>153</b>
5.1.	Introduction and Task . . . . .	153
5.1.1.	The Principle of the CaBER Experiment . . . . .	155
5.2.	Theoretical Description of the CaBER Experiment . . . . .	158
5.2.1.	Conservation of Mass and Volume . . . . .	159
5.2.2.	The Force Balances of the Filament . . . . .	161
5.2.3.	Material Laws . . . . .	162
5.3.	Experimental Set-up of the CaBER . . . . .	164
5.3.1.	Description of the CaBER Apparatus . . . . .	164
5.3.2.	Newly Designed Measurement Device for the Axial Forces in the CaBER . . . . .	165
5.4.	Calibration and Determination of the Force Sensitivity of the CaBER . . . . .	169
5.5.	Measuring Axial Forces with the CaBER . . . . .	170
5.5.1.	Comparing the Diameter-based Analysis with the New Axial Force-based Analysis . . . . .	171
5.5.2.	Results of the PDMS . . . . .	180
5.5.2.1.	Conclusions for Application of the Measurement of the Axial Force in the CaBER Experiment . . . . .	181
5.5.3.	The Curing Behaviour of Commercial Glue Studied in the CaBER with the Normal Force Measurement . . . . .	182
5.5.3.1.	The Adhesive Energy, Separation Energy and Tack . . . . .	182
5.5.3.2.	Separation Energy of Different Glues . . . . .	184

5.5.3.3. Conclusions for Measurement of the Axial Forces in the CaBER for Commercial Glues	191
5.6. Conclusions and Prospects for the Modification of the CaBER	195
<b>6. Conclusions and Outlook</b>	<b>197</b>
<b>A. Short Introduction to Tensor Calculus</b>	<b>203</b>
A.1. Vector Space . . . . .	203
A.2. Euclidean Vector Space . . . . .	204
A.2.1. Magnitude of a Vector . . . . .	204
A.2.2. Vector Product . . . . .	205
A.2.3. Orthonormal Basis and Kronecker Symbol . . . . .	205
A.2.4. Alternating Symbol . . . . .	206
A.3. Change of Basis . . . . .	207
A.3.1. Euclidean Point Space . . . . .	208
A.4. Tensors . . . . .	209
A.4.1. Tensor Product/ Dyadic Product . . . . .	210
A.4.2. Contraction of a Tensor . . . . .	211
A.4.3. Isotropic Tensors . . . . .	211
A.5. Tensor Algebra . . . . .	211
A.6. Eigenvalues and Eigenvectors . . . . .	213
A.6.1. Symmetric Tensors of Second Order . . . . .	214
A.6.2. Antisymmetric Tensors of Second Order . . . . .	215
A.7. Orthogonal Tensors of Second Order . . . . .	216
A.7.1. Mapping from one Euclidean Space to Another . . . . .	216
A.8. Reciprocal Basis: Contravariance and Covariance Basis . . . . .	217
<b>B. Properties of the Fourier Transform</b>	<b>219</b>
<b>C. The Maxwell Model under Oscillatory Shear</b>	<b>221</b>
<b>D. Derivation of the Fundamental Equation of the FT-Rheology</b>	<b>223</b>
<b>E. Special Units for the Spatial Frequency</b>	<b>225</b>
<b>F. Tack: An Adhesive Material Property</b>	<b>229</b>
<b>G. Mass and Conservation of Mass</b>	<b>233</b>

<b>H. Material Derivative</b>	<b>237</b>
<b>I. Improved Mass Balance</b>	<b>239</b>
<b>J. Surface Tension</b>	<b>241</b>
<b>K. The Young-Laplace Equation and its Application on a Cylindrical Body</b>	<b>243</b>
K.1. Application of the Young-Laplace Equation on a Cylindrical Body . . . . .	244
<b>L. Technical Drawings</b>	<b>247</b>
<b>M. A Short Genealogical Tree of this Work</b>	<b>251</b>
<b>References</b>	<b>274</b>
<b>Acknowledgement</b>	<b>275</b>



# Zusammenfassung

Diese Arbeit widmet sich dem Studium des nicht-newtonschen rheologischen Verhaltens von polymeren Flüssigkeiten. Ein besonderes Augenmerk liegt dabei auf der Messung der Normalkraft/ -spannung oder -druck (der Kraft oder des Drucks senkrecht zur Fließrichtung) einer polymeren Flüssigkeit unter definierten Strömungsbedingungen.

Diese definierten Strömungsbedingungen werden mit Laborrheometern erzeugt, z.B. die Torsions-Scherströmung eines Rotationsrheometer, die laminare Rohrströmung in einem rechteckigen Kanal eines Kapillarrheometers und eines Extruders und die uniaxiale Dehnströmung eines CaBERs (Capillary Break-up Extensional Rheometers). Um eine Messung der Normalkraft oder -druck an diesen Geräten zu ermöglichen, werden vorhandene Rheometer mit eigenen Konstruktionen erweitert. Die erreichte Sensitivität der Normalkraftmessungen liegt bei ca.  $5 \cdot 10^{-5}$  N und bei der Messung von Normaldrücken bei ca.  $10^{-5}$  bar. Diese Sensitivität wird u.a. dadurch erreicht, dass bei der hochfrequenten Datenerfassung ( $> 100$  kHz) die Oversamplingmethode angewendet wird. Die entsprechenden Erweiterungen der Rheometer werden im Detail dargestellt. Zu den konstruktiven Maßnahmen zur Messung der Normalkraft oder -spannung werden auch fortgeschrittene Methoden zur Datenanalyse, z.B. die Fourier-Transformation oder die Autokorrelationsfunktion, angewendet.

Anhand von Messungen von verschiedenen Polystyrol- und Polyethylenproben mit verschiedener molekularer Architektur wird durch Anwendung der Fourier-Transformation auf die Daten der Normalkräfte bei oszillatorischer Scherung am Rotationsrheometer gezeigt, dass bei stark nichtlinearer Beanspruchung höhere gerade harmonische Frequenzanteile im Amplitudenspektrum der Normalkräfte auftreten. Zur Auswertung der Spektren der Normalkräfte wird ein nichtlinearer Parameter  $Q_{NF}$  ein-

geführt, in Analogie zum nichtlinearen Parameter  $Q$  aus den Schubspannungsspektren. Die Resultate der scheramplitudenabhängigen nichtlinearen Parameter  $Q_{NF}(\gamma_0)$  und  $Q(\gamma_0)$  werden verglichen. Dabei zeigen sich Unterschiede zwischen linearen Polymerketten und verzweigten Polymerketten abhängig vom Polymer entweder bei  $Q_{NF}(\gamma_0)$  oder bei  $Q(\gamma_0)$ .

Für Messungen am Kapillarrheometer und Extruder wird anhand von verschiedenen Polyethylenproben gezeigt, dass beim Auftreten von Schmelzinstabilitäten charakteristische Frequenzanteile in den Fourierspektren der zeitabhängigen Normalspannungen in der Düse zu beobachten sind. Diese charakteristischen Frequenzanteile werden mit den Frequenzen verglichen, die durch eine neu angewandte Fourier-Transformations-Analyse der Bilder der Extrudatproben bestimmt werden. Des Weiteren wird am Extruder untersucht, ob sich die Detektion der Schmelzinstabilitäten mit Hilfe der Messung der Normalspannung und deren Fourieranalyse dafür eignet eine automatisierte Regelung der Verarbeitungsbedingungen des Extruders zur Herstellung von Extrudaten ohne Schmelzinstabilitäten zu gewährleisten. Zusätzlich zur Fourier-Transformation wird auch die Autokorrelationsfunktion verwendet, um Informationen über die Beschaffenheit der Schmelze am Extruder zu bekommen.

Anhand von dehnreologischen Messungen am CaBER mit einer Polystyrollösung wird gezeigt, dass die neue Messung der Normalkraft während des CaBER Experimentes eine Bestimmung der Dehnaviskosität ermöglicht. Dafür wird die Massenbilanz neu formuliert und die Kräftebilanz wird um einen zusätzlichen Kräfteterm erweitert. Außerdem wird mit der neuen Normalkraftmessung am CaBER gezeigt, dass schon während der Fadenziehphase wichtige Informationen über die Probe gewonnen werden können. Dies wird verdeutlicht an Experimenten mit zwei verschiedenen Weißleimproben (auf Basis von Polymeren). Dabei wird untersucht in wie weit sich die Härtezeit auf die gemessene Kraft auswirkt. Dazu wird eine neue Größe die Separationsenergie eingeführt. Diese Experimente am CaBER stehen im engen Zusammenhang mit den sogenannten Tack-Messungen bei denen eine Ablöseenergie bestimmt wird.

# Abstract

This work concerns the studies of the non-Newtonian rheological behaviour of polymeric liquids. Special attention is drawn to the measurement of the normal force or normal pressure (the force or pressure perpendicular to the direction of flow) of a polymeric liquid with defined flow conditions. These defined flow conditions are obtained with rheometric devices, i.e. the torsion-shear flow of a rotary rheometer, laminar pipe flow in a rectangular channel of a capillary rheometer and an extruder, and the uniaxial elongational flow of a CaBER (Capillary Break-up Extensional Rheometer). To enable the measurement of the normal force or normal pressure with these devices, the existing rheometers are improved with new constructions. Thus, the sensitivity of the measurement is about  $5 \cdot 10^{-5}$  N for the normal force and about  $10^{-5}$  bar for the normal pressure. This level of sensitivity is obtained amongst others by the application of the oversampling method on a high frequency data acquisition ( $> 100$  kHz). The related extensions of the rheometers are presented in detail. Additionally to the constructive changes for the measurement of the normal force or normal pressure, advanced methods of data analysis are applied, e.g. the Fourier transform or the autocorrelation function.

By means of the measurements with different polystyrene and polyethylene samples, which have a different molecular architecture, it is shown that with the use of the Fourier transform on the data of the normal force obtained from oscillatory shear experiments the higher even harmonic contributions appear in the amplitude spectrum. A new non-linear parameter  $Q_{NF}(\gamma_0)$  is introduced for the evaluation of the spectra of the normal forces. This is analogically done to the non-linear parameter of the spectra of the shear amplitude  $Q(\gamma_0)$ .  $Q_{NF}(\gamma_0)$  and  $Q(\gamma_0)$  show differences between linear and branched polymeric chains for the different polymers.

By using different polyethylene samples in the capillary rheometer and the extruder, it is shown that together with the appearance of melt flow instabilities (MFI) appear characteristic frequency contributions in the spectra of the time-dependent normal pressure inside the die. These characteristic frequency contributions are compared with the frequencies which are obtained from the newly applied Fourier analysis of the images of the related extrudate samples. Furthermore, it is investigated whether the detection of the melt flow instabilities using the measurement of the normal pressure and the following Fourier analysis is suitable for an automatic control of the extrusion parameters in order to produce an extrudate without melt flow instabilities. Additionally to the Fourier transform, the autocorrelation function is utilized to gain information about the constitution of the melt at the extruder.

On the basis of extensional measurements with the CaBER using a polystyrene solution it is shown, that the measurement of the normal force during the CaBER experiment allows the calculation of the elongational viscosity. Therefore, a new balance of mass is formulated and an additional force term is added to the balance of forces. Additionally, it is shown on the CaBER with the new measurement of the normal force, that it is already possible during the filament stretch phase to obtain important information about the sample. This is illustrated by performing experiments with two different wood glues (on polymeric basis). Thus, the influence of the curing time on the measured force is studied. Therefore, a new property, the separation energy, is introduced. These experiments on the CaBER are closely related to the so called tack measurements, which determine the energy of detachment.

## Nomenclature

In this thesis the following conventions have been observed where possible: Bold faced letters (e.g. **A**, **B**) stand for tensors of second order and matrices. Tensors of first order (vectors) are indicated by an arrow, e.g.  $\vec{u}$ . Fraktur letters (e.g.  $\mathfrak{C}$ ) are used for constants and fitting parameters, if the parameters have no predefined meaning. Capital letters as e.g.  $\mathbb{E}$ ,  $\mathbb{V}$  are used to describe mathematical sets and spaces. Script capital letters (e.g.  $\mathcal{E}$ ) define point spaces. Lower case Roman letters stand for variables, e.g.  $t$  the time or  $r$  the radial coordinate. Capital Roman letters stand for parameters, e.g.  $T$  the time interval, and set geometrical values, e.g.  $D_0$  the initial diameter. Combined with a frequency dependency, a capital Roman letter indicates the Fourier-transform of a time-dependent function, e.g.  $F(\omega)$  is the Fourier-transform of  $f(t)$ . This rule is sometimes broken in this thesis due to commonly used other definitions, e.g.  $F$  the mechanical force or  $W$  the mechanical work. Greek letters are applied as they are commonly used in the literature, e.g. the stress  $\sigma$  or the strain  $\gamma$ . Indices are used for two purposes. Once to indicate a speciality of the value, e.g.  $T_{meas}$  indicates a time interval of a measurement and  $\nu_{extr}$  a frequency related to an extrudate, and once to count elements, e.g.  $x_i$  ( $x_1, x_2, x_3, \dots$ ) or  $\sigma_{ij}$  ( $\sigma_{11}, \sigma_{12}, \sigma_{13}, \sigma_{21}, \dots$ ). In the second case the indices  $i, j, k, l, m, n, o, p, q, r$  and  $s$  are used, and the indices represent natural numbers.

## Capital Letters

$\mathfrak{A}_0, \mathfrak{A}_n, \mathfrak{B}_n,$	<i>a.u.</i>	Fourier coefficients
<b>A, B</b>	<i>a.u.</i>	tensor of second order
<i>A</i>	$m^2$	surface area
$A_p$	$m^2$	perimeter area
$A_C$	$m^2$	cross-sectional area
$A(x, t)$	$m^2$	cross-sectional area of the filament
$A_{reservoir}$	$m^2$	cross-sectional area of the reservoir of a capillary rheometer
<i>B</i>	<i>m</i>	width/ broadness
<i>C</i>	<i>Pa</i>	integration constant
$\mathfrak{C}_1, \mathfrak{C}_2, \mathfrak{C}_3, \mathfrak{C}_4$	<i>a.u.</i>	coefficients of fitting functions
$C_1$	–	first constant for the WLF equation
$C_2$	<i>K</i>	second constant for the WLF equation
$C_{ijkl}$	<i>Pa</i>	material stiffness tensor
<b>D</b>	<i>a.u.</i>	symmetric tensor of second order
<i>D</i>	<i>m</i>	diameter
$D_0$	<i>m</i>	diameter of a plate geometry
$D_B$	<i>m</i>	barrel/reservoir diameter
$D_{piezo}$	<i>m</i>	diameter of sensor area of a piezoelectric transducer
<i>E</i>	<i>Pa</i>	Young’s modulus
<b>E</b>	–	strain tensor
$E_a$	<i>J/mol</i>	activation energy
<i>F</i>	<i>N</i>	force
$F_{contact}$	<i>N</i>	contact force
$F(t)$	<i>N</i>	time-dependent force
$F(\omega)$	<i>a.u.</i>	Fourier transform of $f(t)$
$F_k$	<i>a.u.</i>	discrete Fourier transform of $f_k$
$F_z$	<i>N</i>	axial force
$F_{cap}$	<i>N</i>	capillary force
<i>G</i>	<i>Pas</i>	shear modulus
$G'_p$	<i>Pas</i>	plateau modulus
<i>H</i>	<i>m</i>	height
<b>I</b>	–	identity tensor
$I_1, I_2, I_3, \dots$	<i>a.u.</i>	first, second, third, ... higher harmonic in the FT- magnitude spectrum of the stress
$I(\mathbf{A})$	<i>a.u.</i>	first invariant of the tensor <b>A</b>
$II(\mathbf{A})$	<i>a.u.</i>	second invariant of the tensor <b>A</b>
$III(\mathbf{A})$	<i>a.u.</i>	third invariant of the tensor <b>A</b>
<i>J</i>	–	functional determinate $\frac{\partial x_i}{\partial \xi_j}$

---

$L$	$m$	length
$L_0$	$m$	initial gap
$L_{strike}(t)$	$m$	final position, sample displacement
$L_x$	$m$	length in x-direction
$L_y$	$m$	length in y-direction
$M$	$kg/mol$	molecular weight
$M_i$	$kg$	weight of a single fraction
$\overline{M}_n$	$kg/mol$	number averaged molar mass
$\overline{M}_w$	$kg/mol$	weight averaged molar mass
$N$	–	length of discrete data set $N \in \mathbb{N}$
$N(t)$	$N$	time-dependent normal force
$N(v)$	$N$	frequency-dependent normal force
$N_1, N_2, N_3, \dots$	$a.u.$	first, second, third, ... higher harmonic in the FT-magnitude spectrum of the normal force
$N_{4/2}$	–	ratio of the fourth and the second higher harmonic of the magnitude spectrum of the normal force
$N_L$	–	Loschmidt number
$N_1(t)$	$Pa$	first normal stress difference
<b>P</b>	$Pa$	frictional pressure tensor
$P_{ij}$	$Pa$	components of the frictional pressure tensor
$PDI$	–	polydispersity index
<b>Q</b>	$a.u.$	orthogonal tensor of second order
$Q$	–	intrinsic non-linearity, Q-parameter
$Q_{NF}$	–	Q-parameter of the normal force spectrum
$R_0$	$m$	radius of a geometry
$R$	$m$	outer radius of a geometry
$R_m$	$J/molK$	universal gas constant
$R_{P/C_i}$	–	ratio of perimeter and cross-section area
$SNR$	–	signal-to-noise ratio
$S_1, S_2,$	–	slope of the first (1) and the second (2) region of $I_3/I_1$
$S_{Q1}, S_{Q2},$	–	slope of the first (1) and the second (2) region of $Q$
$S_{N1}, S_{N2},$	–	slope of the first (1) and the second (2) region of $N_{4/2}$
$S_{QN1}, S_{QN2},$	–	slope of the first (1) and the second (2) region of $Q_{NF}$
<b>S</b>	$Pa$	stress tensor
$T_z$	$Nm$	torque around the z-axis
$T$	$s$	time interval
<b>T</b>	$a.u.$	tensor of second order
$T_2$	$s$	time constant
$T_{deta}$	$s$	detachment/ separation time
$U$	$V$	voltage
$U_{meas}$	–	measurement uncertainty
$V$	$m^3$	volume

$\mathbf{W}$	<i>a.u.</i>	antisymmetric tensor of second order
$W_{adh}$	$J/m^2$	detachment work per unit area
$W_S$	$J$	surface energy
$W_{sep}(t)$	$J/m^2$	time-dependent separation energy per unit area
$W_V$	$J$	volume energy
$W(\omega), W(\nu)$	–	Fourier transform of $w(t)$

## Small Letters

$a_T$	–	TTS shift factor
$a_0, a_n, b_n$	<i>a.u.</i>	Fourier coefficients
$c_{ff,k}$	–	discrete autocovariance function of $f$
$d(x, t)$	$m$	time- and axial position-dependent diameter
$f(t), f_1(t), f_2(t)$	<i>a.u.</i>	time-dependent function
$f_g$	$m^3$	fractional free volume
$f_k$	<i>a.u.</i>	discrete function
$f_V$	$m^3$	free volume
$i$	–	imaginary unit $i = \sqrt{-1}$
$k_w$	$m^{-1}$	spatial angular frequency
$m$	$kg$	mass
$n$	–	integer number $n \in \mathbb{N}$
$n_{pl}$	–	flow index (power law fluid)
$n_{rot}$	$1/min$	screw rotations of the extruder
$p$	$Pa$	pressure
$\bar{p}$	$Pa$	hydrostatic pressure
$\check{p}$	$Pa$	drift-reduced time-dependent pressure fluctuations
$q$	–	number of waves
$r$	$m$	radial coordinate
$r_{COD}^2$	<i>a.u.</i>	coefficient of determination
$r_{ff}(\tau)$	–	autocorrelation function of the function $f$
$r_{ff,k}$	–	discrete autocorrelation function
$s(t)$	<i>a.u.</i>	time-dependent signal
$t$	$s$	time variable
$t_0$	$s$	starting time of the filament stretching
$t_1$	$s$	ending time of filament stretching
$t_2$	$s$	time of filament break up
$t_{break}$	$s$	time to filament break-up
$t_{contact}$	$s$	contact time
$t_{cure}$	$s$	curing time
$u$	$m/s$	axial velocity
$v(t)$	$m/s$	separation rate, separation velocity

---

$v_{strike}(t)$	$m/s$	strike time
$v_{piston}$	$mm/s$	piston velocity of the capillary rheometer
$w(t)$	–	time-dependent window function
$w_i$	–	weight fraction
$x$	$m$	axial position
$x_i$	$1/mol$	mole fraction of $M_i$
$\ddot{x}$	$m/s^2$	acceleration in $x$ -direction

## Greek Letters

$\alpha$	$rad$	cone angle
$\alpha_F$	$m^3/K$	thermal expansion coefficient of the free volume
$\Gamma$	$Nm$	surface tension
$\gamma$	–	shear strain
$\gamma_0$	–	strain amplitude
$\dot{\gamma}$	$s^{-1}$	shear/strain rate
$\dot{\gamma}_H$	$s^{-1}$	strain rate of a Hookean element
$\dot{\gamma}_N$	$s^{-1}$	strain rate of a Newtonian element
$\delta$	$rad$	phase angle
$\delta_{ij}$	–	Kronecker delta/ symbol
$\Delta S_{exit}$	$m$	distance to the exit of a die
$\Delta x$	$m$	elongation
$\varepsilon$	–	elongational strain
$\varepsilon_{ij} = \gamma_{ij}$	–	components of the strain tensor
$\varepsilon_{new}$	–	elongational strain based on the chap. I
$\varepsilon_{ijk}$	–	alternator, alternating symbol
$\varphi$	$rad$	FT-phase angle
$\varphi$	$rad$	angular coordinate
$\eta$	$Pas$	shear viscosity
$\eta_E$	$Pas$	elongational viscosity
$\eta_{E,N}$	$Pas$	elongational viscosity of a Newtonian fluid
$\eta_{E,B}$	$Pas$	elongational viscosity of a Bingham fluid
$\eta_{E,Pl}$	$Pas$	elongational viscosity of a power law fluid
$\lambda$	$s$	relaxation time
$\lambda$	$a.u.$	eigenvalue (only used in chap. A)
$\lambda_{Lame}$	$Pas$	first Lamé constant
$\lambda_w$	$mm$	wavelength
$\nu_0$	$Hz$	excitation frequency
$\nu_{DAQ}$	$Hz$	sampling rate
$\nu_l$	$Hz$	lower end of a frequency interval
$\nu_{Nyquist}$	$Hz$	Nyquist frequency

$\nu_h$	<i>Hz</i>	higher end of a frequency interval
$\nu_{Poisson}$	–	Poisson number
$\rho$	<i>kg/m<sup>3</sup></i>	density
$\sigma$	<i>Pa</i>	stress
$\sigma_\Gamma$	<i>Pa</i>	stress of to the surface tension
$\sigma_{ij} = \tau_{ij}$	<i>Pa</i>	components of the stress tensor
$\sigma_{noise}$	<i>a.u.</i>	standard deviation of the noise
$\sigma_{std}(\dot{\gamma})$	<i>bar</i>	standard deviation of $\dot{\gamma}(t)$ as function of $\dot{\gamma}$
$\sigma_{std,E}(\dot{\gamma})$	<i>bar</i>	standard deviation of the elongational viscosity
$\sigma_{yield}$	<i>Pa</i>	yield stress
$\tau$	<i>s</i>	correlation time
$\tau_H$	<i>Pa</i>	stress in a Hooke element
$\tau_N$	<i>Pa</i>	stress in a Newton element
$\tau_0$	<i>Pa</i>	stress amplitude
$\theta$	°or rad	angle between two vectors
$\vartheta$	°C or K	temperature
$\vartheta_0$	°C	ambient temperature
$\vartheta_g$	°C or K	glass transition temperature
$\vartheta_m$	°C	melting point
$\vartheta_{VF}$	°C or K	Vogel-Fulcher temperature
$\Omega_0$	<i>Hz</i>	frequency interval
$\omega$	<i>rad/s</i>	variable angular frequency
$\omega_0$	<i>rad/s</i>	excitation angular frequency

## Operators and Special Notations

$\Delta \langle \bullet \rangle$	–	difference of two states of $\langle \bullet \rangle$
$\delta(\langle \bullet \rangle)$	–	infinitesimal small value of $\langle \bullet \rangle$
$\langle \dot{\bullet} \rangle$	–	fluctuation part of $\langle \bullet \rangle$
$\langle \bullet \rangle'$	–	real part of $\langle \bullet \rangle$
$\langle \bullet \rangle''$	–	imaginary part of $\langle \bullet \rangle$
$\langle \bullet \rangle^*$	–	$\langle \bullet \rangle$ is a complex number/function
$\langle \widehat{\bullet} \rangle$	–	value of $\langle \bullet \rangle$ will be redefined in the equation
$\langle \overline{\bullet} \rangle$	–	mean value of $\langle \bullet \rangle$
$\langle \bullet \rangle_{\vec{r}}$	–	spatial origin of $\langle \bullet \rangle$
$\langle \bullet \rangle^e$	–	ensemble average of $\langle \bullet \rangle$
$\dot{\langle \bullet \rangle}$	–	first order time derivative of $\langle \bullet \rangle$
$\ddot{\langle \bullet \rangle}$	–	second order time derivative of $\langle \bullet \rangle$
$\vec{\langle \bullet \rangle}$	–	$\langle \bullet \rangle$ is a cartesian vector
$\langle \bullet \rangle _f$	–	function $\langle \bullet \rangle$ for a constant value of $f$

---

## Mathematical Spaces and Sets

$\{x, y, z\}$	– cartesian coordinate system
$\{r, \varphi, z\}$	– cylindrical coordinate system
$\vec{e}_i$	– covariant vector basis
$\vec{e}^i$	– contravariant vector basis
$\mathbb{C}$	– set of complex numbers
$\mathbb{E}$	– Euclidian vector space
$\mathbb{I}$	– interval used for the DACF
$\mathbb{N}$	– set of integer numbers
$\mathbb{R}$	– set of real numbers
$\mathbb{K}, \mathbb{L}, \mathbb{M}, \mathbb{V}$	– special defined sets of numbers
$\mathcal{E}, \mathcal{M}, \mathcal{L}$	– point spaces

## Indices

$\langle \bullet \rangle_{i,j,k,l,m,n,o,p,q,r,s}$	– counting indices for $\langle \bullet \rangle$
$\langle \bullet \rangle_0$	– initially set value of $\langle \bullet \rangle$
$\langle \bullet \rangle_{app}$	– apparent value of $\langle \bullet \rangle$
$\langle \bullet \rangle_{char}$	– characteristic value of $\langle \bullet \rangle$
$\langle \bullet \rangle_{contact}$	– the value of $\langle \bullet \rangle$ refers to a contact area
$\langle \bullet \rangle_{cross}$	– crossover value of $\langle \bullet \rangle$
$\langle \bullet \rangle_{die}$	– value of $\langle \bullet \rangle$ concerns a die of an extruder or a capillary rheometer
$\langle \bullet \rangle_{error}$	– error term of $\langle \bullet \rangle$
$\langle \bullet \rangle_{extr}$	– the value $\langle \bullet \rangle$ refers to extrudate
$\langle \bullet \rangle_{fit}$	– the value $\langle \bullet \rangle$ refers to a fit function
$\langle \bullet \rangle_{image}$	– the value $\langle \bullet \rangle$ results from an image
$\langle \bullet \rangle_{inst}$	– the value $\langle \bullet \rangle$ refers to a melt flow instability
$\langle \bullet \rangle_{local}$	– locally determined value of $\langle \bullet \rangle$
$\langle \bullet \rangle_{max}$	– maximum value of $\langle \bullet \rangle$
$\langle \bullet \rangle_{min}$	– minimum value of $\langle \bullet \rangle$
$\langle \bullet \rangle_{ref}$	– reference value of $\langle \bullet \rangle$
$\langle \bullet \rangle_{strike}$	– value of $\langle \bullet \rangle$ during the filament stretch phase
$\langle \bullet \rangle_{true}$	– true value of $\langle \bullet \rangle$
$\langle \bullet \rangle_{F,n}$	– $\langle \bullet \rangle$ is the Fourier coefficient with the number $n$

## Abbreviations

<b>ACF</b>	autocorrelation function
<b>ADC</b>	analog-digital converter
<b>ASTM</b>	American society of testing and materials
<b>CaBER</b>	capillary break-up extensional rheometer
<b>CCD</b>	coupled charged device
<b>CCF</b>	cross correlation function
<b>CMOS</b>	complementary metal oxide semiconductor
<b>COD</b>	coefficient of determination
<b>DACF</b>	discrete autocorrelation function
<b>DACVF</b>	discrete autocovariancy function
<b>DAQ</b>	data acquisition
<b>DFT</b>	discrete Fourier transform
<b>DOP</b>	dioctylphthalate
<b>FFT</b>	fast Fourier transform
<b>FT</b>	Fourier transform
<b>FT-R</b>	Fourier transform- rheology
<b>GMF</b>	gross melt fracture
<b>HDPE</b>	high density polyethylene
<b>LDA</b>	LASER Doppler anemometry
<b>LAOS</b>	large amplitude oscillatory shear
<b>LASER</b>	light amplification by stimulated emission of radiation
<b>LCB</b>	long chain branched
<b>LDPE</b>	low density polyethylene
<b>LDV</b>	LASER-Doppler velocimetry
<b>LLDPE</b>	linear low density polyethylene
<b>MAOS</b>	medium amplitude oscillatory shear
<b>MDPE</b>	medium density polyethylene
<b>MFI</b>	melt flow instability
<b>NBR</b>	nitrile butadiene rubber
<b>NoForGe</b>	normalforce geometry
<b>ODE</b>	ordinary differential equation
<b>PCL</b>	Ponal-Classic
<b>PDI</b>	polydispersity index
<b>PDMS</b>	polydimethylsiloxane
<b>PE</b>	polyethylene
<b>PET</b>	polyethylene-terephthalate
<b>PEX</b>	Ponal-Express
<b>PP</b>	polypropylene
<b>PS</b>	polystyrene
<b>PTFE</b>	polytetrafluoroethylene

---

<b>PU</b>	polyurethane
<b>PUR</b>	polyurethane
<b>PVAc</b>	polyvinylacetate
<b>SAOS</b>	small amplitude oscillatory shear
<b>SCB</b>	short chain branched
<b>SEC</b>	size exclusion chromatography
<b>SNR</b>	signal-to-noise ratio
<b>SSD</b>	sharkskin die
<b>TTS</b>	time temperature superposition
<b>WLF</b>	Williams-Landel-Ferry



# Chapter 1

## Introduction

The term rheology was coined in the early 20th century. Its linguistic origin lies in the ancient Greek words  $\rho\epsilon\omega$  meaning 'flow' and  $\lambda\omicron\gamma\omicron\varsigma$  meaning 'word' or 'science'. Rheology, the science of flows, was introduced as an own branch of science in 1929 by E.C. Bingham\* and M. Reiner<sup>†,3,4</sup>

Rheology studies the flow behaviour and the deformation behaviour of physical matter. It is closely related to mechanics and fluid dynamics. Most of the problems in classical fluid mechanics can be analysed with the Navier<sup>‡</sup>-Stokes<sup>§</sup> equations. The Navier-Stokes equations are only valid for the flow of viscous and not shear rate dependent (Newtonian) fluids<sup>¶</sup>. Thus, the Navier-Stokes equations are useful for low molecular fluids, i.e. water, alcohol, mineral oils, etc.. For more advanced applications, e.g. in chemical engineering, the flows of more complex materials (non-Newtonian) are of interest. One of the best known non-Newtonian effect

---

\* Eugene Cook Bingham (\*8. December 1878 in Cornwall, USA; +6. November 1945, USA) was an American scientist and a founder member of the society of rheology (SOR) in 1929. See vol. 1 iss. 1 of the J. Rheol. in 1929 p.93-95.<sup>2</sup>

† Markus Reiner (\*5. January 1886 in Czernowitz, Austro-Hungarian Empire; +25. April 1976 in Isreal) was an Israeli engineer and rheologist. He was a founder member of the society of rheology (SOR) in 1929.<sup>3</sup>

‡ Claude-Louis Marie Henrie Navier (\*10. February 1785 in Dijon, France; +21. August 1836 in Paris, France) was a French engineer and physicist.<sup>5</sup>

§ Sir George Gabriel Stokes (\*13. August 1819 in Skreen, Ireland; +1. February 1903 in Cambridge, England) was an English mathematician and physicist.<sup>5</sup>

¶ The term Newtonian fluid is explained in chap. 2.3.1.

is the Weissenberg<sup>11</sup>-effect, also called rod climbing of a viscoelastic fluid.

**Example 1. The Weissenberg effect**

*A non-Newtonian (viscoelastic) fluid (thin dough) is filled in a beaker and steered with a rod, as seen in fig. 1.1c. It can be observed that the viscoelastic fluid moves upwards on the rod while it is steered, see fig. 1.1a. This is in contrast to the observation made for a Newtonian fluid, see fig. 1.1b, which has a concave surface shape when steered strongly (see fig. 1.1d).*

□

The example showed that the flow behaviour of complex materials can be completely different than that of Newtonian fluids. Thus, the complex fluids are insufficiently described by the theory of Newtonian fluids. Many different fluids show non-Newtonian fluid behaviour, e.g. polymeric\* liquids (polymer solutions and polymer melts), adhesives, synthetic oils, slurry, dough, molten metals and often some multi-phase flows (e.g. emulsion, dispersions).

In fig. 1.2 different types of flow behaviour are shown. The viscous fluid is represented by the flow curve<sup>†</sup> of the Newtonian fluid (fig. 1.2e). The flow curves of fig. 1.2a - d represent non-Newtonian flow behaviour, i.e. dilatant materials (fig. 1.2c), pseudoplastic materials (fig. 1.2c), ideal-plastic materials (fig. 1.2d) or the Bingham fluids (fig. 1.2a). The mathematical description of the non-Newtonian fluids needs appropriate equations. One aspect of rheology is to determine these equations supported by the rheometry. Rheometry delivers the experimental data to set up and to validate different non-Newtonian rheological models. Since M. Couette<sup>‡</sup> many different instruments for measuring the non-Newtonian flow behaviour of complex materials have been invented, i.e. the cone-plate rheometer by Mooney,<sup>9</sup> the Weissenberg Rheogoniometer,<sup>10</sup> the sliding plate

---

<sup>11</sup> Karl Weissenberg (★11. June 1893 in Vienna, Austria; †6. April 1976 in Den Haag, Netherlands) was an Austrian physicist and rheologist.<sup>6</sup>

\* The word polymer is composed by the two ancient Greek words πολυ meaning 'much' or 'a lot' and μέρος meaning 'part'. Therefore, a polymer is something made out of many parts. Polymers are macromolecules (large molecules).

† The graphical representation of the shear rate  $\dot{\gamma}_{xy}$  dependent shear stress  $\tau_{xy}$  ( $\dot{\gamma}_{xy}$ ) for a fluid is called the flow curve.

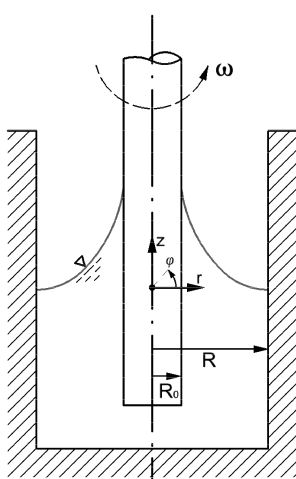
‡ Maurice Marie Alfred Couette (★9. January 1858 in Tours, France; †18. August 1943 in Angers, France) was a French physicist and rheologist. He invented the Couette viscosimeter.<sup>7,8</sup>



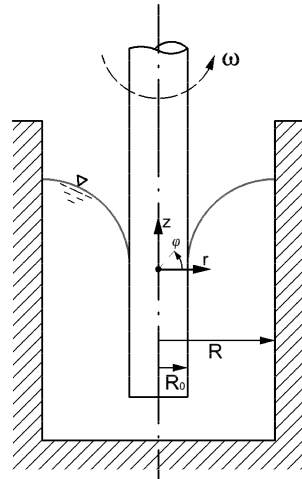
(a)



(b)



(c)



(d)

**Figure 1.1.** – Comparison of the rod climbing behaviour of (a) a non-Newtonian fluid (dough) and (b) a Newtonian fluid (dispersion colour). A drop of dark ink was added to colour the sample at the rim of the beaker for a better visualization. In (c) the principle of the rod climbing of a viscoelastic fluid is shown and in (d) the principle of the Newtonian fluid is shown.

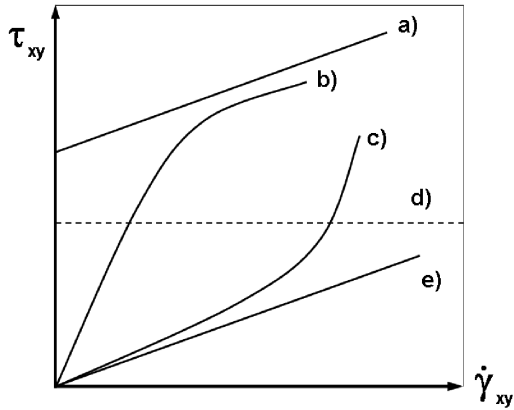


**Figure 1.2.** – Characteristic flow curves  $\tau_{xy}(\dot{\gamma}_{xy})$  for different materials: (a) a Bingham fluid, (b) a pseudoplastic fluid, (c) a dilatant fluid, (d) an ideal plastic body and (e) a Newtonian fluid.

rheometer,<sup>11,12</sup> to name just a few. The fundamental demand on such experimental devices is that the kinematic flow inside the instrument is well defined and that this flow is as simple as possible. The latter demand is the reason why some old devices are still widely in use (like the Couette viscosimeter), whereas some others vanished quickly or never made it to a broad use (like the sliding plate rheometer).

Coming back to the topic of complex fluids, especially the field of polymeric liquids (e.g. polymer melts) is of large economical interest. The annual production of polymers has been increasing nearly continuously since 1950.<sup>13,14</sup> In 2010, about  $250 \cdot 10^6$  t of polymer were produced.\* The reason for this lies in the partly excellent material properties of polymers. They typically have a low density ( $\rho \approx 1 \text{ g/cm}^3$ ), while at the same time their mechanical properties, e.g. their stiffness, are sufficiently large. Thus, they can be used instead of classical materials, e.g. wood or steel. Another big advantage of polymers is their easy processibility in comparison to the classical materials which they replace. Polymers<sup>†</sup> can easily be shaped

\* Source: [www.plasticseurope.org](http://www.plasticseurope.org)

† In this introduction polyethylene (PE) and polypropylene (PP) as known from daily life (e.g. plastic bags) are used as an object of illustration. More information about polymers is given in chap. 2.4.

---

by melt flow injection or extrusion. The temperature at which most polymers become liquid or liquid-like is low; about 100 - 280 °C. Thus, the amount of energy needed for the production is reduced in comparison to e.g. steel. Additionally, the energy demand to recycle thermoplastic\* polymers is much lower than that for metals.<sup>14</sup>

For the processing methods mentioned above, e.g. melt flow injection, the polymer melt is processed at high shear rates, at which the non-Newtonian flow behaviour of polymer melts becomes evident (e.g. see chap. 4.2). Nevertheless, the flow behaviour of polymeric liquids has to be understood in order to optimize the fabrication of the products and to avoid inefficient and wasteful<sup>†</sup> processes. For this, the common rheometric instruments have to be improved to further enlarge the knowledge about polymeric flows.

The scope of this thesis is to improve the measuring capabilities of three different rheometric devices. Furthermore, additional information is obtained about the non-Newtonian properties of the samples.

---

\* Explained in chap. 2.4.

† In this context, wasteful means both physical waste by polymer products with poor quality and waste of electrical and thermal energy.

## 1.1 Thesis Outline

This thesis contains four main chapters with fundamentals and applications of the rheometric methods and a supplementary appendix with additional information. Different text objects, for i.e. definitions, algorithms, assumptions and examples, are used to structure the text clearly and to highlight paragraphs which are not part of the main text of a chapter.

Chap. 2 provides the theoretical background which is needed in all three subsequent chapters. It begins in chap. 2.1 with an introduction to the mathematical methods used for the analysis of the data, namely the detailed description of the Fourier-analysis and the correlation functions. This is followed by a part about data acquisition systems in chap. 2.2. The fundamentals of the mechanical description of materials is provided by chap. 2.3. It introduces the fundamental models of rheology which describe the flow of different materials. The last section in chap. 2, chap. 2.4, is specifically dedicated to polymeric materials. This part contains information about molecular structure and general physical properties of common polymers.

The three chapters chap. 3 - chap. 5 are dedicated to the actual work of research within this thesis. Each of those chapters focuses on a specific type of rheometric experiment, see fig. 1.3. These three different types are:

- The oscillatory shear flow (with the rotational shear rheometer); chap. 3
- The high shear rate steady state flow (with the extruder and the capillary rheometer); chap. 4
- The elongational flow (with the extensional rheometer); chap. 5

Each of the following three chapters contains an introduction, the respective theory, the results and the conclusion for the actual field of investigation.

Chap. 3 shows the work concerning the application of a highly sensitive measurement of normal forces in the plate - plate rotational rheometer. Already Weissenberg<sup>15</sup> worked in this field of rheology, but as shown in the introduction to chap. 3.1, there are still open questions. The theory of oscillatory experiments is introduced in chap. 3.2. To complete the introduction of oscillatory shear experiments, chap. 3.3 gives an overview

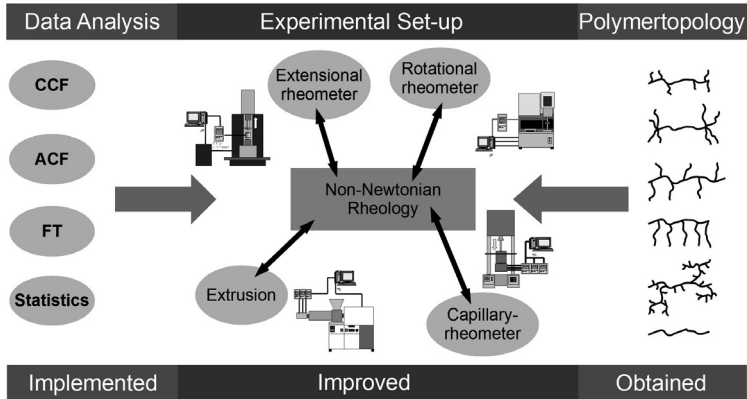


**Figure 1.3.** – Fields of application for this thesis. With the improved rheometric instruments and a specially implemented data analysis polymers of different topology can be studied.

of the FT-Rheology (FT-R), which was introduced by Wilhelm.<sup>16</sup> The experimental set-up and the newly applied changes on the set-up are described in chap. 3.4 - chap. 3.5. In chap. 3.6 the state-of-the-art analysis of the data is improved by the application of a non-linear parameter for the measurement of the normal force. The experimental set-up is validated in chap. 3.7. The application of the new set-up to polymers of different topologies is shown in chap. 3.9. The progress made in this part is summarized in chap. 3.10.

The second part of this thesis concerns the topic of polymer extrusion and melt flow instabilities. The chapter begins with an introduction and a definition of the aim in chap. 4.1. In chap. 4.2 melt flow instabilities are defined. The aim of this work is to transfer the sharkskin die technology from the capillary rheometer to an extruder. The set-up of the capillary rheometer is shown in chap. 4.3. The subsequent section chap. 4.4 contains the information of the construction of the new dies for the extruder and the description of the extruder set-up. For the analysis of the pressure fluctuations measured on the extruder mathematical specialities have to be considered. These are explained in chap. 4.4.4. The set-up to optically study the melt flow instabilities is introduced and validated in chap. 4.4.6. A survey of the experimental settings follows in chap. 4.4.7. The three con-

secutive sections will discuss the experimental results achieved with the new dies; see chap. 4.5. These sections provide a validation of the capabilities of the sharkskin dies, chap. 4.5.1, and a comparison between optical methods and sharkskin die, chap. 4.5.4. The findings of the extruder set-up and the related analysis are concluded in chap. 4.6.

The last experimental chapter is towards the improvement of the capillary break-up extensional rheometer (CaBER) with an axial force measurement, as explained in chap. 5.1. Chap. 5.1.1 introduces the principle of the basic CaBER experiment. The improvement of the CaBER with an axial force measurement requires an adaption of the related theory. Chap. 5.2 - chap. 5.2.3 describe the extension of the related theory of the CaBER. These sections are followed by a description of the state-of-the-art experimental set-up, chap. 5.3 and chap. 5.3.1, and a description of the improvements applied in this work in chap. 5.3.2 - chap. 5.4. The experimental results are divided into two parts (sections). The first part validates the application of the improved CaBER, chap. 5.5.1, and the second part, chap. 5.5.3, presents a new field of application, the observation of the curing behaviour of adhesives. These measurements are similar to tack measurements. Finally, the results and achievements of the improvement of the CaBER are summarized in chap. 5.6.

Conclusions of the whole thesis and prospects for the work are given in chap. 6.

## Chapter 2

# Data Acquisition, Data Analysis and Material Properties

This chapter summarizes the basic concepts of

- the applied mathematical data analysis (chap. 2.1),
- the description of measurement systems (fig. 2.2),
- the mechanical properties (chap. 2.3) of materials and
- the chemical properties (chap. 2.4) of the investigated materials.

## 2.1 Mathematical Methods for Data Analysis

One part of this thesis is to implement data analysis algorithms for the data, i.e. the time-dependent pressure, the time-dependent shear stress, the time-dependent normal force and digital images, obtained by the different mechanical experiments. The simplest method to analyse data is to calculate statistical moments of different order, e.g. the mean value or the standard deviation. Statistical moments are a basic mathematical tool and details can be found in the book of e.g. Bendat et al.<sup>17</sup> More advanced methods of data analysis that include implicitly the time-dependence, i.e. the autocorrelation function (ACF) and the Fourier transform (FT), are introduced in this section. Furthermore, the FT and the ACF are additionally presented in terms of discrete sets of data.

## 2.1.1 Fourier Series

The Fourier series<sup>18–21</sup> is used to express infinite functions and signals as a superposition of periodic trigonometric functions. In case of a finite signal the signal will be periodically continued. This means that the longest period is given by the complete length of the finite time series  $T_{max}$ . This defines also the spectral resolution (see chap. 2.1.3).

Every periodic signal can be approximated via the superposition of basic trigonometric functions (i.e. sine, cosine). The resulting time series is named after J. Fourier\*, the Fourier series.

$$f(t) = \sum_{n=-\infty}^{+\infty} (a_{F,n} \cos(\omega_0 nt) + b_{F,n} \sin(\omega_0 nt)), \quad \forall n \in \mathbb{N}. \quad (2.1)$$

Eq. 2.1 uses the angular frequency as given by

$$\omega_0 := 2\pi\nu_0 := \frac{2\pi}{T}. \quad (2.2)$$

In eq. 2.1 the so-called Fourier coefficients  $a_{F,n}$  and  $b_{F,n}$  appear. They are defined by the following three equations<sup>21</sup>

$$a_{F,0} = \frac{2}{T} \int_0^T f(t) dt \quad \text{for } n = 0, \quad (2.3)$$

$$a_{F,n} = \frac{2}{T} \int_0^T f(t) \cos(nt) dt \quad \text{for } n > 0 \text{ and} \quad (2.4)$$

$$b_{F,n} = \frac{2}{T} \int_0^T f(t) \sin(nt) dt. \quad (2.5)$$

Due to the symmetry of the trigonometric functions<sup>†</sup> the Fourier series is reduced to

$$f(t) = \frac{a_{F,0}}{2} + \sum_{n=1}^{+\infty} (a_{F,n} \cos(\omega_0 nt) + b_{F,n} \sin(\omega_0 nt)). \quad (2.6)$$

\* Jean Baptiste Joseph Fourier, (\*21. March 1768 by Auxerre, France; †16. May 1830 in Paris, France) was a French mathematician and physicist.<sup>5</sup>

† Symmetry properties of the trigonometric functions:

$$\begin{aligned} \text{odd: } \sin(t) &= -\sin(-t) \text{ and} \\ \text{even: } \cos(t) &= \cos(-t). \end{aligned}$$

In eq. 2.6, the Fourier coefficients are given by

$$\begin{aligned}\mathfrak{A}_{F,n} &= \mathfrak{a}_{F,n} + \mathfrak{a}_{F,-n} \text{ and} \\ \mathfrak{B}_{F,n} &= \mathfrak{b}_{F,n} - \mathfrak{b}_{F,-n}.\end{aligned}\tag{2.7}$$

The Fourier series, as a sum of sine and cosine terms, can be easily brought into a complex form as

$$f(t) = \sum_{n=1}^{+\infty} \mathfrak{C}_{F,n} e^{i\omega_0 n t}\tag{2.8}$$

with the complex Fourier coefficients

$$\mathfrak{C}_{F,n} = \frac{2}{T} \int_0^T f(t) e^{-i\omega_0 n t} dt.\tag{2.9}$$

**Example 2. Fourier series of the rectangular function**

For the rectangular function with a period of  $T = 4\pi$  the Fourier series of different orders  $n$  is shown in fig. 2.1a - fig. 2.1d. It is obvious from the plots in fig. 2.1 that the Fourier series approximates better the original function with increasing order  $n$ . Attention should be paid to the overshoots of the Fourier series which are visible for all orders  $n$ . This phenomenon is called the Gibbs\* phenomenon and is typical for the Fourier series. □

## 2.1.2 Fourier Transform

The representation via discrete frequencies is sufficient for a periodic function with a period of  $T < \infty$ . However, in the case of  $T \rightarrow \infty$  (aperiodic limit) the summation is transformed into an integration and the discrete set of frequencies is transformed into a continuous spectrum of frequencies. This representation via an integration is called the Fourier transform or Fourier integral of a function  $f(t)$  and is given by<sup>18,22</sup>

$$F(\omega) = \int_{-\infty}^{+\infty} f(t) e^{-i\omega t} dt.\tag{2.10}$$

\* Josiah Willard Gibbs, (\*11. February 1839 in New Haven, USA; †28. April 1903 in New Haven, USA) was an American theoretical physicist, chemist and mathematician.<sup>5</sup>

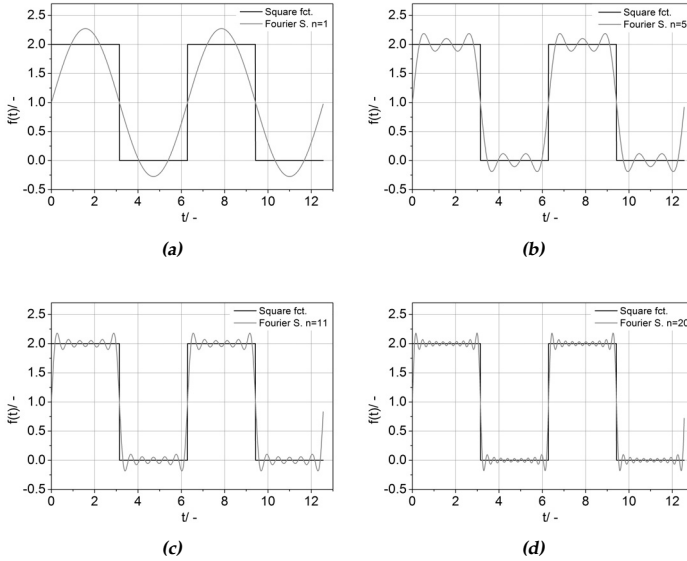


**Figure 2.1.** – Fourier series of a rectangular or square function. The Fourier series is calculated with different orders (a)  $n = 1$ , (b)  $n = 5$ , (c)  $n = 11$  and (d)  $n = 20$ . The black line in each diagram indicates the rectangular function and the grey line the according Fourier series of order  $n$ .

The symmetry properties of the  $f(t)$  are also valid for its Fourier transform  $F(\omega)$ . The Fourier transform is a completely invertible transformation, so the inverse transformation from the frequency domain back into the time domain is analogously defined as

$$f(t) = \frac{1}{2\pi} \int_{-\infty}^{+\infty} F(\omega) e^{+i\omega t} d\omega. \quad (2.11)$$

A short summary of the properties of the Fourier transform can be found in chap. B.

### 2.1.3 Discrete Fourier Transform

For the application in signal processing the integral formalism of the FT is not useful. While measuring a discrete set of data points,  $f_k$  is achieved and this set is a finite one (with  $N$  data points) and not infinite. Due to this point, it is necessary to introduce a discrete version of the Fourier Transform,<sup>23</sup> further referred to as the discrete Fourier transform (DFT),

$$F_j = \frac{1}{N} \sum_{k=0}^{N-1} f_k e^{-\frac{i2\pi}{N}kj} \quad \forall k, j \in \mathbb{M} = \{x \mid x \in \mathbb{N}_0, x \leq N\}. \quad (2.12)$$

The backward transformation ( $\text{DFT}^{-1}$ ) is obtained via,

$$f_k = \sum_{j=0}^{N-1} F_j e^{\frac{i2\pi}{N}kj} \quad \forall k, j \in \mathbb{M} = \{x \mid x \in \mathbb{N}_0, x \leq N\}. \quad (2.13)$$

The definition used in eq. 2.13 lacks the prefactor  $\frac{1}{N}$ ; other definitions of the prefactors are possible (e.g.  $1/\sqrt{N}$ ). The eq. 2.12 and eq. 2.13 are written in terms of discrete data points. The index  $k$  indicates the data points in the time domain and  $j$  indicates the data points in the frequency domain. The transformation law between the discrete point space and the variable time  $t$  is given by  $t = k \cdot T/N$ . A similar transformation law holds for the frequency domain  $\omega = j \cdot \pi \cdot \nu_{\text{Nyquist}}/N$ .\*

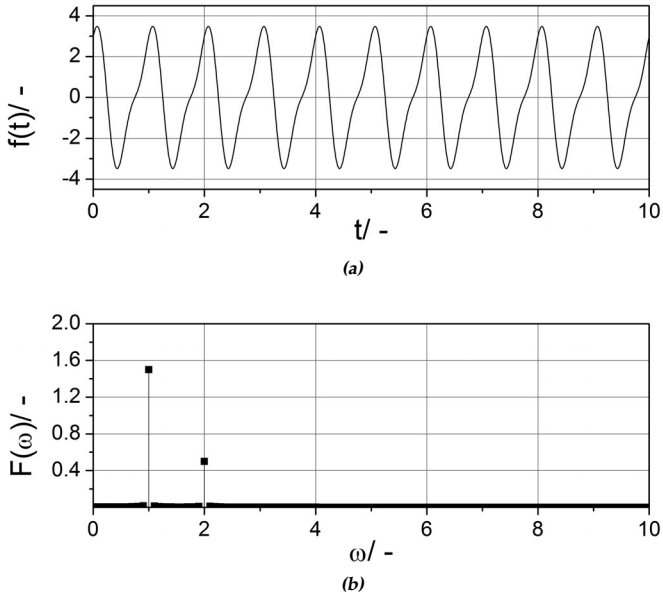
#### Example 3. Application of the DFT

Fig. 2.2 plots the DFT of the discrete data set of the function  $f(t) = 3 \cos(2\pi t) + \sin(4\pi t)$ .<sup>†</sup> The Nyquist<sup>‡</sup> frequency is defined by the parameters used in the program to  $\nu_{\text{Nyquist}} = 50$  Hz. In fig. 2.2 the observation is made that the amplitudes of the peaks in the FT spectrum are only of half the size (i.e.  $F = 1.5$  and  $F = 0.5$ ) than the prefactors from the original equation (i.e.  $F = 3$  and  $F = 1$ ). The

\*  $\nu_{\text{Nyquist}}$  is the Nyquist frequency.<sup>17,24</sup> It is the highest frequency which can be measured and is explained in chap. 2.2.

† This calculation used a self-written program using the MATLAB software. MATLAB is a programming environment system for numerical calculations.<sup>25</sup> Especially, this program made use of the function `fft()`, which is based on the FFTW (Fastest Fourier Transform of the West) algorithm.<sup>26</sup> This algorithm is widely used for the computation of the FFT. It optimizes the FFT algorithm according to the data set and the used computer hardware.

‡ Harry Nyquist (\*7. February 1889 in Nilsby, Sweden; †4. April 1976 in Harlingen; USA) was an American electrical engineer and physicist.<sup>27</sup>



**Figure 2.2.** – DFT of a data set obtained from the function  $f(t) = 3 \cos(2\pi t) + \sin(4\pi t)$ . (a) the time-dependent function and (b) the frequency-dependent spectrum.

*FT spectrum of a function or signal contains usually both positive and negative frequencies. The axis of ordinate is a mirror axis and the spectrum at negative frequencies and the axis at positive frequencies have got peaks at the same absolute value of the frequency. Both peaks have the same amplitude, the half amplitude of the one in the according original function or data. Thus, if the amplitude of both peaks is summed up it will be the value of the original function or data. □*

## 2.1.4 Window Functions

The FT requires that the function  $f(t)$  can be proceeded continuously. In the application of the data acquisition (DAQ) all sets of time-dependent data are finite. Thus, a direct FT of these data can be problematic, as fig. 2.3 shows. Whereas, the function of fig. 2.3a can be continuously proceeded, the function in fig. 2.3c cannot be continuously proceed. Therefore, the FT of fig. 2.3a, shown in fig. 2.3b, shows very sharp peaks. Whereas, the FT of fig. 2.3c, shown in fig. 2.3d, shows broad peaks with reduced amplitude. This phenomenon is called leakage. The intensity of the sharp (single point) peak is distributed to several points.

One possible way to avoid or reduce the leakage is to use window functions<sup>23,28,29</sup>  $w(t)$ . Window functions are special mathematical function, e.g. a Gaussian\* function or a von-Hann† window, see tab. 2.1 and fig. 2.4, which are multiplied with the function in the time domain in order to force the function to be continuously proceeded. The multiplication in the time domain represents a convolution in the frequency domain,<sup>22</sup> see chap. B. The general properties of window functions are:

1. They are always even functions.
2. Their FT does not have an imaginary part.

The quality of a window function can be quantified e.g. by the intensity of the central peak and by the 3-dB bandwidth. The intensity of the central peak in the frequency domain should be as large as possible. This causes the side-loops to be as small as possible.

The application of a window function demands the choice of one or more parameters which are used in the chosen window function, as seen in

---

\* Carl Friedrich Gauß (\*30. April 1777 in Brunswick, Germany; †23. February 1855 in Göttingen; Germany) was a German mathematician and physicist. Due to his maxim "Pauca, sed matura." (Few, but mature) he published only a small part of his work during his lifetime.<sup>5</sup>

† Julius Ferdinand von Hann (\*23. March 1839 by Linz, Austria; †1. October 1921 in Vienna; Austria) was an Austrian meteorologist. He influenced largely the modern meteorology.<sup>5</sup>

‡ Hendrik Anton Lorentz (\*18. July 1853 in Arnhem, Netherland; †4. February 1928 in Harlem, Netherlands) was a Dutch theoretical physicist. He obtained the Nobel prize in physics in 1902 "in recognition of the extraordinary service they rendered by their researches into the influence of magnetism upon radiation phenomena".<sup>5</sup>

**Table 2.1.** – Examples of frequently used window functions in the time domain. Their representation in the frequency domain is given in tab. 2.2.<sup>23</sup>

window	function in the time domain (t)
rectangular	$w(t) = \begin{cases} 1, & -\frac{T}{2} \leq t \leq \frac{T}{2} \\ 0 & \text{else} \end{cases}$
von Hann	$w(t) = \begin{cases} \cos^2 \frac{\pi t}{T}, & -\frac{T}{2} \leq t \leq \frac{T}{2} \\ 0, & \text{else} \end{cases}$
Hamming	$w(t) = \begin{cases} \mathfrak{C} + (1 - \mathfrak{C}) \cos^2 \frac{\pi t}{T}, & -\frac{T}{2} \leq t \leq \frac{T}{2} \\ 0, & \text{else} \end{cases}$
Gauß	$w(t) = e^{-\frac{\mathfrak{C}t^2}{2}}$
exponential	
decay	$w(t) = e^{-\mathfrak{C} t }$

**Table 2.2.** – Examples of the representation in the frequency domain of the frequently used window functions of tab. 2.1.<sup>23</sup>

window	Fourier transform in the frequency domain ( $\omega$ )
rectangular	$ W(\omega) ^2 = \left( \frac{\sin(\omega \frac{T}{2})}{\omega \frac{T}{2}} \right)^2 = \left  \text{sinc} \left( \omega \frac{T}{2} \right) \right ^2$
von Hann	$W(\omega) = \frac{T}{4} \sin \left( \frac{\omega T}{2} \left( \frac{1}{\pi - \omega \frac{T}{2}} + \frac{2}{\omega \frac{T}{2}} - \frac{1}{\pi + \omega \frac{T}{2}} \right) \right)$
Hamming	$W(\omega) = \frac{T}{4} \sin \left( \frac{\omega T}{2} \left( \frac{1 - \mathfrak{C}}{\pi - \omega \frac{T}{2}} + \frac{2(1 + \mathfrak{C})}{\omega \frac{T}{2}} - \frac{1 - \mathfrak{C}}{\pi + \omega \frac{T}{2}} \right) \right)$
Gauß	$W(\omega) = \frac{1}{\sqrt{\mathfrak{C}}} e^{-\frac{\omega^2}{2\mathfrak{C}}}$
exponential	
decay	$W(\omega) = \frac{1}{\sqrt{\frac{2}{\pi}}} \frac{\mathfrak{C}}{\omega^2 + \mathfrak{C}^2}$ (Lorentzian <sup>‡</sup> function)

tab. 2.1. The choice of the parameters for the window function defines the

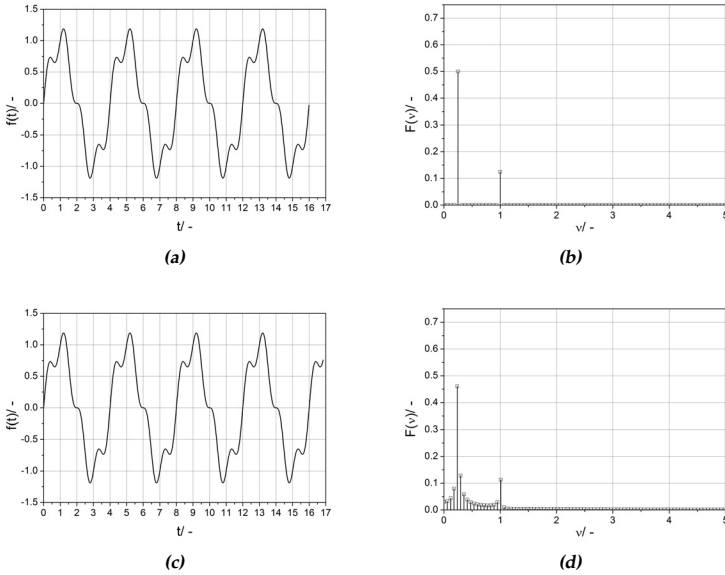


**Figure 2.3.** – Influence of leakage on the FT spectrum. The time-dependent function is  $f(t) = \sin(0.5\pi t) + 0.25 \sin(2\pi t)$ . (a) shows a data set which can be continuously processed. (b) shows the FT of the data from (a) with the magnitude of the sharp peaks of  $F(\omega = 0.25) = 0.5$  and  $F(\omega = 1) = 0.125$ . (c) shows a data set which cannot be continuously processed. (d) shows the FT of the data from (c) with the reduced magnitude of the broad peaks of  $F(\omega = 0.25) = 0.46$  and  $F(\omega = 1) = 0.11$ .

size of the window function. The parameters can be adjusted empirically or by use of reference values from literature.<sup>23</sup>

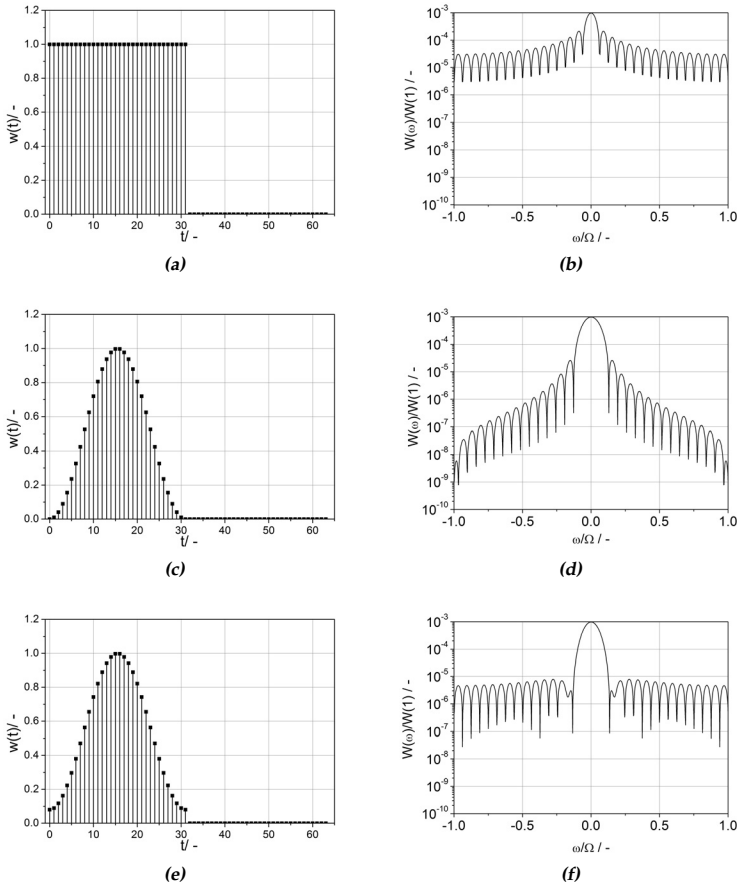


**Figure 2.4.** – Window functions in the time domain and in the frequency space: (a) rectangular function in the time domain, (b) rectangular function in the frequency space, (c) von-Hann window in the time domain, (d) von-Hann window in the frequency space, (e) Hamming window in the time domain, and (f) Hamming window in the frequency space.

## 2.1.5 Autocorrelation Function

The autocorrelation function (ACF)<sup>17,30</sup> of a continuous signal or function  $f(t)$  is defined as

$$r_{ff}(\tau) = \int_0^{\infty} f(t) \cdot f(t + \tau) dt. \quad (2.14)$$

Eq. 2.14 represents a comparison of values of the continuous signal or function. Thus, the ACF reveals the memory of the function using the correlation time  $\tau$  as its variable of choice. The definition of the correlation time is the distance in time between two points of a function.

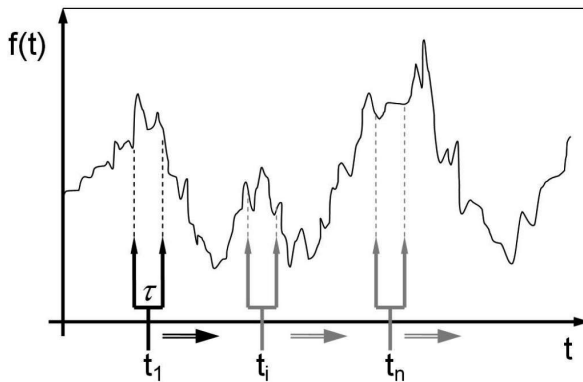


**Figure 2.5.** – The ACF is obtained by correlating all points  $f(t)$  with its neighbours  $f(t + \tau)$  at the temporal distance  $\tau$ .

### Example 4. Illustration of the ACF-algorithm

Fig. 2.5 shows the basic algorithm for the determination of the ACF. If assuming a fixed temporal distance of exact  $\tau$ , every function value  $f(t)$  will be correlated to the function value which is at  $t + \tau$ , namely  $f(t + \tau)$ . These values will be summed up to  $r_{ff}(\tau)$ . This is done for all times  $t$  and for variable correlation times  $\tau$ . This way, the continuous autocorrelation function  $r_{ff}(\tau)$  is obtained.  $\square$

## 2.1.6 Discrete Autocorrelation Function

The ACF is only defined for continuous functions, e.g.  $f(t)$ . This is problematic for discrete experimental data  $f_k$  which depends on discrete data points  $k \in \mathbb{M} = \{x | x \in \mathbb{N}_0, 0 \leq x \leq N\}$ . Therefore, it is necessary to define a discrete autocorrelation function (DACF). For stationary processes, it is valid to assume that they are ergodic\*. For an ergodic process the time average<sup>†</sup> for every particle/point can be replaced by an ensemble average<sup>‡</sup> over all particles.<sup>33,34</sup> By introducing these assumptions into the definition of the autocorrelation function, eq. 2.14 results in the discrete autocorrelation function (DACF)

$$r_{ff,k} = \frac{1}{N} \sum_{j=0}^{N-1-k} f_j f_{j+k}. \quad (2.15)$$

### Example 5. The DACF-algorithm

Fig. 2.7 shows the first two steps of the calculation algorithm of the DACF for a given equidistantly scanned signal as in fig. 2.6. At first (fig. 2.7a), every point is multiplied with its own value. This represents the evaluation of eq. 2.15 for  $j = 0$ . Then, all the values of these multiplications are summed up to a single value representing the autocorrelation function at  $\tau = 0$ . In the next step (fig. 2.7b), the values of every point are multiplied with the value of its right-handed neighbour point (at  $t + j \cdot \Delta t$  with  $j = 1$ ) and afterwards the values of these multiplications are summed up to gain the second point of the autocorrelation function. This procedure is done for all  $j \in \mathbb{M} = \{x | x \in \mathbb{N}_0, 0 \leq x \leq N - 1\}$ .  $\square$

As the summation succeeds for  $j \rightarrow N$ , the number of summands decreases until at last,  $j = N - 1$ , only one multiplication is left. Because of this, the coefficient  $\frac{1}{N}$  of the summation does not any longer represent the used amount of function values. Therefore, this coefficient is replaced by  $\frac{1}{N-k}$ . This provides an unbiased value. The technical term for  $\frac{1}{N-k}$  is a

\* Ergodic Hypothesis:<sup>23,31,32</sup>

$$\bar{f} \rightarrow f^e, \text{ if } T \rightarrow \infty$$

† time average:  $\bar{f} = \lim_{T \rightarrow \infty} \frac{1}{T} \int_{t_0}^{t_0+T} f(\vec{x}, t) dt$

‡ Ensemble average:  $f^e = \lim_{N \rightarrow \infty} \frac{1}{N} \sum_{n=1}^N f_n(\vec{x})$

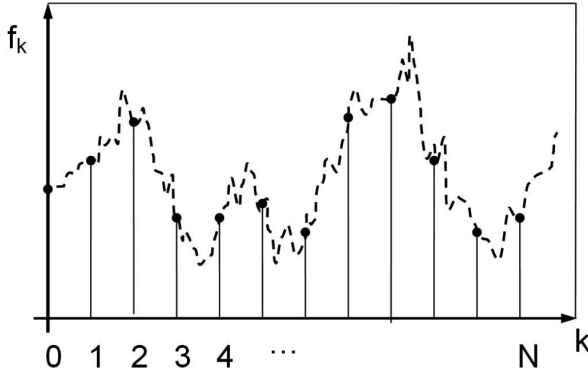


**Figure 2.6.** – Example function. The stroked line ( - - ) describes the continuous physical signal  $f(t)$  and the points (●) are the discrete, but not quantized, measurement points  $f_k$ .

window function (weight function). The unbiased DACF is given by

$$r_{ff,k} = \frac{1}{N-k} \sum_{j=0}^{N-1-k} f_j f_{j+k}. \quad (2.16)$$

The values of the time-dependent function can be arbitrarily large or small and for this reason, the values of the ACF and the DACF as defined right now can also be arbitrarily large. To obtain a better and general comparability of the DACF their values are normalized to the value of the DACF at  $k = 0$  (or  $\tau = 0$ ). Thus, the unbiased normalized DACF is expressed by

$$r_{ff,k} = \frac{1}{N-k} \sum_{j=0}^{N-1-k} \frac{f_j f_{j+k}}{f_j f_j}. \quad (2.17)$$

This normalization of the values of  $r_{ff,k}$  maps the values of the DACF to the interval  $\Pi = [-1, +1]$  and the values of this interval have the following meaning

$$r_{ff,k} = \begin{cases} +1, & \text{total correlation} \\ 0, & \text{no correlation} \\ -1, & \text{total anti-correlation} \end{cases} \quad (2.18)$$

At last it is possible to subtract the expectation value  $\bar{f}$  of the time-dependent data from the time-dependent data. If the DACF is calculated in this

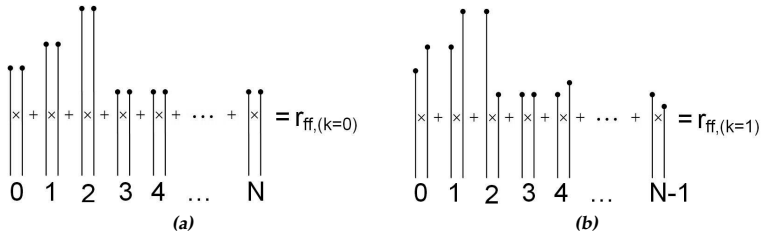


**Figure 2.7.** – The first two steps of the calculation of the DACF for the signal in fig. 2.6. The cross ( $\times$ ) symbolizes the multiplication of the representative values. (a) illustrates the first summation for  $k = 0$ , which represents the  $\tau = 0$ . (b) illustrates the second summation for  $k = 1$ , which represents the  $\tau = 0 + 1 \cdot \Delta t$ .

way it is called discrete autocovariancy function (DACVF)

$$c_{ff,k} = \frac{1}{N-k} \sum_{j=0}^{N-1-k} \frac{(f_j - \bar{f})(f_{j+k} - \bar{f})}{(f_j - \bar{f})(f_j - \bar{f})}. \quad (2.19)$$

In case of a function or data set with the expectation value of zero, the DACF and the DACVF are identical.

## 2.2 Introduction to Data Acquisition

This chapter gives an introduction into the basic terms of data acquisition (DAQ) in experiments. More details about DAQ can be found in the book of Doebelin,<sup>35</sup> Tropea<sup>28</sup> or Holler.<sup>36</sup> Experiments have to be conducted in order to obtain an insight into the physical or chemical processes. In experiments sensors are used to record data of the observed variables. This data is mostly analogously measured. Thus, an analogue signal is transferred from the sensor/ transducer to an amplifying device. This amplifying device usually scales its analogue input to an analogue voltage signal of a defined range. This electrical signal is transferred to a computer with an analogue/digital converter board (ADC board) which transforms the analogue signal into a digital signal. The whole chain starting from the sensor to the ADC board is called the DAQ system.

Depending on the ADC board of the DAQ system the physical signal is discretised both on its time axis and in its amplitude. The discretisation on the time axis is called sampling and depends on the sampling rate of the ADC board. The discretisation in the amplitude is called quantisation\* and depends on the resolution of the ADC board.<sup>17,23</sup> Both quantities define how well the signal can be measured. An example of sampling and quantization is shown in fig. 2.8. If the values of these quantities are badly

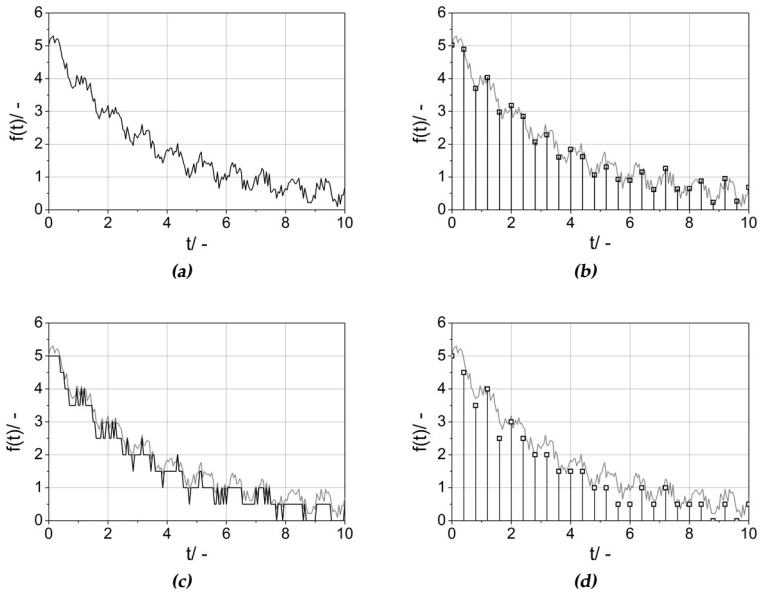


**Figure 2.8.** – Influence of sampling and quantization on the data. The single plots show examples of:

- (a) a continuous analogue data (black line).
  - (b) the continuous analogue data after sampling (with a constant sampling rate) (black squares).
  - (c) the quantization of the analogue data (black line).
  - (d) the sampled and quantized analogue data (black squares).
- In (b) - (d) the grey line is the original analogue data.

\* The term quantisation is related to the quantum mechanics. Where the particle can only access defined (quantized) energy levels.

chosen the data can be corrupted by system-dependent artefacts. One of the best known phenomena is the aliasing which appears if the sampling rate is badly chosen.

**Example 6. Aliasing**

If two periodic signals  $f_1(t) = 2 \sin(9\pi t)$  and  $f_2(t) = 2 \sin(\pi t)$ , as shown in fig. 2.9, are sampled in such a way that all sampled points (the circles in fig. 2.9) lie on both curves. Then, both curves cannot be differentiated from their sampled data. This effect is called aliasing. In case of a Fourier transform (see chap. 2.1.2), the signal with the higher frequency (4.5 Hz) would only have a peak at the lower frequency (0.5 Hz).  $\square$

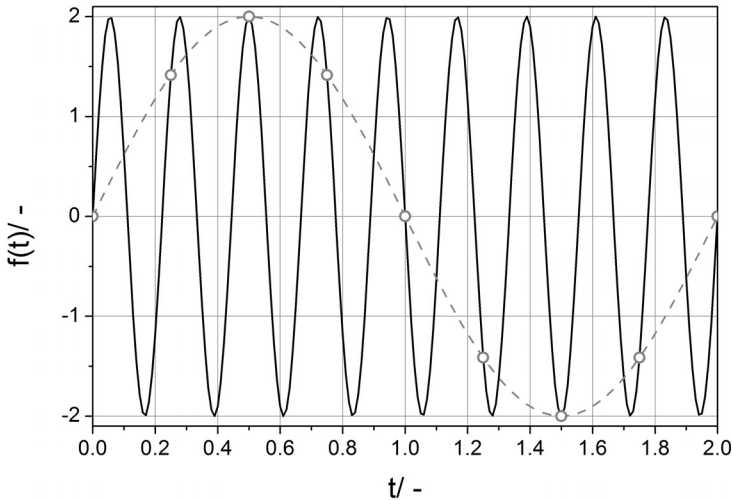


**Figure 2.9.** – An example of aliasing. The black line shows the function  $f_1(t) = 2 \sin(9\pi t)$  and the grey dashed line shows the function  $f_2(t) = 2 \sin(\pi t)$ . The circles represent a sampling with 4 Hz.<sup>24</sup>

In order to avoid aliasing the Nyquist–Shannon\* sampling theorem<sup>17</sup> has to be obeyed. The sampling theorem states that for a measured discrete

\* Claude Elwood Shannon (\*30. April 1916 in Petoskey, USA; †24. February 2001 in Medford; USA) was an American electrical engineer and physicist.<sup>37,38</sup>

signal there exists a maximum frequency which can be detected. This frequency is called the Nyquist frequency<sup>17</sup>  $\nu_{Nyquist}$  and is given by the relation

$$\nu_{Nyquist} = \frac{1}{2\Delta t} \text{ with } \Delta t = \frac{T}{N}. \quad (2.20)$$

The Nyquist frequency is related to the time step  $\Delta t$  of the data acquisition. The next example will illustrate the relationship between the parameters of the DAQ set-up and the Nyquist frequency.

**Example 7. Determination of the Nyquist frequency**

*Assuming an arbitrary measurement of a time-dependent value  $f(t)$  with the duration time of the measurement  $T = 10$  s. The sampling rate of the ADC was set to be  $\nu_{DAQ} = 500$  pts/s. This constraints gives a total amount of measured data of  $N = T \cdot \nu_{DAQ} = 5000$  pts. The time step  $\Delta t = T/N = 0.002$  s. With eq. 2.20 the Nyquist frequency of this measurement is determined to be  $\nu_{Nyquist} = 250$  Hz. This means that any frequency higher than 250 Hz (e.g. 300 Hz) can not be detected by a measurement with the above given sampling rate.  $\square$*

## 2.3 Mechanical Models for Ideal Materials

Materials have specific properties, e.g. optical, electrical, chemical etc.. Those properties have to be characterized to optimize their use. For a technological application, the mechanical properties of a material are often of great importance. For example objects in daily life are characterized by their stiffness (e.g. plastic containers), flexibility (e.g. rubber tires, nylon stockings), flow behaviour (e.g. ketchup, toothpaste) and many more. Chap. 2.3.1 presents widely known concepts of mechanical relationships of basic variables, i.e. the stress or the viscosity. A variety of books about engineering mechanics<sup>4,39</sup> describe them. In chap. 2.3.2 a more advanced description of mechanical variables is given. In addition the stress tensor is introduced. The chap. A gives an introduction into tensor calculus. The tensor calculus is further used to explain the improved description of material behaviour in chap. 2.3.3. More advanced literature references are found for general non-linear flows in text books e.g. Böhme,<sup>40</sup> whereas the behaviour of polymers is discussed in detail in the books of Larson,<sup>41</sup> Dealy,<sup>42</sup> Schwarzl<sup>14</sup> or Lovell.<sup>43</sup> The three sections, chap. 3.2.1 - chap. 3.2.3, focus on the special case of polymer melts<sup>41,43</sup> under oscillatory shear.<sup>44-47</sup> Chap. 3.2.3 - chap. 3.3 explain the experimental set-up and the procedure for the oscillatory shear experiment.\* In the chap. 2.3 the mechanical bodies will be always treated as a continuum. This means that every point of the mechanical body possesses an according mass.<sup>49</sup>

### 2.3.1 Basic Ideas About Mechanical Bodies

It is observed that every real and physical body deforms under an applied stress, or vice versa a mechanical body responds with a certain force to an applied strain (e.g. see Gross<sup>4</sup>). The mechanical response of the body is dependent on its material properties.

For an ideal elastic body, like a spring (see fig. 2.10a), the mechanical properties of a material are defined by the ratio of the stress  $\sigma_{xx}$  and the strain  $\epsilon_{xx}$  (both in x-direction and normal to the y - z plane, chap. 2.3.2). In the

---

\* Generally, the lecture notes of Prof. Wilhelm<sup>48</sup> (KIT) provides a good overview of the rheology of polymers.

most common case the Hooke's law<sup>\*51</sup> for tension is used

$$\sigma_{xx} = E\varepsilon_{xx}. \quad (2.21)$$

The strain is defined as the ratio between deformation  $\Delta x$  and a characteristic length scale  $L_x$ ,

$$\varepsilon_{xx} := \frac{\Delta x}{L_x}. \quad (2.22)$$

In eq. 2.21  $E$  is called the Young's<sup>†</sup> modulus and in the most simple case it is a material-dependent constant. The main assumptions for eq. 2.21 are that the material is isotropic<sup>‡</sup>, simple<sup>§</sup>, and that the deformation is directed only in one direction (uniaxial).

An second fundamental equation exists which relates the shear stress to the shear strain. If a shear strain

$$\gamma_{xy} := \frac{\Delta x}{L_y} \quad (2.23)$$

is applied on a body, as shown in fig. 2.10c, the Hooke's law for shear is used

$$\tau_{xy} = G\gamma_{xy}. \quad (2.24)$$

In eq. 2.24  $\tau_{xy} \equiv \sigma_{xy}$  is the shear stress and  $G$  is the shear modulus.

Both cases of the Hooke's law exhibit a proportional relationship between the stress and the strain. However, they are only valid for simple materials under uniaxial stress or shear. And they can only be applied on materials which show a finite deformation under load.

In contrast to the ideal elastic bodies, an ideal fluid shows an infinite deformation under the load in form of a force. For an ideal viscous fluid, the

\* Robert Hooke (\*28. June 1635 in Freshwater, England; †14. March 1703 in London, England) was an English scientist. Hooke's law was first published in an encoded version in "*A description of helioscopes and some other instruments*"<sup>50</sup> in 1676.<sup>5</sup>

† Thomas Young (\*13. June 1773 in Milverton, England; †10. May 1829 in London, England) was an English physicist.<sup>5</sup>

‡ Isotropic means that the behaviour of a simple material is independent of the direction of the load. If the assumption of a simple material is dropped than the isotropy of a material can be function of the investigated scale.

§ In this context the term simple material stands for an incompressible, homogeneous and frictionless material.

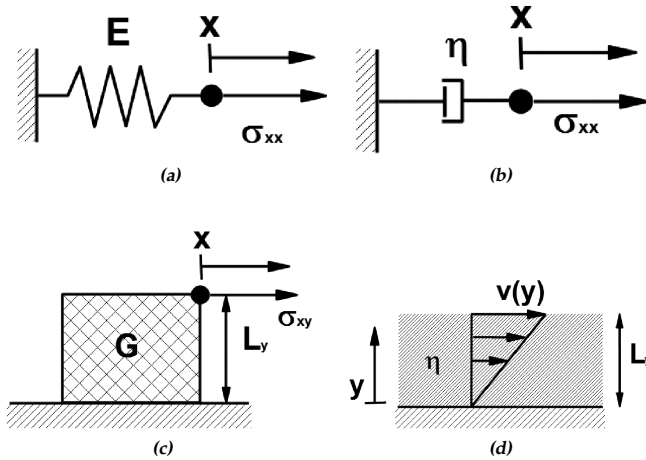


**Figure 2.10.** – Mechanical models as representation of the eq. 2.21, eq. 2.24 and eq. 2.25. (a) an ideal spring, (b) an ideal damper, (c) an elastic body under shear and (d) a Newtonian fluid under shear (with lamellar flow).

governing equation, the Newton's\* law for liquids is

$$\tau_{xy} = \eta \dot{\gamma}_{xy}. \quad (2.25)$$

Eq. 2.25 equals the shear stress  $\tau_{xy}$  in a liquid to the product of the material property, the shear viscosity  $\eta$  and the kinematic value of the shear strain rate

$$\dot{\gamma}_{xy} = d\gamma_{xy}/dt = v(y) / L_y. \quad (2.26)$$

The Newton's law is used for simple shear flows, as in fig. 2.10d. In the mechanical modelling it is formally represented by a dash pot element, as seen in fig. 2.10b.

\* Isaac Newton (\*4. January 1643 in Lincolnshire, England; †31. March 1727 in Kensington, England) was an English physicist and mathematician. His most famous work is the "*Philosophiae Naturalis Principia Mathematica*",<sup>52</sup> in which he states his three fundamental laws of mechanics.<sup>5</sup>

## 2.3.2 The Stress Tensor

Chap. 2.3.1 showed for the case of one dimensional problems, that stress and strain are connected via a material-dependent constant. For an investigation of the material behaviour, a definition of the stress is required. The stress  $\sigma$  is defined as the force\*  $F_x$  applied normal to the surface  $A_x$  of a body. Thus,

$$\sigma_{xx} := \lim_{A_x \rightarrow 0} \frac{F_x}{A_x} = \frac{\delta(F_x)}{\delta(A_x)}. \quad (2.27)$$

For simple materials and uniaxial tension or deformation, the equations from chap. 2.3.1 are sufficient for calculations. For the description of more dimensional load states or complex materials, e.g. anisotropic materials<sup>†</sup> the eq. 2.21 or eq. 2.24 must be written in tensor notation,<sup>‡</sup>

$$\sigma_{ij} = C_{ijkl} \varepsilon_{kl}. \quad (2.28)$$

The stress tensor  $\mathbf{S}$  can be separated in a hydrostatic pressure  $p^{\S}$  and the frictional pressure  $\mathbf{P}$  with the components  $P_{ij}$

$$\sigma_{ij} = p \delta_{ij} + P_{ij}. \quad (2.29)$$

The average normal pressure is expressed through the elements of the main diagonal by using the Einstein<sup>¶</sup> notation,<sup>53,54</sup> as

$$\bar{p} = \frac{1}{3} \sigma_{ii}. \quad (2.30)$$

\* There are two ways to apply a force to a body. The first is via force fields and the resulting forces are called body forces. The second is via surface interactions by which the force is transmitted between atomic or molecular bonds. Those forces are called surface forces or contact forces.<sup>49</sup>

† Materials which have an orientation, e.g. compound materials, block copolymers, liquid crystals, glass fibre improved materials, etc.. Depending on the orientation of the mechanical load the material will respond differently.

‡ See chap. A

§  $p$  is a scalar.

¶ Albert Einstein (\*14. March 1873 in Ulm, Germany; †18. April 1955 in Princeton, USA) was a theoretical physicist. In 1921 he was rewarded with the Nobel prize in physics "for his services to Theoretical Physics, and especially for his discovery of the law of the photoelectric effect".<sup>5</sup>

The nine components  $\sigma_{ij}$  of the stress tensor  $\mathbf{S}$ , in eq. 2.28, have the form of

$$\mathbf{S} = \sigma_{ij} \vec{e}^i \otimes \vec{e}^j = \begin{pmatrix} \sigma_{xx} & \tau_{xy} & \tau_{xz} \\ \tau_{yx} & \sigma_{yy} & \tau_{yz} \\ \tau_{zx} & \tau_{zy} & \sigma_{zz} \end{pmatrix} \quad (2.31)$$

and the components of the strain are

$$\mathbf{E} = \varepsilon_{ij} \vec{e}^i \otimes \vec{e}^j = \begin{pmatrix} \varepsilon_{xx} & \gamma_{xy} & \gamma_{xz} \\ \gamma_{yx} & \varepsilon_{yy} & \gamma_{yz} \\ \gamma_{zx} & \gamma_{zy} & \varepsilon_{zz} \end{pmatrix}. \quad (2.32)$$

The elements of the main diagonal of the stress tensor  $\mathbf{S}$  are the normal-

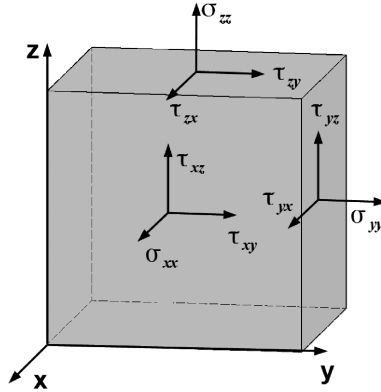


**Figure 2.11.** – Direction of the different stress components  $\sigma_{ij}$  on a quadratic mechanical body. The first index  $i$  names the normal direction of the surface to which the stress or strain is applied. The second index  $j$  names the direction in which the stress or strain is directed.

stresses  $\sigma_{ij}$ .

They represent the stresses in the normal directions on a plane (see fig. 2.11). The elements on the secondary diagonals are the shear stresses which are frequently written as  $\tau_{ij}$  instead of  $\sigma_{ij}$ . They are the stresses in the plane of a body (see fig. 2.11). Because of the invariance of the angular momentum,<sup>39</sup> the stress tensor is symmetric,

$$\tau_{ij} = \tau_{ji}. \quad (2.33)$$

With eq. 2.33 the number of independent components of  $\sigma_{ij}$  is reduced from nine to six. Similar statements are used for the strain tensors. The elements on the principal diagonal are the strains  $\varepsilon$ , while the components of the secondary diagonals are the shear strains  $\gamma$ . The strain tensor is also symmetric.

The components  $C_{ijkl}$  of  $\mathbf{C}$  are in the simplest case constants. However, these components can generally be functions of e.g. temperature  $\vartheta$ , deformation history  $\check{t}$ , shear rate  $\dot{\gamma}$ , angular frequency  $\omega$  etc..

$$C_{ijkl} = \hat{C}_{ijkl}(\vartheta, \check{t}, \dot{\gamma}, \omega, \dots). \quad (2.34)$$

Next, three examples of typical materials are shown, as well as their mathematical description with the stress tensor.

**Example 8. The ideal elastic body**<sup>55</sup>

The stress tensor of an ideal elastic material only has deformation dependent elements, like

$$\mathbf{S} = \begin{pmatrix} \lambda_{Lame} I(\mathbf{E}) + 2G\varepsilon_{xx} & G\gamma_{xy} & G\gamma_{xz} \\ G\gamma_{yx} & \lambda_{Lame} I(\mathbf{E}) + 2G\varepsilon_{yy} & G\gamma_{yz} \\ G\gamma_{zx} & G\gamma_{zy} & \lambda_{Lame} I(\mathbf{E}) + 2G\varepsilon_{zz} \end{pmatrix}. \quad (2.35)$$

If the shear stresses are negligible,  $\tau_{ij} = 0$  and if  $\sigma_{xx} = \sigma_{yy} = \sigma_{zz}$ ,  $\mathbf{S}$  is isotropic and is called the hydrostatic stress tensor.  $I(\mathbf{E}) = \text{tr}(\mathbf{E}) = \varepsilon_{ii}$  is the first invariant of the strain tensor\*.  $\lambda_{Lame}$  is called the Lamé<sup>†</sup> constant. The Lamé constant is related to the Poisson<sup>‡</sup> ratio  $\nu_{Poisson}$  by  $\lambda_{Lame} = \frac{\nu_{Poisson} E}{(1+\nu_{Poisson})(1-2\nu_{Poisson})}$ .  $\square$

**Example 9. The ideal viscous body**

The stress tensor of an ideal viscous material only has components in the secondary diagonals, like

$$\mathbf{S} = \begin{pmatrix} 0 & \eta\dot{\gamma}_{xy} & \eta\dot{\gamma}_{xz} \\ \eta\dot{\gamma}_{yx} & 0 & \eta\dot{\gamma}_{yz} \\ \eta\dot{\gamma}_{zx} & \eta\dot{\gamma}_{zy} & 0 \end{pmatrix}. \quad (2.36)$$

\* The definition of the second and the third invariant of the stress tensor is given in chap. A eq. A.112 and eq. A.113

† Gabriel Lamé (★22. July 1795 in Tours, France; †1. May 1870 in Paris, France) was a French mathematician who contributed to the field of differential geometry.<sup>5</sup>

‡ Siméon-Denis Poisson (★21. June 1781 by Loiret, France; †25. April 1840 in Paris, France) was a French mathematician and physicist.<sup>5</sup>

Because of the symmetry, the extra stress tensor has only three independent components ( $\tau_{xy}$ ,  $\tau_{xz}$  and  $\tau_{yz}$ ). If a shear stress in the upper  $x - y$ -plane is applied in  $y$ -direction, a small element of a viscous body deforms as fig. 2.12 shows.  $\square$

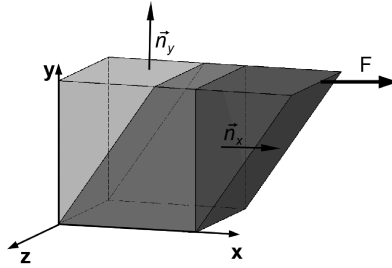


**Figure 2.12.** – An infinitesimal small volume element of an ideal viscous material of infinite expansion under shear. The light grey body represents the volume element in its initial state; no load, while the dark grey body represents the deformed volume element. The  $\sigma_{xz} = \tau_{xy}$  and the  $\sigma_{yz} = \tau_{yz}$  components of  $\sigma_{ij}$  are identical to zero.

#### Example 10. The viscoelastic body

The stress tensor of an ideal viscoelastic material has in principal all components in the matrix. For most shear experiments, e.g. oscillatory shear, only the shear stress components in one plane (e.g.  $x - y$  - plane) are observed. Therefore, the viscoelastic stress tensor takes the form of

$$\mathbf{S} = \begin{pmatrix} \sigma_{xx} & \tau_{xy} & 0 \\ \tau_{yx} & \sigma_{yy} & 0 \\ 0 & 0 & \sigma_{zz} \end{pmatrix}. \quad (2.37)$$

The elements on the main diagonal are non-zero and do not have to be equal. The viscoelastic body is further discussed in chap. 2.3.3.  $\square$

### 2.3.3 Rheological Models

In chap. 2.3.1 two of the basic models of material behaviour were discussed, the Hookean body in eq. 2.24 and the Newtonian body in eq. 2.25. In the engineering mechanics simple elements such as springs, dash pots and their combinations are used to model the behaviour of different types of materials (as seen in fig. 2.10).

The serial connection of a Hookean body and a Newtonian body is called a Maxwell\* element (see fig. 2.13a). This model describes the behaviour of viscoelastic bodies, like polymer melts, if they are in the linear regime (see chap. 3.2.3 fig. 3.5).

By using several Maxwell models in a parallel array (see fig. 2.13b), the response of more complex viscoelastic bodies can be predicted. This ensemble of Maxwell elements is called a multi mode Maxwell element or a multi mode Maxwell model.

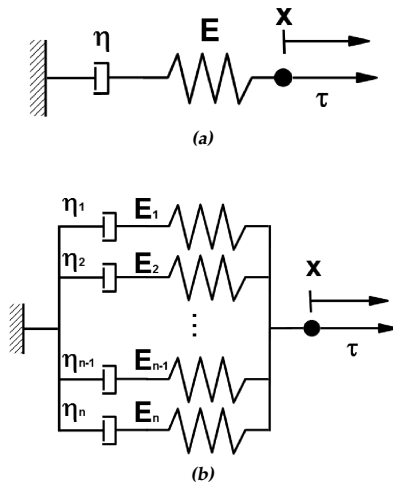


**Figure 2.13.** – (a) the single Maxwell model and (b) the multi-mode Maxwell model.

### Example 11. *The Maxwell model*

*For a Maxwell element the stress in both of its components, dash pot (Newtonian*

\* James Clerk Maxwell (\*13. June 1831 in Edinburgh, Scotland; †5. November 1879 in Cambridge, England) was a Scottish physicist. He is best known for his works on electrodynamics,<sup>5</sup> but also his work on the kinetic theory of gases is acknowledged.<sup>56</sup>

body) and spring (Hookean body), are the same<sup>‡</sup>

$$\tau_H = \tau_N. \quad (2.38)$$

Whereas, the strain  $\gamma$  and the strain rate  $\dot{\gamma}$  is the sum of the strain or strain rate of both components

$$\gamma = \gamma_H + \gamma_N, \quad (2.39)$$

$$\dot{\gamma} := \frac{d\gamma}{dt} \quad (2.40)$$

$$= \dot{\gamma}_H + \dot{\gamma}_N. \quad (2.41)$$

The differential equation for Maxwell element is deduced from eq. 2.41

$$\begin{aligned} \dot{\gamma} &= \frac{\dot{\tau}}{G} + \frac{\tau}{\eta}, \\ \eta\dot{\gamma} &= \lambda\dot{\tau} + \tau. \end{aligned} \quad (2.42)$$

In the second line of eq. 2.42, the relaxation time  $\lambda$  is introduced with the relation

$$\lambda = \frac{\eta}{G}. \quad (2.43)$$

From eq. 2.42 a relaxation function  $G(t)$  can be derived by assuming a step-strain experiment\*, see fig. 2.14, which defines an initial strain

$$\gamma = \gamma_0 \quad (2.44)$$

and a strain rate

$$\dot{\gamma} = 0, \quad \forall t > 0. \quad (2.45)$$

With eq. 2.45 the differential equation eq. 2.42 simplifies to

$$0 = \lambda\dot{\tau} + \tau. \quad (2.46)$$

<sup>‡</sup> This examples bases on fig. 2.13a which is a one dimensional model. Thus, stress and strain can only work in one direction. Therefore, the notation can be simplified by dropping the indices for the coordinates (xy).

\* Step-strain experiment:<sup>44</sup> An investigated sample is deformed instantaneously by a constant strain  $\gamma_0$  at the time  $t = 0$ . The deformation lasts as long as the experiment itself (ideal case  $t \rightarrow \infty$ ). The stress as a function of time is measured.

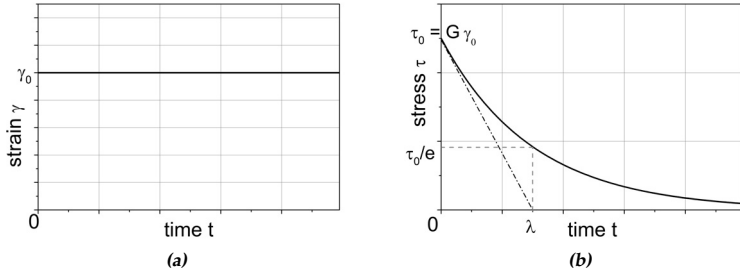


**Figure 2.14.** – (a) shows the applied step strain and (b) shows the viscoelastic stress response.

*This is an ordinary differential equation (ODE) of the first order and can be solved via an exponential ansatz for the stress*

$$\tau(t) = C_0 \cdot e^{-\frac{t}{\lambda}}. \quad (2.47)$$

*The constant  $C_0$  in the ansatz function eq. 2.47 can be determined by using the initial condition given in eq. 2.44.*

*In the first instant ( $t = 0$ ), only the Hookean element (see eq. 2.24) is responsible for the response. Thus,*

$$C_0 = G\gamma_0. \quad (2.48)$$

*With eq. 2.46 and the value for  $C_0$  from eq. 2.48 the relaxation function*

$$G(t) = \frac{\tau(t)}{\gamma_0} = G \cdot e^{-\frac{t}{\lambda}}. \quad (2.49)$$

□

By using the spring and the damper element, it is possible to model the mechanical behaviour of many different materials just by combining the basic elements in different orders and numbers.<sup>4</sup> Generally, the long-time behaviour of solid bodies is ruled by elastic elements. Whereas, the long-time behaviour of viscous bodies is ruled by damper elements.

## 2.4 Polymers

This chapter gives a summary of the possible structural properties of polymers (chap. 2.4.1) as found in many textbooks about polymer science, e.g. Lechner,<sup>57</sup> Lovell,<sup>43</sup> Osswald<sup>55</sup> or Schwarzl.<sup>14</sup> The second part of this chapter (chap. 2.4.2) presents the polymeric materials which have been used in this thesis.

### 2.4.1 Introduction to the Structure of Polymeric Materials

Polymers or macromolecules\*, as already introduced in chap. 1, are molecules built up from smaller molecule units (repeat units) covalently bound to each other. A definition is found in the book of Schwarzl:<sup>14</sup>

“Macromolecular materials (polymers) are materials which are built up from large molecules  $10^3 \text{ g/mol} < M < 10^7 \text{ g/mol}$ .”<sup>†</sup>

A polymer built from just one type of repeat unit is called homopolymer. The choice of the repeat unit defines the properties of the polymer.

---

\* The term macromolecules, meaning large molecules, was introduced by H. Staudinger<sup>†</sup>.

† Herman Staudinger (\*23. March 1881 in Worms, Germany; †8. September 1965 in Freiburg, Germany) was a German organic and macromolecular chemist. He received the Nobel prize in 1953 “for his discoveries in the field of macromolecular chemistry”.<sup>5</sup>

†  $M$  is the molecular weight, which is a function of the Avogadro<sup>‡</sup> number  $N_L = 6.0225 \cdot 10^{23} \text{ mol}^{-1}$  and the mass of one molecule  $m$  in g.<sup>14</sup>

$$M = N_L m. \quad (2.50)$$

‡ Lorenzo Romano Amedeo Carlo Avogadro (\*9. August 1776 in Turin, Italy; †9. July 1856 in Turin, Italy) was an Italian physicist. He only proposed that a defined volume of all gases under the same condition contains the same amount of molecules (Avogadro’s law). In German speaking countries the Avogadro number is called Loschmidt’s number.<sup>5,58</sup>

§ Johann Joseph Loschmidt (\*15. March 1821 by Carlsbad, Bohemia; †8. July 1895 in Vienna, Austria) was an Austrian physical chemist. He calculated the number of molecules in a gas per  $\text{cm}^3$ .<sup>5,58</sup>

Fig. 2.15 gives examples of different common homopolymers and their repeat units.<sup>43,59</sup>

It is also possible to use more than one repeat unit in the synthesis of a polymer.\* Thus, copolymers are obtained.<sup>43</sup> The chain structure is then defined by the arrangement of the single repeat units. The types of copolymers are:<sup>43,59</sup>

**Statistical copolymers** consist of statistically<sup>†</sup> alternating repeat units, as shown in fig. 2.16a.

**Alternating copolymers** consist of strictly alternating repeat units, as presented in fig. 2.16b.

**Block-copolymers** are created by long sequences of each repeat unit. In fig. 2.16c a di-block-copolymer is shown. It consists of one sequence of each of the two repeat units.

**Grafted copolymers** are formed by a linear chain made of one repeat unit (called backbone) and blocks made of the other repeat unit (side arms, branches) which are grafted onto the backbone (seen in fig. 2.16d).

As seen in fig. 2.16d, polymers do not only exist as strictly linear topologies (see fig. 2.17a), but also as branched molecules. The type of branching defines the mechanical properties of the polymers. Typical branched structures are:<sup>43,59</sup>

**Short chain branched (SCB):** Short chains made of a few repeat units are grafted onto a linear backbone (see fig. 2.17b).

**Long chain branched (LCB):** Long chains are grafted onto a linear backbone (see fig. 2.17c). These side branches are physically entangled and consist typically of e.g. more than 300 carbons.

---

\* The term repeat unit includes the term monomer. However, when used for copolymers it is referred to larger molecules built up from monomers and not only to different monomers used, this would be the case also for e.g. polyethyleneterephthalate (PET) which is built up from a repeat unit composed from ethylene glycol and terephthalic acid. PET is considered as a homopolymer.

† Statistically means following a statistical law<sup>18</sup> (e.g. Markovian<sup>‡</sup>).<sup>43</sup> A special case of this would be the random copolymer with a truly random arrangement of the repeat units.

‡ Andrej Andrejewitsch Markov (\*2. June 1856 in Rjasa, Russia; †20. June 1922 in Petrograd, Russia) was a Russian mathematician.<sup>5</sup>

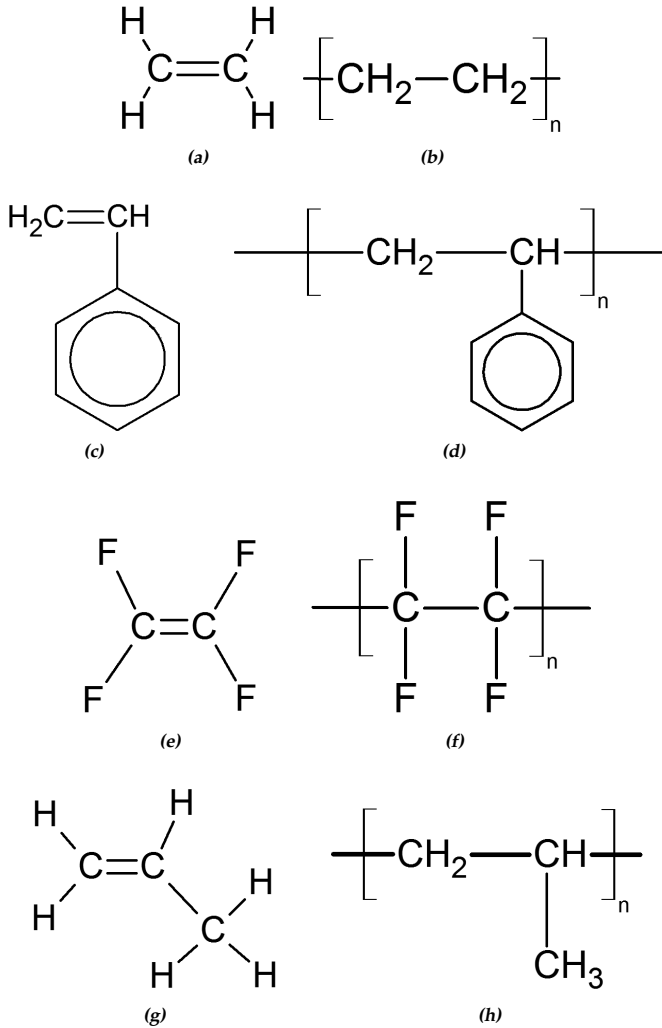


**Figure 2.15.** – Examples of different repeat units (monomers) and their homopolymers: (a) ethylene, (b) polyethylene (PE), (c) styrene, (d) polystyrene (PS), (e) tetrafluoroethylene, (f) polytetrafluoroethylene (PTFE), (g) propylene and (h) polypropylene (PP).

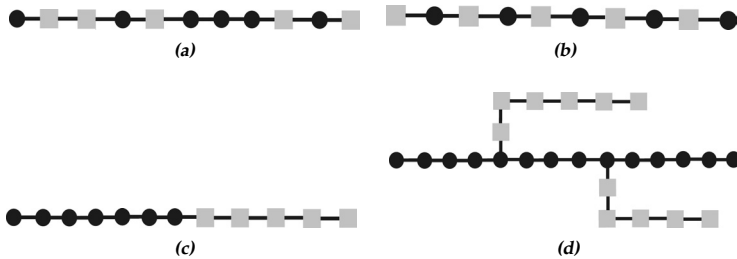


**Figure 2.16.** – Typical structures of copolymers, as (a) statistical copolymer, (b) alternating copolymer, (c) block copolymer (diblock) and (d) graft copolymer. The one repeat unit is symbolized by the black circles and the other repeat unit is symbolized by the grey squares.

**Pom-pom-like:** Pom-pom shaped polymers have a linear backbone with their side chains connected the both ends of the backbone. Pom-pom-like polymers are of special interest because there is an advanced constitutive model<sup>60</sup> which connects the molecular topology\* with the rheology of those materials (see fig. 2.17d).

**Star like:** Several long chains are connected in one point (see fig. 2.17e).

**Network polymers:** Polymers can also form three dimensional networks with crosslinks (see fig. 2.17f).

Polymeric materials are divided in three mayor groups describing their properties:<sup>43,59</sup>

**Thermoplasts** are polymers which can be melted and thus shaped. Examples are PE or PP.

**Thermosets (Duromers)** are highly crosslinked polymers, which are typically rigid. Once formed they can not be melted again. Examples are polyurethane (PUR and PU) or epoxy resins.

**Elastomers** are elastic and rubber-like networks. The network has a low crosslinking density. Examples are natural rubber or nitrile rubber (NBR).

\* The parameters are the length of the backbone and the number of side chains and the length of the side chains.

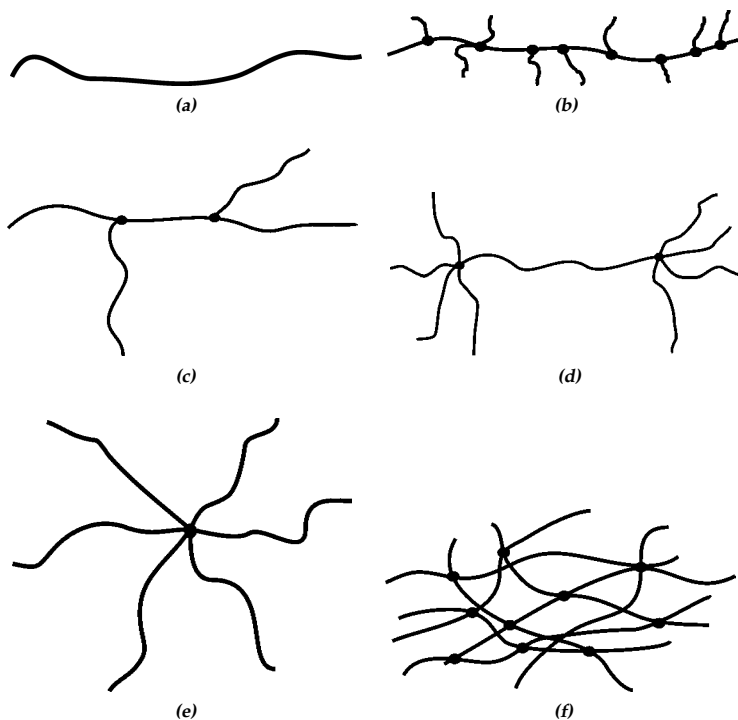


**Figure 2.17.** – Typical chain topologies of polymers are (a) linear chain, (b) short chain branched chain, (c) long chain branched chain, (d) pom-pom shaped chain (with  $q = 4$  side branches on each side), (e) star branched chain and (f) network polymer.

Additionally to the characteristics described above, polymers are defined by their molar mass. Depending on the strategy of the synthesis of the polymer, the length of the polymer chains and thus also the molar mass can differ in one batch. There are two main definitions of the molar mass of a macromolecule. One is the number-averaged molar mass  $\overline{M}_n$  which is defined as given by Lovell:<sup>43</sup>

“The sum of the products of the molar mass of each fraction multiplied by its mole fraction.”

This citation is transformed into an equation by eq. 2.51.

$$\overline{M}_n = \sum_{i=1}^N x_i M_i. \quad (2.51)$$

In eq. 2.51,  $x_i$  is the mole fraction and  $M_i$  is the mass of the single fraction. The second definition for the molar mass is the weight-averaged molar mass  $\overline{M}_w$  which is defined as given by Lovell:<sup>43</sup>

“The sum of the products of the molar mass of each fraction multiplied by its weight fraction.”

This citation is transformed into an equation by eq. 2.52.

$$\overline{M}_w = \sum_{i=1}^N w_i M_i. \quad (2.52)$$

In eq. 2.52,  $w_i$  is the weight fraction.

The ratio of the number-averaged molar mass and the weight-averaged molar mass defines the polydispersity which is also called the polydispersity index *PDI*:

$$PDI = \frac{\overline{M}_w}{\overline{M}_n}. \quad (2.53)$$

For a homopolymer, a polydispersity of 1 means that the polymer is monodisperse.\* The composition of a polymer sample by fractions with different molar masses is represented by the molar mass distribution.<sup>†</sup>

\* It consists of chains with identical chain length.

† The full molar mass distribution is measured e.g. by size exclusion chromatography (SEC). More information about this can be found in Schwarzl<sup>14</sup> or Lechner.<sup>57</sup>

## 2.4.2 Materials of Investigation

For the research conducted in this work and presented in the next three chapters, different polymeric materials have been used.

In order to study the behaviour of the flows of polymer melts of industrial importance, commercial PE samples of different molecular structures were used as listed in tab. 2.3 for the experiments which are presented in this work. The individual samples of the PE represent different molecular topologies. The LDPE is a low density PE with long chain branching and the MDPE is a medium density PE with a more linear topology. Both samples have a broad polydispersity and are obtained from LyondellBasell. The LLDPE is a linear low density PE from Exxon Mobil and has a linear molecular structure.<sup>61</sup> The samples named PE-SCB07\* and PE-SCB13<sup>†</sup> are ethylene/1-octene copolymeres from DOW Chemicals. Due to their comonomer content, both samples have short chain branches along their backbone. The HDPE is PE with a high density obtained from Borealis. It has a linear molecular topology with very rare side branches.

**Table 2.3.** – Material and molecular properties of the used PE.

Sample	$\rho_{20^\circ\text{C}}$	$\overline{M}_w$	$\overline{M}_n$	PDI	$\vartheta_m$	estimated topology
	$\frac{\text{g}}{\text{cm}^3}$	$\frac{\text{kg}}{\text{mol}}$	$\frac{\text{kg}}{\text{mol}}$	-	$^\circ\text{C}$	
LDPE	0.92	186	16	11.7	114	LCB
MDPE	0.94	193	20	9.6	128	linear
LLDPE <sup>61</sup>	0.93	148	35.2	4.2	125	linear
PE-SCB07	0.9	100	45	2.2	100	SCB
PE-SCB13	0.87	85	37	2.3	64	SCB
HDPE	0.93	110	23.4	4.7	131	linear

In the part concerned with the determination of the normal forces under oscillatory shear, different samples of PE have been compared with samples of PS. Whereas, the PE samples have a broad molecular mass distribution as well as the type of branching and the amount of branching is not

\* 7% mol SCB caused by the copolymerization of octene.<sup>62</sup>

† 13% mol SCB caused by the copolymerization of octene.<sup>62</sup>

**Table 2.4.** – Molecular properties of the anionically synthesized PS.

Sample	$\overline{M}_w$ kg/mol	PDI -	Remarks -
PS-L	261	1.18	commercial
PS-Comb	765	1.07	synthesised by Kempf <sup>64</sup>

**Table 2.5.** – Material properties of the polymeric liquids.

Sample	$\rho$ g/cm <sup>3</sup>	$\Gamma$ mN/m	$\eta_E$ Pas
PDMS	0.95	21.5	291
PS-DOP	0.9	30.05	85

exactly defined, the PS have a well defined molecular structure, as shown in tab. 2.4. The PS-Comb has a well defined branching structure due to the special synthesis introduced by Kempf.<sup>63</sup> The PS-Comb has in average 14 side branches of a molar mass of 42.000 which are statistically distributed along the backbone.

For the experiments with the CaBER, two groups of lower viscous polymeric liquids have been used:

1. Commercial silicon oil and a lab made polymer solution (for chap. 5.5)
2. Commercial wood glues (for chap. 5.5.3)

The silicone oil (Rhodorsil 47V300000)\* was produced from the company Rhodia. The polymer solution was a lab made sample donated by Dr. Klein<sup>65</sup> which is similar to the sample studied by Hilliou et al.<sup>66</sup> It is polystyrene (PS) solved in dioctylphthalate (DOP). In the following this sample will be called PS-DOP. The relevant material properties of these samples are summarized in tab. 2.5. The wood glues samples are obtained from the Henkel company. Both samples are commercial products and are commonly used in daily life. One glue is a Ponal-Classic and the other is a

\* Silicone oils are polydimethylsiloxanes (PDMS). These are polymers built from Si (silicon) atoms.

Ponal Express-glue (further referred to as Ponal-Express). Wood glues are known to be based on an atactic polyvinylacetate (PVAc).

## Chapter 3

### Rotational Rheology

In our daily life shear flows of fluids are omnipresent, e.g. the Hagen\*<sup>68</sup>-Poiseuille<sup>†70</sup> flow inside the water tubes, the blood flow in veins, the refilling of traditional cars with gasoline and many more. Shear flows are not only omnipresent, they are also of great importance for the industry. In many processing operations the fluids have to be pumped to their place of action in order to get a customers product or the fluids have to flow in order to gain a desired effect, e.g. power generation in hydro-power plants.

Other examples of the importance of industrial flows, which are more up to the scope of this work, are the polymer extrusion and the melt flow injection. In both cases, the fluid is a molten polymer which is driven by pressure in a special die or form in order to obtain one of the many plastic products. The polymer flows under non-linear conditions. However, this industrial process still has to guarantee the final product quality, the design life of the machine and the safety of the operators. These demands depend highly on the right choice of flow conditions for the polymeric working fluid. The flow of a polymer melt is not as easily controllable as a Newtonian fluid, because it is a complex viscoelastic fluid. This viscoelastic behaviour is fundamentally caused by the molecular topology of the polymer chain and is explained in chap. 2.3.3. It is usually complicated to

---

\* Gotthilf Heinrich Ludwig Hagen (\*3. March 1797 in Königsberg, Germany; †3. February 1884 in Berlin, Germany) was a German hydraulic engineer.<sup>67</sup>

† Jean Louis Leonard Marie Poiseuille (\*22. April 1797 in Paris, France; †26. December 1869 in Paris, France) was a French physiologist and physicist.<sup>69</sup>

access the knowledge of all topological parameters and also the ultimate relations between topology and mechanical forces are not known. It is desirable to obtain a certain estimate of the molecular parameters via the mechanical properties as those obtained via the shear rheology. E.g. the content of the long chain branches in a polymer melt can be estimated via the elongational behaviour of a sample.<sup>71-75</sup>

As an indicator for the elasticity of a melt the normal forces are essential. This has been proved by basic studies in the linear regime.<sup>76-78</sup> Gleißle built a rheometer which was able to measure the normal forces and the radial distribution of the normal force under steady shear.<sup>76-78</sup> His set-up had the mayor drawback of pressure holes in the surface of the geometries. For low viscous fluids this might be of low impact on the measurements but for high viscous polymer melts the disturbances caused by these physical holes can be of undefined influence.

In 2003 Baek et al.<sup>79</sup> introduced a new geometry for measuring the normal forces. With their set-up they were able to overcome the drawback of Gleißle. Instead of using pressure holes they used a monolithic plate geometry. The sensors are capacitive membrane sensors. They are directly put on the backside of the geometry plate by etching processes and by deposition of a metal layer. Thus, very small (diameter  $\approx 1$  mm) and radial distributed transducers are applied. The etching process reduces the thickness of the geometry locally to several  $\mu\text{m}$ . The sensitivity of the transducer was in the best case of about  $2 \times 10^{-4}$  N. However, the studies of Baek et al. have been limited to the steady shear rate experiments.

Studies have been conducted by Schweizer (2002 - 2006)<sup>80,81</sup> for different polymer melts (different PS) with steady state experiments and step shear experiments with commercial rheometers and plate-plate geometry, as well as cone-plate geometry. An additional focus in his works lay on the compliance of the rheometer frames.<sup>81</sup>

Nam et al.<sup>82</sup> simulated the shear stress and normal force response of a fluid modelled with the Giesekus model for LAOS (large amplitude oscillatory shear, chap. 3.2.1) experiments and obtained FT-spectra for the normal forces with even higher harmonics from those (see chap. 3.3 for details on the FT-rheology).

## 3.1 Detection of Normal Forces under Oscillatory Shear

The works of Nam et al.<sup>82</sup> are the starting point of the present work. The aim of this study is to measure the normal forces in LAOS experiments in the non-linear regime. According to the theoretical studies of Nam<sup>82</sup> the normal forces per area of the polymer melts are expected to be small in comparison to the shear stresses. For this reason a highly sensitive tool is needed for the rheometric measurement of the normal forces.

For the investigations an ARES rheometer from TA-Instruments was used. This rheometer is a high performance rheometer and in combination with the FT-Rheology (FT-R, see chap. 3.3) of Wilhelm et al.<sup>83</sup> its sensitivity\* concerning the torque is further improved. Nevertheless, it has a limited sensitivity when it is about to measure the normal forces<sup>†</sup>. In addition to the poor sensitivity it lacks the capacity to measure normal forces in oscillatory measurement. With its software it is only possible to measure normal forces under steady shear.

Thus, two approaches are possible to obtain the normal forces under oscillatory shear with the ARES rheometer:

**Improving the FT-R set-up:** The set-up from the FT-R, as published by Wilhelm et al.,<sup>16,84,85</sup> is extended to additionally measure the normal force. This is achieved by connecting the PC directly to the hardware of the ARES and using the special LabVIEW software of the Wilhelm group.<sup>65</sup> Thus, the normal force data can be obtained but it is still limited to the given sensitivity of the force transducer installed in the ARES.

**Designing a new geometry:** A new geometry is designed for the ARES with a highly sensitive force measurement. This could improve the sensitivity of the first approach. A special set-up which contains a highly sensitive piezoelectric force transducer was designed in this thesis and this set-up was installed and tested in the ARES. With this

---

\* Torque sensitivity as specified by the manufacturer: 0.002 - 200 mNm.

† Between 0.02 - 20 N, as specified by the manufacturer. Other rheometer, e.g. the MCR502 from Anton Paar can detect normal forces in the range of 0.005 - 50 N. Nevertheless, it is still not sufficient for this work. An estimated value is  $< 10^{-3}$  N.

set-up the normal forces can be measured under oscillatory shear.

The results of both of these approaches are compared with the results obtained from the new generation (since 2009) of the high performance shear rheometer the ARES G2\*. The ARES G2 is the successor of the ARES and initially has the capabilities to measure the normal forces under oscillatory shear, however only with a stated sensitivity of  $10^{-3}$  N. This means that, the sensitivity of the transducer of the ARES G2 is improved by one decade in comparison to the transducer installed in the ARES.

## 3.2 The Rotational Shear Rheometer

For shear strain experiments in rotational shear rheometers, a sample disc is placed between the two geometries.

There are two types of basic plate geometries for the rotational rheometers

- plate-plate (fig. 3.1a) or
- cone-plate (fig. 3.1b).

The lower geometry applies the deformation ( $\gamma$ ) on the sample, while the upper geometry keeps its position and thus the response of the sample (torque  $T_z$ ) is measured. The advantage of a cone-plate geometry is the homogeneous flow field and the lower amount of needed sample. The advantage of a plate-plate geometry is its easy sample preparation and the easy construction of the geometries.

The loading of the sample is of main importance for the reproducibility of the measurements.<sup>45</sup> For best results the free boundary has to be straight or slightly convexly curved, as seen in fig. 3.2a, and never concavely curved as fig. 3.2b shows. The measurement uncertainty  $U_{meas}$  taken into account by an incorrect loading can be estimated as<sup>45</sup>

$$U_{meas} = \frac{\Delta\eta}{\eta_{true}} = \frac{\eta_{true} - \eta_{app}}{\eta_{true}} = 1 - \frac{(R - \Delta r)^4}{R^4}. \quad (3.1)$$

The true viscosity is  $\eta_{true}$  and the apparent viscosity is  $\eta_{app}$ . The geometrical parameters are explained in fig. 3.2. The difference between true and

---

\* Torque sensitivity as specified by the manufacturer: 0.05  $\mu$ Nm - 200 mNm. Normal force sensitivity as specified by the manufacturer: 0.001 N - 20 N.

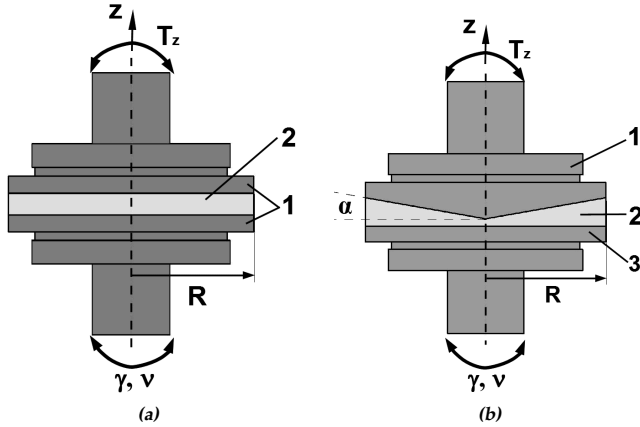


**Figure 3.1.** – (a) Plate-plate geometry, as it is used in rheometers. Between the plates (1), there is the sample disc (2), which has to be investigated. (b) Cone-plate geometry, as it is used in rheometers. The sample disc (2) is placed between the plate (3) and the truncated cone (1). The typical cone angle  $\alpha$  lies between 0.02 and 0.1 rad.

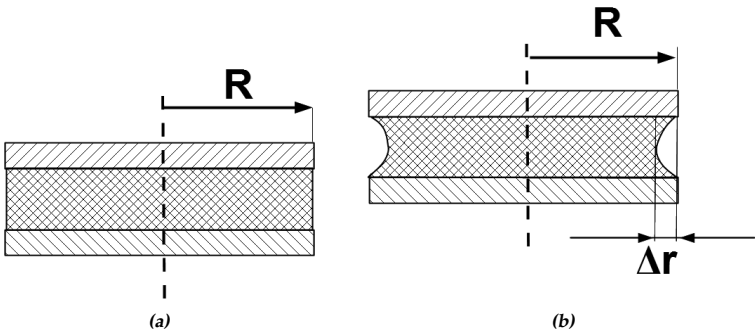


**Figure 3.2.** – Loading of a sample disc in a rotational rheometer. (a) correct loading and (b) wrong loading.

apparent viscosity is  $\Delta\eta$ . With the viscosity difference eq. 3.1 written as

$$\Delta\eta = U_{meas} \cdot \eta_{true}. \quad (3.2)$$

**Example 12. Measurement uncertainty**

For a sample with the radius of  $R = 10 \text{ mm}$ , a cavity of  $\Delta r = 0.1 \text{ mm}$  is assumed. This results in a measurement uncertainty of  $U_{meas} = 0.04$ , about 4%. For the same sample size a cavity of  $\Delta r = 1 \text{ mm}$  is assumed, which gives a measurement uncertainty of  $U_{meas} = 0.34$ .  $\square$

### 3.2.1 Oscillatory Shear

One important experiment in rheology is the oscillatory shear experiment. A disc of a sample is placed between two geometries, e.g. two plates. One plate is oscillated with an amplitude  $\gamma_0$  and a defined angular frequency  $\omega_0 = 2\pi\nu_0$ , while the other plate is connected to a torque transducer and measures the response of the sample. Usually the excitation amplitudes are small, so the experiments are called small amplitude oscillatory shear (SAOS) experiments. The small amplitude of strain should allow measurements in the linear regime (see chap. 3.2.3). The oscillating excitation strain is given by

$$\gamma(t) = \gamma_0 \sin(\omega_0 t). \quad (3.3)$$

The stress \*  $\tau$  of the system is the response of the deformation and is measured. For the linear regime the stress response has the same frequency as the strain, but  $\tau$  follows the strain excitation with a phase shift  $\delta$ , so

$$\tau(t) = \tau_0 \sin(\omega_0 t + \delta). \quad (3.4)$$

The stress can be decomposed in an in-phase  $\tau'$  and out-of-phase  $\tau''$  part. Defining  $\tau_0$  as the amplitude of the stress oscillations, the stress can be stated as

$$\begin{aligned} \tau(t) &= \tau'(t) + i\tau''(t) \\ &= \tau_0' \sin(\omega_0 t) + i\tau_0'' \cos(\omega_0 t). \end{aligned} \quad (3.5)$$

The decomposition of the stress is shown in fig. 3.3.

\* In this chapter the indices of the stress tensor and the strain tensor are dropped. From the settings of the oscillatory shear experiment it is obvious that the only shear strain present lies in the  $r - \varphi$ -plane (see fig. 3.1a), and so does the shear stress. The measured normal force is perpendicular to this plane.

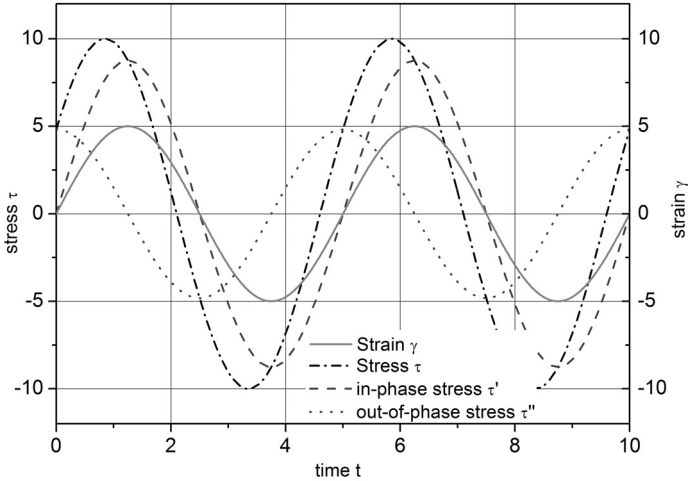


**Figure 3.3.** – Decomposition of the stress (dash-dotted line) into the in-phase (dashed line) and out-of-phase part (dotted line).

Besides Newton's law from eq. 2.25 and the shear rate from eq. 2.40, another important rheological measure is the loss angle  $\delta$ , or the  $\tan \delta$ . It is obtained from the basic definition of the stress in eq. 3.4 and its decomposition in eq. 3.5. With the angle sum formula\* for the sine eq. 3.4 is written as,

$$\tau(t) = \underbrace{\tau_0 \cos \delta}_{=const.=\tau_0'} \sin \omega_0 t + \underbrace{\tau_0 \sin \delta}_{=const.=\tau_0''} \cos \omega_0 t. \quad (3.6)$$

Using eq. 3.6,  $\tan \delta$  is given by the ratio of  $\tau_0''$  and  $\tau_0'$ . Thus,

$$\begin{aligned} \frac{\tau_0''}{\tau_0'} &= \frac{\tau_0 \sin \delta}{\tau_0 \cos \delta} \\ &= \tan \delta. \end{aligned} \quad (3.7)$$

The stress-strain relation induces the dynamic moduli  $G'$  and  $G''$  via eq. 2.24.  $G' = \frac{\tau_0'}{\gamma_0}$  is the elastic or storage modulus and  $G'' = \frac{\tau_0''}{\gamma_0}$  is the viscous or loss modulus. With the dynamic moduli, the eq. 3.7 can be

\* See mathematical text books:<sup>18,86</sup>  $\sin(x \pm y) = \sin x \cos y \pm \cos x \sin y$

written in its most frequently used form

$$\tan \delta = \frac{G''}{G'}. \quad (3.8)$$

The advantage of eq. 3.8 is that the value of  $\tan \delta$  is less sensitive concerning the errors of  $G'$  and  $G''$  than the dynamic moduli. This is caused by the fact that each component is affected by the errors of the measurement  $\Delta G'$  and  $\Delta G''$  in a similar way (see example).

**Example 13. The error of measurement for  $G'$  and  $G''$**

The elastic modulus and the loss modulus are both affected by the error of measurement. Thus, the true values of the moduli  $G'_{true}$  and  $G''_{true}$  are corrupted by the error of the measurement as

$$G' = G'_{true} + \Delta G' \text{ and} \quad (3.9)$$

$$G'' = G''_{true} + \Delta G''. \quad (3.10)$$

The error of measurement is given by a percentage value of the true values of the moduli by

$$\Delta G' = n \cdot G'_{true} \text{ with } 0 \leq n < 1 \text{ and} \quad (3.11)$$

$$\Delta G'' = n \cdot G''_{true} \text{ with } 0 \leq n < 1. \quad (3.12)$$

In eq. 3.11 and eq. 3.12 it was assumed that both moduli are similarly erroneous and for this have the same value of  $n$ . Using eq. 3.11 and eq. 3.12 in eq. 3.9 and eq. 3.10, eq. 3.8 can be written as

$$\begin{aligned} \tan \delta &= \frac{G''_{true} + n \cdot G''_{true}}{G'_{true} + n \cdot G'_{true}} \\ &= \frac{G''_{true} (1 + n)}{G'_{true} (1 + n)} \\ &= \frac{G''_{true}}{G'_{true}}. \end{aligned} \quad (3.13)$$

Therefore, eq. 3.13 proves that the  $\tan \delta$  is not affected by the error of measurement.  $\square$

Another important quantity for fluids is the viscosity. In case of the oscillatory shear experiment a complex viscosity\* is given by the use of the

\* The concept of a complex viscosity is based on the works of A. Gemant<sup>†,87,88</sup>

† Andrew Gemant (★27. July 1895 in Nagyvarad, Hungary; †Februar 1983 in Detroit, USA) was a Hungarian physicist.<sup>89</sup>

complex shear stress  $\tau^*$  and the complex strain rate  $\dot{\gamma}^*$  :

$$\eta^* = \frac{\tau^*}{\dot{\gamma}^*} = \eta' - i\eta'' \quad (3.14)$$

In eq. 3.14 the complex viscosity is decomposed into the dynamic viscosity

$$\eta' = \frac{\tau_0''}{\dot{\gamma}_0} = \frac{G''}{\omega} \quad (3.15)$$

and an elastic part

$$\eta'' = \frac{\tau_0'}{\dot{\gamma}_0} = \frac{G'}{\omega} \quad (3.16)$$

In eq. 3.15 and eq. 3.16  $\dot{\gamma}_0$  is the amplitude of the oscillatory strain rate.

For a time-dependent strain, the strain rate  $\dot{\gamma}(t)$  is simply the time derivative of the strain (see eq. 2.40). Thus, for an oscillatory excitation,

$$\dot{\gamma}(t) = \underbrace{\gamma_0 \omega}_{=\dot{\gamma}_0} \cos \omega_0 t \quad (3.17)$$

In fig. 3.4 the oscillating strain, the resulting stress and strain rate are plotted.

#### **Example 14. The Maxwell element under oscillatory shear**

A Maxwell body, as described by eq. 3.3, is excited by an oscillatory deformation. The mechanical values of the strain amplitude, the strain rate and the shear stress are given in complex notation (see chap. C). Thus, the eq. 3.3, eq. 3.4 and eq. 3.17 are restated to eq. C.1, eq. C.2 and eq. C.3. With further operations as in detail described in chap. C and the definition of the complex modulus

$$G^* := \frac{\tau^*(t)}{\dot{\gamma}^*(t)}, \quad (3.18)$$

a complex formula for the behaviour of a Maxwell body under oscillatory shear is found to be

$$G^*(\omega) = G \cdot \frac{i\lambda\omega + \lambda^2\omega^2}{1 + \lambda^2\omega^2} \quad (3.19)$$

The complex modulus, as every complex number, can be split in the real part  $G'(\omega) = \text{Re}\{G(\omega)\}$  and the imaginary part  $G''(\omega) = \text{Im}\{G(\omega)\}$ .

$$G^*(\omega) = \underbrace{G \cdot \frac{\lambda^2\omega^2}{1 + \lambda^2\omega^2}}_{=G'(\omega)} + i \underbrace{G \cdot \frac{\lambda\omega}{1 + \lambda^2\omega^2}}_{=G''(\omega)} \quad (3.20)$$

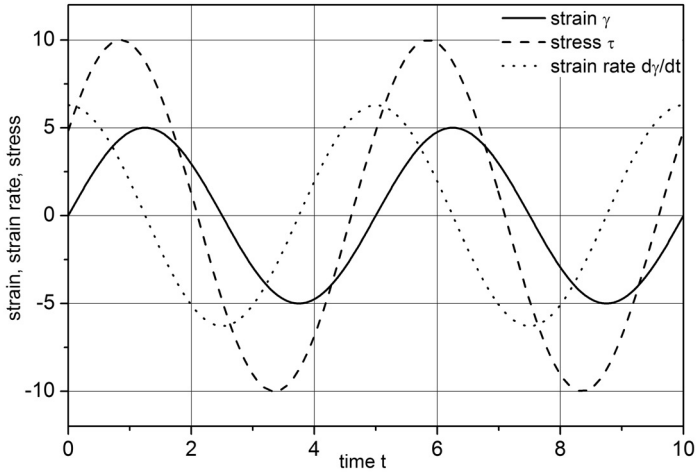


**Figure 3.4.** – Sinusoidal oscillating shear strain (full line), the resulting shear stress (dashed line) and the shear rate (dotted line) for a viscoelastic material.

*The Maxwell model is a good approximation of the viscoelastic behaviour in the linear regime. By eq. 3.20 the crossover frequency  $\omega_{cross}$  at which  $G'(\omega) = G''(\omega)$  can be determined from  $G'(\omega)$  and  $G''(\omega)$ .* □

### 3.2.2 Time-Temperature-Superposition (TTS)

Standard rheological instruments typically have a frequency range of 3 to 4 decades. For a complete characterization of the material behaviour of polymer melts, a frequency range of about 10 decades is often needed. This frequency range cannot be measured in one single measurement, but it is possible to shift the results of several measurements at different temperatures to gain a master-curve, which shows the characteristic behaviour of a polymer melt at a certain reference temperature for a wider frequency range. To obtain a master curve, the data at different temperatures is multiplied with specific shift factors  $a_T$ , which can be calculated via the WLF-equation (Williams-Landel-Ferry).<sup>90</sup>

The WLF-equation can be derived from the basic expression for the tem-

perature dependence of the viscosity of a liquid,<sup>43</sup>

$$\eta(\vartheta) = \eta_0 e^{\frac{E_a}{R_m(\vartheta - \vartheta_{VF})}}. \quad (3.21)$$

$\vartheta$  is the variable temperature,  $E_a$  is the activation energy,  $R_m$  is the universal gas constant and  $\vartheta_{VF}$  is the Vogel-Fulcher<sup>91</sup> temperature. With the Newton's law from eq. 2.25 and the strain rate from eq. 3.17 the stress is a function of strain and frequency  $\tau_0 = \eta\dot{\gamma}_0 \Rightarrow \tau_0 = \eta\dot{\gamma}_0\omega$ . For two measurements at different temperatures  $\vartheta_1$  and  $\vartheta_2$  a ratio of the viscosity is defined by

$$\frac{\eta_1(\vartheta_1)}{\eta_2(\vartheta_2)} := \frac{\eta_1}{\eta_2} = \frac{\omega_2}{\omega_1}. \quad (3.22)$$

Further it is assumed that the viscosity ratio in eq. 3.22 is described by

$$\frac{\eta_1}{\eta_2} = f_V \cdot \eta_1(\vartheta_1) \quad (3.23)$$

with the free volume  $f_V$ .<sup>\*</sup> The eq. 3.21 and eq. 3.22 are inserted in eq. 3.23 to derive

$$\frac{\omega_2}{\omega_1} = f_V \cdot \eta_0 e^{\frac{E_a}{R_m(\vartheta - \vartheta_{VF})}}. \quad (3.24)$$

The form of the WLF-equation is obtained by taking the common logarithm of the expression from eq. 3.24

$$\log \frac{\omega_2}{\omega_1} = \log(f_V \eta_0) + \frac{E_a}{R_m(\vartheta - \vartheta_{VF})} \log e. \quad (3.25)$$

Three definitions are further introduced

$$C_1 \cdot C_2 := \frac{E_a}{R_m} \log e, \quad (3.26)$$

$$\vartheta_2 - C_2 := \vartheta_{VF} \text{ and} \quad (3.27)$$

$$C_1 := \log(f_V \eta_0). \quad (3.28)$$

$C_1$  and  $C_2$  are constants which depend on the choice of  $\vartheta_2$ . If  $\vartheta_2 = \vartheta_g$  then typical values are  $C_1 = 17.4$  and  $C_2 = 51.6$  K. These values are called universal values and give in the most cases a good prediction of the behaviour

\* The free volume  $f_V$  represents the space of a liquid or solid which is not occupied by a polymer molecule.<sup>43</sup> The free volume is given by  $f_V = f_g(\vartheta - \vartheta_g) \alpha_F$ , with the thermal expansion coefficient of the free volume  $\alpha_F$ , the glass transition temperature  $\vartheta_g$  and the fractional free volume  $f_g$ .

of the studied polymer melt. Thus, the WLF-equation is finally derived in form of

$$\log \frac{\omega_2}{\omega_1} = \log a_T = \frac{-C_1 (\vartheta_1 - \vartheta_2)}{C_2 + (\vartheta_1 - \vartheta_2)}. \quad (3.29)$$

For generating a master-curve via the WLF-equation it is important that all of the relaxation processes of the polymer melt have the same temperature dependence.

The generalized Maxwell-model (compare fig. 2.13b) implies the influence of temperature on the dynamic moduli and introduces the relaxation times  $\lambda_i$ . A change in temperature will affect the coefficient  $\rho R_m \vartheta / M_e^*$  and the molecular relaxation time  $\lambda_i$ . The storage modulus is described for  $\vartheta_1$  and  $\vartheta_2$  by

$$G'(\omega)_1 = \frac{\rho_1 R_m \vartheta_1}{M_e} \sum g_i \frac{\omega^2 \lambda_i^2(\vartheta_1)}{1 + \omega^2 \lambda_i^2(\vartheta_1)}, \quad (3.30)$$

$$G'(\omega)_2 = \frac{\rho_2 R_m \vartheta_2}{M_e} \sum g_i \frac{\omega^2 \lambda_i^2(\vartheta_2)}{1 + \omega^2 \lambda_i^2(\vartheta_2)}. \quad (3.31)$$

If comparing relaxation functions at different temperatures the coefficients have to be equal. For this purpose one temperature (e.g.  $\vartheta_2$ ) is chosen as the reference temperature. With eq. 3.30 and eq. 3.31 it is obtained that

$$G'(\omega)_{ref} = G'(\omega)_2 \frac{\rho_1 \vartheta_1}{\rho_2 \vartheta_2} \sum g_i \frac{\omega^2 \lambda_i^2(\vartheta_2)}{1 + \omega^2 \lambda_i^2(\vartheta_2)}. \quad (3.32)$$

Therefore, the shift factor can be described by the relaxation time  $\lambda$  as

$$a_T = \frac{\lambda(\vartheta_2)}{\lambda(\vartheta_1)}. \quad (3.33)$$

### 3.2.3 Polymer Melts under Oscillatory Shear

Fig. 3.5 shows a qualitative example of a master-curve of a mono-disperse linear homopolymer melt. The curves of the frequency dependent moduli can be divided in four regions which show different characteristic material behaviour. Region one is called the linear regime and it is mathematically described by the Maxwell-model (eq. 3.20). For small frequencies  $\omega$  the storage modulus  $G'(\omega)$  is proportional to  $\omega^2$  and the loss modulus  $G''(\omega)$

\*  $M_e$  is the entanglement molecular weight.

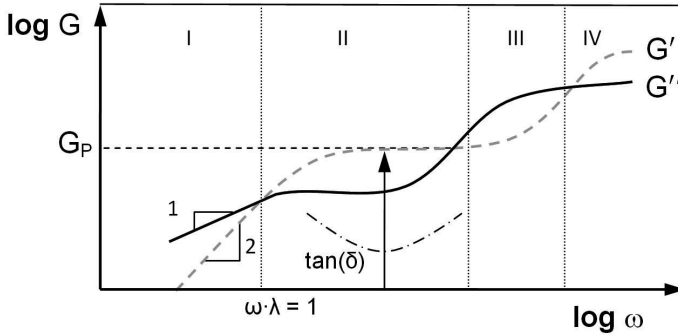


**Figure 3.5.** – Typical shape for  $G'(\omega)$  (dashed line) and  $G''(\omega)$  (full line) for a mono-disperse linear homo-polymer melt. The regions of different rheological behaviour are separated by the dotted lines. The dash dotted line shows the  $\tan \delta$  in region II.

is proportional to  $\omega$ . This can be seen in eq. 3.20. For values of  $\omega \cdot \lambda < 1$ ,  $G'(\omega) \propto \omega^2$  and  $G''(\omega) \propto \omega$ . The elastic and the viscous module cross each other at a value of  $\omega \cdot \lambda = 1$ . This is the upper limit for the first region. In the second region the response is dominated by the elastic part  $G'(\omega)$ . Additionally, the  $\tan \delta$  has its minimum. This corresponds to a first plateau reached by  $G'$ . This plateau is called rubber plateau  $G'_p$ . The entanglement molecular weight  $M_e$  can be calculated with  $G'_p$  via

$$M_e = \frac{\rho R_m \vartheta}{G'_p}. \quad (3.34)$$

As de Gennes\* (1971)<sup>94</sup> showed, the plateau viscosity  $\eta_0^\dagger$  for a linear amorphous and mono-disperse physical entangled homopolymer is proportional to the third power of the molecular weight  $M_n$

$$\eta_0 \propto M_n^3. \quad (3.35)$$

\* Pierre-Gilles de Gennes (\*24. October 1932 in Paris; France; +18. May 2007 in Versailles, France) was a French physicist. He received the Nobelprize in 1991 "for discovering that methods developed for studying order phenomena in simple systems can be generalized to more complex forms of matter, in particular to liquid crystals and polymers".<sup>92,93</sup>

† For low shear rates the plot of the viscosity against the shear rate has a plateau. The value of this plateau is called the plateau viscosity or the zero shear viscosity  $\eta_0$ .

From eq. 2.43 it is evident that also the relaxation time at low frequencies is proportional to the molecular weight,  $\lambda \propto M_n^3$ , because  $G' \neq \hat{G}'(M_n)$ . In experiments it was found that  $\eta$  varies typically with  $\eta \propto M_n^{3.4}$ .

Thus, a shift in the molecular weight will shift the plateau, but it will not affect its value  $G'_p$ .

In the third region, the influence of the viscous modulus  $G''(\omega)$  on the mechanical response begins to be dominating. Both  $G'(\omega)$  and  $G''(\omega)$  have a strong increase. This region is mainly a transition region to the glass plateau.

The glass plateau forms region four and it is difficult to obtain it in measurements, because it lies in the range of high frequencies.

### 3.3 Fourier Transform Rheology (FT-R)

The original idea of the oscillatory shear experiment was to study the material behaviour in the linear regime. In the linear regime, the rheological behaviour of most materials is easily described by the previously given equations. However, it is also limited in terms of application to real life process (e.g. to processing operations, which are mostly in the non-linear regime) or limited in terms of the sensitivity to certain topological parameters (e.g. the branching amount of polymeric materials or polydispersity). Therefore, the SAOS (small amplitude oscillatory shear) experiments are not sufficient to obtain this information about the materials.

The LAOS (large amplitude oscillatory shear) experiment can provide information about the non-linear behaviour. Nevertheless, interpreting the results of the LAOS experiments is not easy. First approaches by Tee and Dealy<sup>95</sup> used phase plots<sup>96</sup> by which the Lissajous\* figures were obtained. In rheology, the Lissajous figures are plots of the shear stress against the shear strain. For the oscillatory experiments of any viscoelastic material in the linear regime, the curves will have the shape of ellipsoids, due to the linear display of the both axes. If the experiments are executed in the non-linear regime, then the Lissajous figures will be deformed into box-like shapes. The sensitivity of those plots is not high.

---

\* Jules Antoine Lissajous (\*4. March 1822 in Versailles, France; +24. June 1880 in Plompierre, France) was a French physicist.<sup>5</sup>

Another approach for obtaining precise information from the LAOS experiments is the Fourier transform-rheology (FT-R). This approach was already made in the late 1960s by e.g. Onogi et al.,<sup>97–99</sup> Dogde<sup>100</sup> or Philippoff.<sup>101</sup> All their studies were limited by the low computational power available and by the less sensitive rheological instruments. It took until 1998 when Wilhelm successfully launched the FT-R.<sup>16,83,84</sup> Since then, the FT-R has been widely used and by the year 2010 has become a state of art method in oscillatory rheology.\* The FT-Rheology as founded by Wilhelm<sup>16,83</sup> has its basis in the Taylor<sup>†</sup> expansion of the viscosity.‡ By Substituting the viscosity  $\eta$  in the Newtonian law, eq. 2.25 via eq. D.2 and replacing  $\dot{\gamma}$  with help of eq. D.4, the shear stress is given by

$$\tau = \underbrace{i\omega_0\gamma_0\eta_0}_{=I_1} e^{i\omega_0 t} - \underbrace{i\omega_0^3\gamma_0^3 a}_{=I_3} e^{i\cdot 3\omega_0 t} + \underbrace{i\omega_0^5\gamma_0^5 a}_{=I_5} e^{i\cdot 5\omega_0 t} + \dots \quad (3.36)$$

Comparing the coefficients  $I_1, I_3, I_5, \dots$  of eq. 3.36 with the coefficients of a complex Fourier series<sup>19,22,127</sup> it is obvious, that  $I_1, I_3, I_5, \dots$  are the values or intensities. The frequencies are well defined by the excitation frequency  $\omega_0$  and its odd multiples  $\omega_n = n \cdot \omega$  with  $n = \{x \mid x, k \in \mathbb{N}^+, x = 2k - 1\}$ . Eq. 3.36 gives the explanation why only the odd harmonics can be observed in the FT magnitude spectra of LAOS experiments.§ The presence of odd higher harmonics directly indicates the appearance of non-linear phenomena in the flow and by forming certain ratios of the amplitude of the higher harmonics, i.e.  $I_3/I_1$  or  $I_5/I_3$ ¶, a new method for classifying

\* It was first commercialised with the ARES G2 from TA-instruments. Research groups in the whole world, in both academia and industry make use of it.<sup>64,102–125</sup> A simple search in Web of science for Fourier-Transform Rheology resulted in 26 hits only for 2011 and 144 at all.

† Brook Taylor (\*18. August 1685 in Edmonton, England; †29. December 1731 in London, England) was an English mathematician. His main work is the "*methodus incrementorum directa et inversa*"<sup>126</sup> from 1717 in which among others the Taylor expansion is introduced.<sup>5</sup>

‡ Details are given in chap. D.

§ In real experiments it is sometimes possible to observe the even harmonics additionally. The origin of the even harmonics is not completely understood yet. However, the common agreement is that they are caused by the sample-rheometer interaction, i.e. slip or shear bands.<sup>65,128–132</sup>

¶ The ratio of the higher harmonics is especially interesting for studies on emulsions, as Reinheimer et al.<sup>115</sup> showed for the determination of the size distribution of emulsions.

materials is given.

Based on the FT-R, Hyun et al.<sup>105,106,133</sup> introduced a new non-linear parameter  $Q$  to optimize the characterisation via FT-R. Hyun et al. found that the non-linearity is strain independent, if the ratio of  $I_3/I_1$  and  $\gamma_0^2$  is taken, so

$$Q := \frac{I_3}{I_1 \cdot \gamma_0^2}. \quad (3.37)$$

For  $\gamma_0 \rightarrow 0$  the non-linearity of eq. 3.37 does not vanish but results in a limiting value, like

$$\lim_{\gamma_0 \rightarrow 0} Q := Q_0. \quad (3.38)$$

This limit is called the intrinsic non-linearity  $Q_0$ .

Another experimental way to study the LAOS behaviour of materials is to use the sliding plate rheometer. This was mainly used by Giacomini et al.<sup>12,134-137</sup> This set-up was never commercialized. This might have been caused by the problems which rise from flow inhomogeneities.\*

## 3.4 An Improved Normal Force Geometry

For a highly sensitive measurement of the axial normal force  $F_z(t)$  in oscillatory shear experiments, e.g. LAOS, in the ARES it was necessary to design a new upper geometry. This new normal force geometry (NoForGe), shown in fig. 3.6, contains a highly sensitive force transducer (from Kistler company) with a sensitivity of  $5 \cdot 10^{-5}$  N. The maximum force which can be measured is 20 N. The NoForGe was designed to work with different plate and cone geometries, so the geometry part (fig. 3.6.1) is easy to exchange. The results presented in this work are obtained with a plate of a 8 mm diameter.

Constraints for the design of the NoForGe were given by the geometry of the ARES, ARES G2 and the ovens of both rheometers. Further practical features such as easy installation and axial and radial alignment were included.

---

\* A review of the FT-R, the Q-parameter approach and the other non-linear methods is given by Hyun et al.<sup>106</sup>

The inclusion of the commercial piezoelectric force transducer demanded a multi-part assembly of the NoForGe. The transducer (fig. 3.6.2) is screwed from below in the upper flange (fig. 3.6.3). The transducer is fixed inside the flange with three M3 fixing screws. Thus, even a very strong torsion cannot loosen the transducer and downgrade the data. The upper flange is fixed with four screws\* in the hollow lower shaft (fig. 3.6.6). The outer diameter of the shaft has to be smaller than the opening holes of the oven, which can be installed on the ARES and ARES G2. Through this shaft the cable is laid to connect the transducer and the charge amplifier (Kistler type 5015). At its bottom, the shaft has a slot which allows the cable to exit. The shaft is connected to the ARES with the adapter piece (fig. 3.6.7). The shaft can be radially adjusted on the adapter piece with three fixing screws. This is how the set-up is aligned. This assembly is both built in stainless steel (316L) and in alumina.

### 3.4.1 Data Acquisition for the Rotational Rheometer

The piezoelectric transducer sends a low voltage signal to a charge amplifier (from Kistler company), which amplifies the analogue signal to a maximum of  $\pm 10V$ . The signal is then acquired by a ADC board (PCI-MIO-16XE-10 from National Instruments) which has a data acquisition rate of 100 kHz and the ability of multiplexing up to 16 channels. The data acquisition on the PC is conducted with the LabVIEW software, as already used for the FT-R.<sup>83,138,139</sup> In order to reduce the amount of data points and for improving the signal-to-noise ratio, the oversampling method, as described by Dusschoten (2001),<sup>138</sup> was used within this LabVIEW program.

## 3.5 Experimental Set-up for the Oscillatory Shear Experiments

The oscillatory shear experiments were performed in two different high performance rheometers. Once in the ARES and once in the ARES G2.

\* In a second design the amount of screws was reduced to three to reduce weight and reduce assembly work.

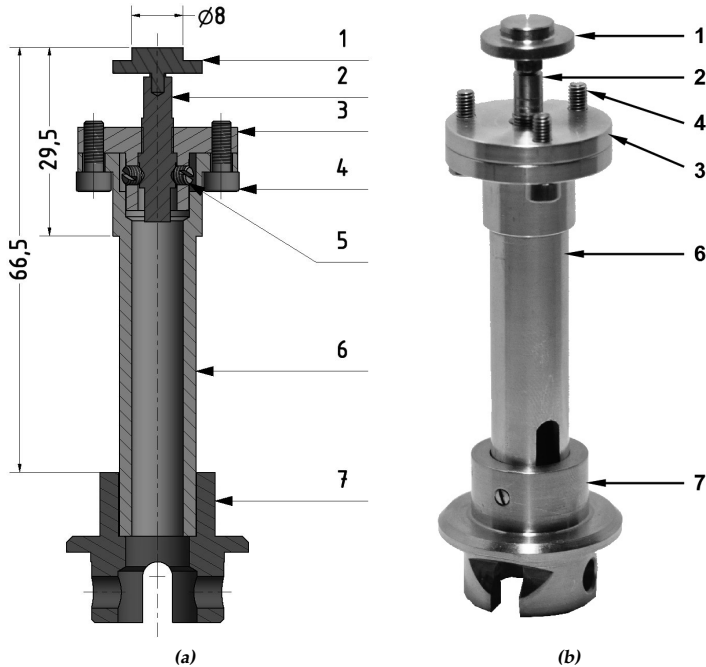


**Figure 3.6.** – Assembly sketch and image of the NoForGe. (a) Sketch of the NoForGe and (b) image of the built NoForGe with (1) replaceable geometry (e.g. plate  $\varnothing 8$  mm), (2) force transducer, (3) upper flange (4) 4×screw M4, (5) 3×fixing screw M3, (6) geometry lower shaft and (7) ARES adapter.

Both are fabricated from TA Instruments. In the ARES two possibilities were used to study the normal forces under oscillatory shear. One was to use the new normal force geometry (NoForGe), see chap. 3.4, to obtain the normal force data from the piezoelectric transducer and the other way was to use the direct voltage output of the normal force transducer of the ARES. This was necessary, because the ARES software is not capable of measuring normal forces in the oscillatory shear experiment. The new ARES G2 is able to measure normal forces under oscillatory shear. The results of the three set-ups are compared in order to determine how different

the sensitivity of the three methods are.

First the linear shear rheological experiments were conducted and compared. The experimental boundary conditions and the investigated flow field should be similar for the three set-ups. A sketch of the principle and the geometric parameters for the oscillatory shear experiment is given in fig. 3.7.

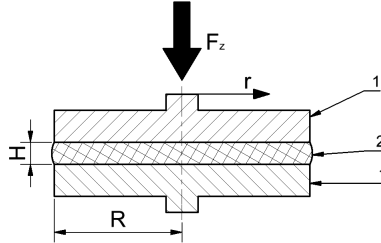


**Figure 3.7.** – Sketch of a plate-plate geometry for oscillatory shear experiments and the measurement of the axial normal force  $F_z$ . The geometry plates (1) and the sample disc (2) have a diameter  $D = 2R$ . The gap size equals the plate to plate distance  $H$ . The gap size  $H$  was set identically to be 1 mm for all experiments. The radial coordinate is given by  $r$ , the angular coordinate is  $\varphi$  and the axial coordinate is  $z$ .

The experiments were performed under similar conditions, i.e. in an oven under nitrogen atmosphere to prevent the sample from degradation. The temperature was chosen to be far above the melting point (e.g.  $\vartheta = \vartheta_m + 50$  °C; thus, 50 °C above the melting point). At first the strain amplitude dependent moduli were measured with a low frequency oscillation, as seen in fig. 3.8. From this measurement the linear region and the onset of the non-linear region could be estimated. This was important in order to determine the right settings for the later following studies of the non-linear parameters. Fig. 3.8 also indicates how the three set-ups are matching, especially in the linear regime. The results of the NoForGe and the ARES G2 are matching within 3 %. The matching between the results of the ARES and the both other set-ups is smaller; 7.5 % for the matching with the NoForGe and 11 % for the matching with the ARES G2.

Next, the frequency-dependent moduli were recorded. This measurement of the the frequency-dependent moduli was conducted with low shear

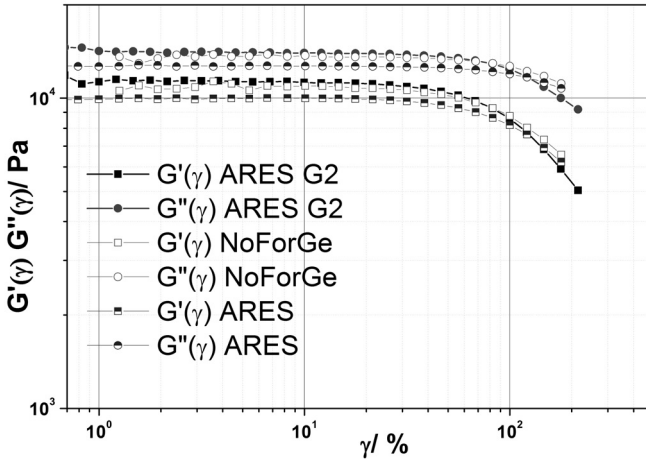


**Figure 3.8.** – Elastic modulus and viscous modulus as a function of strain for the MDPE sample (tab. 2.3) at 180 °C and a frequency  $\nu_0 = 0.1$  Hz. The full symbols represent the data from the ARES G2, the open symbols indicate the data from the ARES with installed NoForGe and the semi-filled symbols are the results from the ARES. From these plots the linear regime can be determined.

amplitude ( $\gamma_0 = 1\%$ ), to obtain the elastic modulus  $G'(\nu)$  and the viscous modulus  $G''(\nu)$  as functions of the excitation frequency  $\nu_0$  (fig. 3.9). From the plots of  $G'(\nu)$  and  $G''(\nu)$  the crossover point was determined. As for the measurement of the strain-dependent moduli, also the measurement of the frequency-dependent moduli of all three set-ups matched within less than 10%.\* Further, the crossover frequency was determined for the three set-ups. The crossover frequencies matched within 2% (ARES  $\nu_{cross} = 1.09$  Hz, ARES G2  $\nu_{cross} = 1.10$  Hz and NoForGe  $\nu_{cross} = 1.11$  Hz). Resulting from this, it is assumed that each set-up represents similar flow conditions, when used with the same parameters. Therefore, they can be called to be equal in terms of linear rheology.

The experiments in this work are set up to study the non-linear behaviour

\* The matching between NoForGe and ARES G2 was within 3% while the matching of both with the ARES was within 8%.

of polymer melts. For this purpose, for the next sequence of experiments, an excitation frequency was chosen which is larger than the crossover frequency.

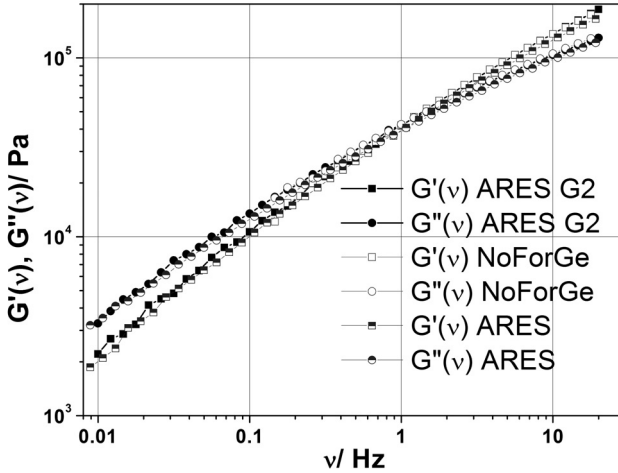


**Figure 3.9.** – Elastic modulus and viscous modulus as a function of frequency for the MDPE sample (tab. 2.3) at 180 °C and a strain  $\gamma_0 = 1 \%$ . The full symbols represent the data from the ARES G2, while the open symbols indicate the data from the ARES with installed NoForGe and the semi-filled symbols are the results from the ARES. From these plots, the crossover point could be determined.

For measuring the non-linear parameters, the time-dependent behaviour of the material is measured.\* This type of experiments is used for the FT-R and other non-linear rheological measurements.<sup>83–85,140,141</sup> With the measurement of the time-dependent properties, data is acquired in form of the time-dependent shear stress  $\tau(t)$  and the time-dependent axial normal force  $F_z(t)$ . All parameters were set to be constant, i.e.  $v_0 = const.$ ,  $\dot{\theta} = const.$  and  $\gamma_0 = const.$ . The applied shear amplitude  $\gamma_0$  was varied between 2 % and 150 % in different measurements of the time-dependent properties. The rheometer hardware would allow higher shear ampli-

\* The obtained quantities of the measurement of the time-dependent behaviour are e.g. moduli, viscosity or torque.

tudes. However, as the shear amplitude gets large, the probability increases strongly that edge fracture of the sample or wall slip of the sample appears. Thus, measuring at higher shear amplitudes than  $\gamma_0 = 150\%$  gave no reliable results for the chosen samples.

The frequency of the experiments was chosen in such a way that already the first measurement of the time-dependent properties would be in the region of non-linear behaviour.

## 3.6 Analysing the Data from the Oscillatory Shear Experiments

The data obtained from the measurement of the time-dependent properties was a signal proportional to the time-dependent shear stress and a signal proportional to the time-dependent axial force.\* The treatment of the signal of the shear stress is in complete accordance to the one used in the literature on the FT-Rheology, e.g. Hyun et al.<sup>105</sup> The algorithm is briefly sketched:

**Algorithm 1.** *FT-Rheology algorithm for the oscillatory shear stress data*

1. The data is acquired with a high sampling rate ADC board .
2. The data is boxcar averaged<sup>†</sup> (over e.g. 100 - 1000 data points).
3. The data is Fourier transformed and the magnitude spectrum is calculated.
4. From the magnitude spectrum, the peak values of the fundamental frequency  $I_1$  and the odd higher harmonics  $I_3, I_5, \dots$  are determined.
5. The  $Q$ -parameter is determined and plotted as function of the strain.  $\square$

The data analysed as shear stress is actually the voltage output of the torque transducer of the rheometer. This voltage is proportional to the shear stress and if only the ratio of the peaks is studied there is no need to calibrate these values.<sup>83</sup>

\* In the following the term time-dependent shear stress is shortened to shear stress, because no other dependence is studied in this chapter. A similar abbreviation is used for the time-dependent normal force.

<sup>†</sup> This is known under the term of oversampling and is a crucial tool to significantly improve the signal to noise ratio.

A similar algorithm is used for the normal force data. However, in order to obtain the quantitative values for the axial force as well, a calibration of the signal has to be made.

**Algorithm 2. FT-Rheology algorithm for the oscillatory normal force data**

1. The data is acquired with a high sampling rate ADC board.
2. The data is boxcar averaged (over e.g. 100 - 1000 data points).
3. The data is multiplied with the calibration factor.
4. The data is Fourier transformed and the magnitude spectrum is calculated.
5. From the magnitude spectrum, the peak values of the fundamental frequency  $I_1$  and the even higher harmonics  $I_2, I_4, \dots$  are determined.
6. A new non-linear parameter for the normal forces  $Q_{NF}$  is determined and plotted as function of the strain.\* □

For the measurement at the ARES, either with NoForGe or by direct read out of the ARES own normal force transducer, the signal had to be calibrated to obtain quantitative values of the normal forces. For the piezoelectric transducer used in the NoForGe, the calibration was done by the manufacturing company; in this case the company Kistler. The calibration values were taken from the calibration certificate of each transducer and could be directly used in the algorithm above.

The voltage signal of the normal force transducer of the ARES had to be calibrated in house. This was done by attaching several defined weights (10 g, 20 g, 100 g, 200 g, 500 g) to the ARES rheometer. The plot of the measured voltage signal against the applied weight follows a linear relation. Via a linear regression curve the relation between voltage output and gravitational force, see fig. 3.10, was determined. The proportionality factor obtained from the linear regression was used for the calibration of the normal force data.

As known from the FT-R, the non-linear behaviour of a material is visible via its FT-spectrum, especially via the higher harmonics of the excitation frequency  $\nu_0$ .<sup>†</sup> A similar information can be expected from the FT-

\* The definition of  $Q_{NF}$  will be given later in this chapter (chap. 3.8).

† The excitation frequency is identical with the frequency of the first harmonic,  $\nu_0 \equiv \nu_1$ . in the following equations and data analysis the angular frequency  $\omega$  is substituted by  $\nu/2\pi$ , because  $\nu$  uses the units of 1/s instead of rad/s.

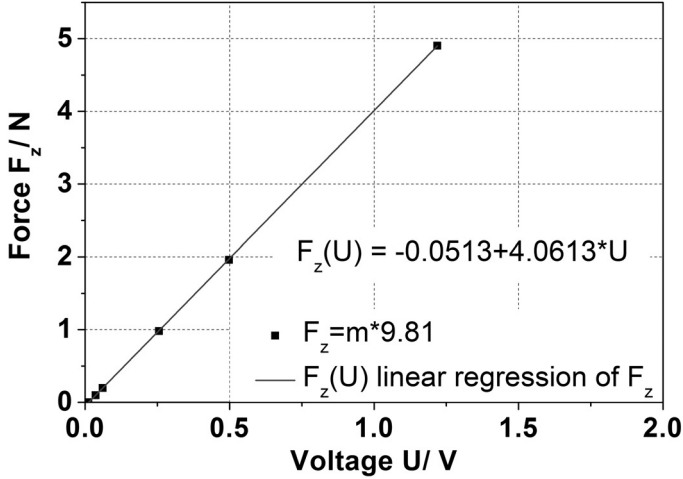


**Figure 3.10.** – Data points from defined weights (symbols) and the linear regression of the data points (line). The coefficient of determination (COD)<sup>142–144</sup>  $r_{COD}^2 = 0.9999$ .

spectrum of the axial normal force. The FT of the axial normal force  $F_z(t)$  is defined in eq. 3.39.

$$N(\nu) = \frac{1}{T} \int_0^{+\infty} F_z(t) e^{-i2\pi\nu t} dt. \quad (3.39)$$

The spectra is scanned for the appearance of higher harmonics of the excitation frequency  $\omega_1 = 2\pi\nu_1$ . From these spectra, the values

$$N_n = N(n \cdot 2\pi\nu_1) \quad (3.40)$$

with  $n \in \mathbb{N}^+$  are taken.

Further, the sensitivity is compared of the three set-ups. For this purpose, the signal-to-noise ratio (SNR) is determined as defined in eq. 3.41.

$$SNR = \frac{\max(N_n(\nu))}{\sigma_{noise}}. \quad (3.41)$$

Within eq. 3.41  $\sigma_{noise}$  is the standard deviation of a closed set, which represents the lowest level of noise, in the spectra, as seen in the inset of fig. 3.11.

This set of data is taken off the minimum signal,  $\nu_l \leq \nu \leq \nu_h$ . The length of this set is given by  $\Omega = \nu_h - \nu_l$ . This is illustrated in fig. 3.11 and defined in eq. 3.42 with the help of the local mean value  $\bar{N}_{local}$  as defined in eq. 3.43.

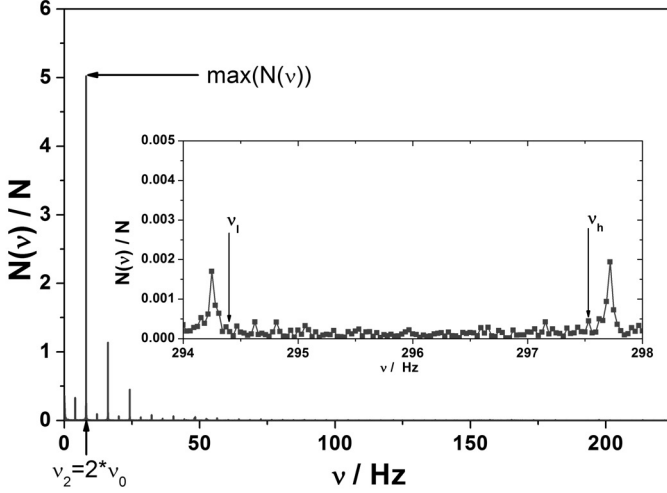


**Figure 3.11.** – Example of a FT-spectrum with indication of the excitation frequency  $\nu_0 \equiv \nu_1 = 4$  Hz and the maximum value  $\max(N_n)$ . The inset plot shows the region from which the data was taken to calculate the sensitivity limit. This region is limited by the frequency values of  $\nu_l$  and  $\nu_h$ .

$$\sigma_{noise}^2 = \frac{1}{\Omega} \int_{\nu_l}^{\nu_h} \left( N(\nu)^2 - \bar{N}_{local}^2 \right) d\nu \quad \text{with} \quad (3.42)$$

$$\bar{N}_{local} = \frac{1}{\Omega} \int_{\nu_l}^{\nu_h} N(\nu) d\nu. \quad (3.43)$$

The information gained by the normal force spectra is condensed to the strain-dependent normalized characteristic normal force amplitude ratio  $N_{4/2}(\gamma)$  (see eq. 3.46). Each single measurement, defined as a measurement of the time-dependent properties, creates a data set of the time-dependent normal force  $F_z(t)$ . Nevertheless, these measurements are also de-

pendent on the choice of the temperature  $\vartheta$ , the excitation frequency  $\nu_0$  and the excitation amplitude  $\gamma_0$ . That is why the normal force is a function, as

$$F_z(t) = \hat{F}_z(\vartheta, \nu_0, \gamma_0; t). \quad (3.44)$$

In the first step of data analysis the dependence on the time is changed using the Fourier transform to a dependence on the frequency  $\nu$ , as

$$N(\nu) = \hat{N}(\vartheta, \nu_0, \gamma_0; \nu). \quad (3.45)$$

Furthermore, the influence of the excitation deformation amplitude or the excitation strain amplitude  $\gamma_0$  on the normal force spectra is studied. For this purpose the ratio of the fourth higher harmonic of the normal force spectra  $N_4 := N(4\nu_0)$  and the second normal force higher harmonic of the normal force spectra  $N_2 := N(2\nu_0)$  is plotted as a function of the excitation strain amplitude under a constant excitation frequency  $\nu_0$  and at a constant temperature. Thus,  $N_{4/2}$  is defined as

$$N_{4/2}(\gamma) := \frac{N_4(\gamma_0)}{N_2(\gamma_0)} = \hat{N}_{4/2}(\nu, \vartheta; \gamma). \quad (3.46)$$

## 3.7 Validation of the Normal Force Geometry

The data of the measurements of the axial force under oscillatory shear performed with the three different set-ups was further analysed with the Fourier transform (FT). From these the FT magnitude spectra (see chap. B) were calculated. Those spectra were obtained for each measurement of the time-dependent properties. Similar measurements of the time-dependent properties were performed in all three set-ups and the spectra of those similar experiments can be compared as fig. 3.12 indicates. As fig. 3.12 reveals, all three methods give in principle similar results. A remarkable observation is that the high performance ARES G2 is also able to measure the normal force down to  $10^{-5}$  N.\* However, at the same time it is also remarkable that the frequencies of the harmonics are significantly lower than expected. The excitation frequency in the presented data of fig. 3.12 was

---

\* The manufacturer (TA-Instruments) only claims a sensitivity of  $10^{-3}$  N.

5 Hz. Because of this, the higher harmonics should appear at 10 Hz, 15 Hz, 20 Hz etc.. All small deviations, in terms of a few data points (meaning less than 0.005 Hz), can be caused by the leakage effect<sup>22</sup> (see chap. 2.1.4) of the FT. Nevertheless, for the results of the ARES G2 the deviation from the fundamental frequency is larger than 0.1 Hz. This deviation was found in the FT-spectra of the shear stress and in the FT-spectra of the normal force. The absolute values of the intensities of the peaks in the spectra of fig. 3.12 are in the range of  $N = [10^{-4}, 1]$  N. An overview for the absolute values of the intensities of the peaks in the spectra of fig. 3.12 is given in tab. 3.1.

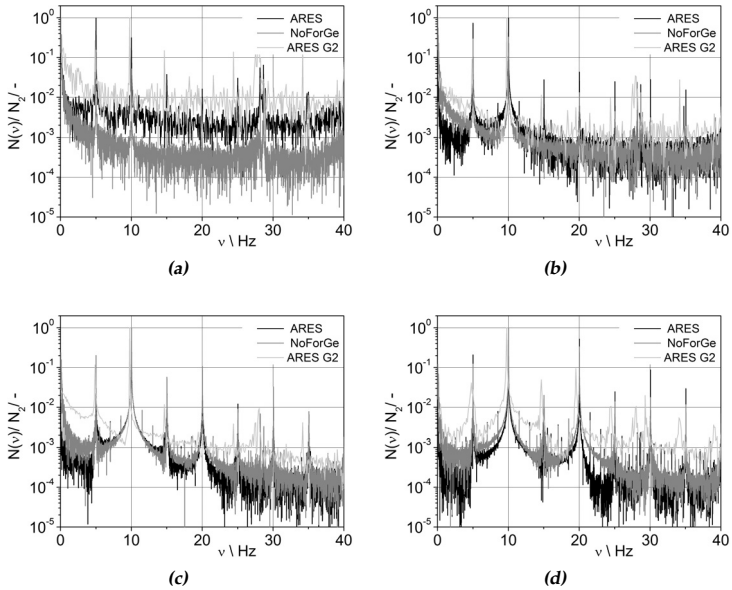


**Figure 3.12.** – Comparison of the FT spectra of the axial force measurement with the ARES (black line), NoForGe (grey line) and ARES G2 (light grey line) with a  $D = 8$  mm plate-plate geometry. Each plot represents the FT spectra for the measurement of the time-dependent properties with the same parameters, as  $\vartheta = 180^\circ$ ,  $\nu_0 = 5$  Hz and  $\gamma_0$ , for the same MDPE sample, for the three different set-ups. Between the different plots the shear amplitude  $\gamma_0$  has been altered, as (a)  $\gamma_0 = 10\%$ , (b)  $\gamma_0 = 30\%$ , (c)  $\gamma_0 = 70\%$  and (d)  $\gamma_0 = 150\%$ .

**Table 3.1.** – Comparison of absolute values of the intensities of the peaks in the spectra of fig. 3.12 of the NoForGe set-up for the measurement of the normal forces with a  $D = 8$  mm plate-plate geometry; using a MDPE sample (tab. 2.3) at  $\vartheta = 180$  °C and  $\nu_0 = 5$  Hz.

$\gamma_0$	$N_2$	$N_4$	$N_6$	$N_8$
%	N	N	N	N
10	0.02	$3 \cdot 10^{-4}$	-	-
30	0.11	0.022	0.003	-
70	0.17	0.05	0.009	0.005
150	0.62	0.045	0.005	0.002

By determining the standard deviation of the noise in the spectra (as defined in chap. 3.6) and the maximum peak in the signal, a signal-to-noise ratio could be found for the three set-ups, see tab. 3.2.

As tab. 3.2 shows, best SNR is obtained by the NoForGe. In combination with the observation that the frequency of the higher harmonics is shifted for the ARES G2. Thus, it can be stated that the NoForGe performed best and will be the method of choice for the further investigation about the non-linear material behaviour of polymers in this work.

**Table 3.2.** – Comparison of the signal to noise ratio (SNR) of the three different set-ups for the measurement of the normal forces with a  $D = 8$  mm plate-plate geometry; using a MDPE sample at  $\vartheta = 180$  °C and  $\nu_0 = 5$  Hz. From the  $\gamma_0$  dependent measurements always the maximum SNR was taken. In the case of the ARES and the ARES G2  $\gamma_0 = 70$  % and in case of the NoForGe  $\gamma_0 = 100$  %.

set-up	ARES	NoForGE	ARES G2
SNR	7,000:1	16,000:1	9,000:1

## 3.8 Non-linear Parameters from the FT-Measurement

Using the algorithm for the FT-rheology, as described in chap. 3.6, each measurement of the time-dependent properties provides time-dependent oscillatory stress  $\tau$  data (e.g. in fig. 3.13a) and time-dependent data of the normal force  $F_z(t)$  (e.g. in fig. 3.13b).

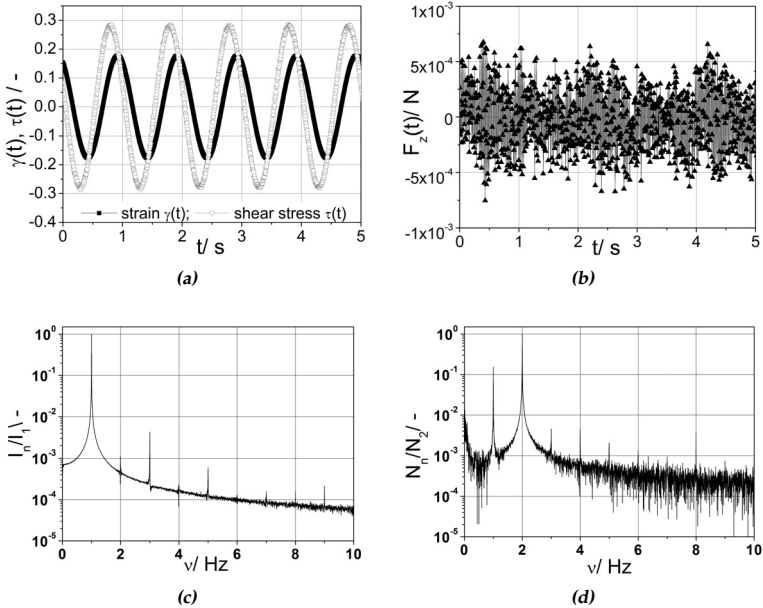


**Figure 3.13.** – Example of the FT-rheology, time-dependent data and the FT analysis of LDPE (tab. 2.3) at 180 °C oscillated with  $\nu_0 = 1$  Hz and  $\gamma_0 = 70$  % in an  $D = 8$  mm plate-plate geometry. (a) The time-dependent shear stress  $\tau(t)$ , (b) the time-dependent normal force  $F_z(t)$ , (c) the FT  $I_n(\nu)$  of the time-dependent shear stress  $\tau(t)$  and (d) the FT  $N_n(\nu)$  of the time-dependent normal force  $F_z(t)$ . In (a) and (b), only a small part of the whole dataset is shown; for better visualisation. The length of the whole dataset used for the FT has  $N \approx 52000$  pts and/or  $T_{meas} \approx 260$  s; with  $\nu_{Nyquist} = 100$  Hz.

For the spectra of the shear stress the ratio of the third harmonic normalized to the intensity of the fundamental peak  $I_3/I_1$  can be plotted as a function of the strain amplitude at a constant temperature, e.g. as seen in fig. 3.14a for a LDPE sample at 180 °C. The curve of  $I_3/I_1$  shown in fig. 3.14a can be quantified by the slope of the decreasing region  $S_1$  (at low strains) and by the slope of the subsequent region  $S_2$ .

By further normalizing  $\frac{I_3}{I_1}$  to the applied strain  $\gamma$  the  $Q$ -parameter is found (see chap. 3.3).<sup>106</sup> As an example, the data is used from fig. 3.14a of a LDPE sample at 180 °C. The plot of  $Q$  versus the strain  $\gamma$  can also be quantified by two slopes named  $S_{Q1}$  and  $S_{Q2}$  and indicated in fig. 3.14b.

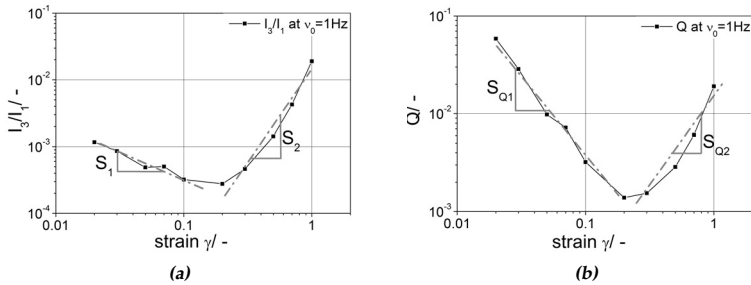


**Figure 3.14.** – Example of the results from the FT analysis and example of the determination of  $Q(\gamma)$  of LDPE (tab. 2.3) at 180 °C in an 8 mm plate-plate geometry. (a) The strain dependent normalized 3rd harmonic as a function of strain and (b) the non-linear parameter of  $Q(\gamma)$  of LDPE as a function of strain. The black squares ■ represent the experimental data. Whereas, the grey dash-dotted line indicates the linear inclination of the experimental data.

A similar analysis as for the shear stress can also be applied on the normal force data, as shown in fig. 3.15. For the normal force data, the fourth harmonic is normalized to the second harmonic  $N_4/N_2$ , as given in eq. 3.46 of chap. 3.6.  $N_4/N_2$  is plotted as a function of the strain amplitude  $\gamma$  at a constant temperature, e.g. as seen in fig. 3.15a for a LDPE sample at 180 °C. As for the  $I_3/I_1$  from the shear stress, the curve of fig. 3.15a has two regions which can be quantified by their slopes  $S_{N1}$  and  $S_{N2}$ , as indicated in fig. 3.15a.

Similar to the  $Q$ -parameter a normalisation of  $N_4/N_2$  to  $\gamma^2$  can be conducted. From this a new non-linear parameter for the axial normal force  $Q_{NF}$  is defined as a counter part to the  $Q$ -parameter.

**Definition 1. Non-linear parameter for the axial normal force  $Q_{NF}$**

*In style of the definition of the  $Q$ -parameter for the non-linearity of a material in relation to its shear stress response in LAOS, a parameter for non-linearity of the axial normal force can be defined from the FT-spectra of the normal force response of a material under LAOS. A FT-spectrum of the axial normal force in LAOS will include peaks at the even higher harmonic  $N_2, N_4, N_6$ . These peaks are scaling with the applied strain  $\gamma_0$  like  $\frac{N_n}{\gamma_0^n}$ . Accordingly, the  $Q_{NF}$ -parameter is defined as the ratio of the fourth harmonic and the second harmonic including the according scaling of  $\gamma_0$ .*

$$Q_{NF} := \frac{N_4}{N_2 \cdot \gamma_0^2}. \quad (3.47)$$

□

An example of  $Q_{NF}$  from the  $N_4/N_2$  curve in fig. 3.15a is shown in fig. 3.15b. Also this curve is quantified by two slopes, as indicated,  $S_{QN1}$  and  $S_{QN2}$ .

With the definition in eq. 3.47 the  $Q_{NF}$ -parameter can be calculated from fig. 3.15a and is shown in fig. 3.15b.

The second region of the curves related to the spectra of the normal force are not developed, as fig. 3.15 shows. A linear regression could not be applied, as for the first region of these curves and for both regions in the curves related to the spectra of the shear stress, see fig. 3.14. However, in fig. 3.15 the slopes of the second region are indicated just as a figure of illustration. Because the results presented in chap. 3.9 make use of this quantification values.

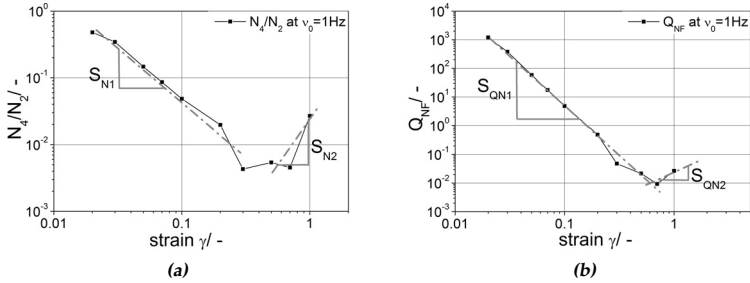


**Figure 3.15.** – Example of the results from the FT analysis and example of the determination of  $Q_{NF}(\gamma)$  of LDPE at 180 °C in an 8 mm plate-plate geometry. (a) The strain dependent normalized 4th harmonic of the normal force  $F_z(\nu)$  as a function of strain and (b) the non-linear parameter of  $Q_{NF}(\gamma)$  of LDPE as a function of strain. The black squares ■ represent the experimental data. Whereas, the grey dash-dotted line indicates the linear inclination of the experimental data.

### 3.9 Comparison of the Results of the Non-linear Behaviour of PS and PE Samples

In this chapter the results from the non-linear quantities as described in chap. 3.8 are shown. The first results shown in this chapter were obtained from measurements of PE samples. The non-linear values of a LDPE was already given as an exemplification in chap. 3.8. As introduced in

chap. 2.4.2, the LDPE contains longchain branching which influence the rheological behaviour of the melt flow.<sup>145,145,146</sup> The results of the LLDPE are presented in fig. 3.16.

Both types of plots,  $Q(\gamma)$  and  $Q_{NF}(\gamma)$ , show qualitatively a characteristic behaviour which all\* polymers exhibit. At low shear amplitudes, meaning a first region, the curves are decreasing with the slope  $S_1$  until they reach a

\* Referring to all polymers which have been studied in this work.

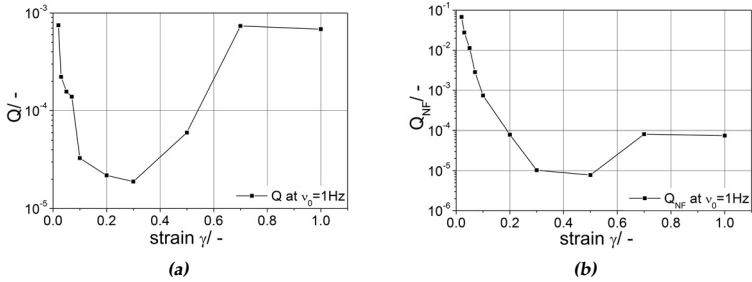


**Figure 3.16.** – Non-linear values for the LLDPE sample. The plots show (a) the  $Q$ -parameter for the LLDPE and (b) the  $Q_{NF}$ -parameter for the LLDPE. For measurements at  $\vartheta = 180^\circ\text{C}$  and  $\nu_0 = 1\text{Hz}$ .

local minimum. After passing this point the curves enter a second region, in which the curves start to increase with the slope  $S_2$  together with the shear amplitude. The slopes of the two regions and for both types of plots are calculated via a linear regression<sup>142,147</sup> and the values are summarized in tab. 3.3. In addition the values of this table are graphically shown in fig. 3.18 and fig. 3.19. Thus, it can be seen that the slope of region one  $S_{QN1}$  in the  $Q_{NF}(\gamma)$  plots is different for different types of polymers, e.g. the values of both PE samples are smaller than those of both PS samples.

The slope of region two  $S_{Q2}$  in the  $Q(\gamma)$  plots stays similar for the branched PS (comb-PS) and the linear PE (LDPE) (both samples contain long chain branches). The slope  $S_{Q2}$  for the comb-PS and the LDPE are small in comparison to the  $S_{Q2}$  for the PS-L, which has the largest observed value, and the  $S_{Q2}$  of the LLDPE, which is still about a factor of 2.0 larger than the one of the branched samples.

The absolute slope values of the  $Q_{NF}$ -parameter are also affected by the polymer topology in case of the PS samples and even stronger for the PE samples. For the PE samples, the slope values of the normal force  $S_{QN2}$  are largely changing, i.e. the  $S_{QN2}$  value of the LLDPE is about a factor of 10 larger than the one of the LDPE. For the PS samples, between the comb-PS and the PS-L is a factor of 1.5.

The bar plots from fig. 3.18 and fig. 3.19 are in absolute values which allows the gathering of all values in one plot. This is also justified by com-

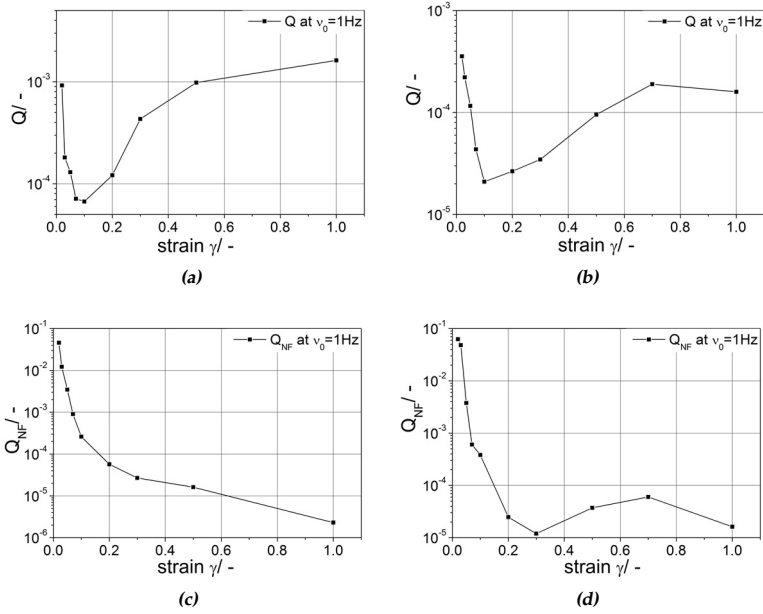


**Figure 3.17.** – Non-linear values for a PS-L and a comb-PS sample. The plots show (a) the  $Q$ -parameter for a PS-L, (b) the  $Q$ -parameter for a comb-PS, (c) the  $Q_{NF}$ -parameter of a PS-L and (d) the  $Q_{NF}$ -parameter of a comb-PS. For measurements at  $\vartheta = 170$  °C and  $\nu_0 = 1$  Hz.

parison to tab. 3.3, where it can be seen that for one parameter the sign is the identical for all polymer samples. This is valid for all values except for the slope  $S_{QN2}$  of the normal force. It appears that the PS-L sample has a negative value for the slope  $S_{QN2}$  of the normal force whereas all other samples have a positive value for the slope  $S_{QN2}$  of the normal force. Thus, a strong difference can also be found between the linear and the branched PS, however in an inverse proportion as for the PE samples. This means that the PS-L has got smaller (negative) values of  $S_{QN2}$  and the comb-PS has got positive values of  $S_{QN2}$ . In case of the PE, the LLDPE has got larger values of  $S_{QN2}$  than the LDPE.

The slopes of  $I_3/I_1$  show qualitatively a similar behaviour as the slopes

obtained from the  $Q$ -parameter. However, the quantitative differences are stronger for the slopes of the  $Q$ -parameter. Thus, the values of the slopes of  $I_3/I_1$  are shown in fig. 3.18 and fig. 3.19. Though, they are not independently discussed as their discussion does not provide new information. A similar reasoning is valid for the analysis of the slopes obtained from the spectra related to the normal force, i.e.  $N_4/N_2$  and  $Q_{NF}$ . Thus, the discussion of the slopes  $S_{QN1}$  and  $S_{QN2}$  contains similar information as the slopes  $S_{N1}$  and  $S_{N2}$ , but more pronounced.

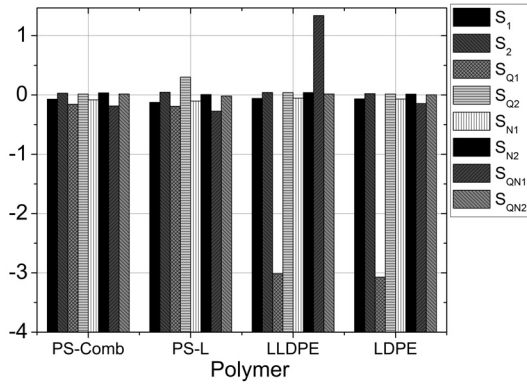
Concluding this section, the slope  $S_{Q1}$  differentiates between the different polymer types (PS and PE). The values of  $S_{QN1}$  have been larger for the PS sample. This means that the non-linearity  $Q$  of the shear stress are decreasing strongly for increasing shear strains at low shear strains. The slope  $S_{Q2}$  differentiates between the different branching types for both types of polymer (PS and PE). Thus, the content of long chain branches have an influence on the rheology for high shear strains. The increase of the non-linearity  $Q$  of the shear stress is higher for the linear chains. Thus, long side chains are reducing the non-linearity.

**Table 3.3.** – Comparison of the non-linear parameters for the four different polymers.

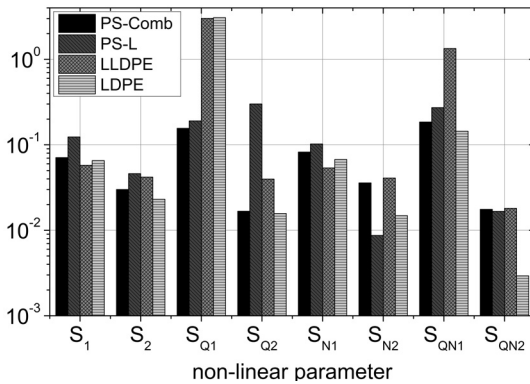
Polymer	$S_1$	$S_2$	$S_{N1}$	$S_{N2}$
Comb-PS	-0.0709	0.0300	-0.0824	0.0359
PS-L	-0.1238	0.0461	-0.1025	0.0087
LLDPE	-0.0577	0.0419	-0.054	0.041
LDPE	-0.0654	0.0231	-0.0675	0.0148

Polymer	$S_{Q1}$	$S_{Q2}$	$S_{QN1}$	$S_{QN2}$
Comb-PS	-0.1560	0.0167	-0.1852	0.0176
PS-L	-0.1905	0.3008	-0.2726	-0.0166
LLDPE	-0.1472	0.0398	-0.1308	0.0180
LDPE	-0.1505	0.0157	-0.1446	0.0029



**Figure 3.18.** – The non-dimensional absolute values of the slopes from tab. 3.3 for the four investigated polymers, sorted according to the polymer.



**Figure 3.19.** – The absolute values of the slopes from tab. 3.3 for the four investigated polymers, sorted according to the parameter.

## 3.10 Summary and Conclusions for the NoForGe

Comparing the requirement specifications which had been set in the beginning of this chapter with the results, that have been achieved, it can be concluded that:

- The set-up of the FT-R has been modified to measure the normal force directly via the ARES-normal force-transducer.
- A new geometry for measuring the axial normal force under oscillatory shear was designed, installed and tested; (the NoForGe).
- The reproducibility of the new installed geometry has been tested and also compared to different other set-ups.
- The signal of the axial normal force has been calibrated and thereafter this signal has been Fourier-transformed.
- Definitions of the sensitivity of the FT have been applied to the spectra of the axial normal force.
- Further, the measurement of the normal forces has been done with one truly commercial set-up, the ARES G2, one modified commercial set-up, the ARES with improved DAQ, and the new designed normal force geometry (NoForGe) installed in an ARES. All three set-ups had been able to measure non-linearities in the normal forces with similar results. The new normal force geometry (NoForGe) performed best ( $SNR = 16000 : 1$ ). However, only a factor of three is between the NoForGe and the worst performing instrument the ARES. Thus, all three instruments are fulfilling the requirements for a highly sensitive normal force measurement.\* It should be mentioned at this point that the new normal force geometry (NoForGe) technology still has the advantage of being transferable to other rheometers than the ARES. Even very basic rheometers could that way be upgraded into a high performance tool for non-linear rheology.

---

\* Although, the ARES G2 shows a significant shift of the frequency of the harmonics of the FT-spectra.

- A new non-linear parameter ( $Q_{NF}$ ) was introduced for the analysis of the FT-spectra of the axial normal force.
- The measurements of different polymers with different topologies illustrated that with the help of the non-linear measurements differences could be found for branched and linear polymer samples in the slope values of the  $Q$ -parameter and the  $Q_{NF}$ -parameter. The  $Q$ -parameter showed its sensitivity on the branching type in the range of high strains. In case of PS samples the stress spectra gave the best indication while for the PE samples the normal force spectra were indicating large differences between linear and branched samples. Further, the  $Q_{NF}$ -parameter showed differences in its slope  $S_{QN1}$  for PS and PE at low strains.

## Chapter 4

### Detection of Mechanical Instabilities in the Capillary Rheometer and the Extruder

During the extrusion of polyethylene (PE) and other polymer melts, visible surface distortions\* of the extrudate appear at increasing shear rates. At a defined range of shear rates the surface distortions show a characteristic behaviour and are classified as e.g. shark-skin, stick-slip or melt-fracture. During the extrusion occur pressure fluctuations inside the die; preliminary studies<sup>62,146,148–150</sup> showed that those fluctuations seem to correlate with the mechanical instabilities.

For the efficient processing of polymer melts these mechanical instabilities must be known for the polymer under processing in order to optimize the extrusion while simultaneously guaranteeing the quality of the product. In this thesis, the relationship between pressure fluctuations and mechanical instabilities was first investigated for PE melts via a commercial capillary rheometer with a unique die set-up and an advanced data analysis.<sup>146,148</sup> With this laboratory set-up<sup>†</sup> it is possible to qualify and quantify the mechanical instabilities via advanced mathematical tools such as the Fourier transform and correlation functions.

This laboratory set-up shows promising characteristics which could be used for the extrusion processing. In the subsequent section (chap. 4.1), the general aims of this chapter are defined. Thereafter, the term mechan-

---

\* Also called melt flow instabilities or mechanical instabilities.

† The Göttfert GmbH recently commercialized this special die in cooperation with our group.

ical instabilities or melt flow instabilities (MFI) are explained including an abbreviated version of the research in this field. Subsequently, the special experimental set-ups used in this thesis are presented, for the capillary rheometer in chap. 4.3 and for the extruder in chap. 4.4. In particular the section about the extruder contains a detailed technical description of the newly designed dies for measuring the time-dependent pressure inside the die. For the analysis of the time-dependent pressure data the Fourier transform is not sufficient. Because of this a special pre-processing of the raw data is necessary<sup>148,151</sup> which is illustrated in chap. 4.4.4.

The chap. 4.4.6 contains the description of the experimental set-up and the results of the optical set-ups which have been used to study the mechanical instabilities on the cold samples of the extrudate.

After the introduction of the optical analysis, the experiments on the extruder (chap. 4.4.7) and the results from those experiments are presented and discussed in chap. 4.5. This chapter begins with a basic definition about the contribution of the mechanical extruder-system, the contribution of the material to the pressure signal and the advanced analysis of the pressure signal. This sections are followed by chap. 4.5.4 in which the development of mechanical instabilities in the extruder die is illustrated. Chap. 4.6 provides a summary of the chap. 4.

## 4.1 Detection of Melt Flow Instabilities on the Extruder

The work presented in this chapter has the task of transferring and adapting the set-up which had been used on a capillary rheometer<sup>62,146,148</sup> to a lab size extruder, in order to prove whether an application in real process applications is feasible. In detail this task includes the following steps:

1. Transferring the technology from the die of the capillary rheometer to the die of the lab extruder (see chap. 4.4).
2. Defining the conditions under which melt flow instabilities (MFI) for certain polymers can be optically observed.
3. Adapting and using advanced mathematical tools for the analysis of the time-dependent pressure data obtained from the special die for the lab extruder.

4. Identifying the characteristic patterns of the instabilities in the results of the data analysis.
5. Comparing the results from the optical analysis with the results from the analysis of the time-dependent pressure.
6. Concluding whether the set-up has the potential to be developed further into a self controlled process device (the "smart-extruder").

## 4.2 Melt Flow Instabilities

Melt flow instabilities (MFI) are a topic of research since the early 1960s.<sup>152–155</sup> From the beginning a large amount of research has been undertaken by academic groups world wide.<sup>156–166</sup> The temporal process has been documented in reviews e.g. by Larson<sup>167</sup> or by Denn.<sup>168</sup>

The melt flow instabilities of polymer melts can be qualitatively split in at least three basic categories.<sup>164</sup>

1. sharkskin
2. stick-slip
3. gross melt fracture

The three types of melt flow instabilities have different origins. The next paragraphs provide a summary of the research in the field of the melt flow instabilities.<sup>164</sup>

At low shear rates sharkskin is the first mechanical instability which can be observed if the shear rate is continuously increased. Only some polymers exhibit sharkskin, i.e. linear low density polyethylene (LLDPE), polypropylene (PP) or polydimethylsiloxane (PDMS). In the literature, a surface instability is called sharkskin if it appears only as a distortion of the surface on the polymer extrudate. Its origin is still unknown and scientific debates about the mechanism of the origin are ongoing (e.g. between Cogswell and Wang<sup>169</sup>). Cogswell et al. assume that the rupture mechanics at the die exit control the sharkskin instability.<sup>170–174</sup> Migler<sup>175,176</sup> relates the sharkskin instability to rupture caused by elongational stress at the die exit. The group of Prof. Münstedt basically supports this theory with their studies of the velocity fields inside and outside the die with different PE samples.<sup>61</sup> Another theory of the origin of the sharkskin melt flow instability is given by Wang et al.<sup>177–180</sup> To explain the sharkskin instability

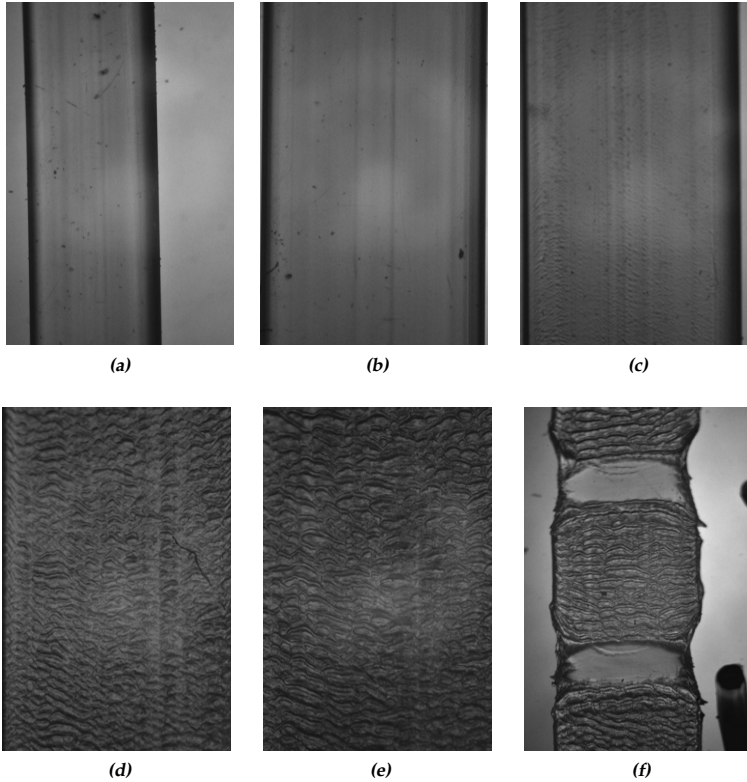


**Figure 4.1.** – Examples of observable melt flow instabilities for PE-SCB07 (the height of each image, except of (f), is 3.75 mm) at  $\vartheta = 180\text{ }^{\circ}\text{C}$  and at different apparent shear rates: (a)  $\dot{\gamma}_{app} = 8\text{ s}^{-1}$ , (b)  $\dot{\gamma}_{app} = 39\text{ s}^{-1}$ , (c)  $\dot{\gamma}_{app} = 79\text{ s}^{-1}$ , (d)  $\dot{\gamma}_{app} = 129\text{ s}^{-1}$ , (e)  $\dot{\gamma}_{app} = 157\text{ s}^{-1}$  and (f)  $\dot{\gamma}_{app} = 196\text{ s}^{-1}$ , the height of of this image is 7.5 mm.

they introduce a slippage at the wall caused by molecular entanglement and disentanglement.

In addition to the understanding of the origin of sharkskin it is of practical interest how the onset of sharkskin can be shifted to higher shear rates. Different researchers participated in this field, e.g. Piau et al. focused on slippery surfaces.<sup>181,182</sup> Miller and Rothstein studied the influence of the temperature gradients along the die wall on the sharkskin instability.<sup>156,183</sup> Arda and Mackley observed how the sharkskin instability changes under several geometrical and material-dependant factors<sup>184</sup> and also under the application of gas-assisted extrusion.<sup>185</sup>

A further increase of the shear rate the extrudate leads to the stick-slip instability. Already early studies<sup>152,154,186</sup> revealed that the stick-slip instability is related to flow mechanisms inside the barrel of a capillary rheometer and also to the elongational properties of the fluid in the region of the die entrance.<sup>164</sup> Later, Wang et al.<sup>177,187-190</sup> studied the molecular origin of the stick-slip instability. The group of Münstedt studied the phenomena of the melt flow instabilities as well. They used the advanced set-up of a LASER-Doppler-Velocimetry (LDV)<sup>\*192,193</sup> which allowed the determination of the velocity fields of an investigated flow. The spatial resolution in three dimensions reached down to approximately  $24 \times 10^{-6}$  m but with a minimum distance to the wall of  $30 \times 10^{-6}$  m.<sup>194,195</sup> The time resolution of this set-up is about  $5 \times 10^{-6}$  s. According to this, the slip velocities at the surface of the wall can be determined via extrapolation, even though a direct measurement at the die wall is not possible.<sup>†</sup>

At high shear rates the extrudate shows strong volume distortions called gross melt fracture (GMF), as defined below. The term GMF includes flow

\* LDV is also known as LASER Doppler Anemometry (LDA) and was already applied to flows in capillary rheometers by Ramamurthy et al.<sup>191</sup> However, their studies were limited to the velocity fields at the entrance of the die.

† Another possible explanation for the origin of the stick-slip instability is given in a work by Molenaar et al.<sup>196,197</sup> who postulates a basic set of equations of conservation for the flow inside the barrel. By introducing the compressibility of the fluid the solution for the equations of conservation results in pressure fluctuation as qualitatively observed in the experiments on the capillary rheometer at the exit of the barrel. Quantitative results are difficult to obtain by this method. The compressibility is also included in the model of Adewale et al.<sup>198</sup> Their model includes further factors such as hardening effects and the stick-slip boundary condition inside the die.

phenomena with different origin. One is the spurt instability which is related to the compressibility of the melt in the reservoir and to the non-Newtonian behaviour inside a capillary die, which is caused by the slip at the die wall.<sup>164,199,200</sup> Another form of GMF is the helicoidal instability. It appears as a clearly visible spiral flow (helix) on the extrudate and is influenced and determined by the die entrance, as Piau et al. showed.<sup>164,201</sup> Finally, the real GMF is found to be basically of a completely irregular structure. Bagley et al.<sup>154</sup> found that this is caused by the chaotic flow conditions at the die entrance. This is confirmed by Kim et al.<sup>202,203</sup> by using carbon black tracer particles to visualize the flow. Kim added that the true rupture of the melt is an additional mechanism of the origin of GMF. Meller et al.<sup>204,205</sup> supported this observation by using a converging flow in which the severity of the instability could be decreased with increasing convergence. Already in 1968 Giesekus<sup>206</sup> studied the influence of different die entrance geometries on the development of the flow and the development of the melt flow instabilities. Object of his studies were polymeric solutions. However, he expected polymer melts to behave in a similar way. In his opinion the melt flow instabilities are caused by hydrodynamic instabilities for which he introduced the term of a rheodynamic stability problem.\*

From the processing point of view GMF is of low importance, because it only appears at high shear rates. Nevertheless Lee et al.<sup>207</sup> tried to figure out which factors influence the GMF. Kulikov and Hornung<sup>208–210</sup> studied the melt flow instabilities in order to find a practical solution to suppress the melt flow instabilities. Related to this, the studies of Larrazabal et al. showed how the onset of instabilities is influenced by the choice of material of the die (e.g. brass, steel, nickel-plated steel, Teflon coating).<sup>211</sup>

Each of these basic categories of melt flow instabilities has its own characteristics by which it can be classified. In addition to the description of the mechanical instabilities summarized above, the following three definitions<sup>†</sup> of the classification of the mechanical instabilities are used to discuss the research presented in this chapter.

---

\* This term includes the equations of hydrodynamic stability and the rheological information of the material.

† The aim of these definitions is to give the interested practitioner an easily applicable vocabulary for the phenomena of melt flow instabilities which they might have observed.

**Definition 2. Sharkskin**

A melt flow instability can be classified as sharkskin, if it meets the following constraints:\*

1. The instability can be classified as approximately periodic.
2. Starting at low shear rates and with increasing shear rate, the sharkskin instability is the first instability which appears on the originally smooth extrudate.
3. The amplitude  $H_{inst}$  of the instability is small in comparison to the thickness of the extrudate  $H_{extr}$ , so  $\frac{H_{inst}}{H_{extr}} < 1$ .
4. The instability appears at low shear rates.† □

**Definition 3. Stick-slip**

A melt flow instability can be classified as stick-slip, if it meets the following constraints:

1. The extrudate shows approximately periodically alternating regions of smooth (or at least less rough areas) and rough extrudate, which have relatively large spatial expansions,  $\frac{L_{inst}}{D_{extr}} > 1$ .
2. The pressure signal in the reservoir shows large oscillations of the pressure which qualitatively continue in the die. □

**Definition 4. Gross melt fracture (GMF)**

A melt flow instability can be classified as gross melt fracture (GMF), if it meets the following constraints:

1. The amplitude  $H_{inst}$  of the instability is large in comparison to the thickness of the extrudate  $H_{extr}$ , so  $\frac{H_{inst}}{H_{extr}} > 1$ .
2. The instability does not necessarily show an obvious periodic pattern.
3. The instability appears at high shear rates. □

The appearance of the different melt flow instabilities can largely vary depending on parameters, like molecular composition, additives, blend composition, temperature, shear rate, and die geometry. In some cases it is

\* Other authors take the probable origin of the instability as basis of the definition, i.e. Wang et al.. They demand that an instability may only be called sharkskin if the instability disappears when the experiment is performed a second time with the same parameters, but with the die exit region coated with e.g. fluoropolymer.<sup>177,190</sup>

† However, the shear rates are higher than those of the smooth extrudate.

obvious that a melt-flow instability is present, e.g. see fig. 4.1f. In other cases, as e.g. in fig. 4.1c, the instability is not as obviously visible. For defining this observation the terms strong melt flow instabilities and weak melt flow instabilities are introduced as defined below.

**Definition 5. Strong melt flow instability**

*A melt flow instability is called a strong melt flow instability, if its effect on the surface of the extrudate is easily visible; even to the naked eye, e.g. as seen in fig. 4.1a.* □

**Definition 6. Weak melt flow instability**

*A melt flow instability is called a weak melt flow instability, if its effect on the surface of the extrudate is barely visible; even to the naked eye (see fig. 4.1c). However, it is still detectable with special devices, e.g. microscopes, electron microscopes, surface roughness testers.* □

## 4.3 Experimental Set-up for the Capillary Rheometer

A capillary rheometer is basically a testing device for high shear rate flows in capillary tube flows.<sup>44,45</sup> Its origin bases on the work of Poiseuille<sup>69,70</sup> and Hagen.<sup>68</sup> However, their basic law for flows in pipes is only valid for Newtonian fluids. For viscoelastic fluids the basic law has to be improved by several corrections\* as summarized by Philippoff et al.<sup>214</sup> Typically, a sample fluid is located inside the reservoir of the capillary rheometer. After obtaining the chosen initial conditions, e.g. temperature, the fluid is forced through a capillary die by the movement of a piston, by rotating the screw of a feeding extruder or by gas pressure. By measuring the pressure in the reservoir right above the die entrance and knowing the environmental pressure (1 bar) the pressure difference along the die can be calculated and with this the material properties, as the shear rate dependent viscosity can be calculated.<sup>44</sup>

The experiments in the present work were performed in a Göttfert Rheotester 2000. This capillary rheometer uses a constant piston velocity. The

---

\* I.e. the Weissenberg-Rabinowitch correction for the wall shear rate<sup>212</sup> or the Bagley correction<sup>213</sup> taking the geometrical length of the die into account.

reservoir is replaceable; therefore, it is possible to alter the reservoir diameter. Reservoirs with the diameter  $D_B = [9.5, 15, 20]$  mm were used for the experiments. Fig. 4.2 shows a sketch of the used capillary rheometer and the data acquisition set-up.

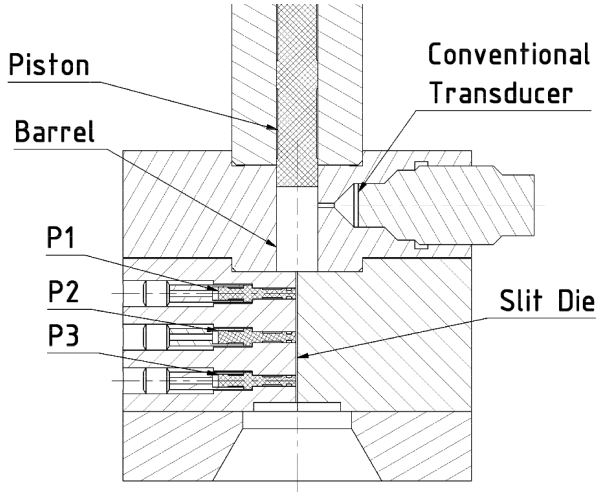


**Figure 4.2.** – The principle of a capillary rheometer as used in the experiments. The elements P1 - P3 are the high sensitive piezoelectric pressure transducers which have been introduced in the work of Filipe et al.<sup>146</sup> The sample fluid is placed inside the barrel (reservoir); then the piston moves down with a defined velocity and pushes the material through the slit die. The conventional pressure transducer (strain gauge) records the pressure inside the barrel (less than 8 data points per second) and from these data, properties like the shear rate dependent viscosity are calculated. The high sensitive pressure transducers (P1-P3) record the time-dependent pressure inside the slit die.

For all experiments, a specially designed slit die (30 mm  $\times$  3 mm  $\times$  0.3 mm), developed and described by Filipe et al.,<sup>146</sup> was used. It includes three high sensitive piezoelectric pressure transducers (Kistler 6182A) with a sensitivity of about 2.5 pC/bar, see fig. 4.3 and a diameter of the measurement surface of  $D_{piezo} = 2.5$  mm. The electrical signal of the piezoelectric transducers was amplified via a Kistler charge amplifier (5015A) and then

digitalized with a 16-bit NI-PCI-MIO-16XE ADC board from National Instruments with a sampling rate of 100 kHz. Each pressure channel was scanned with up to 33 kHz. To reduce the amount of data points and to increase the signal-to-noise ratio oversampling<sup>138</sup> was used. Typically, 100 to 500 raw data points were averaged in the oversampling algorithm. After oversampling, the pressure data of the three piezoelectric sensors\* was used for further mathematical analysis of the pressure fluctuations.

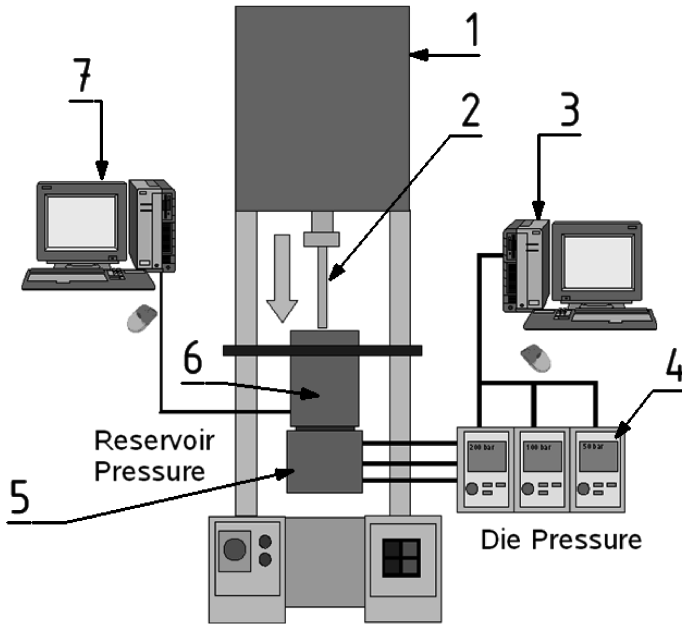


**Figure 4.3.** – Capillary rheometer with a data acquisition system attached. (1) Göttfert Rheotester 2000, (2) piston, (3) data acquisition PC with Labview, (4) charge amplifier (Kistler 5015), (5) sharkskin die (SSD) with piezoelectric transducer, (6) barrel/ reservoir and (7) Rheometer control PC.

Historically, two predecessors have to be mentioned who worked in a

\* Piezoelectric sensors are well known not only for their high sensitivity but as well for their drift of the signal in long time measurement applications. Their main field of application lies in the area of highly dynamic measurements.

similar direction as the group of Prof. Wilhelm.<sup>62,146,149,150,215,216</sup> The first ones are Atwood et al.<sup>217</sup> who used high sensitive hot-film probe inside the die of a capillary rheometer with an advanced data analysis via Fourier-transform and autocorrelation function. They already found characteristic peaks for the instabilities in the FT-spectra.\* Unfortunately, the probes seemed to be difficult to install and to calibrate. Additionally, the hot-film probes had the problem of viscose heating which influenced the results. Also the sensitivity of those measurements was limited to a signal-to noise ratio (SNR) of 100. Another previous work in the field of the high frequency detection of melt flow instabilities was done by den Doelder et al.<sup>197</sup> They installed a high sensitive piezoelectric pressure transducer inside the barrel of a capillary rheometer. Thus, they were able to observe stick-slip instabilities and gross-melt fracture inside the die. They used the Fourier-transform to extract the time periods of these instabilities. Their results, as published,<sup>197</sup> showed only for high shear rates ( $\dot{\gamma} > 400 \text{ s}^{-1}$ ) a characteristic peak in the FT-power spectrum (see chap. B). An information of the signal-to-noise ratio (SNR) is missing and due to the linear axis of the FT an estimation of the sensitivity is difficult. However, den Doelder et al. did not use oversampling to improve the sensitivity of their set-up.

## 4.4 Experimental Set-up for the Extrusion

In this work the principle of the sharkskin die was transferred to lab-size extruder for studying the melt flow instabilities under processing-like conditions. For this purpose, a Brabender single-screw extruder 19/25D (with a screw diameter of  $D = 19 \text{ mm}$  and a length of the screw of  $25 \times D$ ) driven by a Brabender Labstation was used to melt and feed the polymer granulate. For the highly sensitive pressure measurement, as it has been used on the capillary rheometer and explained in chap. 4.3, two special slit dies (SSD) (see fig. 4.4 and fig. 4.7) were built for the extruder.

1. First, a flat slit die was built with a length of 100 mm, a slit cross sec-

---

\* Related to the measurement principle only the information about the frequency could be drawn from the FT-spectra, while the y-axis contained no information. This is in strong contrast to the works of Filipe et al. and Palza et al.,<sup>62,149</sup> where the y-axis of the FT-spectra contains the information about the amplitude of the pressure fluctuations.

tional area of 20 mm × 0.8 mm and a biconical die entrance region; further to be called sharkskin die-1.

2. Later on, it was convenient to build a further slit die with a length of 80 mm, a slit cross sectional area of 10 mm × 1 mm and a 180° die entrance angle; further referred to as sharkskin die-2.

#### 4.4.1 The First Generation Sharkskin Die (SSD-1)

The sharkskin die-1 was designed to be able to reach high shear rates due to its flat shape. It was built at the Brabender GmbH. The sharkskin die-1 was built with a biconical die entrance region, which was necessary to homogeneously feed the broad slit ( $B = 20$  mm), if compared to the feed hole of  $D = 8$  mm, with polymer melt. The very first version is shown in fig. 4.4a. It revealed the problem of polymer leakage along the sides of the die. This problem could be fixed by drastically reducing the contact area of both the halves of the die, thus increasing the contact pressure on the contact surface.\* By this modification the leakage of polymer melt was stopped. In the first series of measurements it was observed that due to a maximum pressure limitation of the extruder of around 600 bar at the die entrance and the maximum temperature of 200 °C which could be used, the shear rates were limited to very low values, below  $20 \text{ s}^{-1}$ . Thus, no strong melt flow instability could be observed.

The task was to reach higher shear rates at which the melt flow would show strong melt flow instabilities. In order to achieve this, the cross-sectional shape of the slit was changed in such a way that the ratio of perimeter area to cross-sectional area,  $R_{P/C,i}$  (see eq. 4.1), would be decreased.

$$R_{P/C,i} := \frac{A_{P,i}}{A_{C,i}}. \quad (4.1)$$

In eq. 4.1  $A_{P,i}$  is the reduced perimeter area<sup>†</sup> of the slit die as defined in

\* The contact area  $A_{\text{contact},1}$  for the first version of the sharkskin die, shown in fig. 4.4a, is  $A_{\text{contact},1} \approx 90 \text{ cm}^2$ . The contact area  $A_{\text{contact},2}$  for the second version of sharkskin die in fig. 4.4b  $A_{\text{contact},1} \approx 36 \text{ cm}^2$ , see fig. 4.4b. The contact pressure is force per area  $p_{\text{contact}} = F/A_{\text{contact}}$ . For a constant applied force  $F$  the contact pressure increases from the first version to the second version like,  $p_{\text{contact},2} = A_{\text{contact},1}/A_{\text{contact},2} \cdot p_{\text{contact},1} = 2.5 \cdot p_{\text{contact},1}$ .

† The perimeter area is normalized to a unit length (circumference).

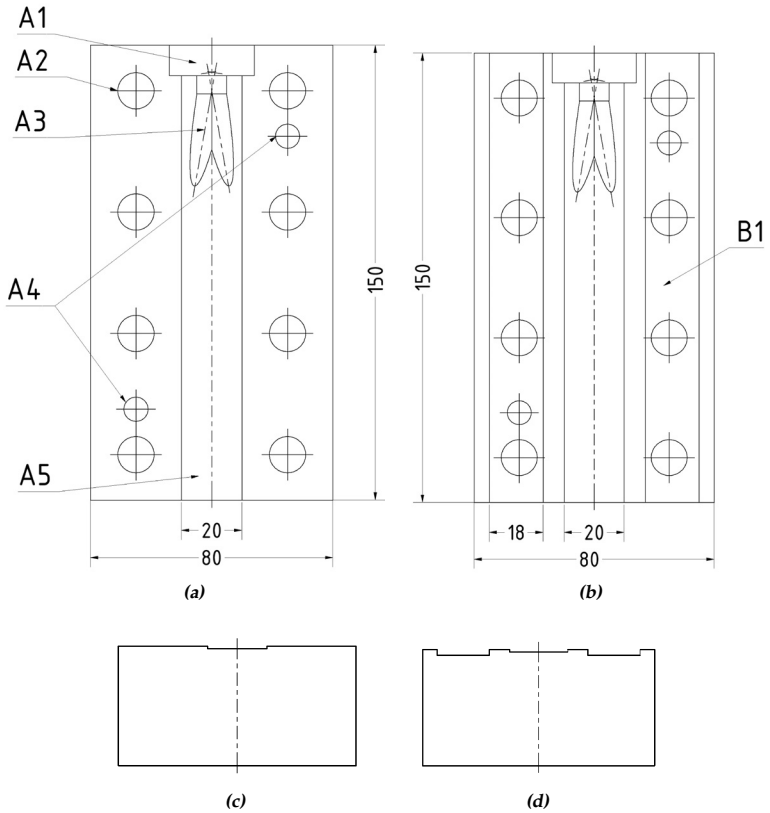


**Figure 4.4.** – Improvement of the sharkskin die-1. (a) shows the initial sharkskin die-1 where polymer melt leakage was possible. (A1) centring region for the flange connection to the extruder, (A2)  $8 \times M12$  screws for fixing upper and lower half of the die, (A3) biconical die entrance region, (A4) centring bolts and (A5) slit  $20 \text{ mm} \times 0.8 \text{ mm}$ . (b) the improved version of the sharkskin die-1. (B1) marks the region, on one side, where material of a 2 mm height was milled away. (c) shows the front view of the initial sharkskin die-1. (d) shows the front view of the improved sharkskin die-1.

eq. 4.2 and  $A_{C,i}$  is the cross sectional area of the slit die as given by eq. 4.3. The different slit die versions are indexed with  $i$ , and their properties are listed in tab. 4.1.

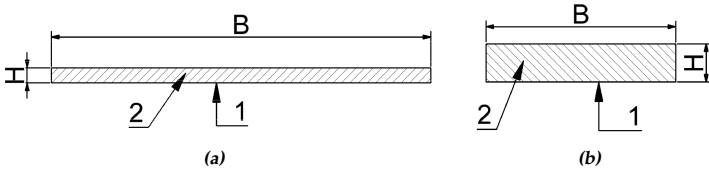


**Figure 4.5.** – Visualization of the change in cross section from sharkskin die-1 to sharkskin die-2. (1) indicates the boundary surface and (2) indicates the cross-section area. (a) shows the cross-section of sharkskin die-1 and (b) shows the cross-section of sharkskin die-2 or sharkskin die-1 with the inlay (see tab. 4.1).

$$A_{P,i} = (2 \times B_i + 2 \times H_i), \quad (4.2)$$

$$A_{C,i} = B_i \times H_i. \quad (4.3)$$

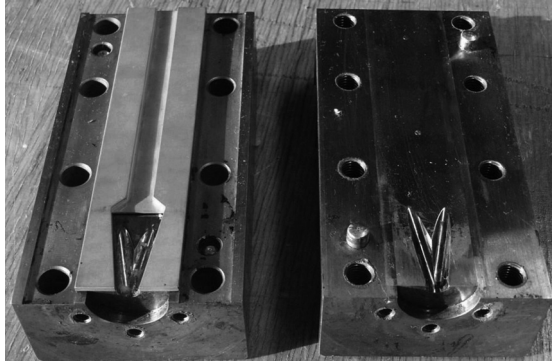
**Table 4.1.** – Comparison of the geometrical properties of the sharkskin die-1 and sharkskin die-1 with brass inlay (see fig. 4.6).

Die	B mm	H mm	$A_{P,i}$ mm	$A_{C,i}$ mm	$R_{P/C,i}$ -	$\dot{\gamma}_{app}$ $s^{-1}$
1	20	0.8	41.6	16	2.6	22
1 with inlay	10	2	24	20	1.2	260

For varying the cross-section of sharkskin die-1 special die inlays have been constructed, i.e. for a cross-section of 10 mm  $\times$  2 mm, see fig. 4.6. The die inlays were made of brass to guarantee an optimum sealing of the die channel due to the larger heat expansion coefficient. Additionally, a copper disk was placed between the die and the connection to the extruder to prevent leakage at this position. Using the sharkskin die-1 with the brass inlay allowed to reach higher volume flows of polymer melt which meant

higher shear rates. Accordingly, strong melt flow instabilities appeared. Thus, decreasing the  $R_{B/C}$  value was successful.

Even though the brass inlay served its purpose quite well and was manu-



(a)



(b)

**Figure 4.6.** – Brass inlay for the sharkskin die-1, applied on the sharkskin die-1. (a) brass inlay inserted in the opened die. (b) front view of the closed sharkskin die-1 with brass inlay with a slit cross-section of 10 mm × 2 mm.

factured and installed rather easily and fast, it got one major disadvantage. When the extruder was used at high pressure,  $p > 500$  bar, and for a longer period of time,  $T > 30$  min, and for materials with a relatively low viscosity, leakage appeared between the brass inlay and the die at the position

where the biconical die entrance geometry is placed. Consequently, a completely new die was built, the sharkskin die-2, to overcome this drawback. The values of tab. 4.1 for the sharkskin die-1 with the brass inlay are also valid for the sharkskin die-2.

## 4.4.2 The Second Generation Sharkskin Die (SSD-2)

As seen in the previous section, the sharkskin die-1 showed only strong melt flow instabilities when used with a brass inlay which decreased its  $R_{p/C}$  value. As shown in fig. 4.7, the sharkskin die-2 was built to simplify the set-up, to reduce the amount of parts, and to avoid leakage. The sharkskin die-2 was initially designed with a 10 mm × 2 mm slit, for obtaining the range of shear rate of strong melt flow instabilities. Additionally, the biconical die entrance was set aside and a 180° die entrance was applied instead. This would later allow, if required, to use brass inlays with best sealing properties. The homogeneous feeding of the slit was guaranteed by the slimness of the slit ( $B = 10$  mm) in comparison to the feed hole of  $D = 8$  mm. Because of this, the length of the slit could also be reduced (to  $L = 75$  mm), since the amount of die entrance eddies\* and turbulences would be of much smaller length scales.† As a further change in functionality, the position of the pressure transducer at the die exit was placed as close to the exit as possible ( $\Delta S_{exit} = 2.0$  mm).

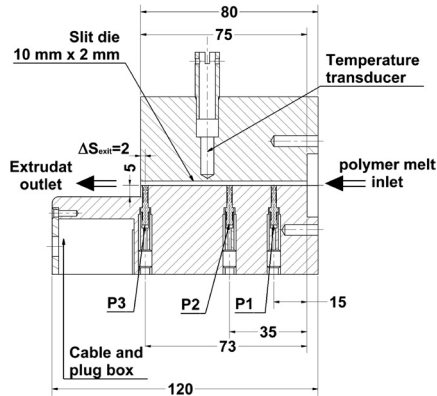


**Figure 4.7.** – Technical scheme of the sharkskin die-2. (P1), (P2) and (P3) are indicating the position of the piezoelectric pressure transducer. The distance between the center of (P3) and the die exit is 2 mm.

\* An eddy is a vortex-like area in a liquid flow.

† Meant are here the phenomena which appear in the entrance region of the die and not those outside the die in the barrel.

### 4.4.3 Data Acquisition

Both types of sharkskin die used similar piezoelectric pressure transducers and the same data acquisition set-up. Along the die, three high sensitive piezoelectric pressure transducers (Kistler 6182A) have been set, similar to the special die of the capillary rheometer. Furthermore, a similar data acquisition set-up as for the capillary rheometer set-up has been used. This is shown in fig. 4.8 and includes high resistive charge amplifiers from Kistler (5015A) and a data acquisition board, i.e. E3026 or a NI-PCI-MIO-16XE from TA-Instruments. The data acquisition boards are capable of measuring at least 100,000 data points per second. The maximum temperature which should be applied on the piezoelectric transducers is about 230 °C.\*

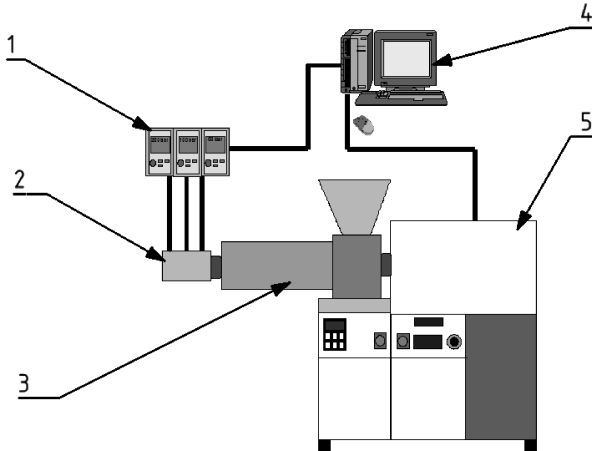


**Figure 4.8.** – Scheme of the extrusion set-up with the Brabender extruder. (1) Kistler charge amplifier (3 × 5015A), (2) special slit die, i.e. sharkskin die-1, (3) Brabender extruder 19/25D, (4) desktop computer for data acquisition (E3026, TA-Instruments) and extruder control (CAN-BUS) and (5) Brabender Labstation.

\* This temperature should only be applied for a short time. For a long longer period of time 200 °C should be the limit.

### 4.4.4 Mathematical Treatment of the Pressure Raw Data

This chapter provides an overview of the necessary pre-treatment of the pressure data obtained from the measurements with a sharkskin die either on the capillary rheometer or on the extruder.

The time-dependent pressure data  $p_i(t)$  was acquired by the measurements of the high sensitive piezoelectric pressure transducers inside of the die. The time-dependent pressure  $p_i(t)$  can be decomposed into a constant mean pressure  $\bar{p}_i$ , a time-dependent pressure fluctuation term  $\dot{p}_i(t)$  and a systematic error term  $p_{error}(t)$ , i.e.

$$p_i(t) = \bar{p}_i + \dot{p}_i(t) + p_{error}(t). \quad (4.4)$$

The inherent drift of the piezoelectric pressure transducer is part of the error term  $p_{error}(t)$ . For the further mathematical analysis of the data,  $p_{error}(t)$  had to be determined or approximated and then subtracted from  $p_i(t)$  of eq. 4.4. A quadratic fit functions (polynomial approximation of the second order)\*, i.e.

$$f_1(t) = \mathfrak{C}_1 + \mathfrak{C}_2 \times t + \mathfrak{C}_3 \times t^2, \quad (4.5)$$

were calculated of  $p_i(t)$  and afterwards the time-dependent terms of eq. 4.5 were subtracted from  $p_i(t)$ . By doing so, the drift-reduced time-dependent pressure

$$\begin{aligned} \check{p}_i(t) &= \bar{p}_i + \dot{p}_i(t) + p_{error}(t) - (\mathfrak{C}_2 \times t + \mathfrak{C}_3 \times t^2) \\ &= \bar{p}_i + \dot{p}_i(t) \end{aligned} \quad (4.6)$$

is introduced.

With the statistical analysis the mean value  $\bar{p}_i$  and the standard deviation  $\sigma_i$  of the pressure  $p_i(t)$  were obtained. The standard deviation is a measure of  $\dot{p}_i(t)$ .

In order to gain characteristic mathematical measures for the melt flow instabilities the drift-reduced pressure  $\check{p}_i(t)$  (eq. 4.6) was analysed via statistical moment analysis, Fourier transform (FT), autocorrelation function (ACF) and cross correlation function (CCF).

\* Basically, the drift was found to be nearly a linear function. The coefficient  $\mathfrak{C}_3$  of the second order term was almost negligibly small  $\mathfrak{C}_3 \ll 10^{-4}$ .

By computing the Fourier transform, the pressure data (e.g.  $\check{p}_i(t)$ ) is transformed into frequency ( $\nu$ ) space. All experiments related to periodical mechanical instabilities have characteristic peaks at frequencies higher than the zero frequency ( $\nu = 0$  Hz) in the spectra of the FT of the pressure data  $P_i(\nu)$ . Each Fourier spectrum, obtained by using  $\check{p}_i(t)$  or  $p_i(t)$ , includes a peak at the zero frequency ( $\nu = 0$  Hz) which represents the mean pressure  $\bar{p}$  of the time domain data  $p_i(t)$ .

The autocorrelation function (ACF)  $r_{ff,i}(\tau)$  of the pressure data  $\check{p}_i(t)$  results in a nearly constant ACF value of one, as seen in fig. 4.9, for nearly all measurements independent of whether a MFI was present or not. This is related to the strong influence of a large mean value of a signal on its ACF. By this no characteristic measure of the MFI could be determined.

For solving this problem, the ACF was not obtained by using the drift-reduced time-dependent pressure  $\check{p}_i(t)$ , but by using the time-dependent pressure fluctuations  $\hat{p}_i(t)^*$ , which are obtained when from  $\check{p}_i(t)$  in eq. 4.6 the mean value  $\bar{p}_i$  is subtracted.

When only the time dependent pressure fluctuations  $\hat{p}_i(t)$  are used for calculating the ACF the plot of the ACF changes completely, as seen in fig. 4.9. With this improvement it is possible to determine characteristic correlation times  $\tau_{char,i}$  of the pressure signal and the melt flow instabilities.

---

\* The time-dependent pressure fluctuations  $\hat{p}_i(t)$  are also referred as the drift-reduced time-dependent pressure fluctuations to point out that the pressure fluctuations are not affected by the systematic errors.

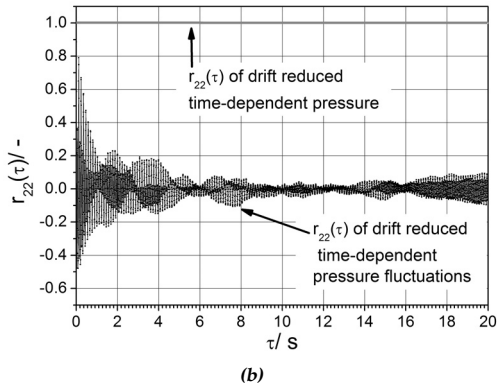
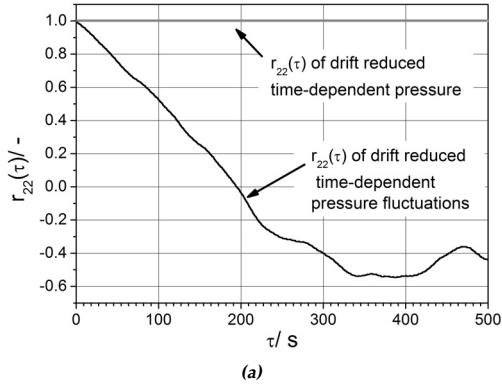


**Figure 4.9.** – ACF  $r_{22}(\tau)$  of the MDPE sample (tab. 2.3) at  $\theta = 180^\circ \text{C}$  measured in the sharkskin die of the capillary rheometer ( $30 \text{ mm} \times 3 \text{ mm} \times 0.3 \text{ mm}$ ). Once the ACF was calculated out of  $p_2(t)$  (grey curve) and once calculated out of  $\hat{p}_2(t)$  (black curve). The extrudate showed for (a) a smooth surface ( $\dot{\gamma}_{app} = 78.5 \text{ s}^{-1}$ ) and for (b) melt fracture ( $\dot{\gamma}_{app} = 3534.3 \text{ s}^{-1}$ ). If  $r_{ff}(\tau)$  is calculated from a set of data with a non-zero mean value, then the ACF has a nearly constant value close to 1. This is shown in both examples, the grey curve in fig. 4.9a and fig. 4.9b. However, by using the time-dependent pressure fluctuations, the ACF  $r_{ff}(\tau)$  gives a detailed view of the behaviour of the pressure in the time domain. Please be aware of the different scaling of the correlation time  $\tau$  axis.

### 4.4.5 Analysing the Pressure Fluctuations of Melt Flow Instabilities with the Sharkskin Die

This section introduces the algorithm of the analysis of melt flow instabilities with a sharkskin die in general. This algorithm can be applied to pressure data obtained with the extruder or the capillary rheometer.

The sharkskin die was introduced in chap. 4.3. It has been developed in the group of Prof. Wilhelm<sup>62,146,149</sup> and allows an advanced analysis of the melt flow instabilities (e.g. in fig. 4.10). The main improvements of the sharkskin die are:

- The use of a fast and highly sensitive piezoelectric pressure transducer\* inside the die.
- The use of the oversampling method, see Dusschoten.<sup>138</sup> Thus, the quality of the data (i.e. the signal-to-noise ratio) is improved.
- The application of advanced mathematical analysis. This allows the determination of characteristic measures of the instabilities.

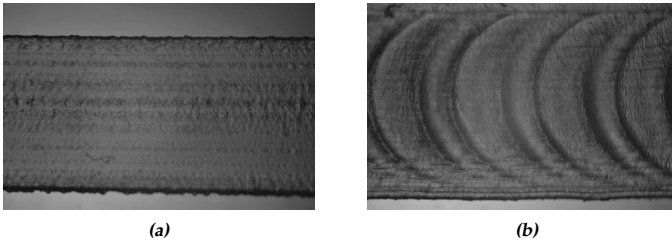


**Figure 4.10.** – Images of melt flow instabilities on extrudates of HDPE (tab. 2.3). The experiments were conducted in the capillary rheometer with the sharkskin die. The sample was HDPE at  $\theta = 190$  °C and the apparent shear rates of (a)  $\dot{\gamma}_{app} = 50$  s<sup>-1</sup> and (b)  $\dot{\gamma}_{app} = 1500$  s<sup>-1</sup> were applied. The width of each image is 7.5 mm.

The algorithm of the data acquisition and the data analysis is given by:

\* They have a large dynamic range (about 6 decades in pressure).

**Algorithm 3. Algorithm for the analysis of the time-dependent pressure of the sharkskin die**

1. The raw data  $s(t)$  is acquired with a high sampling rate ADC board.
2. The raw data is boxcar averaged.<sup>36</sup>
3. The averaged data  $\bar{s}(t)$  is multiplied with a predetermined calibration factor. Thus, the time-dependent pressure  $p(t)$  is obtained.
4. According to chap. 4.4.4, corrections for the drift and the mean value are applied.
5. The time-dependent drift-reduced pressure fluctuations  $p'_i(t)$  are Fourier transformed, the ACF and the CCF is calculated.
6. From the magnitude spectrum of the FT, the frequency values of the first characteristic peak of the melt flow instabilities  $v_{inst}$  are determined. Whereas, the ACF gives the zero correlation time\*  $\tau_{inst}$ .
7.  $v_{inst}$  and  $\tau_{inst}$  are plotted as functions of the apparent shear rate  $\dot{\gamma}_{app}$ .  $\square$

The results of this algorithm can be plotted as the three dimensional instability function  $f_{inst} = \hat{f}_{inst}(v_{inst}, \tau_{inst}, \dot{\gamma}_{app})$ . With this algorithm it is possible to study melt flow instabilities in both the frequency domain and in the domain of the correlation time. Therefore, new measures for the melt flow instabilities are accessible, as  $v_{inst}$  and  $\tau_{inst}$  (see fig. 4.16). With these measures a new insight for the behaviour and the dynamics of the melt flow instabilities and their transition can be gained.<sup>62,146,216†</sup> The following example shows the application of the above given algorithm on two sets of the time-dependent pressure of an HDPE.

**Example 15. HDPE studied with the sharkskin die**

The HDPE (tab. 2.3) was measured with the sharkskin die at a constant temperature (i.e.  $\vartheta = 190$  °C) but at varying apparent shear rates<sup>‡</sup> in the capillary rheometer. As a figure of illustration, the data and the results of two of those measurements is given, i.e.  $\dot{\gamma}_{app} = 50$  s<sup>-1</sup> and  $\dot{\gamma}_{app} = 1500$  s<sup>-1</sup>.

\* The zero correlation time in this thesis is defined as the time when the ACF first crosses the line  $r_{ff}(\tau) = 0$ .

† E.g. Filipe et al.<sup>146</sup> used the frequency of the melt flow instabilities  $v_{inst}$  to study the influences of the molecular weight  $\overline{M}_w$  and the topology (linear, SCB or LCB) for different PE samples.

‡ In this example called shear rate.

The time-dependent pressure fluctuations\* indicates that the extrudate looks different, see fig. 4.11.  $\dot{p}_i(t)$  for the low shear rate shows a very small fluctuation of less than 1 bar. This is in strong contrast to the pressure fluctuations of the data from the high shear rate which exhibits large (up to 50 bar) and periodic oscillations. According to the work of Palza et al.,<sup>62,149</sup> the low shear seems to produce a smooth extrudate, whereas the large shear rate produces a stick-slip instability on the extrudate. Applying statistical methods<sup>†17,30</sup> on the pressure fluctuations,

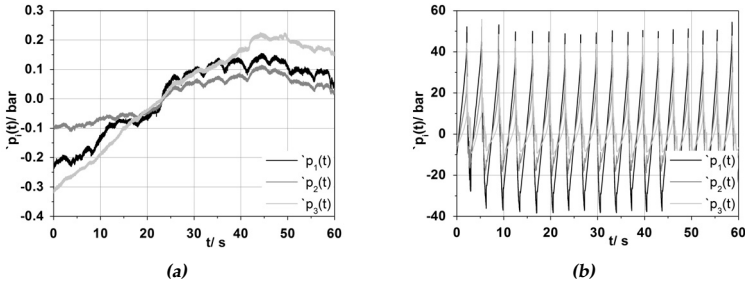


**Figure 4.11.** – The time-dependent pressure fluctuations  $\dot{p}_i(t)$  for the advanced data analysis. The experiments were conducted in the capillary rheometer with the sharkskin die. The HDPE sample was measured at  $\theta = 190$  °C and an apparent shear rate of (a)  $\dot{\gamma}_{app} = 50$  s<sup>-1</sup> and (b)  $\dot{\gamma}_{app} = 1500$  s<sup>-1</sup> was applied. The three curves of each plot are representing the three different piezoelectric pressure transducers: black line for P1, grey line for P2 and light grey line for P3 (at the die exit).

the standard deviation  $\sigma_{std}(\dot{\gamma})$  as a function of the shear rate, see fig. 4.12, gives the first information of the appearance of the melt flow instabilities. The curve of the standard deviation starts at low values (ca. 1 bar) for low shear rates and has a strong and steep increase between 200 s<sup>-1</sup> and 300 s<sup>-1</sup>. For higher shear rates the standard deviation stays at high values of ca. 10 bar.‡ Therefore, it can be concluded from the standard deviation that a smooth extrudate appears for low shear rates and an unstable extrudate (probably stick-slip) appears for higher shear

\* In this example called pressure fluctuations.

† Calculation of e.g. the mean value, the standard deviation or higher statistical moments.

‡ The maximum applied shear rate in these experiments was 1500 s<sup>-1</sup>.

rates. The smooth and the stick-slip region are separated by the transition region between  $200 \text{ s}^{-1}$  and  $300 \text{ s}^{-1}$ .

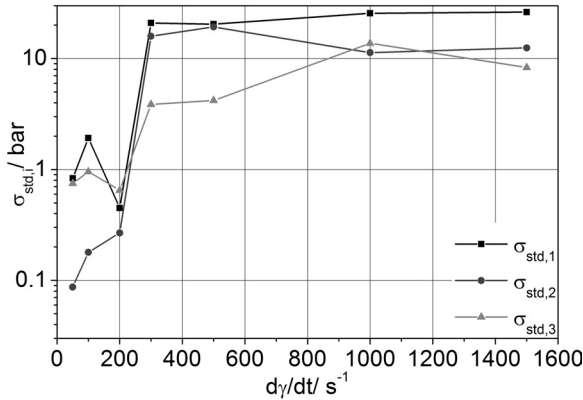


**Figure 4.12.** – The standard deviation  $\sigma_{std,i}$  of the time-dependent pressure fluctuations as a function of the apparent shear rate. The experiments were conducted in the capillary rheometer with the shark-skin die. The sample was HDPE at  $\vartheta = 190 \text{ }^\circ\text{C}$  and was measured at different apparent shear rates  $\dot{\gamma}_{app}$ . The three curves of each plot are representing the three different piezoelectric pressure transducers: black squares for P1, grey dots for P2 and light grey triangles for P3 (at the die exit).

The conclusions drawn from the standard deviation are partly supported by the results of the ACF, see fig. 4.13. The measurement for low shear rates shows a slow and smooth decay with a correlation time  $\tau_{inst} \approx 26 \text{ s}$ . According to Naue<sup>148</sup> this can be a sign for a smooth extrudate. Whereas, the measurement at the high shear rate (e.g. in fig. 4.13b  $\dot{\gamma}_{app} = 1500 \text{ s}^{-1}$ ) gives a very fast drop ( $\tau_{inst} \approx 1 \text{ s}$ ) of the ACF curve with a small decaying oscillation. This is known to be caused by strongly unstable extrudates, i.e. GMF.

The FT characterizes the instability. The FT-magnitude spectrum of the measurement at the low shear rate contains the typical peaks of the electric current (50 Hz), see fig. 4.14a. However, the spectra of the first two transducer show a characteristic peak at about  $\nu_{inst} = 8.4 \text{ Hz}$  of low amplitude but with a narrow shape. The magnitude of the peak becomes smaller for increasing transducer position, e.g. the

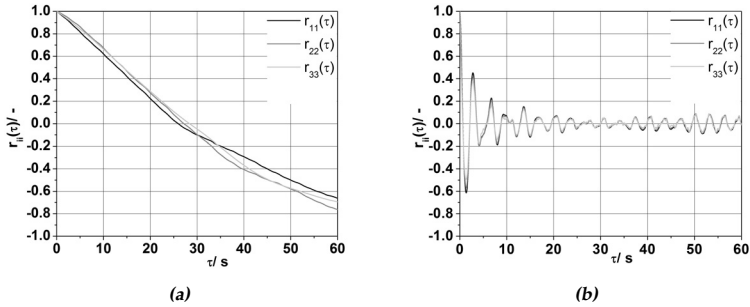


**Figure 4.13.** – The ACF from the data analysis of the time-dependent pressure fluctuations. The experiments were conducted in the capillary rheometer with the sharkskin die. The HDPE sample was measured at  $\vartheta = 190$  °C and it was applied an apparent shear rate of (a)  $\dot{\gamma}_{app} = 50$  s $^{-1}$  and (b)  $\dot{\gamma}_{app} = 1500$  s $^{-1}$ . The three curves of each plot are representing the three different piezoelectric pressure transducers: black line for P1, grey line for P2 and light grey line for P3 (at the die exit).

signal of transducer P1 is larger than the one of transducer P2. In the spectrum of transducer P3 the peak is vanished. Nevertheless, the image of the extrudate indicates a weak melt flow instability, see fig. 4.10a. The spectrum of the high shear rate measurement contains a significant frequency contribution at a low frequency ( $< 1$  Hz), fig. 4.14b. This verifies the assumption that it is a stick-slip instability which is clearly visible on the extrudate. Nevertheless, the spectrum also contains characteristic frequency contributions at higher frequencies, e.g. at  $\nu_{inst,2} = 8.4$  Hz, seen in fig. 4.15. This is a sign of a further high frequency distortion of the extrudate on top of the stick-slip instability, see fig. 4.10b.

Combining the characteristic measures of the melt flow instabilities, the 3-D plot of fig. 4.16 is obtained. Its projection on the  $\tau_{inst}$ - $\dot{\gamma}$ -plane shows that with increasing shear rate the correlation time of the pressure fluctuations decays, with a sudden drop at  $200$  s $^{-1}$ . This means the flow is getting with increasing shear rate more chaotic. The projection on the  $\nu_{inst}$ - $\dot{\gamma}$ -plane shows a curve which starts at frequencies around 1 Hz. With the extrudate showing a sharkskin-like instability. At  $\dot{\gamma} = 100$  s $^{-1}$ ,  $\nu_{inst}$  drops to values which are more than one decade lower. After a minimum value at  $\dot{\gamma} = 300$  s $^{-1}$ ,  $\nu_{inst}$  increases again. However, the val-

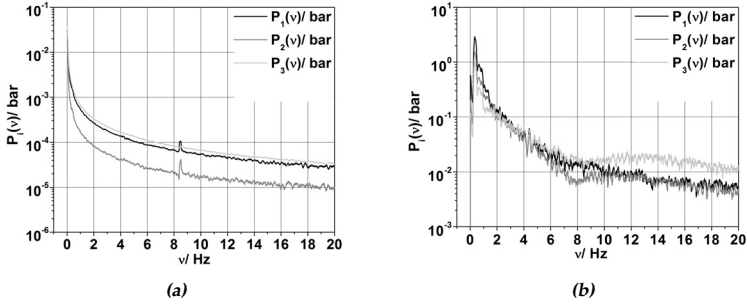


**Figure 4.14.** – The FT from the data analysis of the time-dependent pressure fluctuations. The experiments were conducted in the capillary rheometer with the sharkskin die. The sample was HDPE at  $\vartheta = 190\text{ }^{\circ}\text{C}$  and an apparent shear rate of (a)  $\dot{\gamma}_{app} = 50\text{ s}^{-1}$  and (b)  $\dot{\gamma}_{app} = 1500\text{ s}^{-1}$  was applied. The three curves of each plot represent the three different piezoelectric pressure transducers: black line for P1, grey line for P2 and light grey line for P3 (at the die exit).

ues of  $v_{inst}$  stay smaller than 1 Hz; for measurements up to  $\dot{\gamma} = 1500\text{ s}^{-1}$ . The frequencies below 0.1 Hz are indicating stick-slip instabilities. With increasing shear rate the frequency of the stick-slip instabilities is getting higher.

Summarizing the both projections discussed above, the flow gets more chaotic with increasing shear rate. However, the flow exhibits a more complex behaviour in the frequency domain. This results in a bifurcated curve in the  $v_{inst}$ - $\tau_{inst}$ -plane. For low correlation times  $\tau_{inst} < 1\text{ s}$ ,  $v_{inst}$  is decreasing with increasing  $v_{inst}$ . This means, that the more chaotic flow\* show high frequency instabilities. Whereas, for high correlation times  $\tau_{inst}$  the curve bifurcates and both low frequencies  $v_{inst}$  are observable (e.g. for stick-slip instability) and high frequencies  $v_{inst}$  are observable (e.g. for sharkskin like instabilities). Thus, the correlation time of the instability gives a measure of how chaotic the flow is and the frequency of the instability indicates which type of instability is present.  $\square$

\* This flows have short correlation times.

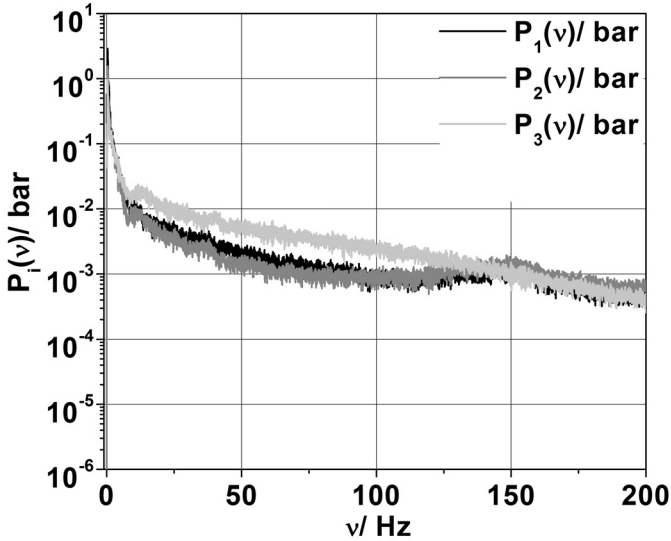


**Figure 4.15.** – The whole spectrum of the FT of the data analysis of the time-dependent pressure fluctuations. A higher frequency shoulder is observable for the three sensor positions at  $\nu_{inst} \approx 10$  Hz. The spectra for the sensor positions P1 and P2 contain an additional broader shoulder at high frequencies ( $\nu_{inst} \approx 150$  Hz). The experiment was conducted in the capillary rheometer with the sharkskin die. The HDPE sample was measured at  $\vartheta = 190$  °C and it was applied an apparent shear rate of  $\dot{\gamma}_{app} = 1500$  s<sup>-1</sup>. The three curves of each plot are representing the three different piezoelectric pressure transducers: black line for P1, grey line for P2 and light grey line for P3 (at the die exit).

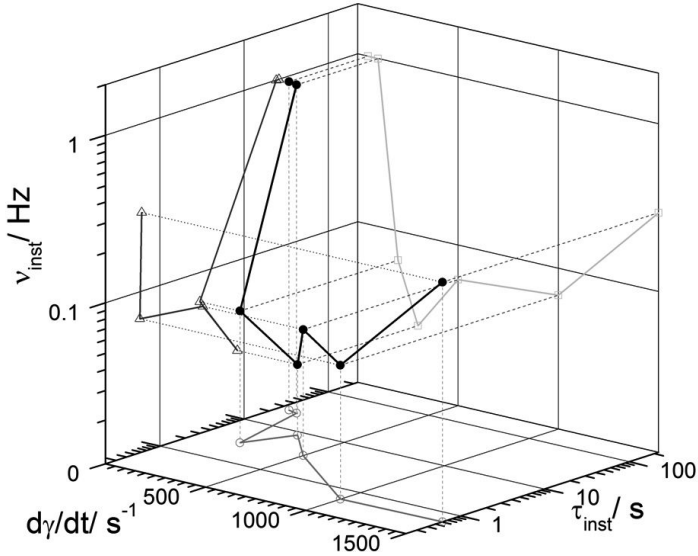


**Figure 4.16.** –  $v_{inst}$  and  $\tau_{inst}$  plotted as functions of the apparent shear rate  $\dot{\gamma}_{app}$ . The experiments were conducted in the capillary rheometer with the sharkskin die. The HDPE sample was measured at  $\vartheta = 190$  °C and it was measured at different apparent shear rates  $\dot{\gamma}_{app}$ . The black curve with the filled circles represents the three-dimensional instability curve  $f_{inst}$ . The curves with the open symbols represent the projection of  $f_{inst}$  on one plane, i.e. the open triangles are  $f_{inst}(v_{inst}, \tau_{inst})|_{\dot{\gamma}_{app}}$ , the open circles are  $f_{inst}(\tau_{inst}, \dot{\gamma}_{app})|_{v_{inst}}$  and the open squares are  $f_{inst}(v_{inst}, \dot{\gamma}_{app})|_{\tau_{inst}}$ .

### 4.4.6 Optical Analysis of the Extrudate

Each extrudate sample was photographed in order to assign each sample to smooth, sharkskin, stick-slip or gross melt fracture. This set of mechanical instabilities was later correlated with the results from the advanced data analysis. During a measurement at the capillary rheometer or at the extruder, samples of the extrudate were collected by manually cutting out a small piece of the solidified extrudate. The extrudate samples were only taken after the pressure inside the barrel and inside the die reached a quasi static state. The extrudate pieces were afterwards taped either to a microscopy slide or to a black cardboard. In either case it was then labelled with the name of the sample and the processing conditions.

Later this collection of extrudate pieces was digitalized using a microscope set-up. Two different optical set-ups were used for the digitalization of the extrudate samples:

1. A Zeiss Axiophot microscope with Panasonic CCD\*-camera ( $\approx 0.5$  MP (Megapixel)) (see fig. 4.17a) and an image acquisition software.
2. A Bresser stereo-microscope with an additional third optical tube, which allows the use with a Nikon D90 (CMOS sensor and  $\approx 12.3$  MP) (see fig. 4.17b) and a Nikon camera control software.

The Zeiss microscope has the clear advantage of being a high performance optical tool that enables the user to use high magnifications (greater than  $\times 100$ ). This is very helpful in case of very weak melt flow instabilities (MFI). Problems appear when high magnifications are used. The area on which can be focused is very small in comparison to the image size; therefore, an analysis of the image would be quite inaccurate. This problem with the focus plane happens if e.g. the sample is not flat at all, as for nearly all samples which were obtained from the extruder experiments. Another problem was the resolution of the attached camera with an image

---

\* W. S. Boyle<sup>‡</sup> and G. E. Smith<sup>§</sup> were rewarded in 2009 with the Nobel prize for the invention of the charged coupled devise (CCD).<sup>36,218</sup>

‡ Willard Sterling Boyle (\*19. August 1924 in Amherst, Canada; †7. May 2011 in Halifax; Canada) was a Canadian physicist.<sup>219</sup>

§ George Elwood Smith (\*10. May 1930 in White Plains, USA) is an American physicist.

size of  $768 \times 636$  pixels. For these reasons the Bresser stereo-microscope was the method of choice for most of the measurements.

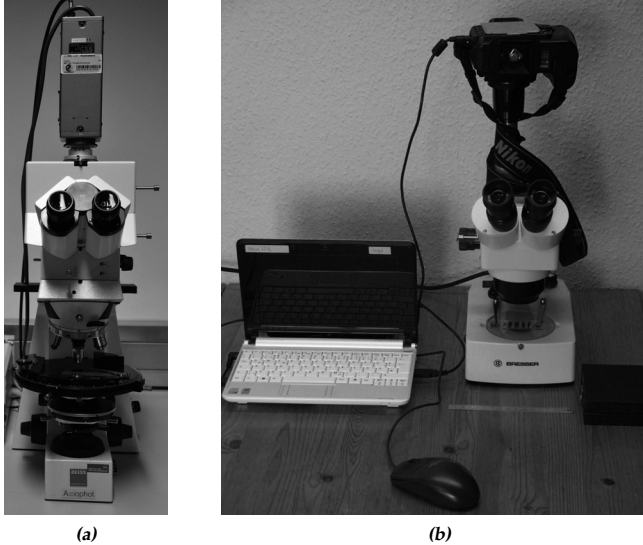


**Figure 4.17.** – Optical set-ups used for the digitalization of the extrudates: (a) Zeiss Axiophot microscope and (b) Bresser stereo-microscope with Nikon D90 attached.

The images of the extrudate can be analysed manually by simply counting the lines in a certain length of sample. However, this method involves the error source of human judgement on what is an instability line and what is not. Besides, it is a time-demanding task to do this for all samples and the use of a lens or a microscope is necessary in most of the cases. To simplify the counting of lines and to reach a higher reproducibility of the results, the extrudate samples were photographed and the FT of the light intensities was used on the images to determine the number of fracture lines in an image.\* In order to do this a self-developed image analysis software has been implemented using the functions of MATLAB.<sup>221</sup>

Generally the melt flow instabilities appear as more or less periodic pat-

\* The theory of the advanced analysis can be found e.g. in the book of Bracewell.<sup>220</sup>

terns of parallel lines in the images. If the images are adjusted so that the lines are vertical, the FT can be used for the analysis. For this purpose a FT of each row of the image gives an average number of lines found in this specific row. An average of all rows gives a good estimate of the average number of lines (instabilities) in one image. The self developed software used the following algorithm for the processing of the images.

**Algorithm 4. Algorithm for the FT-analysis of the images**

1. Transferring the values of the light intensity of the image with its original size in a  $M_0 \times N_0$  matrix (see fig. 4.18a).
2. Asking the user for input how much the image should be rotated, so the lines of the instabilities would be vertically aligned. This can result in a new image size of  $M \times N$  (see fig. 4.18b).
3. Computing for each row  $i$  via the FFT the intensity spectrum  $I_{image,i}(q)$  with  $i = [1, M]$  and  $i \in \mathbb{N}$  for all rows ( $M$ ) of the image (see fig. 4.18c).
4. Calculating the average of all FFT spectra,

$$\bar{I}_{image}(q) = \frac{1}{M} \sum_{i=1}^M I_{image,i}(q). \quad (4.7)$$

5. By the means of point 4 an average spectrum of the image is obtained and the according data is saved and plotted (see fig. 4.18d).

This algorithm is illustrated in fig. 4.18. □

Artificial images were created for testing the functionality of the self-developed software and verifying the interpretation of the results. The artificial images were created using a self-written MATLAB code. The basic idea of these test images was to generate clear and well-defined images, which are not possible to obtain experimentally, to simulate the melt flow instabilities. The melt flow instabilities appear in their simplest form as a nearly periodic pattern of surface cracks. As test image it should be sufficient to create a sine wave with values between 0 and 255\* and 1001 points for one row of the image. This row was further copied into the further 499 rows of the artificial image. Thus, every row contained the function in x-direction and the same value in y-direction. The sine wave was chosen to

\* This will represent the intensity values of a grey scale picture.

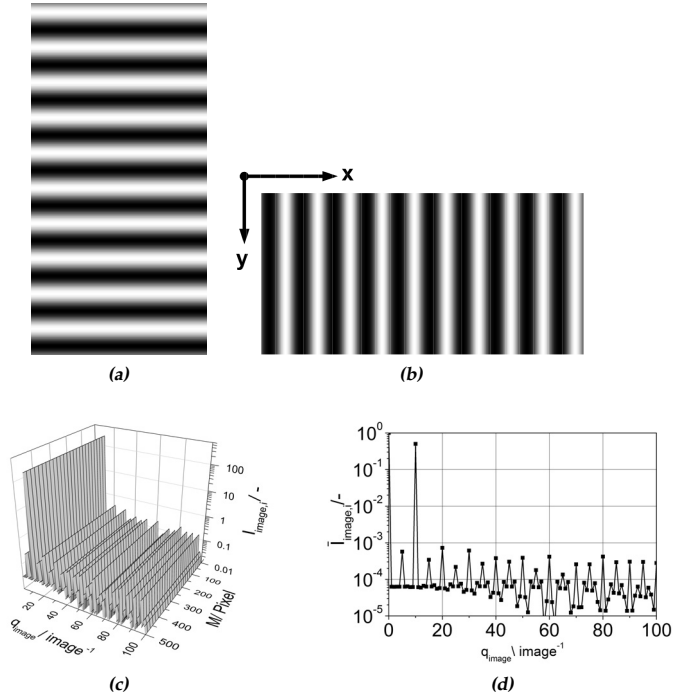


**Figure 4.18.** – Illustration of the algorithm of the software for the image analysis. (a) basic image with horizontal lines (height  $M_0 = 1001$  and width  $N_0 = 500$ ), (b) basic image rotated by  $90^\circ$  (height  $M = 500$  and width  $N = 1001$ ), (c) 3-D plot of the intensity spectra of all rows  $i$ , and (d) the spectrum of the image averaged over the index  $i$ .

have 10 complete waves in the data set. Therefore, the created image had a height (y-direction) of  $M_0 = 500$  pixel and a width of  $N_0 = 1001$  pixel (x-direction), which is shown in fig. 4.19a. This data represents a perfectly homogeneous instability in y-direction with a perfect optical illumination. Above all, the illumination of the sample could strongly affect the images. Therefore, two further manipulations were applied on the initial artificial image (fig. 4.19a). The artificial data was multiplied with

1. a Gaussian function, to simulate a center based illumination (see fig. 4.19d).

2. an exponential function, to simulate an illumination shifted to one side (see fig. 4.19c).

A fourth image was generated containing just binary data (with values of 0 and 1). This results in a strong contrasted image without any smooth transitions and can be seen in fig. 4.19b. This image contains 10 white lines with a broadness of 1 pixel and an equidistant spacing between them. Thus, the image is basically a rectangular function as shown in chap. 2.1.1. The spectra of the FT analysis (see fig. 4.20) of all the analysed images shown in fig. 4.19 contain the basic information of the number of the waves (lines) in the image. Fig. 4.20a of the initial artificial data contains a large peak at the fundamental frequency ( $10 \text{ image}^{-1}$ ). Three decades lower appear peaks which are narrow and most of them are located at multiples of the fundamental frequency. It is interesting to observe that the odd harmonics have the doubled intensity (e.g.  $\bar{I}_{image,3} = 7 \cdot 10^{-4}$ ) of the even harmonics (e.g.  $\bar{I}_{image,2} = 3.4 \cdot 10^{-4}$ ). This is related to the fact that there are exactly ten black and ten white lines in the grey scale image, whereas the next shade of grey already can be found 20 times.

The spectra resulting from the manipulated initial artificial image include the characteristic peak of the fundamental frequency, however the higher harmonics are vanished. The spectra shown in fig. 4.19c and fig. 4.19d show a strong rise in the noise level. Thus, their signal-to-noise ratio is reduced and the peaks get broader. For the spectra of fig. 4.19c which was a convolution of the original artificial image of fig. 4.19a and an exponential function the noise level is increased by two decades. Whereas the spectra of fig. 4.19d which was a convolution of the original artificial image of fig. 4.19a and a Gaussian function the noise level is increased by only half a decade. The spectrum of the binary image shows the clearest peaks with a very large signal-to-noise ratio and with peaks only at the fundamental frequency and its higher harmonics. This could be expected, because the binary image is basically made by an array of rectangular functions, which can be decomposed in a discrete set of frequencies which are all multiples of the fundamental frequency via the Fourier series (see chap. 2.1.1). The values of the comparison of the artificial images and the spectra are tabulated in tab. 4.2.

The analysis of the artificial images showed that periodic arrangements of lines can be successfully detected. However, it is important that an ex-

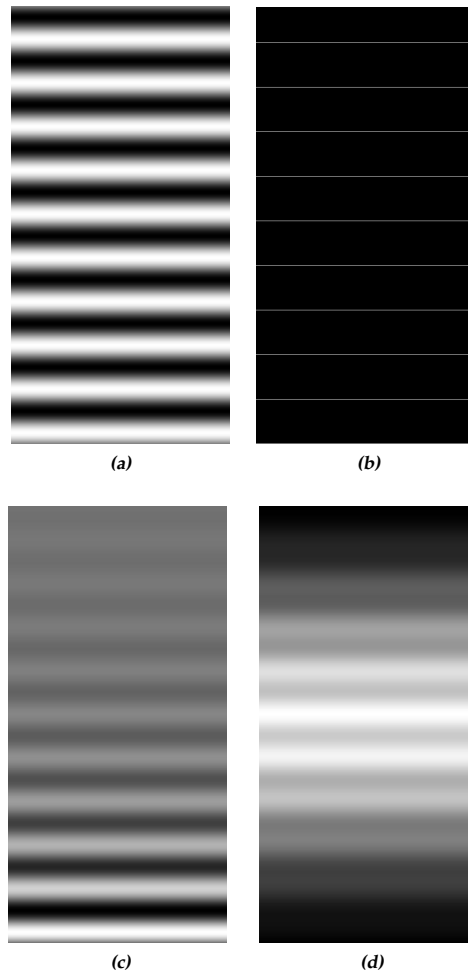


**Figure 4.19.** – Artificial test data for the image analyser. Each image has a width of 1001 pixel and a height of 500 pixel. (a) sinusoidal generated grey scale data, (b) a binary image (having just values of 0 or 1) with 10 white lines of 1 pixel broadness, (c) data from fig. 4.19a multiplied with an exponential decay, and (d) data shown in fig. 4.19a multiplied with a Gaussian function. (Note: Images have been rotated by  $90^\circ$  to fit on the manuscript format.)

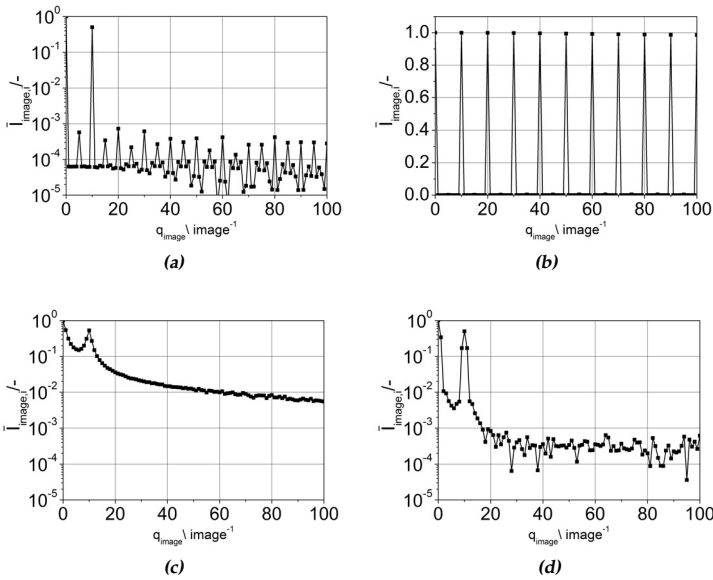


**Figure 4.20.** – FT-spectra of the artificial test data from fig. 4.19. (a) spectrum of the sinusoidal generated grey scale data shown in fig. 4.19a, (b) spectrum of the binary data, (c) spectrum of the data from fig. 4.19c, and (d) spectrum of the data shown in fig. 4.19d.

perimental convolution with a exponential function is avoided. Whereas, an experimental convolution with a Gaussian function is acceptable. The convolution with either an exponential or a Gaussian function can happen while acquiring the image of a melt flow instability with a CCD camera. The reason for this convolution lies in the direction of the light source. A light source which is directed to one edge of the image causes a exponential function. Whereas, a light source which points at the middle of the image causes a Gaussian function.

Before processing the images of real melt flow instabilities, the images of physical gratings and physical meshes were analysed. These gratings and meshes have a precisely predefined line distances or mesh size. The images were made using the Zeiss microscope set-up. In the spectra which were obtained by using the self-developed image analyser software, the

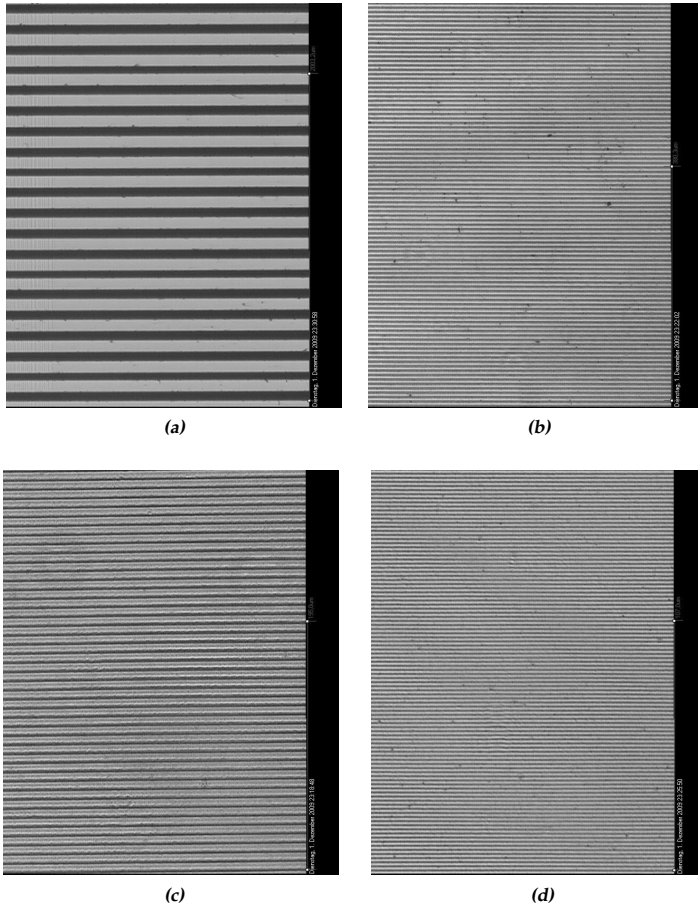


**Figure 4.21.** – Microscope images of the physical gratings with a image size of 768 pixel (width)  $\times$  636 pixel (height). (a) physical grating with 8 lines/mm using a  $2.5\times$  objective (image width  $2500\ \mu\text{m}$ ), (b) physical grating with 140 lines/mm using a  $10\times$  objective (image width  $650\ \mu\text{m}$ ), (c) physical grating with 140 lines/mm using a  $20\times$  objective (image width  $325\ \mu\text{m}$ ) and (d) physical grating with 600 lines/mm using a  $40\times$  objective (image width  $170\ \mu\text{m}$ ). (Note: Images have been rotated by  $90^\circ$  to fit on the manuscript format.)

**Table 4.2.** – Comparison of the number of lines found in the images and in the spectra of the artificial test data and comparison of the intensity values of the fundamental peak at  $10 \text{ image}^{-1}$ .

Property	sine	binary	sine $\times$ exponential	sine $\times$ Gaussian
$n_{image}$	10	10	10	10
$q_{image,spec,01}$	10	10	10	10
$\bar{I}_{image}(10)$	0.5	1	0.53	0.5

number of lines per image can be found by locating the first peak.

The comparison of the number of waves (lines) in the images  $n_{image}$  and the x-axis value of the first peak  $q_{image,1}$  in the respective FT-spectrum is presented in tab. 4.3. In most of the spectra peaks at higher frequencies appear additionally, the next highest to  $q_{image,1}$  are included in tab. 4.3 and named  $q_{image,2}$ . As it can be seen in tab. 4.3 the values of the images and the spectra coincide; in numbers this means that a deviation of  $\Delta n = \pm 3$  is sufficient.

**Table 4.3.** – Comparison of the number of lines\* found in the images and in the spectra of the physical gratings.

Property	2.5 $\times$	10 $\times$	20 $\times$	40 $\times$
$n_{image}$	20	91	45	102
$q_{image,01}$	20	92	44	99
$q_{image,02}$	40	183	89	198

To verify the analysis of the images, a copper mesh, as used for the electron microscopy, was used as a target of study. The images were again taken on the Zeiss microscope set-up. The FT-analysis of the images from fig. 4.23 gives the spectra of fig. 4.24. As for the physical gratings in tab. 4.3, the comparison between the images and the spectra was done. The same comparison method as before was applied to the data from the copper mesh resulting in fig. 4.23, resulting in  $n_{image}$ , and fig. 4.24, resulting in  $q_{image,i}$ .

\* A detailed explanation of the use and the units of  $q_{image}$  can be found in chap. E.

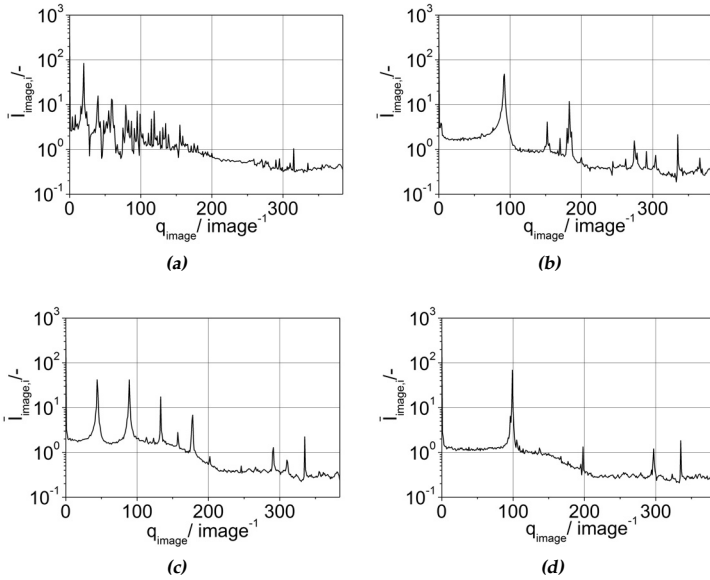


**Figure 4.22.** – FT-spectra of the microscope images of the physical gratings. (a) physical grating with 8 lines/mm using a  $2.5 \times$  objective, (b) physical grating with 140 lines/mm using a  $10 \times$  objective, (c) physical grating with 140 lines/mm using a  $20 \times$  objective and (d) physical grating with 600 lines/mm using a  $40 \times$  objective.

The values of  $n_{image}$ ,  $q_{image,01}$  and  $n_{lines,spec,02}$  are shown in tab. 4.4 and they agree with each other. The results for the artificial data presented above, as

**Table 4.4.** – Comparison of the number of lines found in the images and in the spectra of the images of the copper mesh.

Property	$2.5 \times$	$10 \times$	$20 \times$
$n_{image}$	20	6	3
$q_{image,01}$	20	5	3
$q_{image,02}$	40	11	(5)

well as the results for the physical gratings and the results for the copper

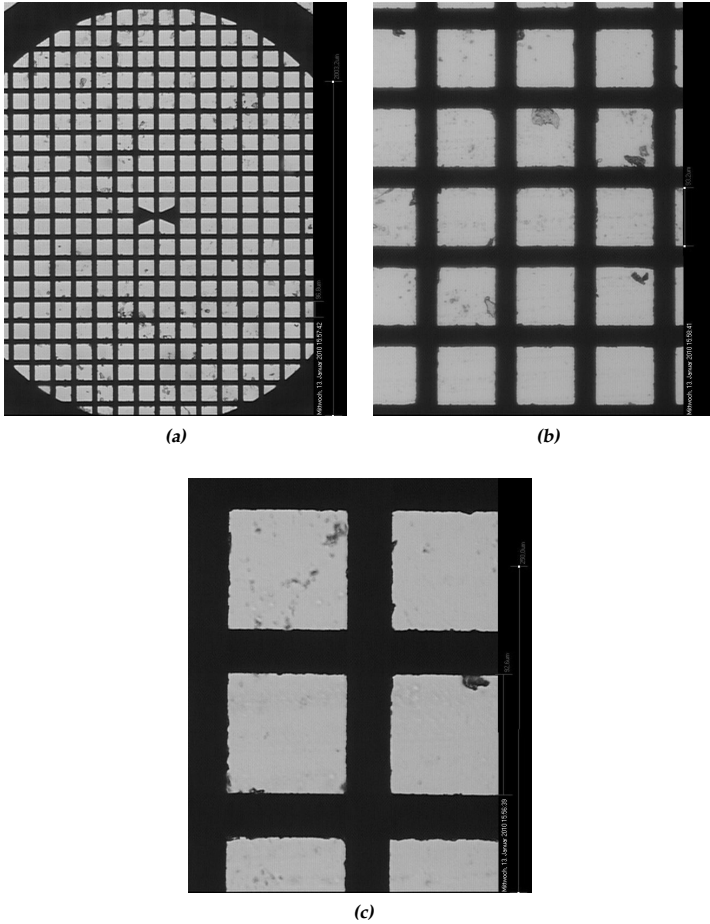


**Figure 4.23.** – Microscope images of the copper mesh with a mesh size of  $90\ \mu\text{m}$ . The image has a width of 768 pixel and a height of 636 pixel. (Note: Images have been rotated by  $90^\circ$  to fit on the manuscript format.) (a) copper mesh using a  $2.5\times$  objective (image width  $2500\ \mu\text{m}$ ), (b) copper mesh using a  $10\times$  objective (image width  $650\ \mu\text{m}$ ) and (c) copper mesh using a  $20\times$  objective (image width  $325\ \mu\text{m}$ ).

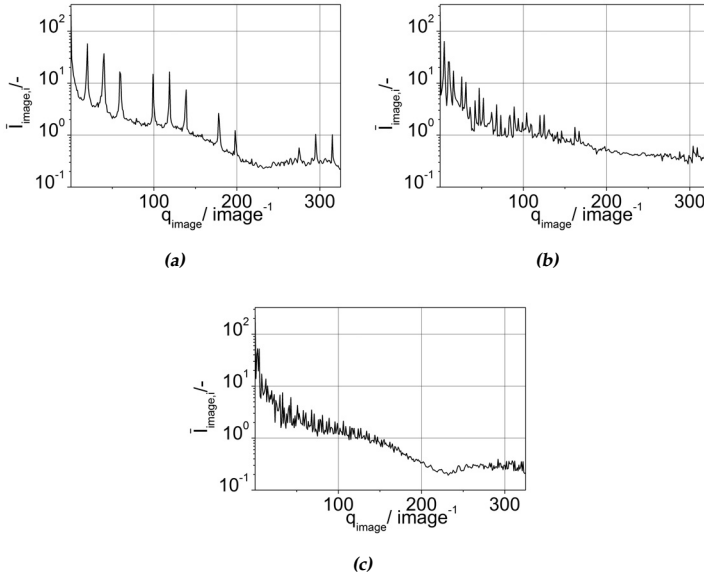


**Figure 4.24.** – FT-spectra of the microscope images of the copper mesh with a mesh size of  $90 \mu\text{m}$ . (a) copper mesh using a  $2.5 \times$  objective, (b) copper mesh using a  $10 \times$  objective and (c) copper mesh using a  $20 \times$  objective.

mesh show that the optical set-up is suitable for analysing the melt flow instabilities. The extrudate samples obtained from the sharkskin die of the capillary rheometer were therefore investigated with this optical analysis. The used polymer was a LLDPE (tab. 2.3) and the images were taken with the Zeiss microscope set-up. The FT-analysis of the images of the real extrudates shows a slightly different behaviour than the test images. Due to the curvature of the surface and the quasi-periodicity of the melt flow instabilities, the peaks in the spectra of the images, seen in fig. 4.25, are much smaller than expected, see fig. 4.26.

The extrudate presented in fig. 4.25a shows a nearly smooth surface of the extrudate. This observation is also made in the FT-spectrum shown in fig. 4.26a. The only peak which appears is at  $336 \text{ image}^{-1}$ . This peak is observed in all measurements done with the Panasonic CCD camera

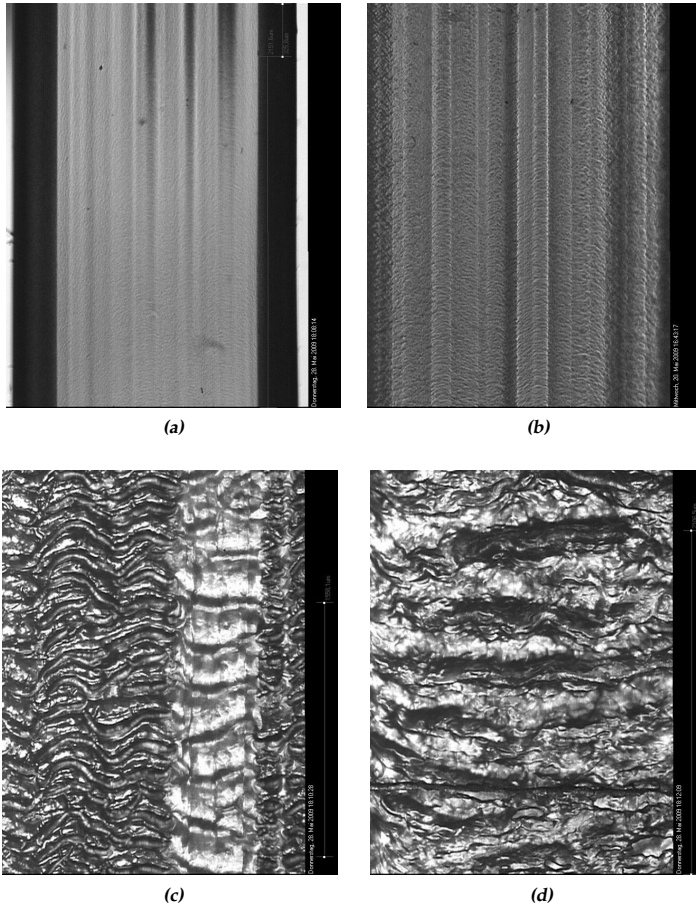


**Figure 4.25.** – Microscope images of the LLDPE extrudate with an image size of 768 pixel (width)  $\times$  636 pixel (height). The objective lens for all images in this figure had a  $2.5\times$  magnification giving a width of the images of  $2500\ \mu\text{m}$ . The images were made at the Zeiss microscope. The LLDPE sample was heated at  $180\ ^\circ\text{C}$  and extruded at the capillary rheometer with the SSD at different apparent shear rates (a)  $\dot{\gamma}_{app} = 10\ \text{s}^{-1}$ , (b)  $\dot{\gamma}_{app} = 30\ \text{s}^{-1}$ , (c)  $\dot{\gamma}_{app} = 300\ \text{s}^{-1}$  and (d)  $\dot{\gamma}_{app} = 790\ \text{s}^{-1}$ . (Note: Images have been rotated by  $90^\circ$  to fit better on the page.)

and can be identified as an artefact created by the camera or the camera control software itself. At increased shear rates the LLDPE extrudate

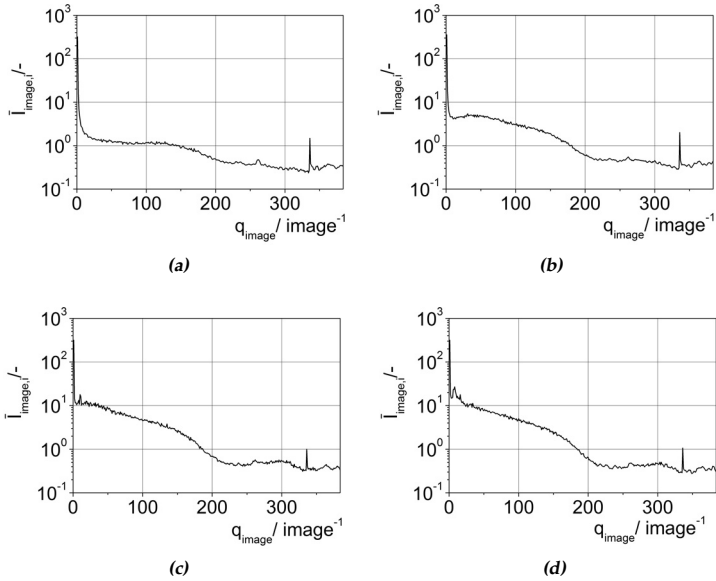


**Figure 4.26.** – FT-spectra of the microscopic images of the LLDPE extrudate, shown in fig. 4.25. The LLDPE sample was heated at 180 °C and extrudated at the capillary rheometer with the SSD at different apparent shear rates (a)  $\dot{\gamma}_{app} = 10 \text{ s}^{-1}$ , (b)  $\dot{\gamma}_{app} = 30 \text{ s}^{-1}$ , (c)  $\dot{\gamma}_{app} = 300 \text{ s}^{-1}$  and (d)  $\dot{\gamma}_{app} = 790 \text{ s}^{-1}$ .

turns from stable (smooth) to unstable (rough). This can be best seen in fig. 4.25d where the melt was extrudated at a relative high shear rate of  $790 \text{ s}^{-1}$ . The extrudate is obviously effected by a strong melt flow instability, which can also be found in the FT-spectrum of fig. 4.26d at a value of  $q_{image} = 7 \text{ image}^{-1}$ . This peak is on top of a broad peak which starts from 0 and lasts up to  $200 \text{ image}^{-1}$ . According to the more irregular structure of the melt flow instabilities in comparison to the artificial and test data, the evaluation of the image without the FT is quite difficult and contains more errors than before and therefore should be avoided.

The extrudate of a measurement at a much lower shear rate (of  $300 \text{ s}^{-1}$ )

contains a smaller melt flow instabilities. However, fig. 4.25c displays a strong instability (e.g. gross melt fracture). The FT-spectrum of this image indicates a peak at a value of  $q_{image} = 9 \text{ image}^{-1}$  which is again on top of a broad peak which starts from 0 and lasts up to  $200 \text{ image}^{-1}$ .

At a low shear rate of  $30 \text{ s}^{-1}$  only a very fine (small amplitude) instability can be observed (fig. 4.25b). This instability is a weak melt flow instabilities. In the FT-spectrum, see fig. 4.26b, it is nearly invisible, only the comparison to the spectrum of the smooth extrudate, see fig. 4.26a, shows that a broad peak appears at values between 0 and  $200 \text{ image}^{-1}$ , which is a sign for an irregular instability with a broad distribution of frequencies. The results and parameters of the analysis of the images of the LLDPE extrudates are summarized in tab. 4.5.

**Table 4.5.** – Flow parameters and results from the analysis of the LLDPE (tab. 2.3) sample. The according extrudates are shown in fig. 4.25 and the spectra of the image analysis, from which  $q_{image}$  is taken are shown in fig. 4.26. The  $q_{image}$  of the extrudate at  $\dot{\gamma}_{app} = 30 \text{ s}^{-1}$  is the maximum of the very broad frequency peak (fig. 4.26b). The classification of the extrudate to an instability type was done via the images of fig. 4.25.

$\dot{\gamma}_{app}$ $\text{s}^{-1}$	$v_{piston}$ $\text{mm/s}$	$v_{extr}^{**}$ $\text{mm/s}$	$t_{image}^{\dagger\dagger}$ $\text{s/image}$	$q_{image}$ $\text{waves/image}$	instability -
10	0.006	0.45	5.30	-	(smooth)
30	0.019	1.5	1.67	( $\approx 40$ )	sharkskin
300	0.19	15	0.17	9	GMF
790	0.5	39.4	0.06	7	GMF

\*\* The velocity of the extrudate when passing the die exit  $v_{extr}$  can be approximated by using the equation of continuity and the assumption of a plug flow.<sup>39</sup>

$$v_{extr} = \frac{A_{die}}{A_{reservoir}} v_{piston}. \quad (4.8)$$

$A_{die}$  is the cross-sectional area of the die,  $A_{reservoir}$  is the cross-sectional area of the reservoir and  $v_{piston}$  is the piston velocity of the capillary rheometer (fig. 4.2).<sup>44</sup>

$\dagger\dagger$   $t_{image}$  is the time which is needed to obtain an extrudate sample of the length  $L_{image} = 2.5 \text{ mm}$ , as represented by the images of fig. 4.25. By using eq. 4.8,  $t_{image}$

#### 4.4.6.1 Comparison of the Optical Analysis of the Extrudate and the Analysis of the Time-dependent Pressure Fluctuations

As in shown by Palza et al.<sup>62,149</sup> and summarized in chap. 4.4.5, the melt flow instabilities of a polymer extrudate are correlated to peaks in the FT-spectrum of the time-dependent pressure fluctuations  $\dot{p}(t)$ . In chap. 4.4.6 it was shown, that the melt flow instabilities can be also analysed via the FT of the grey-scale intensities of the images of the extrudate. In the following, the results of both methods are compared. As a measure of the both approaches, the detected characteristic frequency of the instabilities  $v_{inst,image}$  for the optical analysis and  $v_{inst,extr}$  for the analysis of the pressure fluctuations, are compared (tab. 4.6). The characteristic frequency of the melt flow instabilities for the optical analysis  $v_{inst,image}$  are obtained by using the number of waves  $q_{image}$  in an image of the length  $L_{image}$  (tab. 4.5). With these values the wavelength  $\lambda_w$  can be determined as

$$\lambda_w = \frac{L_{image}}{q_{image}}. \quad (4.10)$$

With the extrudate velocity, eq. 4.8, the frequency  $[v_{inst,image}] = \text{Hz}$  is obtained from the image analysis,

$$v_{inst,image} = \frac{v_{extr}}{\lambda_w}. \quad (4.11)$$

The characteristic frequency of the melt flow instabilities for the analysis of the pressure fluctuations  $v_{inst,extr}$  is found in the FT-spectra of the time-dependent pressure fluctuations. Two examples of those spectra are shown in fig. 4.27. In fig. 4.27a the spectrum of a sharkskin extrudate (fig. 4.25b) is shown. It contains a characteristic peak a  $v_{inst,extr} = 7.3 \text{ Hz}$  (tab. 4.6). The spectrum of fig. 4.27b represents a GMF instability (fig. 4.25d). The spectrum contains two characteristic peaks. One broad peak with a maximum at  $v_{inst,extr} = 166.4 \text{ Hz}$  (tab. 4.6) and one narrower peak at  $v_{inst,extr} = 2.4 \text{ Hz}$ . The low frequency peaks has also higher harmonics.

can be calculated from  $v_{extr}$ , as

$$t_{image} = \frac{L_{image}}{v_{extr}}. \quad (4.9)$$

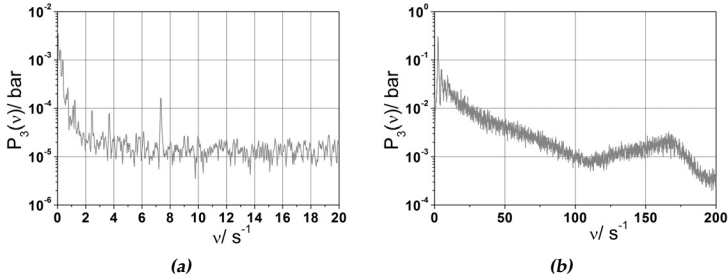


**Figure 4.27.** – Spectra of the FT analysis of the time-dependent pressure fluctuations of the LLDPE extrudate, shown in fig. 4.25. The LLDPE sample was heated at 180 °C and extruded at different apparent shear rates (a)  $\dot{\gamma}_{app} = 30 \text{ s}^{-1}$  and (b)  $\dot{\gamma}_{app} = 790 \text{ s}^{-1}$ . The 3 mm  $\times$  0.3 mm slit die was used on the capillary rheometer.

**Table 4.6.** – Comparisson of the frequency of the melt flow instability obtained from the optical analysis  $v_{inst,image}$  and the frequency of the melt flow instability obtained from the FT of the time-dependent pressure fluctuations  $v_{inst,extr}$ . The values in brackets are by the author estimated values. The according spectrum did not show a significant characteristic peak.

$\dot{\gamma}_{app}$ $\text{s}^{-1}$	$\lambda_w$ mm/wave	$v_{inst,image}$ Hz	$v_{inst,extr}$ Hz	$\frac{v_{inst,image}}{v_{inst,extr}}$ -
10	-	-	-	-
30	(0.063)	( $\approx 24$ )	7.3	3.29
300	0.28	53	27 - 36	1.96 - 1.47
790	0.36	109	166.4	0.66

As tab. 4.6 implies, the optical analysis of melt flow instabilities is limited to strong melt flow instabilities as e.g. the GMF of fig. 4.25c and fig. 4.25d. For the GMF instabilities the frequencies of the image analysis and the analysis of the time-dependent pressure fluctuations are in the same range (a factor of 1.4 - 2 lies between both frequencies). An exact match is not expected, due to following reasons:

1. The calculation of the extrudate velocity is made using the assumption of plug flows inside the capillary rheometer.
2. The extrudate samples represent rather short times, see tab. 4.5,  $t_{max,image} = 5.3$  s. Whereas, the spectra of the FT of the time-dependent pressure fluctuations are based on time data longer than 60 s.
3. The lengths are obtained from the solidified extrudate after the experiment. Thus, the effect from the volume contraction is not taken into account.
4. The changes of volume related to die swell<sup>31</sup> are not taken into account.

The analysis of the time-dependent pressure fluctuations is still capable to detect some weak melt flow instabilities, e.g. the sharkskin of fig. 4.25b. By the optical analysis it is not possible to obtain a characteristic frequency from the spectrum alone. Only, when the spectrum of the sharkskin extrudate, fig. 4.26b, is compared with the spectrum from the smooth extrudate, fig. 4.26a a large bump with a maximum at 40 Hz can be identified. However, to verify the presence of a melt flow instability the image of the extrudate has to be sighted. Whereas, this melt flow instability can be clearly detected by the FT of the time-dependent pressure fluctuations through a characteristic peak at 7.3 Hz, fig. 4.27a and tab. 4.6.

#### 4.4.7 Experimental Conditions for the Experiments with the Extruder

After choosing a die geometry, the typical experiments included two parameters, the temperature  $\vartheta_{ext}$  and the rotational speed of the screw  $n_{rot}$ . The measurements were conducted as a series of stepwise changed rotation rates of the extruder screw  $n_{rot}$  at a constant temperature  $\vartheta_{extr}$ . After these measurements of  $n_{rot}$ , the temperature could be changed and a similar experiment could be started after the altered temperature  $\vartheta_{extr}$  was

stable. The temperature was varied between 100 °C and 200 °C. The minimum temperature which was used depends on the melting point of the used polymer. To ensure that the polymer is molten and can flow inside the extruder the minimum temperature used was about 20 °C above the melting temperature. The rotational speed of the screw was altered between  $5 \text{ min}^{-1}$  up to  $250 \text{ min}^{-1}$ . The second number represents the maximum rotational speed of the extruder in combination with the sharkskin die-2. The rotational speeds which could be obtained with the sharkskin die-1 were between  $5 \text{ min}^{-1}$  and  $30 \text{ min}^{-1}$ . At each  $n_{rot}$  the extruder the time-dependent pressure was recorded for 10 - 20 min and only after the extruder reached a constant mean pressure in front of the die entrance.

## 4.5 Pressure Fluctuations Determined during the Extrusion of Polymer Melts

This section shows how the requirements which were described in the introduction of this chapter (chap. 4.1) can be achieved with the experimental set-ups introduced in chap. 4.4. An example of a typical measurement of a polymer melt is given in fig. 4.28.

### **Example 16.** *Example for data and data analysis of melt flow instabilities*

*Fig. 4.28a obviously shows a strong melt flow instability. However, the pressure recording of pressure transducer 3, fig. 4.28b, does not give an obvious hint of a strong melt flow instability and neither does this the autocorrelation function (ACF)  $r_{33}(\tau)$  of  $\dot{p}_3(t)$ , see fig. 4.28c. However, in the Fourier transform (FT)  $P_3(\nu)$  a significant peak appears at 63 Hz (fig. 4.28d), which is related to the instability. This is an example for the possibilities and problems for the technology transfer to the extruder. First it is possible to create melt flow instabilities with the sharkskin die on the extruder and then to determine them. The time-dependent pressure does not show a characteristic pattern of the melt flow instabilities. However, the FT is capable of detecting certain characteristic peaks even though they are included in a complex spectrum. The ACF can not be used to characterize melt flow instabilities for the data obtained from the extruder. The reasons for this are discussed in chap. 4.5.1. □*

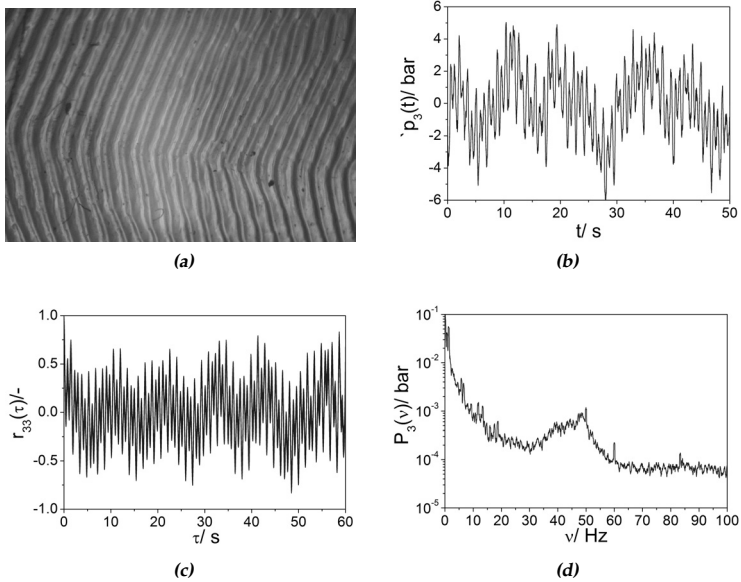


**Figure 4.28.** – An example for the data analysis of the time-dependent pressure measured on the extruder with the sharkskin die-1 with brass inlay. (a) PE-SCB07 (tab. 2.3) at  $\theta = 130^\circ\text{C}$  and  $n_{rot} = 80\text{ min}^{-1}$  (the width of this image is 7.5 mm), (b)  $\dot{p}(t)$ , (c) ACF and (d) FT.

At first in this section (chap. 4.5.1) it is deduced that the melt flow instabilities are related to characteristic peaks in the FT spectra and that other peaks are caused by different but defined means. This verifies the adaptability of the sharkskin die to an extruder.

Subsequently, chap. 4.5.2 deals with a study of the development of the melt flow instabilities for different shear rates. This provides an answer to the question whether it is possible to detect and control the melt flow instabilities via online monitoring. Before a summary of the findings of this chapter is given in chap. 4.6, chap. 4.5.4 presents a study on the correlation between optically detected melt flow instabilities and melt flow instabilities detected by the FT. Fig. 4.29 shows that with the use of the sharkskin die-2 it is possible to obtain strong melt flow instabilities, which can later analysed via the FT of the time-dependent pressure fluctuations.

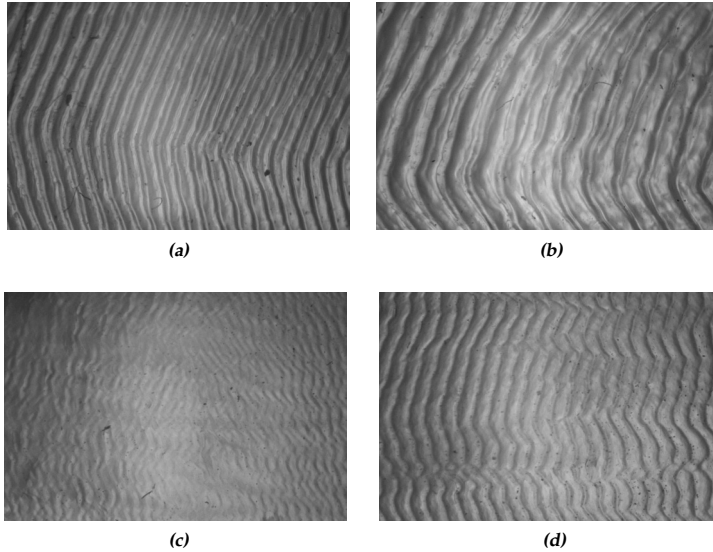


**Figure 4.29.** – Examples of observable melt flow instabilities for PE-SCB07 (the width of each image is 7.5 mm), (a) at  $\vartheta = 130\text{ }^{\circ}\text{C}$  and  $n_{rot} = 80\text{ min}^{-1}$ , (b) at  $\vartheta = 130\text{ }^{\circ}\text{C}$  and  $n_{rot} = 140\text{ min}^{-1}$ , (c) at  $\vartheta = 140\text{ }^{\circ}\text{C}$  and  $n_{rot} = 30\text{ min}^{-1}$ , and (d) at  $\vartheta = 140\text{ }^{\circ}\text{C}$  and  $n_{rot} = 45\text{ min}^{-1}$ .

### 4.5.1 Identification of the Melt Flow Instabilities Inside the Extruder Die

The FT-spectra of the time-dependent pressure from the extruder experiment shows a much more complex behaviour than the spectra obtained at the capillary rheometer.<sup>62,146,150,216</sup> The spectra of the capillary rheometer are simpler, as they show just the frequencies of the instabilities and sometimes, additionally, the frequencies related to the electric current.<sup>148</sup> In contrast, the spectra obtained by the extruder are rather complex. First of all, a stronger decay of the spectra can be observed even for melt flows at low rotation rates in the range of frequencies up to  $\nu = 20 - 40\text{ Hz}$  (see fig. 4.30a). Peaks appear on top of this decay at low frequencies, which can be clearly identified as the frequencies of the screw rotation of the extruder

and their higher harmonics.

**Example 17. Correlation between the low frequency peaks and the rotation of the screw**

In fig. 4.30a and b the extruder runs at  $n_{rot} = 140 \frac{rot}{min}$ . This corresponds to a frequency  $\nu_1 \approx 2.33$  Hz and peaks appear in the spectrum at this frequency at 2.33 Hz and at higher multiples i.e.  $\nu_2 = 4.66$  Hz and so on.  $\square$

Similar to the observations made on the capillary rheometer, there are peaks corresponding to the electric current; i.e. for Germany 50, 100, 150 and 200 Hz.\* Furthermore, there are peaks which could not be directly identified, i.e. the peak at 57 Hz in fig. 4.30.

The spectra in fig. 4.30a shows all these characteristics which have been described in the paragraph above. However, additionally a broad peak is detected. This peak has its maximum between 60 and 70 Hz and has a total broadness of about  $\Delta\nu \approx 25$  Hz, but the maximum amplitude is relatively small with  $10^{-4}$  bar. Still, this peak seems to be a material dependent peak, which is related to the visible melt flow instabilities seen in fig. 4.29b. As a proof of this the same experiment was performed again, but without polymer inside the extruder. The spectrum from the FT should show all spectral parts as described before except the material contribution. In case of fig. 4.30a this would be the broad peak at 60 - 70 Hz. The spectrum from this empty extruder experiment is shown in fig. 4.30b; it is clearly visible that the broad peak disappeared. Therefore, it can be concluded that this peak is dependent on the material. Nevertheless, the extruder set-up dependent peaks remain, for instance the peaks at 2.33 and 4.66 Hz or the electric-current related peaks at 50 and 100 Hz. However, a small reduction in their amplitude can be observed. The decay at low frequencies is also part of this spectrum.

Another experiment was performed to learn more about the properties of the extruder set-up in the frequency space. In this experiment the extruder was set at the same constant temperature, but the screw was stopped ( $n_{rot} = 0 \text{ min}^{-1}$ ). The spectral contributions of the mechanical system of the extruder should disappear in the spectrum of this experiment. Fig. 4.30c indicates that this statement is true. The peaks at low frequencies, which could be clearly correlated by numbers to the screw rotation,

\* In countries which have electric current system based on 60 Hz, this frequencies appear additionally.

vanish and so does the decay at low frequencies. From this, it can be deduced that both spectral contributions are induced by mechanical vibrations of the extruder engine. Still, the peaks at 50 and 100 Hz remain in the spectra as well as some others e.g. at 57 Hz.

As a concluding experiment in this series the whole extruder was switched off to avoid any interaction between the electrical system of the extruder, i.e. inductive currents from the heating belts and others, and the data acquisition system. The spectrum of this experiment is shown in fig. 4.30d. When comparing this spectrum with the previous one no changes can be seen. From the previously stated, it follows that the peaks from the electrical-current and the not identified peak at 57 Hz are related to the data acquisition system itself. These peaks remain stable at their frequencies, which makes them easy to identify.

## 4.5.2 Observing the Development of the Melt Flow Instabilities in the Extruder

In the previous section it was shown that melt flow instabilities can be detected on the extruder with a sharkskin die, but the spectra are not as trivial as in the capillary rheometer.

To continue with the idea of a self-controlling smart-extruder, the next experiments are performed in a way which simulates a control loop. The extruder was set at a defined temperature, in this case 130 °C. The rotational rate of the screw  $n_{rot}$ , was stepwise lowered starting at 170 min<sup>-1</sup> and followed by 140, 80 and 50 min<sup>-1</sup>. Thus, the development of the melt flow instabilities could be observed optically and by the time-dependent pressure fluctuations. The time-dependent pressure inside the sharkskin die of the extruder was recorded for 10 - 20 min at each  $n_{rot}$  and only after the extruder reached a constant mean pressure in front of the die entrance. The resulting spectra are shown in fig. 4.31.

At the first measurement with  $n_{rot} = 170 \text{ min}^{-1}$ , see fig. 4.31d, a broad peak was identified at  $v_{inst} \simeq 95 \text{ Hz}$ . This peak had a broadness  $\Delta v_{inst} \approx 7 \text{ Hz}$  and an amplitude of  $P_{3,inst} = 2 \times 10^{-5} \text{ bar}$ . At the next step of rotational velocity  $n_{rot} = 140 \text{ min}^{-1}$  the peak was shifted to a lower frequency,  $v_{inst} \simeq 78 \text{ Hz}$ , still having a similar shape (fig. 4.31c). The broadness changed to  $\Delta v_{inst} \approx 10 \text{ Hz}$  and the amplitude increased slightly to

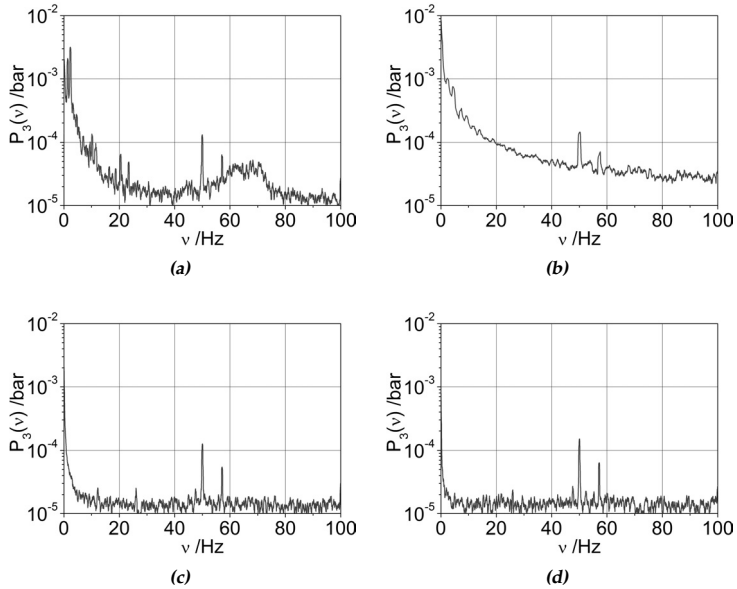


**Figure 4.30.** – Identifying the material dependent pattern via comparison measurements. (a) PE-SCB07 at  $\vartheta = 130\text{ }^{\circ}\text{C}$  and  $n_{rot} = 140\text{ min}^{-1}$ , (b) empty extruder  $\vartheta = 130\text{ }^{\circ}\text{C}$  and  $n_{rot} = 140\text{ min}^{-1}$ , (c) empty extruder  $\vartheta = 130\text{ }^{\circ}\text{C}$  and  $n_{rot} = 0\text{ min}^{-1}$ , and (d) empty extruder  $\vartheta = 20\text{ }^{\circ}\text{C}$  and  $n_{rot} = 0\text{ min}^{-1}$ .

$P_{3,inst} = 3 \times 10^{-5}\text{ bar}$ . At  $n_{rot} = 80\text{ min}^{-1}$  the peak was shifted again to a lower frequency (fig. 4.31b),  $v_{inst} \approx 63\text{ Hz}$ . The peak became much broader,  $\Delta v_{inst} \approx 25\text{ Hz}$ , and its amplitude increased strongly to  $P_{3,inst} = 8 \times 10^{-4}\text{ bar}$ . As a  $n_{rot} = 45\text{ min}^{-1}$  was set the broad peak vanished from the spectrum and instead of it a much narrower,  $\Delta v_{inst} \approx 1\text{ Hz}$ , peak at  $v_{inst} \approx 54\text{ Hz}$  appeared, as can be seen in fig. 4.31a. In all cases of the experiment a melt flow instability was detected on the surface of the extrudate and in the FT-spectra of the related time dependent pressure.

The observations of this experiment can be summarized as the following:

1. The melt flow instability are characterized by a broad peak. This melt flow instability could be followed over a broad range of rota-

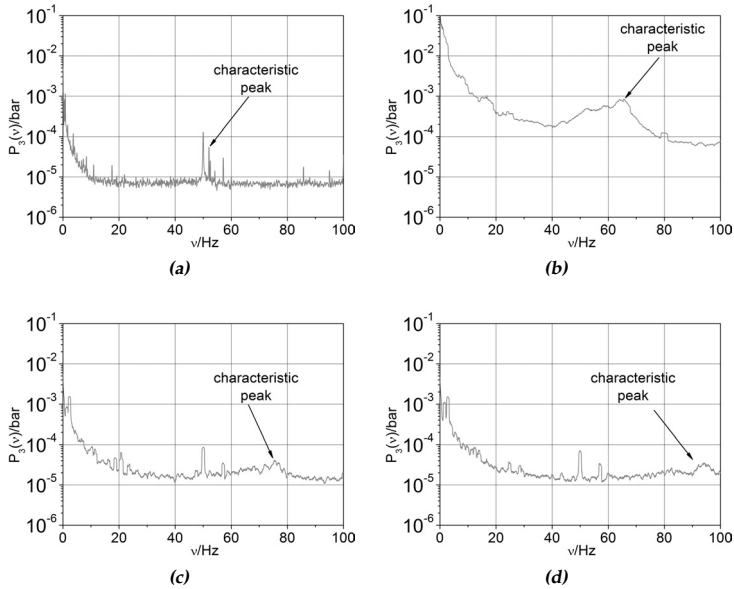


**Figure 4.31.** – Observing the development of characteristic peaks for PE-SCB07 (tab. 2.3) at  $\vartheta = 130 \text{ }^\circ\text{C}$  and at (a)  $n_{rot} = 50 \text{ min}^{-1}$ , (b)  $n_{rot} = 80 \text{ min}^{-1}$ , (c)  $n_{rot} = 140 \text{ min}^{-1}$ , and (d)  $n_{rot} = 170 \text{ min}^{-1}$ .

tional velocities of the screw.

2. An unsteady transition in the shape of the characteristic peak was observed. This could be related to a transition in the mechanism of the origin of the melt flow instability.

### 4.5.3 Using the ACF to Analyse the Time-dependent Pressure Fluctuations from the Sharkskin Die on the Extruder

Chap. 4.4.5 showed how useful the ACF can be in combination with the FT for data obtained in the capillary rheometer. This capability is lost when the ACF is used for data measured in the extruder. This is illustrated in fig. 4.32. Both figures, fig. 4.32a and fig. 4.32b, show strong oscillations

with nearly no decay in amplitude. According to Naue (2007),<sup>148</sup> this would be an obvious sign for a stick-slip instability. However, this conclusion is only true for the capillary rheometer. In the extruder the signal is strongly affected by the rotations of the screw. These cause the large oscillation in the ACF of fig. 4.32. This is easily validated just by counting the amount of cycles found in each plot. For fig. 4.32a the number is 5 cycles per 60 seconds and this number coincides with the applied rotations of the screw  $n_{rot} = 5 \text{ min}^{-1}$ . Similar results are found in fig. 4.32b, the number of cycles is 80 cycles per 60 seconds, and this number coincides with the applied rotations of the screw  $n_{rot} = 80 \text{ min}^{-1}$ . This is the reason why the ACF is not used for the analysis of the time-dependent pressure obtained from the extruder.

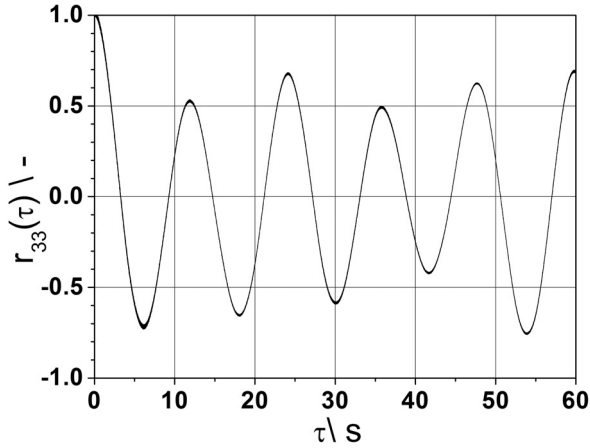
#### 4.5.4 Comparison Between Optical Analysis and Pressure Based Analysis of the Melt Flow Instabilities

The images seen in fig. 4.33 were FT-analysed via the algorithm introduced in chap. 4.4.6. Examples of the resulting spectra are shown in fig. 4.34. All the spectra of the images of the PE-SCB13 (tab. 2.3) show significant peaks. The spatial frequencies and the normalized intensity of the peaks are summarized in tab. 4.7 and are graphically shown in fig. 4.35.

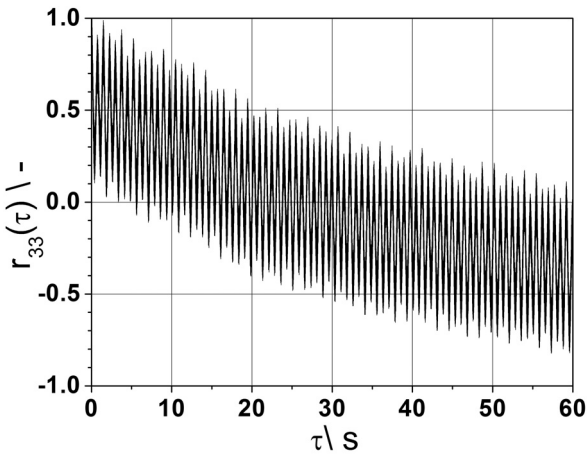
With a known mass flow rate  $\dot{m}$  (see fig. 4.36) for the single experiments it is also possible to calculate a time based frequency of the instabilities, shown in fig. 4.37, from the spatial frequency which was obtained from the image analysis. The mass flow rate shown in fig. 4.36 is, as expected, a linear function of the set screw rotation.\* This was also observed for other polymers. The plot of the mass flow contains data from three different polymers a LDPE, PE-SCB13 and a HDPE. The data was also fitted with a linear function to demonstrate how small the deviation from a linear relation is. In case of the LDPE and the HDPE the data was further linearly extrapolated up to  $n_{rot} = 80 \text{ min}^{-1}$ .

The time-dependent pressure (at sensor position 3) was analysed using the FT in order to correlate the optical analysis to the analysis of the pressure

\* This means also that the mass flow rate is linear dependent on the apparent shear rate  $\dot{\gamma}_{app}$ . Because for low values of  $n_{rot}$ , it follows that  $n_{rot} \propto \dot{\gamma}_{app}$ .



(a)



(b)

**Figure 4.32.** – The ACF from the data analysis of the time-dependent pressure fluctuations. The experiments were conducted in the extruder with the sharkskin die-2. The sample was PE-SCB13 (tab. 2.3) at  $\vartheta = 90\text{ }^{\circ}\text{C}$  and a number of rotations of the screw of (a)  $n_{rot} = 5\text{ min}^{-1}$  and (b)  $n_{rot} = 80\text{ min}^{-1}$  was applied. The raw data was measured with the pressure transducer P3 (at the die exit).

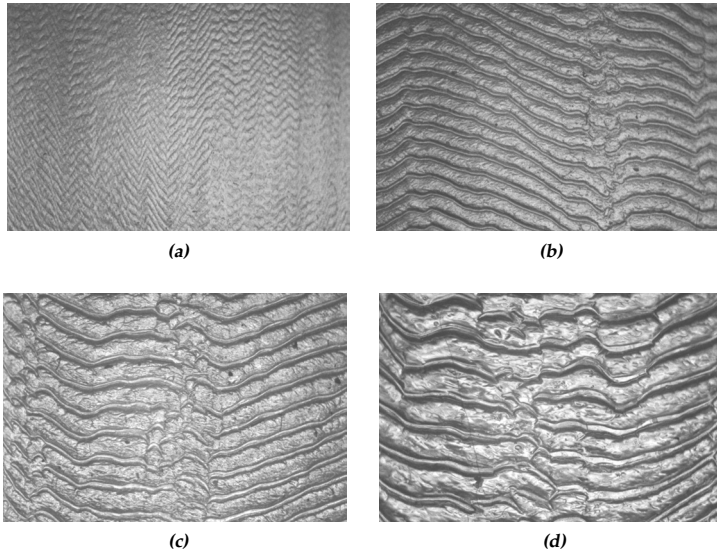


**Figure 4.33.** – Examples of observable melt flow instabilities for PE-SCB13 at  $\vartheta = 90\text{ }^{\circ}\text{C}$  and a number of rotations of the screw of (a)  $n_{rot} = 5\text{ min}^{-1}$ , (b)  $n_{rot} = 15\text{ min}^{-1}$ , (c)  $n_{rot} = 40\text{ min}^{-1}$ , and (d)  $n_{rot} = 80\text{ min}^{-1}$ . (Each image has a width of 7 mm.)

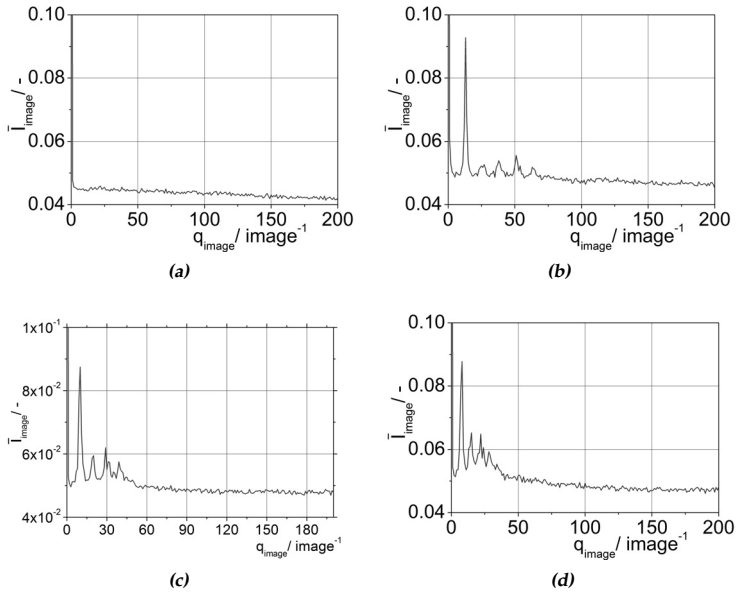


**Figure 4.34.** – Examples of the spectra of the images of the observable MFI for PE-SCB13 at  $\vartheta = 90^\circ\text{C}$  and a number of rotations of the screw of (a)  $n_{\text{rot}} = 5 \text{ min}^{-1}$ , (b) and  $n_{\text{rot}} = 15 \text{ min}^{-1}$ , (c)  $n_{\text{rot}} = 40 \text{ min}^{-1}$ , and (d) and  $n_{\text{rot}} = 80 \text{ min}^{-1}$ .

**Table 4.7.** – Comparison of the peaks found in the spectra of the images from fig. 4.33 and comparison of the intensity values of the first peaks. (a) shows the values of the first and the second peak and (b) shows the values for the third and fourth peak. The sample was PE-SCB13 (tab. 2.3) at  $\vartheta = 90^\circ \text{C}$ .

$n_{rot}$ $\text{min}^{-1}$	$\dot{m} = dm/dt$ $\text{g/s}$	$q_{image,1}$ $\text{image}^{-1}$	$\bar{I}_{image,1}$ -	$q_{image,2}$ $\text{image}^{-1}$	$\bar{I}_{image,2}$ -
5	0.04	22	0.046	38	0.046
10	0.07	17	0.059	34	0.049
15	0.11	13	0.093	27	0.053
20	0.14	11	0.091	21	0.055
40	0.26	10	0.087	20	0.060
60	0.39	10	0.080	19	0.059
80	0.51	8	0.088	15	0.065

(a)

$n_{rot}$ $\text{min}^{-1}$	$\dot{m} = dm/dt$ $\text{g/s}$	$q_{image,3}$ $\text{image}^{-1}$	$\bar{I}_{image,3}$ -	$q_{image,4}$ $\text{image}^{-1}$	$\bar{I}_{image,4}$ -
5	0.04	-	-	-	-
10	0.07	50	0.048	-	-
15	0.11	38	0.054	51	0.056
20	0.14	32	0.055	41	0.055
40	0.26	29	0.062	39	0.058
60	0.39	29	0.063	38	0.062
80	0.51	22	0.065	28	0.059

(b)

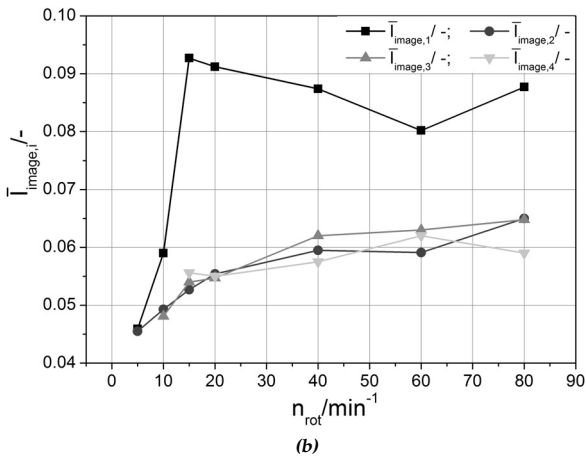
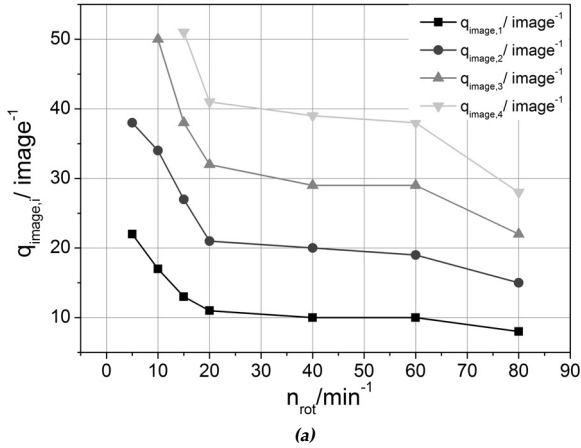


**Figure 4.35.** – Plots of the values of the spatial frequency and the intensity of tab. 4.7. The sample was PE-SCB13 (tab. 2.3) at  $\vartheta = 90^\circ\text{C}$ . (a) The spatial frequency of the first peaks which could be indicated in the FT-spectra of the images, and (b) normalized intensity values of the peaks shown in fig. 4.33.

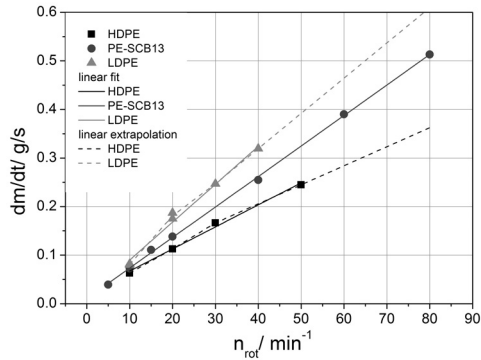


**Figure 4.36.** – Mass flow  $\dot{m} = dm/dt$  of different polymers in the extruder experiments. The symbols indicate the data from measurements, the continuous lines indicate the results from a linear fit of each data set and the dashed lines are indicating the linear extrapolation of the two data sets with less data.

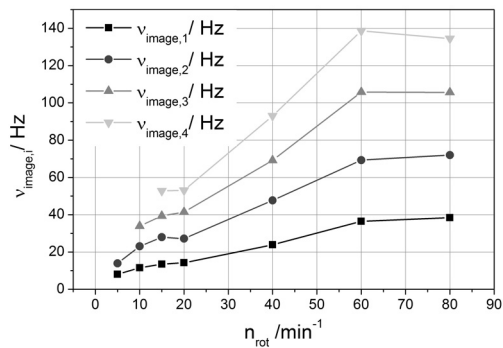


**Figure 4.37.** – The frequency of the melt flow instabilities calculated out of the spatial frequency from the image analysis. Examples of the spectra are show in fig. 4.34. The frequency of the melt flow instabilities is given as a function of applied rotational speed; the index  $i$  indexes the order of the harmonic. (The sample was PE-SCB13 (tab. 2.3) at  $\theta = 90^\circ \text{C}$ .)

readings of the high sensitive piezoelectric transducers.

Examples of the FT-analysis at the die exit are shown in fig. 4.38. In each of the spectra it is possible to find at least one characteristic peak from the material. This has been validated by performing measurements without sample (see fig. 4.39), where no characteristic peaks were found. Thus, the material-dependent peaks could be found. The values of the characteristic frequencies of the peaks are summarized in tab. 4.8 and are plotted in fig. 4.40. In fig. 4.40 the results from the image analysis have been added. This way, a comparison of both methods can be easily done. The first difference between both methods is that the analysis of the image produces in this case spectra with very sharp peaks and the higher harmonics appear. However, the SNR values are small. The FT spectra from the time-dependent pressure include typically only one peak and most of the time this peak is broad. Nevertheless, the SNR values are significantly higher. To include the broadness of the peaks in the comparison between the analysis of the images and the FT-analysis of the time-dependent pressure, the frequency values at the begin of the broad peak and at its end were taken, as seen in tab. 4.8. Thus, it appears in fig. 4.40 that the curve of the characteristic frequency of the spectra of the pressure bifurcates. The upper branch stays in close proximity to the results of the analysis of the image, while the lower branch stays approximately constant. Actually, the peaks of the spectra of the pressure are not only represented by both branches, but by the whole area between them. Comparison measurements were performed without sample, see fig. 4.39. These measurements verify the interpretation of the material-dependent peaks.

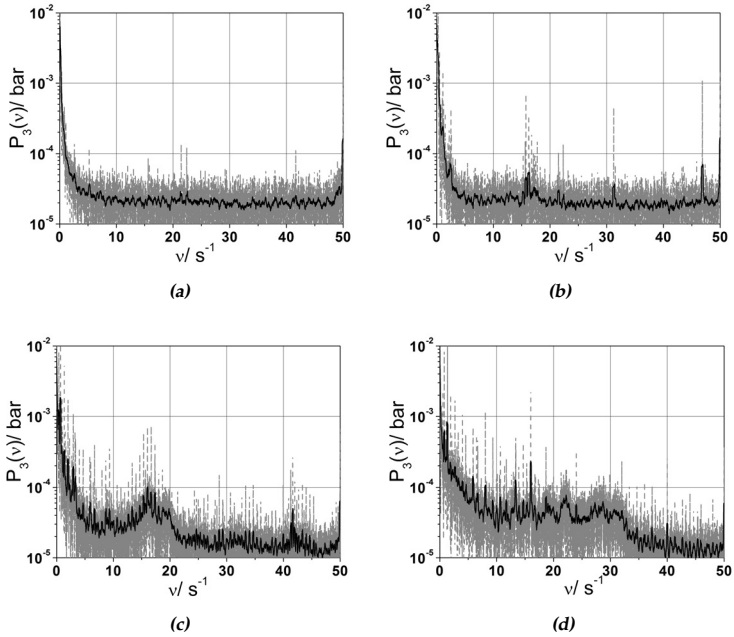


**Figure 4.38.** – Examples of FT-spectra of melt flow instabilities for PE-SCB13 at  $\vartheta = 90\text{ }^{\circ}\text{C}$ . (a)  $n_{rot} = 5\text{ min}^{-1}$ , (b)  $n_{rot} = 15\text{ min}^{-1}$ , (c)  $n_{rot} = 40\text{ min}^{-1}$ , and (d)  $n_{rot} = 80\text{ min}^{-1}$ . The grey curves are the raw FT-spectra and the black curves are the smoothed FT-spectra. The according extrudates are shown in fig. 4.33.

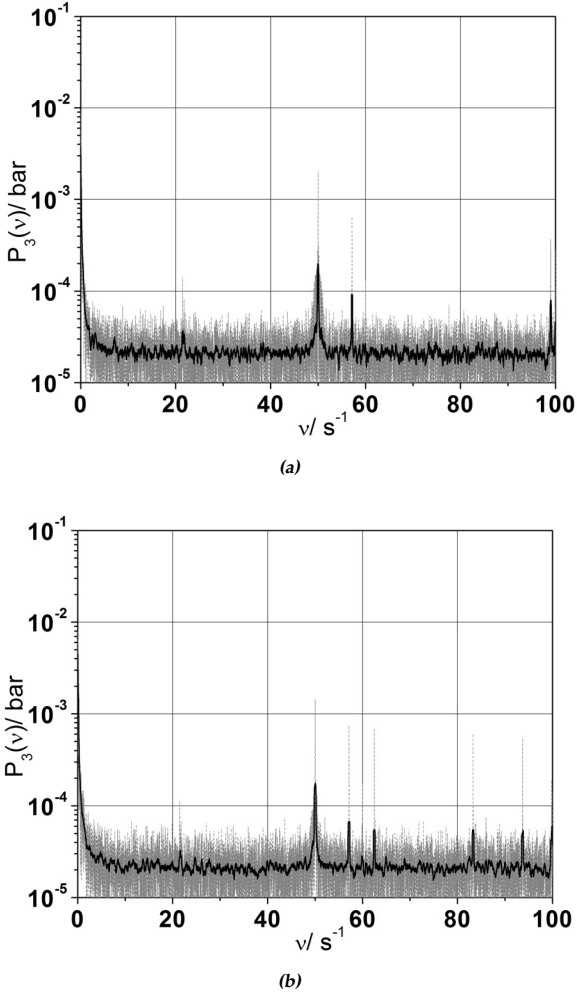


**Figure 4.39.** – Examples of FT-spectra of the extruder running without sample at  $\vartheta = 90 \text{ }^\circ\text{C}$ . (a)  $n_{rot} = 0 \text{ min}^{-1}$  and (b)  $n_{rot} = 5 \text{ min}^{-1}$ . The grey curves are the raw FT-spectra and the black curves are the smoothed FT-spectra.

**Table 4.8.** – Summary of the characteristic frequencies of the first significant peak in the FT spectra of the time-dependent pressure fluctuations of PE-SCB13 in the extruder.

$n_{rot}$ $\text{min}^{-1}$	$\dot{m} = dm/dt$ $\text{g/s}$	$\nu_{extr,1,min}$ $\text{Hz}$	$\nu_{extr,1,max}$ $\text{Hz}$
5	0.04	-	5.2
10	0.07	-	10.4
15	0.11	-	15.8
20	0.14	11	18
40	0.25	8.6	21.3
60	0.39	8.7	31.2
80	0.51	10	32

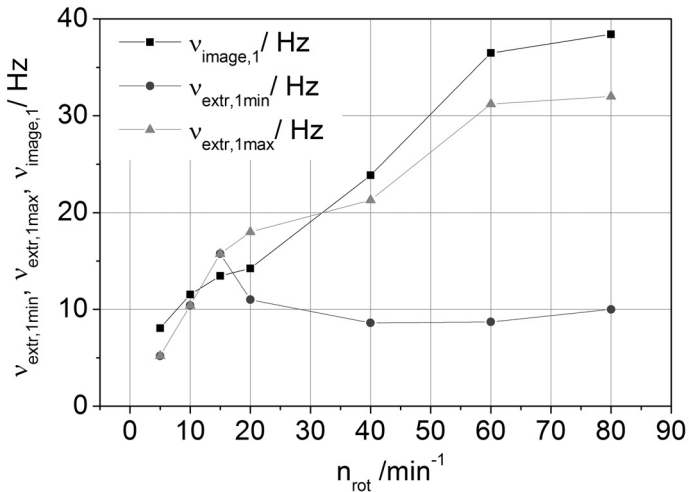


**Figure 4.40.** – The observed characteristic frequencies of the spectra of the time-dependent pressure fluctuations  $\nu_{extr,i}$  and characteristic frequencies of the spectra of the FT-image analysis  $\nu_{image}$  as a function of the applied rotational frequency. The sample was PE-SCB13 (tab. 2.3) at  $\vartheta = 90^\circ \text{C}$ .

### 4.5.5 Noise Reduction for Automated Detection of the Melt Flow Instabilities

The results of chap. 4.5.4 and chap. 4.5.1 can be summarized as follows: The sharkskin die in combination with the extruder is capable to detect the melt flow instabilities. A drawback in comparison to the sharkskin die on the capillary rheometer is the more complex FT-spectrum which is obtained. In the spectrum, the frequency contributions of the instabilities can be seen as well as the system-dependent contributions. These appear in the same order of magnitude as in the melt flow instabilities. This causes problems with the automation of the detection of the melt flow instabilities. Basically, the presence of many peaks which are not caused by the melt flow instabilities make the use of a computer algorithm for the analysis and reduction of the melt flow instabilities during the extrusion process difficult.

To solve this problem, measurements without samples were performed as already explained in chap. 4.5.1. The FT-spectra of this material-independent measurements (see e.g. fig. 4.41) were then compared to measurements with sample. Both types of spectra were normalized to the peak at 50 Hz which is present in all spectra, has similar intensities and is obviously not material-dependent. The normalized spectra from the measurements without sample were afterwards subtracted from the original spectrum. In this way, the contributions caused by the system-dependent peaks should be completely eliminated.

The FT-spectrum of a measurement of PE-SCB13 in the capillary rheometer with the sharkskin die (SSD) is shown in fig. 4.41. The corresponding measurement of the empty channel is added in this plot. It is evident that the subtraction of the empty channel spectrum from the measurement with polymer reduces the system-dependent contributions in the frequency spectrum about one decade. Nevertheless, it does not completely eliminate these system-dependent peaks. Therefore, it can improve the signal-to-noise ratio, but still does not enable the easy use of an algorithm for the control of the melt flow instabilities.

A similar finding can be seen in fig. 4.42 in a comparison of the empty channel experiments. All spectra were normalized to the intensity of the 50 Hz peak. Still, all the peaks other than 50 Hz have different intensities

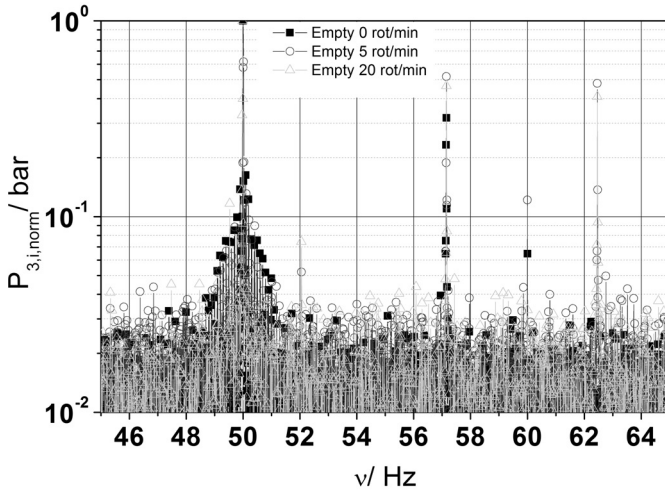


**Figure 4.41.** – The spectra of measurements with the empty extruder. The spectra are composed only by noise and are normalized to the intensity at 50 Hz for different numbers of screw rotations at  $\vartheta = 90^\circ\text{C}$ .

for the different runs. Therefore, it can be stated that the system-dependent contributions to the frequency spectrum vary with the rate of rotation.

## 4.6 Summary and Conclusions for the Extruder

At the end of this chapter the requirement specifications stated in chap. 4.1 could be fulfilled.

At first it was required that the functioning of the commercialized sharkskin die of the capillary rheometer should be transferred to a lab size extruder. This transfer was explained in chap. 4.4. The transfer of the technology led to two different sharkskin dies (SSD): the first one with a shallow slit geometry, which was not able to produce strong melt flow instabilities. The second die had a higher slit geometry, which generated strong melt flow instabilities. The strong melt flow instabilities were necessary in order to obtain peaks which have an amplitude which is large enough to

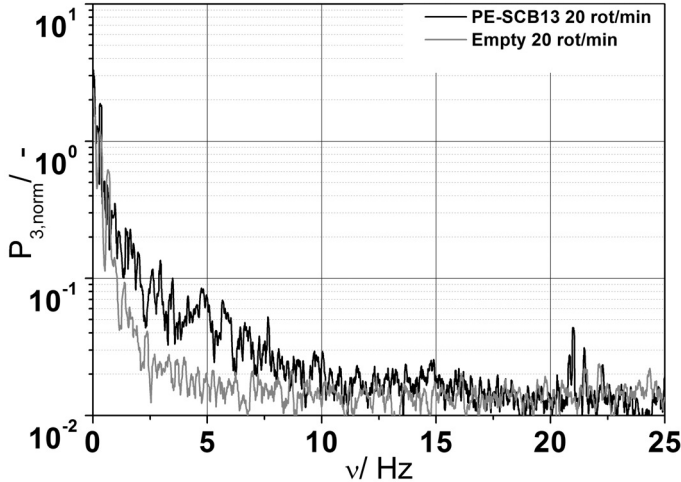


**Figure 4.42.** – Influence of normalization of known noise effects on the spectra of pressure fluctuations on the extruder. Each spectrum is normalized to its intensity at 50 Hz for measurements; without sample (grey curve) and for measurements with polymer (PE-SCB13) sample (black curve). Both measurements used the same parameters; a number of rotation of the screw of 20 rot/min and a temperature of  $\vartheta = 90$  °C.

be detected in the FT spectrum. This was essential for the validation of the function of the new set-up.

With the sharkskin die-02 (2 mm  $\times$  10 mm slit geometry) it was possible to satisfy the second requirement and the range of measurement could be easily chosen due to the appearance of strong melt flow instabilities already at low shear rates. For this purpose the melt flow instabilities were studied with optical methods, see chap. 4.4.6. That way, it was possible to fulfil the third requirement by applying the tools of FT-analysis (chap. 4.5) and ACF (chap. 4.4.4) to the measured time-dependent pressure fluctuations. Thus, it was found that it was not possible to find characteristic patterns of the melt flow instabilities in the ACF on the extruder. This was caused by the large contribution of the extruder engine to the pressure signal.

The FT-analysis proved to be useful for finding the characteristic contributions of the melt flow instabilities in the frequency domain spectra (see chap. 4.5.1). As shown in chap. 4.5.1, the characteristic peaks can clearly be differentiated from the contributions of the mechanical extruder system. Thus, the fourth requirement is satisfied.

The final requirement states that the sharkskin die on the extruder should be able to monitor the melt flow instabilities during the reduction of the extrusion rate. This was studied in chap. 4.5.4 and in chap. 4.5.5. The essence of these studies is, that it is possible to monitor the melt flow instabilities in the extruder. However, for the automation there are still some obstacles to overcome, namely:

- A method has to be found in order to automatically differentiate between material-dependent contributions to the spectrum and the mechanical system-dependent contributions.
- The transition from one type of melt flow instabilities to another (see fig. 4.31a and fig. 4.31b) might cause unstable states of control.

At the end it is promising that an automated control of the extrusion process can be conducted via the measurement of the pressure fluctuations inside the die. However, this requires a more detailed study of the signal analysis of the sharkskin die on the extruder.

Additionally, a comparison between the optical analysis and the pressure analysis both done in the frequency domain was presented in chap. 4.5.4. This showed that in the case of strong melt flow instabilities both methods lead to similar results with slightly different additional information, as for instance the optical analysis typically contains narrow peaks and higher harmonics whereas the pressure data results in broader peaks. As a characteristic difference it was found that weak melt flow instabilities are hardly detected with the used optical methods, whereas the analysis of the pressure data still finds characteristic contributions to the frequency spectrum, chap. 4.4.6.1. This underlines the value of the pressure readings for the automated control of the extrusion process, because at the point of transition between smooth and melt flow instabilities the extrudate will most probably show a weak melt flow instability.



## Chapter 5

# Improving the CaBER with a Measurement of the Axial Force

The CaBER (Capillary Break-up Extensional Rheometer)<sup>222-224</sup> is a rather new\* and rather simple rheological device. Its intentional use is to characterize uniaxial elongational flows of low viscous ( $< 10^3$  mPas) fluids. The functionality of the CaBER will be explained in detail in chap. 5.1.1.

However, the principle can be summarized that a sample of a liquid is brought between two plates. During the experiment, one plate stays stationary while the other moves upwards to its defined end position with a defined velocity. By this upward movement, the liquid will be stretched to form a cylindrical filament. After the stretching is finished the CaBER measures the diameter at the middle of this filament as a function of time and from this measurement the elongational viscosity is calculated.

### 5.1 Introduction and Task

The elongational viscosity is important in many applications, e.g. in the packaging industry for the filling of daycare products or in coating applications. Obtaining the elongational viscosity is a difficult task, as Plog<sup>225</sup> summarizes. Three fundamental types of state-of-art of measuring devices exists for measuring the elongational viscosity for high viscous fluids. One is the Münstedt extensional rheometer for polymer melts<sup>74</sup> another is the

---

\* patent G. H. McKinley et.al. 2004

Meißner extensional rheometer<sup>226</sup> and the third one is the SER (Sentmanat Extensional Rheometer) device from Sentmanat.<sup>227</sup> However, all three methods are only applicable on high viscous liquids ( $\eta > 10^4$  Pas).

Several set-ups have been suggested for low viscosity liquids like the pressure drop method<sup>228</sup> or the opposing-jet method,<sup>229</sup> to name just two of them.<sup>225</sup> A large effort has been made to study the elongational flow of fluids with a low viscosity.<sup>230</sup> However, the experimental correlation between the results of the different methods revealed poor results for the opposing-jet method, as Dontula et al.<sup>231</sup> showed. Starting by 1990, Sridhar et al.<sup>230,232</sup> used a filament stretching devices to obtain the elongational viscosity of a low viscous fluid in a well defined uniaxial flow. These filament stretching rheometers are measuring the force and the shape of a sample of a liquid while it is stretched.

This apparatus is unfortunately not commercialised. Even though a large research effort has been undertaken.<sup>233–237</sup> Nevertheless, the filament stretching rheometer is not easily manageable. In 1997 Bazilevsky<sup>238</sup> and Entov<sup>239</sup> found that the uniaxial deformation of a liquid filament, which is governed by the surface tension, can be used to determine the elongational viscosity. This idea was later improved by the works of Kolte<sup>240</sup> and McKinley et al.<sup>234,241</sup> to be commercialised as the CaBER by the company Thermo Fisher Scientific.

The great advantage of the CaBER is its easy method for determining the elongational viscosity with just the knowledge of one material property (the surface tension) and the measurement of the filament diameter.

Thus, the CaBER seems to be a promising method to obtain the elongational viscosity for low viscous fluids. Nevertheless, the simplicity contains the major draw back of the CaBER experiment. Only one geometrical value, the diameter  $d(0, t)$  (see fig. 5.1), is measured. For the correct interpretation of the results of the CaBER experiment it is important that the sample satisfies all the assumptions made in the theory. To further improve the CaBER and to develop a better insight into the sample behaviour the group of Prof. Willenbacher applied a high-speed optical system on the CaBER. This was done and published by Niedzwiedz<sup>242</sup> and Arnolds.<sup>243,244</sup> A high-speed camera recorded the very fast dynamics of the formation and break of the filament formation. Afterwards, a complex analysis of the curvature of the filament was applied. The mechanism of

break up, for instance the droplet formation or the simple rupture, can be studied with this set-up. This optical tool could justify most of the geometrical assumptions made for the CaBER (see chap. 5.2), but the assumption about the negligible axial force is still not validated.

A task of this thesis was to extend the capabilities of the CaBER by adapting an axial force measurement.<sup>245,246</sup> The limited size of the sample volume of about  $30 \text{ mm}^3$  required a very sensitive force transducer ( $F \approx 1 \text{ mN}$ ). The general constraints of this task were that the additional measurement of the axial force:

- Is installed directly at a commercial CaBER without manipulations involving permanent changes on the CaBER. Thus, it will be easily accessible for other researchers.
- Allows the same measurements as before, but with an additional axial force measurement.
- Can measure down to several mN.

With this new measurement option, it is possible to measure the time-dependent axial force  $F(t)$  to validate the model equations of the CaBER theory. This is shown in chap. 5.5. The objects of study are a viscoelastic polystyrene (PS) solution and viscous silicone oils (PDMS). All of those samples can be used to perform CaBER experiments. Additionally, the balance equations of the theory of the CaBER<sup>244,246</sup> are critically analysed and further developed.

The knowledge of the time-dependent axial force  $F(t)$  makes it possible to observe the curing behaviour of various liquids, e.g. glues. While a glue cures, it changes its material properties. First the glue will behave like a viscous liquid. With increasing curing time it gets more rigid and it responds to the applied deformation with a larger force. Results of the measurement of two different glues are presented in chap. 5.5.3. In this section also a term similar to the tack<sup>247–251</sup> value\* is introduced to describe the stickiness of the glues as a function of curing time.

### 5.1.1 The Principle of the CaBER Experiment

The aim of the CaBER experiment is the determination of the elongational viscosity by optically observing the breakup of a filament of a fluid.

\* The tack value describes the tackiness of a material (chap. F).

The experimental procedure of a measurement with the CaBER can be divided into three main phases (fig. 5.1):

1. Sample loading phase.
2. Filament stretching phase.
3. CaBER experiment.

The experimental procedure starts with the sample loading phase.

**Definition 7. Sample loading phase**

*In this phase the sample is placed between both plates with the same diameter  $D_0$ . The initial distance of both plates  $L_0$  defines the sample volume. The sample should be placed between the plates without any material attached to the outer sides of the plates.*  $\square$

After the loading of the sample the experimental procedure continues with the filament stretching phase.

**Definition 8. Filament stretching phase**

*The filament stretching phase is initiated at the time  $t_0$ . The upper plate moves upwards with a predefined velocity  $v_{\text{strike}}(t)$  until the upper plate reaches its final position  $L_{\text{strike}}$  at  $t = t_1$ . The velocity can e.g. be chosen to be constant as*

$$v_{\text{strike}} = L_{\text{strike}} / t_{\text{strike}} \quad (5.1)$$

*or exponentially decaying as*

$$v_{\text{strike}} = \mathfrak{C}_1 e^{-t/\mathfrak{C}_2} \quad (5.2)$$

*The duration of this phase is defined by the operator by the strike time  $t_{\text{strike}}$ . This phase is not part of the actual CaBER experiment and for this reason its defined, that*

$$t_0 := -t_{\text{strike}} \text{ and} \quad (5.3)$$

$$t_1 := 0. \quad (5.4)$$

$\square$

**Assumption 1. Negligible axial stress**

*After the filament was stretched, it is assumed that the filament nearly rests in axial direction. Thus, it is assumed that no axial forces are present and from this it is further assumed that the stress component in x-direction,  $\sigma_{11}$  is negligible.*  $\square$

According to this assumption the filament stretching phase and the following CaBER experiment are clearly separated on the time axis. Starting at  $t_0$  the CaBER already measures the diameter of the filament with a laser micrometer. However, the position of the laser micrometer is fixed at  $x = 0$  (see fig. 5.1). The diameter measured in the filament stretching phase is the diameter of the upper geometry and of parts of the upper half of the developing filament.

**Definition 9. CaBER experiment**

*The actual CaBER experiment begins at the time  $t = t_1$ . From  $t_1$  on the upper geometry is stationary and the liquid has formed during the filament stretching phase a cylindrical filament between the plates. The diameter  $d(x, t)$  of this filament starts to shrink. The laser micrometer observes the change of the diameter of the middle of the filament  $d(0, t)$ . The experiment lasts until the filament breaks-up at  $t = t_2$ . The extensional rate and the elongational viscosity can be calculated with the measurement of  $d(0, t)$ .<sup>223,252</sup>  $\square$*

For the calculation of the extensional rate  $\dot{\epsilon}$ ,

$$\dot{\epsilon} = -\frac{2}{d(0, t)} \frac{Dd(0, t)}{Dt}, \quad (5.5)$$

the measured time-dependent diameter  $d(0, t)$  is fitted with an exponential function (see Anna et al.<sup>223,252</sup>) like

$$d(0, t) = \mathfrak{C}_1 - \mathfrak{C}_2 t + \mathfrak{C}_3 e^{-\mathfrak{C}_4 t}. \quad (5.6)$$

With eq. 5.6 the extensional rate of eq. 5.5 is given by

$$\dot{\epsilon} = \frac{2(\mathfrak{C}_2 + \mathfrak{C}_3 \mathfrak{C}_4 e^{-\mathfrak{C}_4 t})}{\mathfrak{C}_1 - \mathfrak{C}_2 t + \mathfrak{C}_3 e^{-\mathfrak{C}_4 t}}. \quad (5.7)$$

Eq. 5.7 can now be used in a material law to determine the extensional viscosity  $\eta_E$ . Several material laws (constitutive models<sup>49,253</sup>) exist which describe the behaviour of different materials. Examples for these constitutive models are the Newtonian model, the power law model or the upper convected Maxwell model.<sup>240</sup>

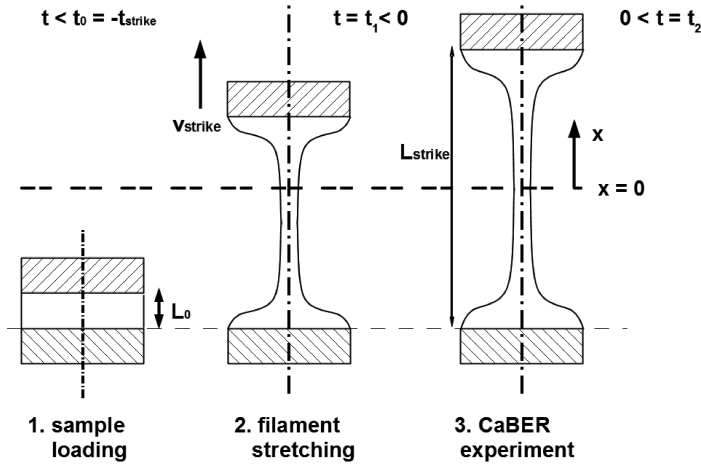


**Figure 5.1.** – The three steps of the CaBER experiment. (1) The sample loading phase: The sample liquid is brought between both plates (diameter  $D_0$ ) and the distance of both plates is  $L_0$ . This defines the initial sample volume  $V_0 = \pi \left(\frac{D_0}{2}\right)^2 L_0$ . (2) The filament stretching phase: Starting at  $t = t_0 := -t_{strike}$  and lasting until  $t = t_1 := 0$  the upper plate moves upward until it reaches the final height  $L_{strike}$ . (3) The CaBER experiment: This phase lasts until the filament breaks at  $t = t_2$ . Meanwhile, the diameter  $d(0, t)$  is measured at  $x = 0$ .

## 5.2 Theoretical Description of the CaBER Experiment

The flow which develops during the CaBER experiment (meaning for  $t > 0$  in accordance to fig. 5.1) can be quiet complex. Especially, if the fluid sample is of higher viscosity or has special properties, i.e. time-dependence of the viscosity. However, for a large amount of fluids the following named assumptions are reasonable:

### **Assumption 2. No-gravity**

*The influence of gravity on the filament can be neglected. This is a sufficient*

condition for viscose and unfilled fluids in a vertical set-up.\* □

**Assumption 3. Symmetry**

The filament shows two types of symmetry. First, the filament is symmetric to the  $r$ - $\varphi$ -plane<sup>†</sup> located in  $x = 0$ <sup>‡</sup>. By this  $A(+x, t) = A(-x, t)$  and so the first derivatives with respect to  $x$  have a local extremum at the point  $x = 0$ . This is expressed by  $\left. \frac{\partial(\dots)}{\partial x} \right|_{x=0} = 0$ . Second, the filament is rotational symmetric to the  $x$ -axis. By this, the flow is independent of  $\varphi$  and  $\frac{\partial(\dots)}{\partial \varphi} = 0$ . □

**Assumption 4. Slenderness**

The filament is slender. Geometrically this demands that  $l \gg d$ . □

**Assumption 5. Cylindrical**

The filament is strictly cylindrical. This leads to  $dA(x, t)/dx \ll 1$ . This allows the flow to be described by an one dimensional model which just depends on  $r(t)$ . □

**Assumption 6. No-inertia**

The inertial forces are negligible. This means that the shrinkage of the filament is slowly. This results in  $\ddot{x}_i \approx 0$ . □

**Assumption 7. Incompressibility**

The fluid is incompressible,  $\rho(t) = \text{const.}$  and the density is homogeneously distributed  $\rho(x) = \text{const.}$  □

With these assumptions the uniaxial extensional flow of the CaBER can be described with a set of equations obtained from the law of the conservation of mass and from the force balances of the filament. The derivation of these equations is shown in the next sections (chap. 5.2.1 and chap. 5.2.2).

## 5.2.1 Conservation of Mass and Volume

As all physical flows the uniaxial extensional flow of the CaBER experiment has to obey the law of conservation of mass, which is detailed illustrated in chap. G. With the rules for the material derivative (chap. H) and

\* Arnolds et al.<sup>244</sup> rotated the CaBER about 90° into a horizontal position in order to obtain a gravity induced bending of the filament. By applying bending theory they were able to calculate the axial force.

<sup>†</sup> A scheme of the whole problem is shown in fig. 5.3.

<sup>‡</sup> The coordinate system is directly located in the middle of the filament (see fig. 5.2).

the transformations shown in chap. G the general law for the conservation of mass can be transferred into an equation for the conservation of volume. In the case of the CaBER experiment this equation is further transformed into an equation for the time-dependent evolution of the cross-sectional area  $A(x, t)$ :

$$\frac{\partial A(x, t)}{\partial t} + u(x, t) \frac{\partial A(x, t)}{\partial x} + A(x, t) \frac{\partial u(x, t)}{\partial x} = 0. \quad (5.8)$$

In eq. 5.8 appears only the the cross-sectional area  $A(x, t)$  and the axial velocity  $u(x, t)$ . Thus, an expression for the elongational rate  $\dot{\epsilon}$  is found based on the conservation of mass and as commonly used in literature.<sup>244, 246, 252</sup> Furthermore, the filament is assumed to be symmetric to the  $r$ - $\varphi$ -plane at

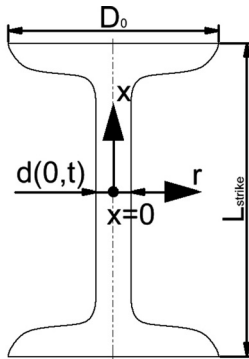


**Figure 5.2.** – Sketch of the filament during the CaBER experiment with all relevant physical parameters.

$x = 0$ . This requires that the derivative of  $A(x, t)$  in  $x$ -direction vanishes at the middle ( $x = 0$ ) of the filament, so

$$\frac{\partial A(0, t)}{\partial x} = 0. \quad (5.9)$$

This represents the local extremum of the function  $A(x, t)$ . Eq. 5.9 can be used in eq. 5.8 for a further simplification

$$\frac{\partial A(0, t)}{\partial t} + A(0, t) \frac{\partial u(x, t)}{\partial x} = 0. \quad (5.10)$$

The eq. 5.10 can be used to determine the extensional rate  $\dot{\epsilon} = \partial u / \partial x$  of the experiment by

$$\dot{\epsilon} = -\frac{\partial A(0, t) / \partial t}{A(0, t)}. \quad (5.11)$$

This equation is dependent on the radius  $r(t)$ , like

$$\dot{\epsilon}(t) = -\frac{2\dot{r}(t)}{r(t)}. \quad (5.12)$$

This equation contains simplifications as explained in detail in chap. I. The eq. 5.12 is compared to eq. I.11, which has the form  $\dot{\epsilon}_{new}(t) = -5\frac{\dot{r}(t)}{r(t)}$ .<sup>\*</sup> Eq. I.11 is the result of the considerations made in this thesis. In the next section (chap. 5.2.2) additionally to the work of McKinley et al.<sup>224</sup> or Klein<sup>246</sup>, a further version of the force balance is postulated. For this new force balance the elongational rate obtained from eq. I.11 is used. While for the older force balances the according elongational rate which is determined by eq. 5.12 is used.

## 5.2.2 The Force Balances of the Filament

In the beginning of this section (chap. 5.2) two types of symmetry have been postulated for the CaBER experiment. From those the rotational symmetry to the  $x$ -axis reduces the dimensionality of the problem from a 3-dimensional one to a 2-dimensional problem. The filament is by this just studied in the  $x$ - $r$ -plane.

Using the assumption of negligible inertial forces simplifies the problem from a dynamic problem with two second order differential equations to two simple force balances. These force balances are quasi static and contain the time-dependence only through the time-dependent variables as the axial force  $F(t)$  and the time-dependent cross-sectional area  $A(x, t)$ .

The force balances are stated once in  $x$ -direction on a plane parallel to the  $r$ - $\varphi$ -plane, shown in fig. 5.3a, and once in  $r$ -direction on a  $x$ - $r$ -plane (see fig. 5.3b).

From fig. 5.3a the force balance in  $x$ -direction is written in form of

$$\sigma_{11}A(x, t) - 2\sqrt{\pi A(x, t)}\Gamma = F(t). \quad (5.13)$$

<sup>\*</sup> The difference results in a factor of 5/2. However, this creates a significant change of the calculated values of the elongational viscosity (as seen in fig. 5.11).

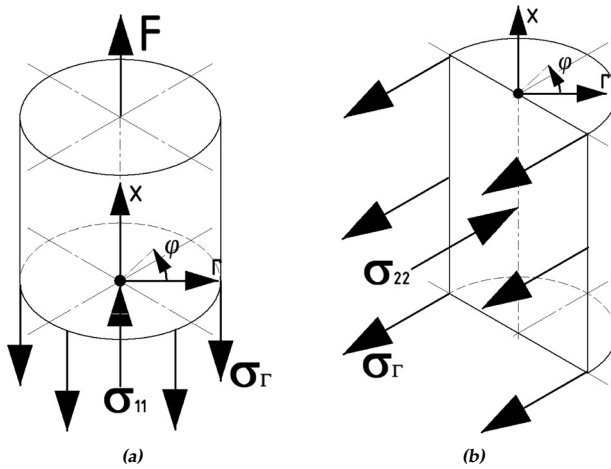


**Figure 5.3.** – Clearance cutting through the filament with the according forces. (a) cut through a plane parallel to the  $r$ - $\phi$ -plane and (b) cut through a  $x$ - $r$ -plane with arbitrary  $\phi$ .

Similar, a force balance in  $r$ -direction, shown in fig. 5.3b, can be obtained as

$$\sigma_{22}A(x, t) - \sqrt{\pi A(x, t)}\Gamma = 0. \quad (5.14)$$

Eq. 5.13 and eq. 5.14 are making use of the term for the surface tension\*  $\Gamma$  and the principal diagonal elements of the stress tensor  $\sigma_{ii}$ .<sup>†</sup> By subtracting eq. 5.14 from eq. 5.13 both equations can be merged to an expression for the first normal stress difference  $N_1 := \sigma_{11} - \sigma_{22}$ , as

$$N_1A(x, t) - \sqrt{\pi A(x, t)}\Gamma = F(t). \quad (5.15)$$

### 5.2.3 Material Laws

In the previous sections a set of two equations is obtained, which describes the flow in the CaBER experiment. By now, an expression for the extensional rate of the experiment as a function of  $A(x, t)$  is given by eq. 5.12 or

\* For further details on the surface tension see chap. J and chap. K.

† Details can be found in chap. 2.3.2 and chap. A.

eq. I.11 and an expression for the first normal stress difference as a function of  $A(x, t)$  and  $F(t)$ , as given by eq. 5.15. This leads to a determined problem with two equations and two variables. Solely, a detailed description of the material (the sample fluid) still has to enter these equations.

For this a constitutive equation/law\* has to be postulated in order to describe different classes of materials. For a uniaxial extensional flow with no memory the easiest and most used material law is that of a Newtonian fluid:

$$N_1 = \eta_{E,N}(\dot{\epsilon}) \dot{\epsilon}. \quad (5.16)$$

Eq. 5.16 is a relation between the first normal stress difference and the extensional rate via the extensional rate dependent extensional Newtonian viscosity  $\eta_{E,N}(\dot{\epsilon})$ . With this relation the eq. 5.15 is written as

$$\eta_{E,N}(\dot{\epsilon}) = \frac{F(t) + \Gamma \sqrt{\pi A(0, t)}}{A(0, t) \dot{\epsilon}(x, t)}. \quad (5.17)$$

Other models for non-Newtonian materials can be e.g.

- the Bingham fluid<sup>256</sup> or
- the power law (Ostwald-de Waele) fluid.<sup>257</sup>

For the Bingham fluid the material law is

$$\dot{\epsilon} = \begin{cases} 0 & \text{for } \sigma < \sigma_{yield}, \\ \frac{1}{\eta_{E,B}} (\sigma - \sigma_{yield}) & \text{for } \sigma > \sigma_{yield} \end{cases}. \quad (5.18)$$

The constitutive equation for the Bingham fluid describes the elongational strain rate with the extensional viscosity for a Bingham fluid  $\eta_{E,B}$  and the yield stress  $\sigma_{yield}$ . For a stress smaller than the yield stress the fluid shows no motion.

The formulation for the power law fluid is given by

$$N_1 = \eta_{E,PL} \dot{\epsilon}^{n_{PL}}. \quad (5.19)$$

The constitutive equation for the power law fluid describes the first normal stress difference with the extensional viscosity for a power law fluid<sup>†</sup>  $\eta_{E,PL}$

\* Constitutive laws are equations which describe for a certain class of materials the relationship of several physical properties of a material. Details found in textbooks as i.e. Truesdell<sup>254</sup> or Ogden.<sup>255</sup>

† Note that  $\eta_{E,PL}$  has the units of  $\text{Pa} \cdot \text{s}^{n_{PL}}$ .

and the flow index\*  $n_{pl}$ .

$$\eta_{E,Pl}(\dot{\epsilon}) = \frac{1}{\dot{\epsilon}(x,t)} n_{pl} \sqrt{\frac{F(t) + \Gamma \sqrt{\pi A(x,t)}}{A(x,t)}}. \quad (5.20)$$

## 5.3 Experimental Set-up of the CaBER

For measuring the axial force in a commercially available CaBER a special geometry has to be designed, which can be installed into the CaBER. In the next section (chap. 5.3.1) the commercial CaBER is introduced and explained. Subsequently, in section chap. 5.3.2 the newly designed set-up for measuring the axial forces is explained in detail. This section will contain a sketch of the data acquisition (DAQ) hardware and the DAQ-software.

### 5.3.1 Description of the CaBER Apparatus

The starting point of the work presented in this chapter (chap. 5) is a commercially available HAAKE CaBER 1 from Thermo Scientific. The scheme of the CaBER instrument is shown in fig. 5.4. The experimental core of the CaBER consists of two parallel plates. The upper plate can move upwards along the  $x$ -direction (see fig. 5.4 the white arrow) controlled by a linear stepper motor. The time  $t_{strike}^\dagger$  for the elevating motion of the upper geometry can be adjusted from 20 ms to several seconds for a final length of stretch of  $L_{end,max} = 20$  mm. Different stretch profiles are available, (e.g., linear and exponential, among others). The lower plate is positioned by a micrometer screw that allows defining the symmetric end distance  $L_{strike}$  of the two plates at the end of the filament stretching phase.

In the experiments, the linear stretching profile was used with strike times between 20 ms and 1000 ms. A linear stretching profile means a constant velocity for the movement of the upper geometry for the whole stretching process (shown in eq. 5.1 or eq. 5.2).

\* For  $0 < n_{pl} < 1$  the material behaviour is pseudo-plastic, for  $n_{pl} = 1$  the material behaviour is Newtonian and for  $n_{pl} > 1$  the material behaviour is dilatant.

† Also called strike time.

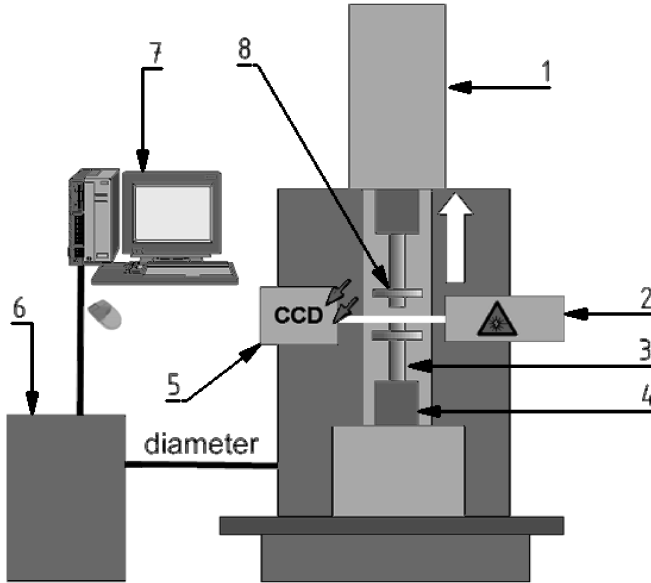


**Figure 5.4.** – Scheme of the commercial CaBER. The white arrow on the top of the CaBER indicates the direction of movement of the upper plate (8). The naming of the single parts: (1) Stepper motor, (2) LASER, (3) lower geometry, (4) micrometer screw, (5) optical sensor, (6) CaBER control unit, (7) PC, and (8) upper geometry.

### 5.3.2 Newly Designed Measurement Device for the Axial Forces in the CaBER

The commercial CaBER apparatus has been modified as illustrated in fig. 5.5. The major change of this set-up is the exchange of the lower plate by a new constructed shaft and plate (see fig. 5.7). The new shaft (fig. 5.7 part (2) and (3)) is hollow. Inside this shaft and at its top is the highly sensitive piezoelectric force sensor (fig. 5.7 part (6)) fixed in fig. 5.7 part (4). The cable of the force transducer exits the shaft at the bottom (see fig. 5.7 part (2)). The whole shaft is connected to the micrometer screw of the CaBER by (fig. 5.7 part (1)) the use of three stud screws (M3). The piezoelectric force sensor (type 9215) and the charge meter (type 5015) were purchased

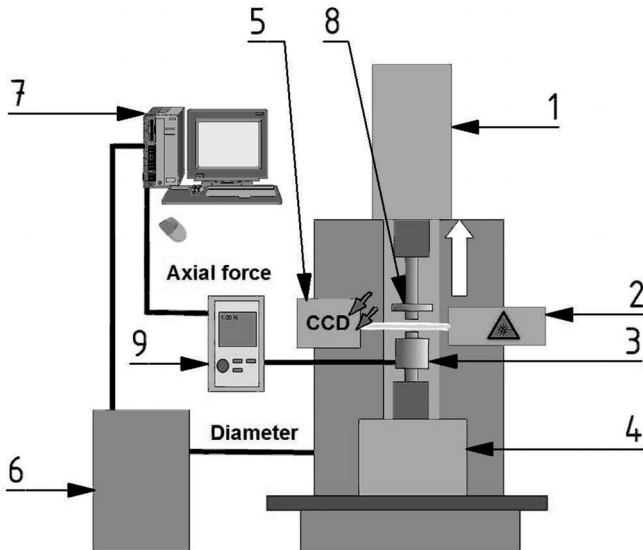


**Figure 5.5.** – Scheme of the CaBER with added axial force measurement. The naming of the single parts: (1) Stepper motor, (2) LASER, (3) lower geometry with piezoelectric force transducer, (4) micrometer screw, (5) optical sensor, (6) CaBER control unit, (7) PC, (8) upper geometry, and (9) charge amplifier.

from Kistler.

A PC controls the CaBER via a RS232 serial connection. The acquisition of the time-dependent diameter and the time-dependent force is integrated in the CaBER software.\* The DAQ-board used in the PC is a PCI 6024-E from National Instruments. The signals of the laser micrometer and the

\* The DAQ with the CaBER software is right now state of the art. It is part of the new commercially available supplement for the CaBER. However, at the beginning of this project, as documented by Klein et. al.,<sup>246</sup> the measurement of the time-dependent force was conducted with a second computer, equipped with a data acquisition (DAQ)-board (PCI-MIO-16XE-10 from National Instruments) and with a home-written LabVIEW DAQ-software.<sup>138,139</sup> The only disadvantage of this set-up was the lack of a temporal trigger between the start of the force measurement and the start and measurement of the CaBER experiment.



**Figure 5.6.** – The newly designed axial force measurement device for the CaBER with a sample loaded. The plates have a diameter of 6 mm. The lower plate geometry is directly screwed into the force transducer and fixed with a counter nut.

piezoelectric force transducer are measured simultaneously by the CaBER. The signal of the laser micrometer is directly send to the DAQ-board in the computer. Whereas, the signal transmitted by the piezoelectric force transducer, which is fixed at the lower plate, is first amplified by the charge meter (also called charge amplifier). Afterwards, the signal is transformed into a voltage  $U \in [-10, 10]$  V. This time-dependent electric-potential is transmitted to the computer and digitized via an DAQ-board. The maximum sampling rate of the PCI 6024-E ADC-board is 200 kHz with a 12-bit resolution.

Both DAQ softwares, the initial home-written one and the proceeding commercial one are using the oversampling principle, as used by Dusschoten<sup>138</sup> and Neidhöfer.<sup>139</sup> Typically about 20 time-dependent raw data points have been boxcar averaged in accordance to reduce the amount of data points which have to be stored on the hard disc and in accordance to increase the signal-to-noise ratio.

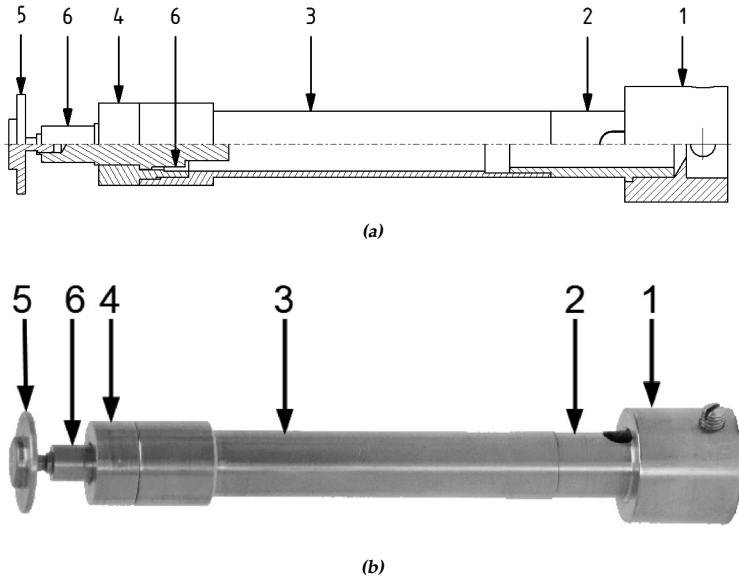


**Figure 5.7.** – Technical details of the newly designed measurement geometry for the axial force device for the CaBER with (1) adapter for the micrometer screw positioning system, (2) lower shaft part with slit opening for the cables, (3) upper shaft, (4) head of the shaft for installing the force transducer, (5) exchangeable geometry (e.g. diameter 6 mm), and (6) the piezoelectric force transducer. (a) technical drawing and (b) real geometry.

## 5.4 Calibration and Determination of the Force Sensitivity of the CaBER

The calibration of the commercially available piezoelectric transducer is already done by the manufacturing company Kistler. The transducer comes along with a calibration certificates. In order to verify the accuracy of those given values and to determine the sensitivity limits an in house calibration of the transducer was realized.<sup>246</sup> For the calibration the set-up was switched on for two hours to ensure that the electronics were warmed up to increase the electrical stability of the DAQ-devices (especially the charge meter). A calibration set of weights (10, 20, 100, 200, 500 g) was used for the calibration. For each weight an individual measurement was performed. In the beginning the weight was placed on top of the force sensor. Then the measurement was started. After several seconds of the measurement the weight was quickly and manually removed. The measured change in the electric potential is linearly correlated to the applied weight. A linear regression revealed the linear dependency of the force on the weight and a calibration factor close to the one written in the calibration certificate was obtained. The lower limit of the sensitivity was determined by measuring the unloaded signal of the sensor for a few seconds. The amplitude of the noise in the data represents the physical limits of the sensitivity of the measurement. A linear regression was done on the noisy data to account for the drift. This drift of the sensor was subtracted and afterwards the standard deviation was used to determine the limiting sensitivity of the set-up (see fig. 5.8) to be 0.05 mN with a time resolution of 0.2 ms. Forces can be measured in the range from  $5 \times 10^{-5}$  N to  $2 \times 10^2$  N. After oversampling the dynamic range exceeds six decades. The part containing the sensor is not moving, therefore the forces due to the acceleration are omitted. When the experiment is performed the weight from the samples is decreased and therefore the measured force is negative. The forces measured have negative values due to the fact that the sensor is at the lower geometry.

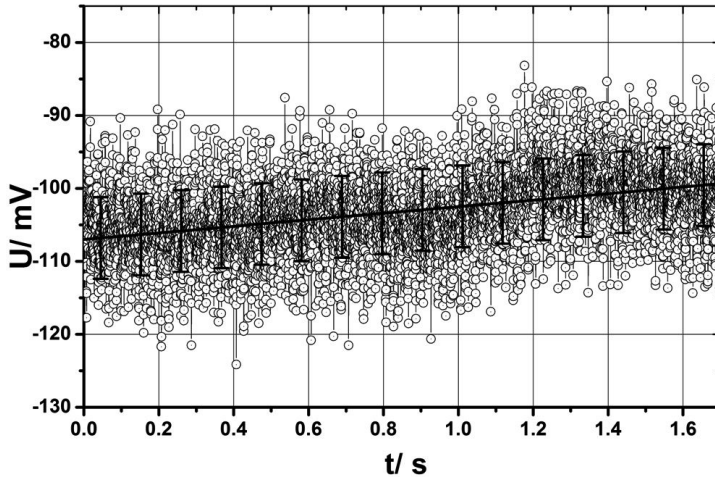


**Figure 5.8.** – Determination of the standard deviation of the calibration measurements for the piezoelectric force transducer installed in the CaBER. The symbols (circles) are indicating the measurement with the force transducer without load and by this they represent the noise. The black line indicates the linear regression of the data and the error bars are the standard deviation of the noisy data.

## 5.5 Measuring Axial Forces with the CaBER

In this chapter the results of different measurements and series of measurements performed on the CaBER are presented and discussed. The experiments were conducted under similar conditions. Typically, those included,

- a constant plate diameter of  $D_0 = 6$  mm,
- a defined and constant final length of  $L_{strike} = 10$  mm,
- an initial gap size of  $L_0 = 1$  mm and
- a similar environmental temperature of  $\vartheta_0 = 20^\circ\text{C}$ .

Only the strike time  $t_{strike}$  was varied. For the silicon oil and the PS-DOP sample (tab. 2.5) this was  $t_{strike} = [20, 40, 60, 80, 100, 300, 500]$  ms. For the wood glue samples was  $t_{strike} = [100, 500, 1000]$  ms. In order to study the curing behaviour of the glues, each glue sample was additionally measured at least at three different curing times. This means the sample was placed on the plate in the initial gap and left there until the curing time has passed. Then the experiment was started.

Each experiment was done at least three times for each strike time and curing time.

### 5.5.1 Comparing the Diameter-based Analysis with the New Axial Force-based Analysis

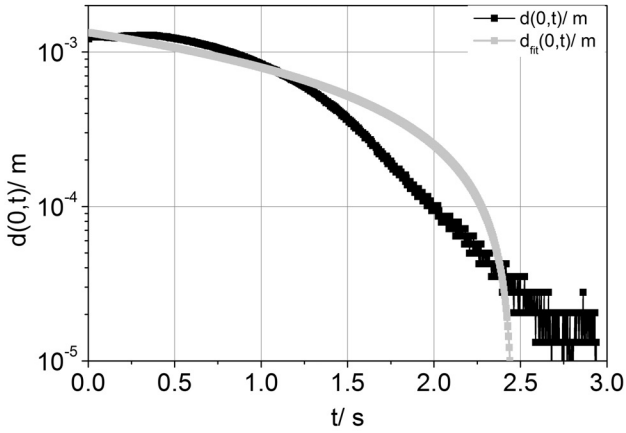
The CaBER instrument is meant to determine the elongational viscosity  $\eta_E$  of a liquid by means of the measurement of the time-dependent diameter  $d(0, t)$  of a thin filament. In this section, the results of the CaBER experiment on a PS-DOP sample and a silicon oil sample are shown and discussed. The focus lies on the comparison between the results obtained by solely measuring the time-dependent diameter  $d(0, t)$  and the results from simultaneously measuring the time-dependent axial force  $F(t)$  and the time-dependent diameter.

Fig. 5.9 shows two examples of the time-dependent diameter as measured with the CaBER for the PS-DOP sample (see tab. 2.5). The experiments were conducted under similar conditions, but with different strike times. Both sets of data are influenced by physical noise\* and digital noise†. Whereas, the diameter of the filament is still large‡ the data is mainly effected by physical noise. When reaching smaller diameters, the signal is obviously affected by the limited resolution of the optical sensor of the CaBER. This results in a visible quantization of the data and by this leading to digital noise (see the visible steps in the plots of fig. 5.9). The presence of noise in the data causes problems in calculating the first derivative of the time-dependent diameter. However, this is needed for the determina-

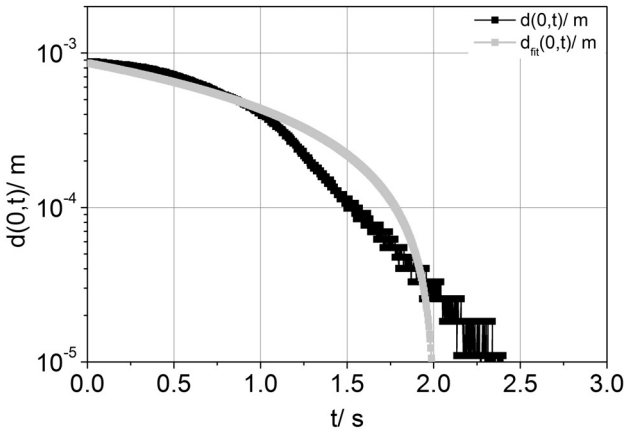
\* The term physical noise means in this context noise which is caused by other reasons than the digitalization.

† The term digital noise refers to noise caused by insufficient quantization of the data during the digitalization.

‡ This means in this case  $d(0, t) > 10^{-4}$  m.



(a)



(b)

**Figure 5.9.** – The time-dependent diameter of the CaBER experiment for the PS-DOP sample (tab. 2.5) at different strike times. The experiments were performed at room temperature  $\vartheta_0 = 20$  °C, an initial gap of 1 mm, a final gap size of 10 mm and a strike time of (a)  $t_{strike} = 0.02$  s and (b)  $t_{strike} = 0.5$  s. The black symbols indicate the measurements and the grey symbols indicate the results of the diameter fit function.

tion of the elongation rate  $\dot{\epsilon}(t)$  in eq. 5.12. Mathematically, the presence of a significant noise level on a signal causes the derivative of the signal to include large values which will largely fluctuate. To avoid these fluctuations the data has either to be adequately smoothed or described by an continuous function.

The presented results of the time-dependent diameter were empirically described by an analytical function as given by Anna and McKinley.<sup>223</sup> The data was fitted with an exponential function of the type:

$$d_{fit}(t) = \mathfrak{C}_1 - \mathfrak{C}_2 \cdot t + \mathfrak{C}_3 e^{-t \cdot \mathfrak{C}_4}. \quad (5.21)$$

The fit function can easily be numerically or analytically\* differentiated and thus be used for the calculation of the elongational rate, as i.e. shown in fig. 5.10b. With the time-dependent diameter, the elongational rate and the constant value for the surface tension of the liquid, the elongational viscosity derived from eq. 5.14 could be determined. The elongational viscosity is in a similar way derived by the software of the CaBER itself, because the software does not include the axial force. The elongational viscosity  $\eta_{E,2}^\dagger$  was derived under the assumption that  $\sigma_{11} = 0$ . The validation of this assumption is presented at the end of this section.

The measured time-dependent diameter as well as the signal of the measured axial force includes noise. Thus, it is fitted with an exponential decay function as:

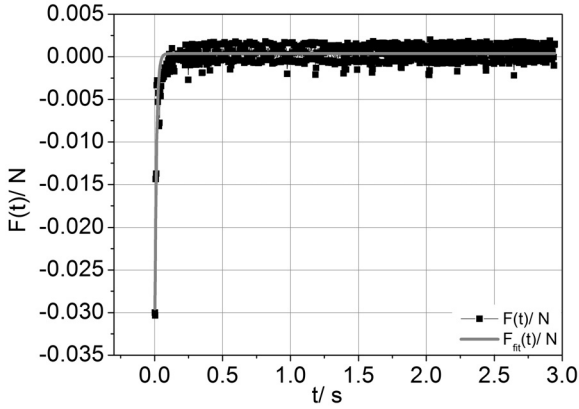
$$F_{fit}(t) = \mathfrak{C}_1 + \mathfrak{C}_2 e^{-(t-\mathfrak{C}_3)/\mathfrak{C}_4}. \quad (5.23)$$

The fit function obtained for the axial force is of acceptable coincidence with the data and can thus be used for the determination of the elongational viscosity according to eq. 5.13. Examples of the calculated functions of the elongational viscosity  $\eta_{E,1}$  and  $\eta_{E,2}$  are shown for different strike times  $t_{strike}$  in fig. 5.11. All plots of fig. 5.11 show two similar features. The first feature is that  $\eta_{E,2}$  is nearly constant in the range of  $0 \leq t \leq 1$  s and

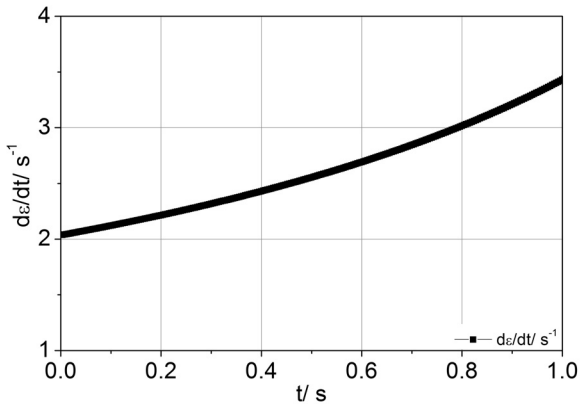
\* Time-derivative of  $d_{fit}(t)$ :

$$\dot{d}_{fit}(0, t) = -\mathfrak{C}_2 - \mathfrak{C}_3 \cdot \mathfrak{C}_4 e^{-t \cdot \mathfrak{C}_4}. \quad (5.22)$$

† The number in the index indicates not a tensorial origin but that this viscosity was obtained by using the second equation of force balance (in  $r$ -direction). The  $x$ -direction is defined as indexed by the number 1.



(a)



(b)

**Figure 5.10.** – The time-dependent force and the calculated elongation rate  $\dot{\varepsilon} = d\varepsilon/dt$  of the CaBER experiment for the PS-DOP sample. The experiments were performed at room temperature  $\vartheta_0 = 20\text{ }^\circ\text{C}$ , an initial gap of 1 mm, a final gap size of 10 mm and strike time of  $t_{strike} = 0.02\text{ s}$ . (a) the time-dependent force measured with the newly installed high sensitive piezoelectric pressure transducer. The black symbols indicate the measurement and the grey line indicates the results of the force fit function. (b) the elongation rate calculated from the fitted diameter is shown in fig. 5.9a.

is always smaller than  $\eta_{E,1}$ . The second obvious observation is, that for strike times  $t_{strike} < 0.5$  s  $\eta_{E,1}$  is not as constant as  $\eta_{E,2}$ . It starts at small values and strongly increases (this region will be further called increasing region) until it enters a region where it reaches a slow increase (this region will be further called final region). The behaviour of  $\eta_{E,1}$  for both regions can be explained as it follows.

**Increasing region:** After the sample has been stretched in the filament stretching phase it is not yet at the stable initial conditions. Furthermore, the shrinking of the filament which is driven by the capillary forces is superposed by a post stretching flow.

**Final region:** The elongational flow entered stable flow conditions and by this reaches approximately a constant value. The superimposed slow increase is caused by the linear drift of the piezoelectric transducers.

These explanations are also supported by the observations made in fig. 5.11d. For experiments with at least this strike time the increasing region is missing. This is caused by the much longer strike time, which allows the flowing sample to reach the stable initial conditions for the CaBER experiment already at  $t = 0$  s.

The mean value  $\bar{\eta}_{E,1}$  and the standard deviation  $\sigma_{std,E,1}$  has been calculated for the final region  $\eta_{E,1}$ . The same was done for  $\eta_{E,2}$  and thus  $\bar{\eta}_{E,2}$  and  $\sigma_{std,E,2}$  were gained. In order to obtain statistic values each CaBER experiment was performed for each strike time at least three times. The results for the  $\bar{\eta}_{E,i}$  and  $\sigma_{std,E,i}$  (for  $i = [1, 2]$  and  $i \in \mathbb{N}$ ) were averaged to obtain an average mean elongational viscosity  $\bar{\sigma}_{std,E,i}$  and an average standard deviation of the elongational viscosity  $\bar{\sigma}_{std,E,i}$ . The averaged properties are summarized in tab. 5.1 and graphically shown in fig. 5.12. When the results of  $\eta_{E,i,mean}$  are compared with the expected values obtained via the by Trouton<sup>258</sup> found relationship (between shear viscosity  $\eta_S$  and elongational viscosity)

$$\eta_E = 3\eta_S, \quad (5.24)$$

it is obvious that  $\eta_{E,2,mean}$  is always at least by a factor of 2 smaller than the expected value of  $\eta_{E,theor.} = 255$  Pas.\* While, for very small strike

\* This value can be found in the work of Hilliou<sup>66</sup> or Klein.<sup>246</sup>

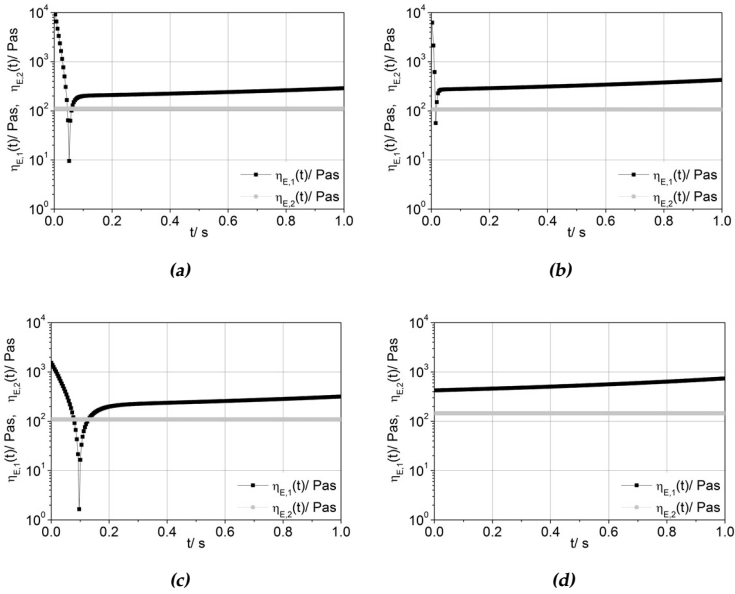


**Figure 5.11.** – The time-dependent elongational viscosity  $\eta_{E,1}$  and  $\eta_{E,2}$  of the CaBER experiment for the PS-DOP sample at different strike times. The experiments were performed at room temperature  $\vartheta_0 = 20$  °C, an initial gap of 1 mm, a final gap size of 10 mm and strike time of (a)  $t_{strike} = 0.02$  s, (b)  $t_{strike} = 0.06$  s, (c)  $t_{strike} = 0.1$  s, and (d)  $t_{strike} = 0.5$  s. The black symbols indicate the time-dependent elongational viscosity  $\eta_{E,1}$  which is calculated under respect of the axial force term (see eq. 5.13) and the grey symbols indicate the results of the time-dependent elongational viscosity  $\eta_{E,2}$  which is calculated only using the capillary force term (see eq. 5.14).

times  $\eta_{E,1,mean}$  is directly in the range of the expected value. However, for increasing values of  $t_{strike}$  the elongational viscosity  $\eta_{E,i,mean}$  overestimates the elongational viscosity  $\eta_{E,theor.}$  by a factor of nearly 1.9.

**Table 5.1.** – Comparison of the average mean values and the standard deviation of the elongational viscosities (shown in fig. 5.11) of the CaBER experiments for the PS-DOP sample. The statistics (standard deviation of the elongational viscosity  $\bar{\sigma}_{std,E,i}$ ) take at least three original mean values of the elongational viscosities into account.

$t_{strike}$ ms	$\eta_{E,1,mean}$ Pas	$\bar{\sigma}_{std,E,2}$ Pas	$\eta_{E,2,mean}$ Pas	$\bar{\sigma}_{std,E,2}$ Pas
20	265.2	27.6	105.4	$\sim 10^{-7}$
40	350.7	53.1	103.3	$\sim 10^{-7}$
60	326.4	43.7	105.6	$\sim 10^{-7}$
100	301.5	43.5	106.9	$\sim 10^{-7}$
500	464.6	95.6	140.4	$\sim 10^{-7}$

As a final point of this study of the PS-DOP sample with the help of the axial force measurement, the first normal stress is directly calculated from the CaBER experiment and approximated for the filament stretching phase. For the CaBER experiment the calculation of the first normal stress  $\sigma_{11}(t)$  is simple because both the cross-section of the filament and the axial force are known. An example of  $\sigma_{11}$  calculated is given in fig. 5.13 for  $t \geq 0$  s. In the filament stretching phase the smallest cross-section of the filament\* is unknown. In order to obtain an approximated value for the stress in the material the diameter in the middle of the filament is assumed to stay approximately constant during the filament stretching phase and by this can be approximated by the first diameter measured in the CaBER experiment  $d(0,0)$ . The results of this are added to fig. 5.13 at  $t < 0$  s. As expected the stress is during the stretching of the filament much larger than in the CaBER experiment, but during the CaBER experiment the first normal stress is still not negligible.

\* It is assumed due to symmetry reasons that the smallest diameter is in the middle of the filament.

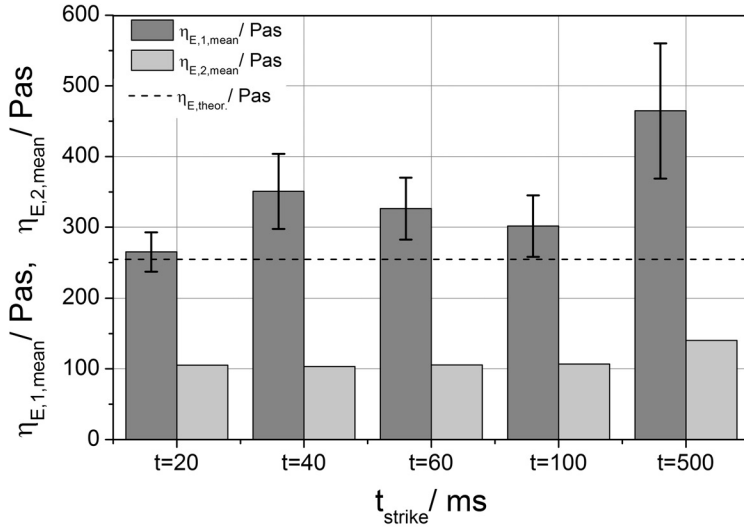
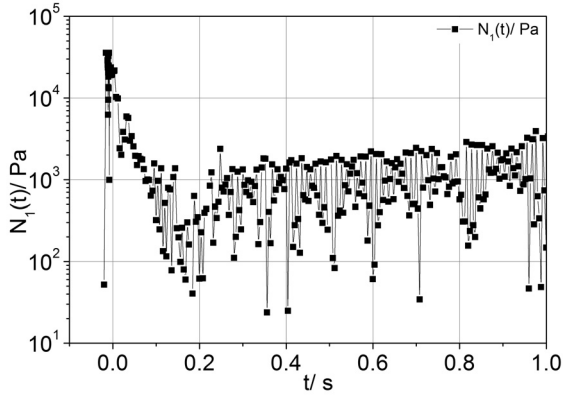
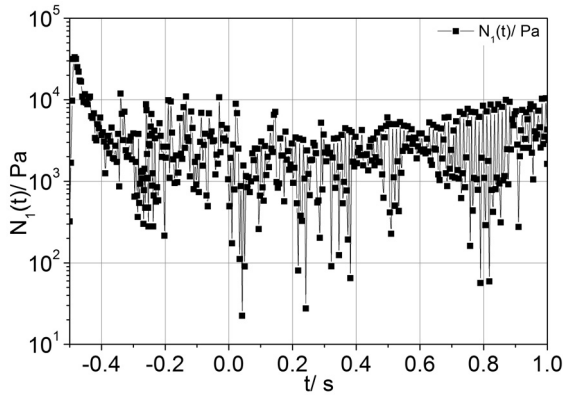


**Figure 5.12.** – Comparison of the average mean value of the elongational viscosities of the CaBER experiment for the PS-DOP sample plotted against the strike times  $t_{\text{strike}}$ . The experiments were performed at room temperature  $\vartheta_0 = 20^\circ\text{C}$ , an initial gap of 1 mm, a final gap size of 10 mm.



(a)



(b)

**Figure 5.13.** – The time-dependent stress of the CaBER experiment is plotted for the PS-DOP sample (tab. 2.5) at two different strike times. The experiments were performed at room temperature  $\vartheta_0 = 20^\circ\text{C}$ , an initial gap of 1 mm, and a final gap size of 10 mm and a strike time of (a)  $t_{\text{strike}} = 0.02$  s and (b)  $t_{\text{strike}} = 0.5$  s. The values at negative times  $t < 0$  are calculated with the measured axial force and the assumption that the smallest diameter of the filament during the filament stretching phase can be approximated via the measured diameter  $d(0,0)$  for  $t = 0$  s. The values for  $t \geq 0$  s are calculated by using both the measured force and the measured diameter of the filament.

## 5.5.2 Results of the PDMS

Chap. 5.5.1 has shown that the elongational viscosity of a polymer solution can be determined with the new axial force measurement by using the improved theory. However, the application of this set-up and theory on arbitrary samples seems not possible. As an example, the calculation of the elongational viscosity of the PDMS samples (silicon oils, tab. 2.5) was not possible. The measurement of the axial force is shown in fig. 5.14a and the according measurement of the diameter is shown in fig. 5.14b. The maximum absolute force is at least ten times larger than those values obtained for the polymer solution (i.e. PS-DOP). Nevertheless, the force decreases very fast. It reaches zero nearly in the strike time, so before the CaBER experiment starts. Caused by the much stronger initial forces the digital resolution of the data acquisition (DAQ) system is reduced (an example is given below). Therefore, it is not possible to calculate trustworthy values of the elongational viscosity from the axial force measurement for this sample. This is caused by

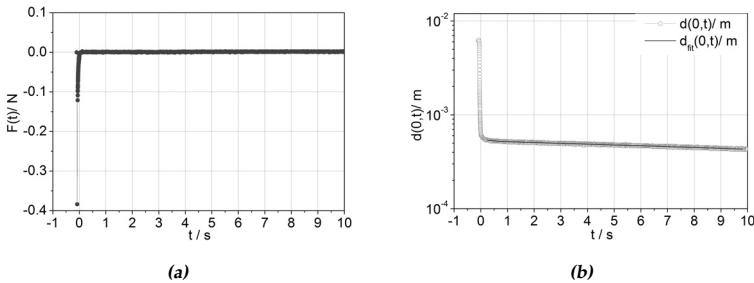


**Figure 5.14.** – (a) the time-dependent force and (b) the time-dependent diameter of the CaBER experiment for the PDMS sample at a strike time of  $t_{strike} = 0.1$  s. The experiments were performed at room temperature  $\vartheta_0 = 20$  °C, an initial gap of 1 mm, a final gap size of 10 mm. (b) the grey symbols indicate the measurements and the black line indicates the results of the diameter fit function.

1. the low quantization of the signal which is caused by the strong force the PDMS builds up directly when drawn apart and

2. the low quantization of the ADC used with the CaBER (12bit).

These reasons affect the measurement in the following way: The signal transmitted from the piezoelectric transducer to the charge amplifier has to be adjusted to a certain signal range in order to be correctly transformed into a voltage which is usable for the ADC board. Thus, the initial signal is always mapped into the same range of output (e.g.  $\pm 10$  V). This amplified output is then digitized by the ADC board. For this operation the predefined range of output is mapped onto a given set of possible values.\* The following examples illustrates this.

**Example 18. DAQ with charge amplifier and ADC board**

*Two time-dependent signals  $s_A(t)$  and  $s_B(t)$  are measured. The signal  $s_A(t) \in \mathbb{M}$  with  $\mathbb{M} = \{x \mid x \in \mathbb{R} \text{ and } 0 \leq x \leq 10\}$ .  $s_B(t)$  reaches values twice as large as those of the signal  $s_A(t)$ . Thus,  $\max s_B(t) = 2 \cdot \max s_A(t)$ . Therefore, signal  $s_B(t) \in \mathbb{N}$  with  $\mathbb{N} = \{x \mid x \in \mathbb{R} \text{ and } 0 \leq x \leq 20\}$ . These signals are amplified with a charge meter. This instrument has to be set for a pre-set range  $\mathbb{L}$  of the expected input values, e.g.  $\mathbb{L} = \{x \mid x \in \mathbb{R} \text{ and } 0 \leq x \leq 50\}$ . Subsequently, the input values are mapped into a standard range of signal  $\mathbb{V}$  which can be interpreted by the ADC board, e.g.  $\mathbb{V} = [-10; +10]$  V or  $\mathbb{V} = [-5; +5]$  V. Therefore,  $\mathbb{V}$  can be digitized by the ADC-board. This process maps the analogue signal  $\mathbb{V}$  into a discrete set of  $n$  points. The size of  $n$  is given by the ADC board and is generally constant.*

*If  $n = 100$  the resolution of this DAQ system would be  $\Delta s = \max \mathbb{L} / n$ , i.e.  $\Delta s = 0.5$ . This is independent of the range of  $s_A(t)$  and  $s_B(t)$ . If it were possible to dynamically adjust the range of  $\mathbb{L}$  to the range of the signal  $\mathbb{M}$  or  $\mathbb{N}$ , the resolution of the system would be increased, e.g.  $\Delta s_A = 0.1$  for  $s_A(t)$  and  $\Delta s_B = 0.2$  for  $s_B(t)$ .  $\square$*

### 5.5.2.1 Conclusions for Application of the Measurement of the Axial Force in the CaBER Experiment

Concluding the observations for the investigated PS-DOP sample, it can be stated that at least for small strike times the axial force and by this the first normal stress  $\sigma_{11}(t)$  is not negligible in the CaBER flow. By this thesis the usually used force balance equations for the CaBER experiment are extended by an axial force term and include an elongation in the axial direc-

\* Defined as the resolution of the ADC board.

tion. The calculated elongational viscosity is much closer to the value predicted by the theory. In this work, the applied force measurement reached its limits in terms of sensitivity and dynamical range. Additionally to the PS-DOP sample, several silicon oil samples (tab. 2.5) were studied. The PDMS samples are Newtonian fluids and show a formation of a stable filament. For those samples the sensitivity of the force measurement was not high enough to apply the stated equations for the elongational viscosity. For further investigations to determine the elongational viscosity with the CaBER, it is recommended to check whether there are more sensitive force transducers available.

### 5.5.3 The Curing Behaviour of Commercial Glue Studied in the CaBER with the Normal Force Measurement

With the newly added measurement of the axial forces at the CaBER, it is possible to determine the adhesive energy of glue or similar materials. This is close related to the term tack\*, see e.g. Zosel.<sup>247-251</sup> For measuring the tack of a material a commercial apparatus exists the TA.XTplus from the company stable micro systems. This instrument has the possibility to measure tack with different force transducers. The sensitivity of the force detection is about  $10^{-3}$  N. Whereas, the largest measurable forces are about 500 N (with the largest force transducer). The force measurement which has been presented in this work has a sensitivity of about  $5 \cdot 10^{-5}$  N, a time resolution of  $10^{-3}$  s and a maximum force of 200 N.

#### 5.5.3.1 The Adhesive Energy, Separation Energy and Tack

Adhesive materials are well spread in our daily life starting from simple glues and glue-sticks over to Post-it's, stickers or Scotch tape. All these materials show a different adhesive behaviour in accordance to their use. Some need a strong adhesion like stickers, which are meant to stay for longer time at one place. Others have weaker adhesion like Post-it's, which

---

\* Zosel (1985):<sup>247</sup> "The adhesive failure energy of adhesive joints formed with low contact pressure during a short contact time is called "tack"."

are meant to be easily attached to a surface but also easily removed from the surface.

To classify the stickiness of those materials the adhesive failure energy or the strength of the adhesive joint is used. For testing the adhesive failure energy, an adhesive material is brought into contact with a surface. After applying a certain force for a certain time the adhesive material is separated from the surface. For this process, a certain energy is needed, which defines the adhesive failure energy, the strength of the adhesive joint or the work of detachment. The physical definition of the work of detachment per unit area  $W_{adh}$  is formulated by Zosel<sup>247</sup> as:

**Definition 10. Work of detachment**

$W_{adh}$  is the integral over the detachment time  $T_{deta}$  of the product of the force  $F(t)$  and the separation rate  $v(t) = \frac{dy}{dt}$ .

$$W_{adh} := \frac{1}{A} \int_{T_{deta}} F(t) \cdot v(t) dt. \quad (5.25)$$

$W_{adh}$  is normalized to the surface area  $A$  and depends on the contact time  $t_{contact}^*$ . The separation rate  $v(t)$ , can be a function of the separation time  $t$ , depending on the experimental conditions (similar to eq. 5.1 and eq. 5.2).  $\square$

If the experiments are performed as follows the adhesive failure energy  $W_{adh}$  is related to the tack index<sup>†</sup> of adhesive materials.

For measuring the tack of a material a sample of the adhesive material is brought onto a small plate geometry (i.e.  $d = 6$  mm). Then this plate is pressed with a constant contact force  $F_{contact}$  against a similar plate without sample material for a certain contact time  $t_{contact}$ . Afterwards both plates are separated with the rate<sup>‡</sup>  $v$  and the time-dependent force  $F(t)$  is measured. With eq. 5.25 the adhesive failure energy  $W_{adh}$  is determined.

This experiment can similarly be conducted with the within this thesis modified\* CaBER; except that it is not possible to apply a defined con-

\* The contact time is not included in eq. 5.25, but is an important parameter of the experiments.

† As defined in the standard: ASTM D(1978)-61T.

‡ In the case of the CaBER set-up the separation rate is given by

$$v = \frac{L_{strike}}{t_{strike}}. \quad (5.26)$$

\* With integrated measurements of the axial force as described in chap. 5.3.2.

tact force on the lower plate before the separation.<sup>†</sup> For this reason not the tack values will be studied in this work but the newly introduced quantity called the separation energy.

**Definition 11. Separation energy**

Similar to the adhesive failure energy  $W_{adh}$  of an adhesive material the separation energy  $W_{sep}(t)$  of a sticky liquid is defined as the time-dependent integral of the time-dependent force  $F(t)$  and the separation rate  $v$  per unit area  $A$ , so

$$W_{sep}(t) := \frac{1}{A} \int_{t_0}^t F(\hat{t}) \cdot v(\hat{t}) d\hat{t}. \quad (5.27)$$

$W_{sep}(t)$  does not depend on the contact force, because the samples are assumed to be liquid and thus can not be set under a initial force. Additionally,  $W_{sep}(t)$  is influenced by additional forces due to fluid flow during the filament stretching of the liquid. □

The separation energy depends on the same parameters and variables as the adhesive failure energy except for the dependence on the contact force.

### 5.5.3.2 Separation Energy of Different Glues

With the measurement of the axial force it is now possible to determine the separation energy as a new physical property of the sample system.

Two different wood glues were studied in the experiments of this thesis. One called Ponal-Classic glue from Henkel and the Ponal-Express glue from Henkel. The intention of the experiments is to study the separation energy  $W_{sep}$  of the samples as a function of the curing time  $t_{cure}$ . For this the glue sample is brought between the CaBER geometries and kept there for the times listed in tab. 5.2. Then the CaBER experiment was executed with the measurement of the time-dependent diameter and the measurement of the time-dependent axial force. With this the separation energy  $W_{sep}(t_{cure})$  as a function of curing time could be identified. The results of the experiments of the Ponal-Classic samples, conducted with the parameters given in tab. 5.2, show in general reproducibility in both time-dependent diameter and the time-dependent axial force, see fig. 5.15.

<sup>†</sup> This is a solvable software problem.

**Table 5.2.** – Experimental conditions for the determination of  $W_{sep}(t_{cure})$  for the Ponal-Classic and the Ponal-Express.

Sample	$t_{cure}$	$L_{strike}$	$t_{strike}$
Ponal-Classic	0 min, 2 min,	10 mm	100 s,
	5 min		1000 s
Ponal-Express	0 min, 1 min,	10 mm	100 s,
	2 min, (4 min)		1000 s

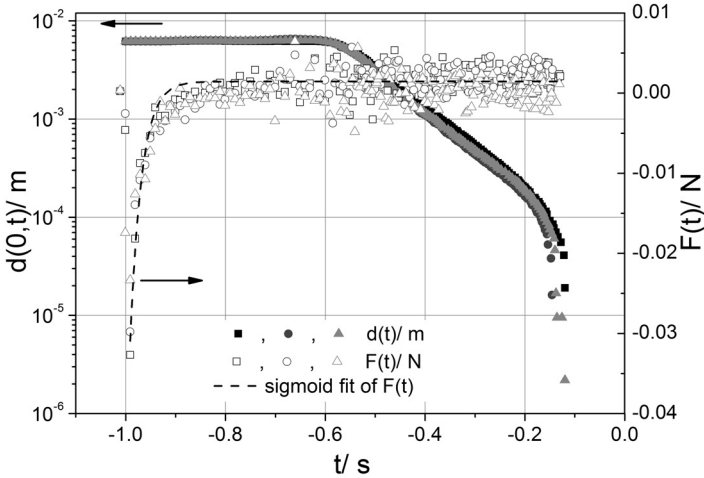


**Figure 5.15.** – Reproducibility of the measurement of the time-dependent force<sup>†</sup> and the time-dependent diameter on the CaBER for the Ponal-Classic at room temperature  $\vartheta = 20$  °C. The strike time was set to be  $t_{strike} = 1$  s and the final gap size was set to be  $L_{strike} = 10$  mm. The measurements were started directly after the sample was filled ( $t_{cure} = 0$  min), so no curing of the Ponal-Classic took place. The closed symbols are representing the time-dependent diameter, while the open symbols are indicating the time-dependent force. The fit parameters are  $\mathcal{C}_3 = 43.5$  and  $\mathcal{C}_4 = -1.19$ ;  $r_{COD}^2 = 0.83$ .

It is obvious in fig. 5.15 that the filament of the Ponal-Classic breaks before the actual CaBER experiment starts. Due to this the normal analysis of the CaBER experiment is not accessible for this sample. Furthermore, fig. 5.15 shows that a significant axial force is already measured during the filament stretching phase and the largest values are reached in this phase. This observation justifies the calculation of the separation energy from the axial force data. For the data of fig. 5.15 the time-dependent separation energy is shown in fig. 5.16. In this figure the absolute value of the time-dependent force is plotted. The separation energy shows good reproducibility in their maximum value (here about  $380 \text{ Jm}^{-2}$ ). The whole integral shape of the time-dependent separation energy shows no good reproducibility for times past the maximum. This is caused by the stability properties of the piezoelectric transducers. As long as a strong signal\* is measured and this for short times the signal of the piezoelectric transducer can be safely assumed to be free of system own error (i.e. drift of the transducer signal or loss of charges). As the measurement times gets larger and/or the signal gets into the range of the noise, the signal is strongly affected by errors due to the physical properties of the transducers.

Fig. 5.15 and fig. 5.16 showed that the separation energy and the axial force itself can be used to describe the change of the mechanical properties during the stretching phase of the liquid Ponal-Classic. The next step is to apply this method to the cured samples, with the curing parameters stated in tab. 5.2. The results of the measurements for a fast filament stretch are given in fig. 5.17a and the results of the slow filament stretch of the Ponal-Classic are plotted in fig. 5.17b. Both figures yield to the observation that the separation energy increases with curing time. It can be estimated that with curing times of about 4 minutes the separation energy already increases by three decades.

Similar to the Ponal-Classic sample also the Ponal-Express was first

† Additionally, the absolute force is fitted with a sigmoid function of the type

$$F(t) = \frac{\mathcal{C}_1 - \mathcal{C}_2}{(1 + e^{\mathcal{C}_3(t - \mathcal{C}_4)})}. \quad (5.28)$$

$\mathcal{C}_1$  and  $\mathcal{C}_2$  are the asymptotes of  $F(t)$  which can be neglected (the lower does not exist and the upper should be 0).  $\mathcal{C}_3$  indicates a growth rate and  $\mathcal{C}_4$  represents the maximum growth.

\* The signal has to be much large than the noise level.

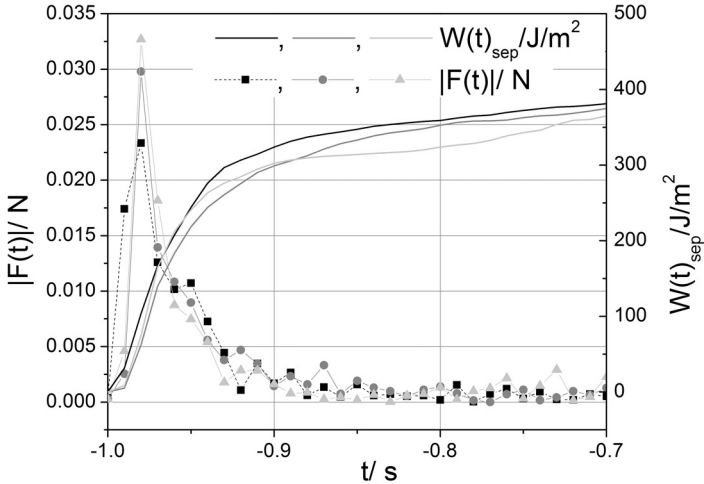
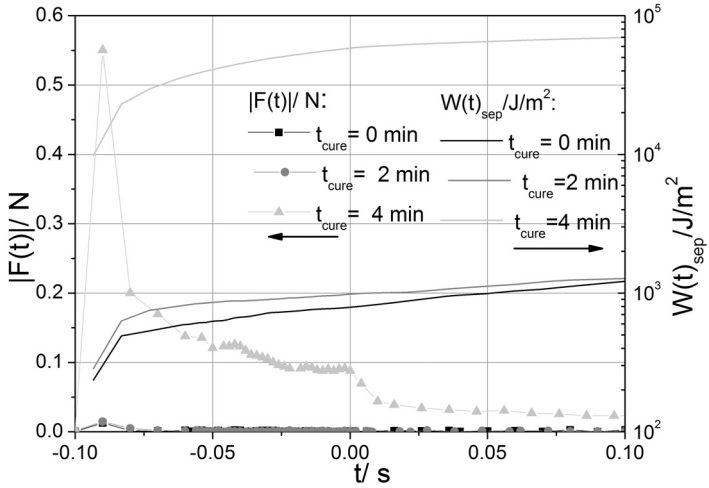


**Figure 5.16.** – Reproducibility and comparison of the absolute time-dependent force and the time-dependent separation energy of the measurements shown in fig. 5.15. (Ponal-Classic sample)

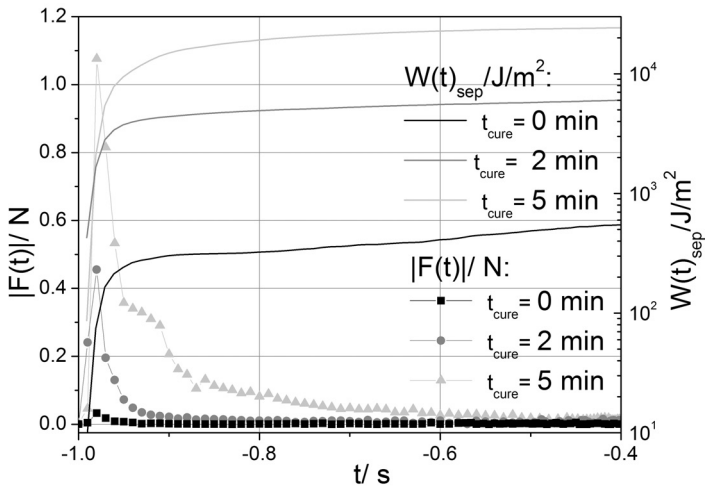
checked for its reproducibility properties in the experiment. Fig. 5.18 shows the results of the time-dependent force and the time-dependent diameter for different runs of the not cured Ponal-Express under the same experimental parameters. The results are reproducible, but especially the time-dependent diameter shows slightly larger deviations for each experimental run. This might be caused by the much faster curing behaviour of the Ponal-Express which leads to a stronger influence of small changes in the sample loading time. The time-dependent axial force has a mean value of  $\bar{F} = 0.044$  N and a standard deviation of  $\sigma_{std} = 0.018$  N for the three curves in fig. 5.18. In comparison to the Ponal-Classic, the Ponal-Express shows a longer stability of the filament which breaks-up during the CaBER experimental phase. Whereas, the filament of the Ponal-Classic breaks-up during the filament stretching phase. This means that the CaBER experiment could be conducted with the Ponal-Express sample.\*

The separation energy calculated from the data shown in fig. 5.18 shows

\* The results of the CaBER experiment of the Ponal-Express are not shown, because there are no corresponding results for the Ponal-Classic.



(a)



(b)

**Figure 5.17.** – Influence of the curing time (0 min, 2 min and 4 min or 5 min) on the values of the separation energy and the maximum force for the Ponal-Clastic, at room temperature  $\vartheta = 20$  °C and a final gap size of 10 mm. The strike time was set to be (a) 0.1 s and (b) 1 s.

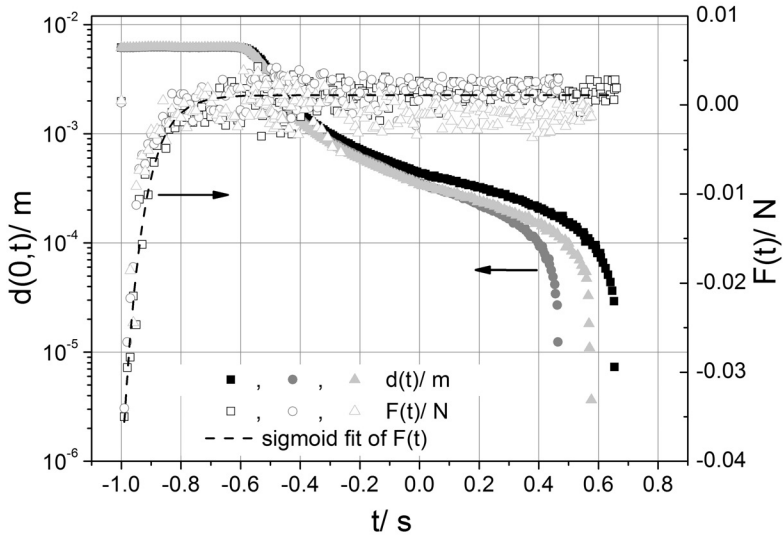


**Figure 5.18.** – Reproducibility of the measurements of the time-dependent force and the time-dependent diameter on the CaBER for the Ponal-Express at room temperature  $\vartheta = 20^\circ\text{C}$ . The strike time was set to be  $t_{strike} = 1\text{ s}$  and the final gap size was set to be  $L_{strike} = 10\text{ mm}$ . The measurements were started directly after the sample was filled ( $t_{cure} = 0\text{ min}$ ), so no curing of the Ponal-Express took place. The closed symbols are representing the time-dependent diameter, while the open symbols are indicating the time-dependent force. The fit parameters (see eq. 5.28) are  $\mathcal{C}_3 = 15.4$  and  $\mathcal{C}_4 = -1.46$ ;  $r_{COD}^2 = 0.91$ .

a good reproducibility for each run (see fig. 5.19). Also the integral shape stays much more similar between the different runs than the Ponal-Classic sample. This might be caused by a stabilizing effect of the faster curing kinetic of the Ponal-Express. During the curing of the Ponal-Express the liquid strongly increases its mechanical strength. The maximum separation energy lies around  $740 \text{ Jm}^{-2}$  and is a factor of two larger than the Ponal-Classic.

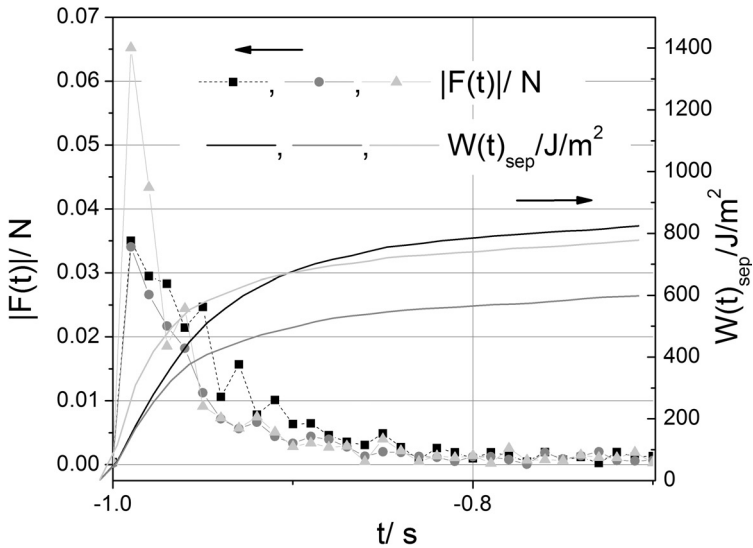


**Figure 5.19.** – Reproducibility and comparison of the absolute time-dependent force and the time-dependent separation energy of the measurements shown in fig. 5.18. (Ponal-Express sample)

Similar to the Ponal-Classic, the Ponal-Express shows an increase of the maximum separation energy for increasing curing times. The range of the separation energy is two decades and therefore smaller than the value of the Ponal-Classic. This value is obtained in only the half of the time (about 2 min). In contrast to the Ponal-Classic sample it was not always possible to measure the Ponal-Express for longer curing times than two minutes. The Ponal-Express showed for fast separation rates rupture. This is caused by the very fast curing of the Ponal-Express. The fast curing

results faster in a larger adhesive forces. Only for slow separation rates, i.e.  $t_{strike} = 1000$  ms, it was feasible to measure the separation energy at a curing time of 4 minutes (fig. 5.20b) without rupture of the sample.

A major aim of this part of this thesis is to compare the curing behaviour of Ponal-Classic and Ponal-Express. The maximum separation energy  $W_{sep,max}$  and the maximum absolute force  $F_{max}$  are taken from the previous plot and are graphically summarized in fig. 5.21a. According to the original CaBER analysis only the time to break up of the filament is accessible for both types of sample and plotted in fig. 5.21b. The numerical values in tab. 5.3 and tab. 5.4 are taken from the plots in fig. 5.21. Tab. 5.3 shows the data for the fast filament stretch ( $t_{strike} = 100$  ms) and tab. 5.4 shows the data for the slow filament stretch ( $t_{strike} = 1000$  ms).

The comparison of the maximum separation energy indicates that the Ponal-Express has larger values of the separation energy. This is most significant for small curing times (up to two minutes) while at larger curing times the values will be much closer to the Ponal-Classic. A similar behaviour is observed for the maximum absolute force.

For the time to break\* up (see fig. 5.21b) it can be observed that the filaments break faster for faster stretching. The faster curing kinetics of the Ponal-Express has the same effect as the longer curing time of the Ponal-Classic. Independent of the stretch rate, the Ponal-Express has a longer lasting filament for the not cured sample. Whereas, for the cured samples only the Ponal-Express at small stretch rates stays larger than the corresponding Ponal-Classic sample. The cured and fast stretched Ponal-Express reveals the smallest times to break up.

### 5.5.3.3 Conclusions for Measurement of the Axial Forces in the CaBER for Commercial Glues

Concluding this chapter, the axial force measurement in the CaBER device was used to introduce and to quantify the separation energy. The comparison of a classical wood glue (Ponal-Classic) and an express wood glue (Ponal-Express) showed how this new observable (axial force) can be used. The analysis of the separation energy showed that the Ponal-Express cures much faster than the Ponal-Classic and the Ponal-Express reaches during

\*  $t_{break}$  is measured from the beginning of the filament stretching phase on and has by this definition only positive values.

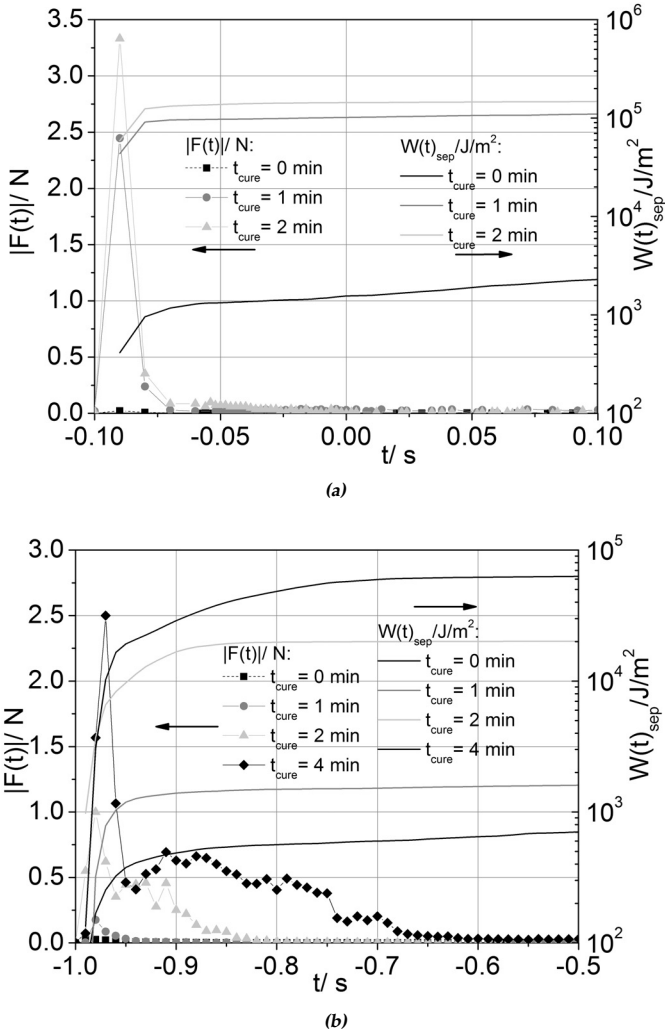
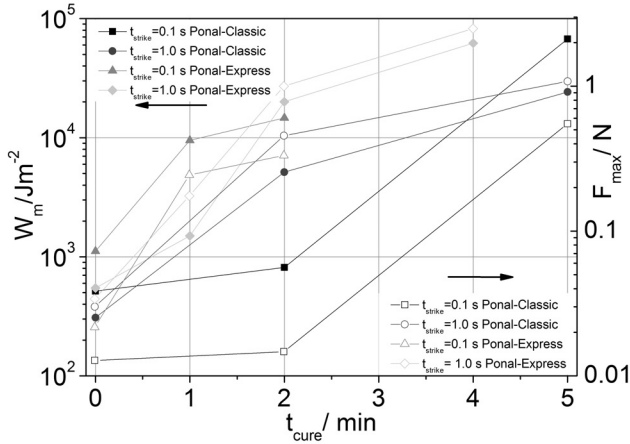
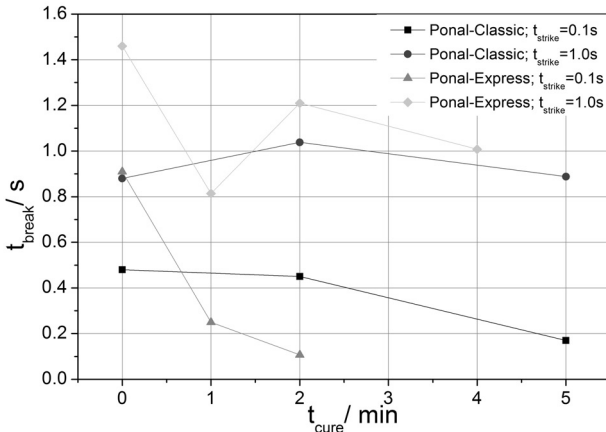


**Figure 5.20.** – Influence of the curing time on the values of the separation energy and the maximum force for the Ponal-Express, at room temperature  $\vartheta = 20$  °C and a final gap size of 10 mm. The strike time was set to be (a) 0.1 s ( $t_{cure} = \{0; 1; 2\}$  min) and (b) 1 s ( $t_{cure} = \{0; 1; 2; 4\}$  min).



(a)



(b)

**Figure 5.21.** – Comparison of the maximum separation energy, the maximum force and the time to break as a function of the curing time of the Ponal-Classic and the Ponal-Express. Experiments at room temperature  $\vartheta = 20^\circ\text{C}$  and a final gap size of 10 mm. The strike time was set to be 0.1 s or 1 s. (a) comparison of the maximum separation energy and the maximum force as a function of the curing time and (b) comparison of the time to break as a function of the curing time.

**Table 5.3.** – Comparison of the values for the separation energy  $W_{sep}(t_{cure})$ , the maximum force and the time to break for the Ponal-Classic (PCL) and the Ponal-Express (PEX) sample for  $t_{strike} = 100$  ms.

$t_{cure}$ min	$W_{sep}$ $\text{Jm}^{-2}$	$W_{sep}$ $\text{Jm}^{-2}$	$F_{max}$ N	$F_{max}$ N	$t_{break}$ s	$t_{break}$ s
	PCL	PEX	PCL	PEX	PCL	PEX
0	1205	2114	0.013	0.022	0.48	0.91
1	–	10516	–	0.24	–	0.25
2	1252	146750	0.015	0.33	0.45	0.107
5	67536	–	0.55	–	0.17	–

**Table 5.4.** – Comparison of the values for the separation energy  $W_{sep}(t_{cure})$ , the maximum force and the time to break for the Ponal-Classic (PCL) and the Ponal-Express (PEX) sample for  $t_{strike} = 1000$  ms.

$t_{cure}$ min	$W_{sep}$ $\text{Jm}^{-2}$	$W_{sep}$ $\text{Jm}^{-2}$	$F_{max}$ N	$F_{max}$ N	$t_{break}$ s	$t_{break}$ s
	PCL	PEX	PCL	PEX	PCL	PEX
0	409	547	0.03	0.03	0.88	1.46
1	–	1500	–	0.18	–	0.81
2	6043	20042	0.455	1	1.04	1.21
4	–	62110	–	2.5	–	1.01
5	24220	–	1.08	–	0.89	–

the curing process also much higher (up to two decades) values of the separation energy. The Ponal-Express cured faster and stronger (during the experimental time).

However, the axial force measurement in the CaBER represents a new tool to quantitatively determine the complete time dependence of the separation process, e.g. to characterize the behaviour of adhesive materials and this also for materials with low adhesive strength.\*

## 5.6 Conclusions and Prospects for the Modification of the CaBER

The work presented in this chapter (chap. 5) achieved the following new developments:

- A new geometry has been designed for the CaBER which measures the axial force.
- The new geometry has been installed and tested.
- Experiments were conducted to study the improvements reached with the new geometry. These results extended the analysis so far available for the CaBER apparatus.
- The mass and the force balance have been restated.
- As extension to the work of detachment, a new term called separation energy was introduced, in order to quantify the stickiness of still liquid samples, e.g. glues.
- Experiments with glues have been conducted to obtain values for the separation energy and to show the new possibilities of the improved CaBER.

With the measurement of the axial forces in a CaBER, new properties of materials can be studied, e.g. the time-dependent force can be observed while the filament is stretched. This gives insight in the time dependence of the stress during the filament stretching phase. This time dependence can affect the filament development during the CaBER experiment. From this various other possibilities are accessible, e.g. the quantification of the

---

\* This is possible due to the high sensitivity of the used piezoelectric force transducer.

time-dependent stress whereas the filament is stretched or the determination of the separation energy.

Furthermore, the restated balance equations have the potential to improve the determination of the elongational viscosity. The assumption of negligible axial stress was dropped and by this a new force balance was gained. The expected values for the elongational viscosity, as given by the Trouton relation,<sup>258</sup> could be received with this new description. However, this is limited to a special set of samples or needs a further improvement of the sensitivity of the force transducer (below  $10^{-5}$  N).

## Chapter 6

### Conclusions and Outlook

Within this thesis, different rheometrical set-ups have been improved to study the non-Newtonian flow behaviour of polymeric liquids. One method to study polymer melts under shear is the rotational rheometer. Due to similar effects as the Weissenberg effect, chap. 1, non-Newtonian fluids, e.g. polymer melts, exhibit, when strongly sheared, normal forces perpendicular to the motion. To measure this effect under oscillatory shear, especially under LAOS, a special geometry was designed within this thesis for the ARES rheometer, chap. 3.4. This new geometry contained a high sensitive piezoelectric force transducer with a sensitivity of about 0.05 mN. The special set-up for the data acquisition and the methods for improving the data quality were explained in chap. 3.4.1. For example the methods used by Dusschoten and Wilhelm<sup>138</sup> for the FT-rheology, e.g. the oversampling, have been applied also on the measurement of the normal force. The typical time resolution laid in the range of 1 ms. The calibration of the geometry inside the ARES was shown in chap. 3.7. In chap. 3.7, FT-spectra of the normal force obtained with the new geometry (NoForGe) were compared with the commercial ARES and the ARES G2. For the investigated sample (MDPE tab. 2.3), the NoForGe performed best in terms of signal-to-noise ratio. A factor of 1.8 lies between the ARES G2 (second place) and the NoForGe.

With the new measurement of the normal force under oscillatory shear it is possible to obtain simultaneously FT-spectra of the normal force and of the shear stress under LAOS. The evaluation of those spectra can be improved by using the from Hyun et al.<sup>105</sup> introduced  $Q$ -parameter for the

higher harmonics of the shear stress, chap. 3.6. In analogy to  $Q$  a non-linear parameter for the normal force spectra  $Q_{NF}$  has been defined in this thesis, chap. 3.8. With the use of  $Q$  and  $Q_{NF}$  both as functions of the strain amplitude  $\gamma_0$  polymer samples with different molecular architecture were studied. The plot of  $Q(\gamma_0)$  and  $Q_{NF}(\gamma_0)$  are composed from a decreasing part at low strain amplitudes and an increasing part at high strain amplitudes, e.g. fig. 3.16. By comparing the different slopes it was found, that the decreasing first slope of  $Q_{NF}$  can be used to differentiate the polymer type, e.g. fig. 3.19. Larger values mean a more viscose dominated material. The slope of the second region of  $Q$  differentiates between the topology of the polymer, e.g. tab. 3.3.

The new normal force geometry (NoForGe) technology has the advantage of being transferable to other rheometers than the ARES. Thus, even very basic rheometers could be upgraded into a high performance tool for non-linear rheology.

In chap. 4 the melt flow instabilities in the extrusion of polymer melts were studied. Therefore, a basic terminology was given in chap. 4.2. This basic terminology included practical approaches for the definition of the three main types of melt flow instabilities (i.e. sharkskin, stick-slip and GMF) and introduced the terms weak melt flow instability and strong melt flow instability. The flow behaviour of different polyethylene melts was studied with special home made slit dies, named sharkskin dies, chap. 4.3 and chap. 4.4. This slit dies were either attached to a capillary rheometer or to an extruder. Along the channel of the slit dies, three high sensitive pressure transducer were placed, which allowed a high sensitive measurement of the time-dependent pressure fluctuations. Depending on the flow conditions, it was possible to reach a sensitivity of  $10^{-5}$  bar in the slit die at a mean pressure in front of the die of about 250 bar. This high sensitivity of a mechanical device was obtained by using high sensitive transducer and special data acquisition algorithms, e.g. the oversampling method.<sup>138</sup> The used time resolution was in the range of  $10^{-3}$  s. The principle of the sharkskin die for the capillary extruder, which was constructed by Filipe,<sup>146</sup> was transferred to the extruder. This changed dramatically the obtained FT-spectra. Whereas, the spectra obtained on the capillary rheometer, chap. 4.4.5, were nearly free of foreign contribution and thus the melt flow instabilities could be easily identified by the appearance of character-

---

istic peaks in the spectra. The spectra obtained from the sharkskin die on the extruder contained large amounts of foreign contributions (e.g. the frequency of the extruder screw rotations, the electrical net frequency), chap. 4.5 and chap. 4.5.1. In chap. 4.5.1, the origin of this contribution was investigated and it was found that the material dependent contributions and the system dependent distributions can be distinguished. After knowing that the melt flow instabilities can be detected with the sharkskin die on the extruder and by using the FT, it was studied how the appearance of the melt flow instabilities changes under changed extrusion rates, chap. 4.5.2. For the investigated PE sample (PE-SCB13) and for high extrusion rates, a large GMF like instability was observed. This instability could be observed for a broad range of extrusion rates from an upper limit of  $n_{rot} = 170 \text{ min}^{-1}$  down to  $n_{rot} = 20 \text{ min}^{-1}$ . Whereas, the optical appearance of the instability changed slightly, fig. 4.33, the FT-spectra changed completely. For high extrusion rates a broad peak (e.g.  $n_{rot} = 170 \text{ min}^{-1}$  with  $v_{inst} = 95 \text{ Hz}$ ) was found which shifted to lower frequencies for reduced extrusion rates (e.g.  $n_{rot} = 80 \text{ min}^{-1}$  with  $v_{inst} = 63 \text{ Hz}$ ). At an extrusion rate with about  $n_{rot} = 45 \text{ min}^{-1}$  the broad peak disappeared and a narrow peak at a slightly lower frequency ( $v_{inst} = 54 \text{ Hz}$ ) appeared. This can be interpreted as a sign that the mechanism of the origin of the melt flow instability changed. However, this has to be studied in further investigations. The second output of chap. 4.5.2 is that the idea of a self controlled extruder, which can control the extrudate appearance by means of the FT-spectra of the time-dependent pressure, needs further work on the background of control system theory. The approach conducted in this thesis by finding characteristic peaks in the FT-spectra and regulate the extrusion rate down until they disappear fails in case of the found transition of the shape of the peak. Thus, a computer algorithm could not detect this and would assume that the melt flow instability has vanished. In chap. 4.5.5, it was studied whether the system dependent contributions to the FT-spectra could be automatically calculated out off the spectra by normalizing the spectra to characteristic peaks of the system dependent contributions, e.g. the peak at 50 Hz and afterwards subtracting a normalized spectra with only system dependent contributions. Thus, it was possible to reduce the system dependent contributions by a factor of 2-3. However, the system dependent contributions stay in the same order

of magnitude as the material dependent contributions to the FT-spectra. A further approach can be to use the integral value of the spectra. Spectra with material dependent contributions, which have normally substantially broader peaks than the system dependent contributions which have rather narrow peaks, could have larger integral values than spectra without material dependent peaks.

A second method of mathematical analysis for the melt flow instabilities is the ACF. The ACF was successfully used in combination with the sharkskin die and the capillary rheometer. In combination with the sharkskin die and the extruder it was found, chap. 4.5.3, that the rotation of the extruder screw and other vibrations are much stronger pronounced in the ACF. Thereby, the ACF could not provide any information about the melt flow instabilities.

Additionally to the FT-Analysis of the time-dependent pressure fluctuation, the FT-analysis was used on grey scale images of the extrudates. Thereof, it was possible to determine characteristic frequencies, which are spatial based, out off the images. This new field of application of the FT-analysis was first applied on artificially made images and on image of defined optical gratings and meshes which have well defined and regular mesh sizes. Hence, it was observed that the peaks of the FT-analysis of those images were at values of  $q_{image}$  which are identical with the number of lines which could be counted on the image. Thus, this method was applicable to determine the amount of instabilities in the images of extrudates. This was both done for extrudate samples obtained on the capillary rheometer, chap. 4.4.6.1, and for samples obtained on the extruder, chap. 4.5.4. The results were in both case compared with the characteristic frequencies obtained from the FT-analysis of the time-dependent pressure fluctuations. For strong melt flow instabilities both method found similar characteristic frequencies, fig. 4.40. Whereas, only the FT-spectra of the time-dependent pressure fluctuations contained characteristic peaks for weak melt flow instabilities, tab. 4.6. This concludes the improvements for the shear flows of polymer melts.

The last chapter of this thesis, chap. 5, describes the improvement of the commercial CaBER with an axial force measurement. The design of the new and improved geometry for the CaBER is shown in chap. 5.3.2. In this chapter, the complete experimental set-up with the new data acquisi-

---

tion is explained. The installation of the new geometry on the CaBER is completed by calibrating the high sensitive transducer while installed in the CaBER, chap. 5.4. Thus, a sensitivity of the sensor of about 0.05 mN was determined. This sensitivity was achieved by using the oversampling method. The temporal resolution of the experiments were typically in the range of 0.2 ms.

The theory of the CaBER experiment, chap. 5.2, assumes negligible axial forces during the CaBER experiment, chap. 5.1.1. That this assumption is only valid for some materials is shown in chap. 5.5.1. Therefore, the theory of the CaBER has to be improved. In chap. I the mass balance is formulated in cylindrical coordinates, which is the appropriate way to treat the CaBER experiment, chap. 5.1.1. Another improvement of the CaBER theory is done via introducing an additional force term in the Young-Laplace equation and to state the Young-Laplace equation for a cylindrical body, as shown in chap. K. The resulting force balance is used in chap. 5.2.2. With this new set of equations it was possible, chap. 5.5.1, to calculate the elongational viscosity for the PS-DOP sample during the CaBER experiment,  $\eta_E = 265$  Pas for small strike times  $t_{strike} = 40$  ms. The predicted value from the Trouton ratio of the elongational viscosity is very close,  $\eta_{E,theory} = 255$  Pas. In this case, the axial stress is not negligible.

In chap. 5.5.3 a new type of measurement on the CaBER is presented. With the additional force measurement the CaBER can be used to measure tack values, as it is done with the probe test apparatus of e.g. Zosel.<sup>247</sup> In comparison to the probe tack test apparatus the CaBER is not capable to apply a defined pre-pressure on a sample. To compensate this and to avoid confusion in the terminology the property of a separation energy  $W_{sep}$  is defined. In comparison to the energy of detachment<sup>247,259</sup>  $W_{adh}$   $W_{sep}$  has no pre-pressure history and it includes strong effects of the elongational flow while the sticky liquid is drawn. Thus,  $W_{adh}$  and  $W_{sep}$  are similar, but not the same. With the help of  $W_{sep}$  the curing behaviour of two different wood-glue sample is examined. The slowly curing Ponal-Classic sample showed lower values of  $W_{sep}$  when compared at the same curing time  $t_{cure}$  with the Ponal-Express sample, e.g.  $t_{cure} = 2$  min  $W_{sep} = 8$  kJ/m<sup>2</sup> compared to  $W_{sep} = 15$  kJ/m<sup>2</sup> (tab. 5.3). The results from the new separation energy  $W_{sep}$  are compared to the values of the time to filament break-up  $t_{break}$  which is accessible with the CaBER without a force

measurement. The filaments of the Ponal-Express glue were significantly longer lasting when slowly drawn ( $t_{strike} = 1$  s), typically about a factor of 1.4 (fig. 5.21 and tab. 5.4), as the filaments of the Ponal-Classic sample. For the fast drawn filaments ( $t_{strike} = 0.1$  s) the filaments of cured Ponal-Express tended to break faster than the filaments of the cured Ponal-Classic, fig. 5.21 and tab. 5.3.

As prospects for further works with the improved CaBER, the potential application for measuring the surface tension is feasible. For this only the zero shear viscosity  $\eta_0$  has to be known. For all samples which are used in the CaBER this is easily done with a rotational shear rheometer. With  $\eta_0$  and the known Trouton relation<sup>258,260</sup> the extensional viscosity is known. By this and with a reordering of eq. 5.15 the surface tension could be determined without needing to have a second device in the lab.

# Appendix A

## Short Introduction to Tensor Calculus

The following subsections present the basics of tensor calculus in a very condensed form. This is added for readers who want to have a deeper understanding of the equations which govern the fluid mechanical problems presented in this work. Most books about continuum mechanics or fluid mechanics include at least a small chapter about tensor calculus, e.g. the book of Chadwick<sup>261</sup> or Ogden.<sup>255</sup> The book of Klingbeil<sup>54</sup> or Schade et al.<sup>262</sup> are recommended for German readers. The following chapter about tensor calculus is based on the above mentioned books.<sup>54,255,261,262</sup>

### A.1 Vector Space

A vector space  $\mathbb{V}$  has the following properties for the vector  $\vec{u} + \vec{v} \in \mathbb{V}$ .  $\forall \vec{u}, \vec{v}, \vec{w} \in \mathbb{V}$  it is valid, that

$$\vec{u} + \vec{v} = \vec{v} + \vec{u}, \quad (\text{A.1})$$

$$\vec{u} + (\vec{v} + \vec{w}) = (\vec{u} + \vec{v}) + \vec{w}. \quad (\text{A.2})$$

$\exists \vec{0} \in \mathbb{V}$  with the property

$$\vec{u} + \vec{0} = \vec{u}. \quad (\text{A.3})$$

$\forall \vec{u} \in \mathbb{V}$ . From eq. A.3 the existence of an inverse element can also be deduced, as

$$\vec{u} + (-\vec{u}) = \vec{0} \quad (\text{A.4})$$

The multiplication with a scalar  $\alpha$  as  $\alpha\vec{u} \in \mathbb{V}$  should have the following properties

$$1\vec{u} = \vec{u}, \quad (\text{A.5})$$

$$\alpha(\beta\vec{u}) = (\alpha\beta)\vec{u}, \quad (\text{A.6})$$

$$(\alpha + \beta)\vec{u} = \alpha\vec{u} + \beta\vec{u}, \quad (\text{A.7})$$

$$\alpha(\vec{u} + \vec{v}) = \alpha\vec{u} + \alpha\vec{v}, \quad (\text{A.8})$$

$\forall \alpha, \beta \in \mathbb{R}$  and  $\forall \vec{u}, \vec{v} \in \mathbb{V}$  and  $1 = \text{unity}$ .

## A.2 Euclidean Vector Space

A vector space  $\mathbb{V}$  is called an Euclidean vector space  $\mathbb{E}$  if there exists the scalar product, as defined by eq. A.9 - eq. A.13, for all vectors  $\vec{u}, \vec{v} \in \mathbb{V}$ . All vectors of  $\mathbb{E}$  are Euclidean vectors.

$$\vec{u} \cdot \vec{v} = \vec{v} \cdot \vec{u}, \quad (\text{A.9})$$

$$\vec{u} \cdot \vec{u} \geq 0. \quad (\text{A.10})$$

In eq. A.10 equality holds only for  $\vec{u} = \vec{0}$ . The scalar product is bilinear, meaning linear in each element of the product, so

$$(\alpha\vec{u}) \cdot \vec{v} = \vec{u} \cdot (\alpha\vec{v}) \quad (\text{A.11})$$

$$\vec{u} \cdot (\vec{v} + \vec{w}) = \vec{u} \cdot \vec{v} + \vec{u} \cdot \vec{w} \quad (\text{A.12})$$

$$(\alpha\vec{u} + \beta\vec{v}) \cdot \vec{w} = \alpha(\vec{u} \cdot \vec{w}) + \beta(\vec{v} \cdot \vec{w}) \quad (\text{A.13})$$

is valid  $\forall \alpha, \beta \in \mathbb{R}$  and  $\forall \vec{u}, \vec{v}, \vec{w} \in \mathbb{E}$ .

### A.2.1 Magnitude of a Vector

The magnitude  $|\vec{u}|$  of a vector  $\vec{u}$  is defined as the positive square root of the scalar product of the vector with himself, as

$$|\vec{u}|^2 = \vec{u} \cdot \vec{u} \text{ or} \quad (\text{A.14})$$

$$|\vec{u}| = (\vec{u} \cdot \vec{u})^{1/2} \quad (\text{A.15})$$

In case of  $|\vec{u}| = 1$  the vector  $\vec{u}$  is a unit vector. If the scalar product of two different vector equals to zero, as  $\vec{u} \cdot \vec{v} = 0$  then the both vectors are perpendicular to each other;  $\vec{u} \perp \vec{v}$  meaning they are orthogonal.

## A.2.2 Vector Product

The definition of vector product demands the following properties:

$$\vec{u} \times \vec{v} = -\vec{v} \times \vec{u}, \quad (\text{A.16})$$

$$(\vec{u} \times \vec{v}) \cdot (\vec{u} \times \vec{v}) = (\vec{u} \cdot \vec{u})(\vec{v} \cdot \vec{v}) - (\vec{u} \cdot \vec{v})^2, \quad (\text{A.17})$$

$$\vec{u} \cdot (\vec{u} \times \vec{v}) = 0, \quad (\text{A.18})$$

$$(\alpha\vec{u} + \beta\vec{v}) \times \vec{w} = \alpha(\vec{u} \times \vec{w}) + \beta(\vec{v} \times \vec{w}). \quad (\text{A.19})$$

The vector product of a vector with himself is always zero.

$$\vec{u} \times \vec{u} = 0 \quad (\text{A.20})$$

$\forall \vec{u} \in \mathbb{E}$ . Assuming two arbitrary vectors of the magnitude 1,

$$|\vec{u}| = |\vec{v}| = 1. \quad (\text{A.21})$$

Then the following relation is valid

$$|\vec{u} \times \vec{v}|^2 + (\vec{u} \cdot \vec{v})^2 = 1 \quad (\text{A.22})$$

The the geometrical interpretation of the scalar product and the vector product is

$$\vec{u} \cdot \vec{v} = |\vec{u}| |\vec{v}| \cos \theta, \quad (\text{A.23})$$

$$\vec{u} \times \vec{v} = |\vec{u}| |\vec{v}| \sin \theta \vec{n} \quad (\text{A.24})$$

for  $|\vec{k}| = 1$  and  $\vec{n} \parallel \vec{u} \times \vec{v}$ .

## A.2.3 Orthonormal Basis and Kronecker Symbol

The basis of the vector space  $\mathbb{E}$  is formed by three linear independent vectors. An orthonormal basis is composed by three linear independent vectors which obey the rule,

$$\vec{e}_i \cdot \vec{e}_j = \delta_{ij} = \begin{cases} 1, & i = j \\ 0, & i \neq j \end{cases}. \quad (\text{A.25})$$

The symbol  $\delta_{ij}$  is called the Kronecker\* symbol or Kronecker delta. With this it is possible write the arbitrary vector  $\vec{u}$  in terms of the basis,

$$\vec{u} = u_j \vec{e}_j = u_1 \vec{e}_1 + u_2 \vec{e}_2 + u_3 \vec{e}_3. \quad (\text{A.26})$$

\* Leopold Kronecker (\*7. December 1823 in Liegnitz, Germany; +29. December 1891 in Berlin; Germany) was a German mathematician.<sup>5</sup>

With this background it is convenient to introduce the index notation. Thus, the scalar product is rewritten as

$$\vec{u} \cdot \vec{v} = u_i v_i. \quad (\text{A.27})$$

The index notation makes use of the Einstein notation<sup>53</sup> which defines that the sum has to be taken over the same indices and that in one summand it is not allowed to have the same index more than twice. The magnitude will be written as

$$|\vec{u}|^2 = u_i^2. \quad (\text{A.28})$$

## A.2.4 Alternating Symbol

For a right handed triad of basis vectors, it follows

$$\begin{aligned} \vec{e}_2 \times \vec{e}_3 &= \vec{e}_1, \\ \vec{e}_3 \times \vec{e}_1 &= \vec{e}_2, \\ \vec{e}_1 \times \vec{e}_2 &= \vec{e}_3. \end{aligned} \quad (\text{A.29})$$

The eq. A.29 leads to the definition of the alternating symbol\*  $\epsilon_{ijk}$ , as

$$\vec{e}_i \times \vec{e}_j = \epsilon_{ijk} \vec{e}_k. \quad (\text{A.30})$$

The epsilon symbol is defined as

$$\epsilon_{ijk} = \begin{cases} 1, & \text{cyclic permutations of } ijk \\ -1, & \text{anti-cyclic permutations of } ijk \\ 0, & \text{else} \end{cases}. \quad (\text{A.31})$$

The alternating symbol has the following properties

$$\epsilon_{ijk} = \epsilon_{kij} = \epsilon_{jki}, \quad (\text{A.32})$$

$$\epsilon_{ijk} = -\epsilon_{ikj} = -\epsilon_{kji} = -\epsilon_{jik}. \quad (\text{A.33})$$

Instead of using the basis vectors in eq. A.30 the same form can be applied on arbitrary vectors, as

$$\vec{u} \times \vec{v} = \epsilon_{ijk} u_i v_j \vec{e}_k. \quad (\text{A.34})$$

---

\* Also called alternator.

The triple scalar product\* it can be written with the use of the alternating symbol,

$$(\vec{u} \times \vec{v}) \cdot \vec{w} = \epsilon_{ijk} u_i v_j w_k = \begin{vmatrix} u_1 & u_2 & u_3 \\ v_1 & v_2 & v_3 \\ w_1 & w_2 & w_3 \end{vmatrix}. \quad (\text{A.35})$$

If  $\vec{u}, \vec{v}, \vec{w}$  are linearly independent then eq. A.35 will equal zero,

$$(\vec{u} \times \vec{v}) \cdot \vec{w} = 0. \quad (\text{A.36})$$

In eq. A.35 the determinant is used, so it is possible to write the determinant of a matrix or tensor as

$$\det \mathbf{A} = \epsilon_{ijk} A_{i1} A_{j2} A_{k3}. \quad (\text{A.37})$$

With eq. A.37 the following transformations are possible

$$\epsilon_{ijk} A_{ip} A_{jq} A_{kr} = (\det \mathbf{A}) \epsilon_{pqr}, \quad (\text{A.38})$$

$$\det \mathbf{A} = \frac{1}{6} \epsilon_{ijk} \epsilon_{pqr} A_{ip} A_{jq} A_{kr}, \quad (\text{A.39})$$

$$\det \mathbf{AB} = \det \mathbf{A} \det \mathbf{B}. \quad (\text{A.40})$$

The triple vector product can be expressed by

$$\begin{aligned} \vec{u} \times (\vec{v} \times \vec{w}) &= \epsilon_{kpq} \epsilon_{krs} v_p w_q u_s \vec{e}_r \\ &= (\vec{u} \cdot \vec{w}) \vec{v} - (\vec{u} \cdot \vec{v}) \vec{w}. \end{aligned} \quad (\text{A.41})$$

## A.3 Change of Basis

Taking two right orthonormal bases  $\{\vec{e}_i\}$  and  $\{\vec{e}'_i\}$ , the rule for transforming one basis into the other is

$$\vec{e}'_i = Q_{ip} \vec{e}_p, \quad (\text{A.42})$$

$$Q_{ij} = \vec{e}'_i \cdot \vec{e}_j. \quad (\text{A.43})$$

With eq. A.43 it follows for orthonormal systems, that

$$\begin{aligned} \delta_{ij} &= \vec{e}'_i \cdot \vec{e}'_j \\ &= Q_{ik} Q_{jk}. \end{aligned} \quad (\text{A.44})$$

\* The triple scalar product describes the signed volume of a parallelepiped.

A matrix  $\mathbf{Q}$  is called to be an orthogonal matrix, if it fulfils the relation

$$\mathbf{Q}\mathbf{Q}^T = \mathbf{1} = \mathbf{Q}^T\mathbf{Q}, \quad (\text{A.45})$$

$$Q_{ik}Q_{jk} = \delta_{ij} = Q_{ki}Q_{kj}. \quad (\text{A.46})$$

If  $\det \mathbf{Q} = +1$  then this proves the right handedness of the basis vectors and the matrix  $\mathbf{Q}$  is called to be proper orthogonal. If  $\det \mathbf{Q} = -1$  then this proves the not right handedness of the basis vectors and the matrix  $\mathbf{Q}$  is called to be improper matrix. Like for the basis vectors the transformation matrix  $Q_{ij}$  can be similarly applied to an arbitrary vector, like

$$v'_{ij} = Q_{ij}v_j, \quad (\text{A.47})$$

$$v_j = Q_{ij}v'_i. \quad (\text{A.48})$$

### A.3.1 Euclidean Point Space

The Euclidean point space represents the Cartesian coordinates  $x, y$ . Let  $\mathcal{E}$  be a set of elements (points) that for each  $(x, y)$  of  $\mathcal{E} \exists \vec{v}(x, y) \in \mathbb{E}$  with the following properties

$$\vec{v}(x, y) = \vec{v}(x, z) + \vec{v}(z, y), \forall y, x, z \in \mathcal{E}, \quad (\text{A.49})$$

$$\vec{v}(x, y) = \vec{v}(x, z), \text{ only if } y = z. \quad (\text{A.50})$$

However, it has to be noted that  $\mathcal{E}$ , the Euclidean point space, is not a vector space. Defining a reference point  $O$ ,  $\vec{x}(O)$  is the position vector. Thus, it can be written

$$\vec{y} = \vec{x}(O) - \vec{y}(O) \quad (\text{A.51})$$

where  $\vec{x}(y)$  is independent of the choice of  $O$ . The distance between two points is

$$d(x, y) = |\vec{x} - \vec{y}| = \{(\vec{x} - \vec{y}) \cdot (\vec{x} - \vec{y})\}^{\frac{1}{2}}. \quad (\text{A.52})$$

A bilinear mapping  $\mathcal{E} \times \mathcal{E}$  to  $\mathbb{R}$  is metric

$$d(x, y) = d(y, x), \quad (\text{A.53})$$

$$d(x, y) \leq d(x, z) + d(z, y), \quad (\text{A.54})$$

$$d(x, y) \geq 0, \text{ equals only if } x = y \forall x, y, z \in E. \quad (\text{A.55})$$

$\mathcal{E}$  is a metric space. The angle  $\theta$  between  $\vec{x}, \vec{y}$  is given by

$$\cos \theta = \frac{\vec{x} \cdot \vec{y}}{|\vec{x}| \cdot |\vec{y}|}. \quad (\text{A.56})$$

Components are given by  $x_i = \vec{x} \cdot \vec{e}_i$ . For the transformation between different systems the known rules can be applied,

$$x'_i = Q_{ij} (x_j - c_j) \quad \text{and} \quad (\text{A.57})$$

$$x_i = Q_{ji} (x'_j - c'_j). \quad (\text{A.58})$$

In this case the matrix  $Q_{ij}$  is called the Jacobian\* matrix and defined as

$$Q_{ij} = \frac{\partial x'_i}{\partial x_j} = \frac{\partial x_j}{\partial x'_i}. \quad (\text{A.59})$$

## A.4 Tensors

The matrix  $\mathbf{T}$  with the components  $T_{ij}$ , with  $n = 2$  indices, to the regular Cartesian basis  $\{\vec{e}_i\}$  is called a tensor of order 2, if it transforms according to the following rules

$$T'_{ij} = Q_{ip} Q_{jq} T_{pq}, \quad (\text{A.60})$$

$$\mathbf{T}' = \mathbf{Q} \mathbf{T} \mathbf{Q}^T, \quad (\text{A.61})$$

$$\mathbf{T} = \mathbf{Q}^T \mathbf{T}' \mathbf{Q}. \quad (\text{A.62})$$

As a short introduction the transformation of a tensor, the known stress tensor<sup>†</sup> is sketched. The stress vector  $\vec{t}$  normal to a surface  $ds$  is

$$\vec{t}(\vec{n}) = \mathbf{T} \vec{n}. \quad (\text{A.63})$$

With the index notation the components of the stress tensor  $\mathbf{T}$  are given by  $T_{ij}$ . Further the identity mapping on  $\mathbb{E}$  is identified with the matrix  $\mathbf{I}$ .

$$t_i = T_{ij} n_j, \quad (\text{A.64})$$

$$t'_i = T'_{ip} n'_p. \quad (\text{A.65})$$

\* Carl Gustav Jacob Jacobi (\*10. December 1804 in Potsdam, Germany; †18. February 1851 in Berlin; Germany) was a German mathematician.<sup>5</sup>

† The word tensor originates from the Latin word *tenderer* meaning "to stretch". The term was first applied to describe the stress and was later generalised for similar mathematical constructs. Thus, the term stress tensors is actually a pleonasm.<sup>54,262</sup>

The stress tensor transforms according to eq. A.60 - eq. A.62. General, a tensor of second order is a mapping of  $\mathbb{E}$  to itself

$$\mathbf{T} : \mathbb{E} \rightarrow \mathbb{E} \Rightarrow \mathcal{L}(\mathbb{E}, \mathbb{E}). \quad (\text{A.66})$$

This definition can be extended to Cartesian tensors of order  $n$ . The matrix  $\mathbf{T}$  with the components  $T_{ijk\dots}$ , with  $n \in \mathbb{N}$  indices, to the regular Cartesian basis  $\{\vec{e}_i\}$  is called a tensor of order  $n$ , if it obeys the transformation rule

$$T'_{ijk\dots} = Q_{ip}Q_{jq}Q_{kr\dots}T_{pqr\dots} \quad (\text{A.67})$$

**Example 19. Tensors of different order**

- A vector is a tensor of the order 1.
- A scalar is a tensor of order 0.
- The Kronecker delta is a tensor of the order 2.

□

### A.4.1 Tensor Product/ Dyadic Product

The following rules are valid for the dyadic product

$$u'_i v'_j = Q_{ip}Q_{jq}u_p v_q, \quad (\text{A.68})$$

$$(\vec{u} \otimes \vec{v}) \vec{w} = (\vec{v} \cdot \vec{w}) \vec{u}, \quad (\text{A.69})$$

$$(u_i \vec{e}_i \otimes v_j \vec{e}_j) w_k \vec{e}_k = v_j w_j u_i \vec{e}_i, \quad (\text{A.70})$$

$$(\vec{e}_i \otimes \vec{e}_j) \vec{n} = n_j \vec{e}_i, \quad (\text{A.71})$$

$$(T_{ij} \vec{e}_i \otimes \vec{e}_j) \vec{n} = T_{ij} n_j \vec{e}_i. \quad (\text{A.72})$$

Writing the tensor  $\mathbf{T}$  in index notation results in

$$\mathbf{T} = T_{ij} \vec{e}_i \otimes \vec{e}_j. \quad (\text{A.73})$$

Eq. A.73 can also be applied on the identity matrix

$$\mathbf{I} = \delta_{ij} \vec{e}_i \otimes \vec{e}_j = \vec{e}_i \otimes \vec{e}_i. \quad (\text{A.74})$$

The tensor product can be continuously applied

$$\mathbf{T} = T_{i_1 i_2 i_3 \dots i_n} \vec{e}_{i_1} \otimes \vec{e}_{i_2} \otimes \vec{e}_{i_3} \otimes \dots \otimes \vec{e}_{i_n}. \quad (\text{A.75})$$

### A.4.2 Contraction of a Tensor

Setting the indices of a tensor the same is called a contraction.

$$T_{ii} = \delta_{pq} T_{pq} = T_{pp}. \quad (\text{A.76})$$

The result of eq. A.76 is also called the trace of  $\mathbf{T}$ , also written as

$$T_{ii} = \text{tr} \mathbf{T}. \quad (\text{A.77})$$

The trace has got the following properties when applied to the contraction of two tensor of second order

$$\text{tr}(\mathbf{ST}) = S_{ij} T_{ji} = \text{tr}(\mathbf{TS}), \quad (\text{A.78})$$

$$\text{tr}(\mathbf{ST}) = \text{tr}(\mathbf{S}^T \mathbf{T}^T), \quad (\text{A.79})$$

$$\text{tr}(\mathbf{ST}^T) = \text{tr}(\mathbf{S}^T \mathbf{T}). \quad (\text{A.80})$$

### A.4.3 Isotropic Tensors

A tensor is called isotropic, if its components stays unchanged if transformed.

**Example 20.** *Isotropic tensors*

- A tensor of order 0 is always isotropic.
- A tensor of order 1 is never isotropic.
- All scalar multiples of  $\mathbf{I}$  are the only tensors of order 2 which are isotropic.

□

## A.5 Tensor Algebra

The tensor  $\mathbf{T}$  is called linear, if

$$\mathbf{T}(\alpha \vec{u} + \beta \vec{v}) = \alpha \mathbf{T} \vec{u} + \beta \mathbf{T} \vec{v}, \quad (\text{A.81})$$

$$T_{ij}(\alpha u_j + \beta v_j) = \alpha T_{ij} u_j + \beta T_{ij} v_j, \quad (\text{A.82})$$

$$(\alpha \mathbf{S} + \beta \mathbf{T}) \vec{u} = \alpha (\mathbf{S} \vec{u}) + \beta (\mathbf{T} \vec{u}). \quad (\text{A.83})$$

$$(\text{A.84})$$

The inner product has to be defined

$$(\mathbf{S}\mathbf{T})\vec{u} = \mathbf{S}(\mathbf{T}\vec{u}). \quad (\text{A.85})$$

$S_{ik}T_{kj}$  means the contraction of the tensor product  $\mathbf{T} \otimes \mathbf{S}$ . Finally, it exists a zero tensor  $\mathbf{0}$ , that maps every vector to the zero vector  $\vec{0}$ , as

$$\mathbf{0}\vec{u} = \vec{0} \quad (\text{A.86})$$

and the identity tensor maps every vector to itself

$$\mathbf{I}\vec{u} = \vec{u}. \quad (\text{A.87})$$

A set of bilinear functions over  $\mathbb{E} \otimes \mathbb{E}$  for the vector space  $\mathbb{R}$  is denoted as

$$\mathcal{L}(\mathbb{E} \otimes \mathbb{E}, \mathbb{R}) \approx \mathcal{L}(\mathbb{E}, \mathbb{E}). \quad (\text{A.88})$$

In this context one speaks of isomorphism.

$$(\vec{e}_i \otimes \vec{e}_j)(\vec{u}, \vec{v}) = u_i v_j, \quad (\text{A.89})$$

$$\mathbf{T}(\vec{u}, \vec{v}) = u_i T_{ij} v_j, \quad (\text{A.90})$$

$$\vec{v} \cdot (\mathbf{T}^T \vec{u}) = \vec{u} \cdot (\mathbf{T} \vec{v}) \Leftrightarrow \mathbf{T}^T(\vec{v}, \vec{u}) = \mathbf{T}(\vec{u}, \vec{v}), \quad (\text{A.91})$$

$$(T_{ij})^T = T_{ji}, \quad (\text{A.92})$$

$$(\mathbf{T}^T)^T = \mathbf{T}, \quad (\text{A.93})$$

$$(\alpha\mathbf{S} + \beta\mathbf{T})^T = \alpha\mathbf{S}^T + \beta\mathbf{T}^T, \quad (\text{A.94})$$

$$(\mathbf{S}\mathbf{T})^T = \mathbf{S}^T \mathbf{T}^T. \quad (\text{A.95})$$

A tensor is called symmetric, if

$$\mathbf{T}^T = \mathbf{T}, \quad (\text{A.96})$$

$$T_{ij} = T_{ji}. \quad (\text{A.97})$$

A tensor is called skew symmetric or antisymmetric, if

$$\mathbf{T}^T = -\mathbf{T}, \quad (\text{A.98})$$

$$T_{ij} = -T_{ji}. \quad (\text{A.99})$$

A symmetric tensor of second order has got six independent components and a skew symmetric tensor of second order has got three independent

components. A second order tensor can be uniquely decomposed in a symmetric part and an antisymmetric part, as

$$\mathbf{T} = \frac{1}{2} \underbrace{(\mathbf{T} + \mathbf{T}^T)}_{\text{D: symmetric}} + \frac{1}{2} \underbrace{(\mathbf{T} - \mathbf{T}^T)}_{\text{W: skew-symmetric}}. \quad (\text{A.100})$$

The trace of the tensor  $\mathbf{T}$  can be defined to a orthonormal basis  $\{\vec{e}_i\}$ , as

$$\text{tr}\mathbf{T} = T_{ii} = \vec{e}_i \cdot (\mathbf{T}\vec{e}_i) = \mathbf{T}(\vec{e}_i, \vec{e}_i). \quad (\text{A.101})$$

If the determinant of a matrix exists,  $\det \mathbf{T} \neq 0$  then a unique inverse tensor  $\mathbf{T}^{-1}$  exists with the properties

$$\mathbf{T}\mathbf{T}^{-1} = \mathbf{I} = \mathbf{T}^{-1}\mathbf{T}, \quad (\text{A.102})$$

$$\det \mathbf{T}^{-1} = \det \mathbf{T}^{-1}, \quad (\text{A.103})$$

$$(\mathbf{S}\mathbf{T})^{-1} = \mathbf{T}^{-1}\mathbf{S}^{-1}. \quad (\text{A.104})$$

The adjugated tensor of  $\mathbf{T}$  is denoted as  $\text{adj}\mathbf{T}$  and is defined as

$$\text{adj}(\mathbf{T}^T) := (\det \mathbf{T}) \mathbf{T}^{-1}, \quad (\text{A.105})$$

$$\det(\text{adj}\mathbf{T}) = (\det \mathbf{T})^2. \quad (\text{A.106})$$

## A.6 Eigenvalues and Eigenvectors

The vector  $\vec{v}$  is called an eigenvector of the tensor  $\mathbf{T}$ , if a scalar  $\lambda$  exists that the relation is satisfied

$$\mathbf{T}\vec{v} = \lambda\vec{v}. \quad (\text{A.107})$$

The scalar  $\lambda$  in eq. A.107 is named the eigenvalue of  $\mathbf{T}$ . There exists only a non trivial solution if

$$\det(\mathbf{T} - \lambda\mathbf{I}) = 0, \quad (\text{A.108})$$

$$\det(T_{ij} - \lambda\delta_{ij}) = 0. \quad (\text{A.109})$$

The solution of the eq. A.108 and eq. A.109 is the characteristic equation of  $\mathbf{T}$ , given by

$$\lambda^3 - I_1(\mathbf{T})\lambda^2 + I_2(\mathbf{T})\lambda - I_3(\mathbf{T}) = 0. \quad (\text{A.110})$$

In eq. A.110 the three principal invariants  $I_1, I_2, I_3$  of  $\mathbf{T}$  were introduced.

$$I_1(\mathbf{T}) = \text{tr}\mathbf{T}, \quad (\text{A.111})$$

$$I_2(\mathbf{T}) = \frac{1}{2} \left\{ (\text{tr}\mathbf{T})^2 - \text{tr}\mathbf{T}^2 \right\}, \quad (\text{A.112})$$

$$I_3(\mathbf{T}) = \det \mathbf{T} = \frac{1}{6} \left\{ (\text{tr}\mathbf{T})^3 - 3(\text{tr}\mathbf{T}) \text{tr}\mathbf{T}^2 + 2\text{tr}\mathbf{T}^3 \right\}. \quad (\text{A.113})$$

$$\mathbf{T}^r \vec{v} = \lambda^r \vec{v}. \quad (\text{A.114})$$

The Cayley\* -Hamilton<sup>†</sup> theorem states that a tensor satisfies its own characteristic equation

$$\begin{aligned} 0 &= \det \left( \mathbf{T}^{-1} - \lambda^{-1} \mathbf{I} \right) \\ &= \mathbf{T}^3 - I_1 \mathbf{T}^2 + I_2 \mathbf{T} - I_3. \end{aligned} \quad (\text{A.115})$$

### A.6.1 Symmetric Tensors of Second Order

The eigenvalue problem is solved for the symmetric tensors as it follows

$$\begin{aligned} \mathbf{D} &= \mathbf{D}\mathbf{I} = \left( \mathbf{D}\vec{v}^{(i)} \right) \otimes \vec{v}^{(i)} \\ &= \sum_{i=1}^3 \lambda \vec{v}^{(i)} \otimes \vec{v}^{(i)}. \end{aligned} \quad (\text{A.116})$$

The  $i$ -th eigenvector is called  $\vec{v}^{(i)}$  and represents the principal axes, from this the spectral representation is gained,

$$I_1(\mathbf{D}) = \lambda_1 + \lambda_2 + \lambda_3, \quad (\text{A.117})$$

$$I_2(\mathbf{D}) = \lambda_2 \lambda_3 + \lambda_3 \lambda_1 + \lambda_1 \lambda_2, \quad (\text{A.118})$$

$$I_3(\mathbf{D}) = \lambda_1 \lambda_2 \lambda_3, \quad (\text{A.119})$$

Two tensors of second order are coaxial, this means their principal axes coincide, only if

$$\mathbf{S}\mathbf{D} = \mathbf{D}\mathbf{S}. \quad (\text{A.120})$$

---

\* Arthur Cayley (\*16. August 1821 in Richmond, England; †26. January 1895 in Cambridge, England) was an English mathematician.<sup>5</sup>

† Sir William Rowan Hamilton (\*4. August 1805 in Dublin, Ireland; †2. September 1865 by Dublin, Ireland) was an Irish mathematician and physicist.<sup>5,58</sup>

The matrix  $\mathbf{D}$  is positive definite if

$$\vec{v} \cdot (\mathbf{D}\vec{v}) > 0 \forall \vec{v} \neq 0 \text{ in } \mathbb{E}. \quad (\text{A.121})$$

The matrix  $\mathbf{D}$  is positive semi-definite if

$$\vec{v} \cdot (\mathbf{D}\vec{v}) \geq 0. \quad (\text{A.122})$$

If a matrix is positive definite and symmetric it follows that all  $\lambda_i > 0$ . If a matrix is positive semi-definite and symmetric it follows that the eigenvalues  $\lambda_i \geq 0$  with at least one eigenvalues equals zero. The positive square root is uniquely defined by

$$\mathbf{D}^{\frac{1}{2}} := \sum_{i=1}^3 \lambda_i^{\frac{1}{2}} \vec{v}^{(i)} \otimes \vec{v}^{(i)}. \quad (\text{A.123})$$

If  $\lambda > 0$  then exists the inverse matrix  $\mathbf{T}^{-1}$  and is uniquely defined as

$$\mathbf{D}^{-1} := \sum_{i=1}^3 \lambda_i^{-1} \vec{v}^{(i)} \otimes \vec{v}^{(i)}. \quad (\text{A.124})$$

## A.6.2 Antisymmetric Tensors of Second Order

Antisymmetric tensors are defined as

$$\mathbf{W}^T = -\mathbf{W} \quad (\text{A.125})$$

and the three invariants are given by

$$I_1(\mathbf{W}) = 0, \quad (\text{A.126})$$

$$I_2(\mathbf{W}) = W_{23}^2 + W_{31}^2 + W_{12}^2, \quad (\text{A.127})$$

$$I_3(\mathbf{W}) = 0, \quad (\text{A.128})$$

By the use of eq. A.126 - eq. A.128 the characteristic equation is reduced to

$$\lambda^3 + I_2(\mathbf{W}) \lambda = 0. \quad (\text{A.129})$$

If  $\mathbf{W}$  is not identical with the zero matrix  $\mathbf{0}$  then  $I_2 > 0$  and only one real eigenvalue  $\lambda = 0$  exists .

$$\mathbf{W}\vec{w} = \mathbf{0}. \quad (\text{A.130})$$

In eq. A.130  $\vec{w}$  is the eigenvector of the skew symmetric matrix. This eigenvector has the properties

$$\mathbf{W}\vec{a} = \vec{w}\vec{a}, \quad (\text{A.131})$$

$$\mathbf{W} = (\mathbf{W}\vec{u}) \otimes \vec{u} - \vec{u} \otimes (\mathbf{W}\vec{u}). \quad (\text{A.132})$$

## A.7 Orthogonal Tensors of Second Order

The scalar product  $\vec{u} \cdot \vec{v}$  is not preserved by linear mapping

$$(\mathbf{T}\vec{u}) \cdot (\mathbf{T}\vec{v}) = \vec{v} \cdot (\mathbf{T}^T \mathbf{T}\vec{u}). \quad (\text{A.133})$$

Therefore

$$\mathbf{Q}\mathbf{Q}^T = \mathbf{I} = \mathbf{Q}^T \mathbf{Q}. \quad (\text{A.134})$$

Thus,  $\mathbf{Q}$  is an orthogonal tensor. If

$$\det \mathbf{Q} = \pm 1, \quad (\text{A.135})$$

then  $\mathbf{Q}$  is called a proper or improper tensor.

### A.7.1 Mapping from one Euclidean Space to Another

The relation between the matrix  $\mathbf{Q}$  and the components  $Q_{ij}$  is that the later contains the direction cosines, which in an orthogonal transformation rotates all vectors bases  $\{\vec{e}_i\}$  to  $\{\vec{e}'_i\}$  (see fig. A.1).

$$\mathbf{Q}^T (\mathbf{Q} - \mathbf{I}) = - (\mathbf{Q} - \mathbf{I}). \quad (\text{A.136})$$

The determinant of eq. A.136 is given by

$$\det \mathbf{Q} - \mathbf{I} = 0. \quad (\text{A.137})$$

Therefore, the eigenvalues of  $\mathbf{Q}$  are  $\lambda = 1$  and from this the eigenvectors are found to be

$$\mathbf{Q}\vec{u} = \vec{u}. \quad (\text{A.138})$$

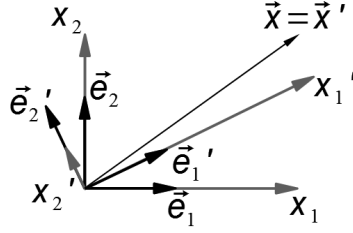


**Figure A.1.** – Rotation of the basis  $\vec{e}_i$  of a vector  $\vec{x}$ .

$\vec{u}, \vec{v}, \vec{w}$  are an orthonormal basis, so

$$\begin{aligned} 0 &= \vec{v} \cdot \vec{u} = \vec{v} \cdot (\mathbf{Q}^T \mathbf{Q} \vec{u}), \\ &= (\mathbf{Q} \vec{v}) \cdot (\mathbf{Q} \vec{u}) = (\mathbf{Q} \vec{v}) \cdot \vec{u}, \end{aligned} \quad (\text{A.139})$$

$$\begin{aligned} \mathbf{Q} &= \vec{u} \otimes \vec{v} + (\vec{v} \otimes \vec{v} + \vec{w} \otimes \vec{w}) \cos \theta \\ &+ (\vec{w} \otimes \vec{v} - \vec{v} \otimes \vec{w}) \sin \theta, \end{aligned} \quad (\text{A.140})$$

$$\mathbf{Q} \vec{a} = \vec{a} \cos \theta + (\vec{a} \cdot \vec{u}) \vec{u} (1 - \cos \theta) + \vec{u} \times \vec{a} \sin \theta. \quad (\text{A.141})$$

For the invariants of  $\mathbf{Q}$  it is valid, that

$$I_1(\mathbf{Q}) = I_2(\mathbf{Q}) = 1 + 2 \cos \theta, \quad (\text{A.142})$$

$$I_3(\mathbf{Q}) = 1. \quad (\text{A.143})$$

## A.8 Reciprocal Basis: Contravariance and Covariance Basis

Is  $\{\vec{e}_i\}$  an arbitrary basis of  $\mathbb{E}$  then  $\vec{e}_1, \vec{e}_2, \vec{e}_3$  are neither unit vectors nor mutually orthogonal, so

$$\vec{u} = u^k \vec{e}_k. \quad (\text{A.144})$$

In eq. A.144  $u^k$  are the contravariance components to the basis  $\{\vec{e}_i\}$ . The reciprocal basis to  $\{\vec{e}_i\}$  is denoted as  $\{\vec{e}^i\}$ , with

$$\vec{e}^i \cdot \vec{e}_i = \delta_j^i = \begin{cases} 1, & i = j \\ 0, & i \neq j \end{cases}. \quad (\text{A.145})$$

Orthonormal bases are self-reciprocal.

$$\bar{u} = u_k \bar{e}^k. \quad (\text{A.146})$$

In eq. A.146  $u_k$  are the covariance components to the basis  $\{\bar{e}^i\}$ . The components of the identity mapping are

$$I_{ik} = \bar{e}_i \cdot \bar{e}_k = I_{ki}, \quad (\text{A.147})$$

$$I^{ik} = \bar{e}^i \cdot \bar{e}^k = I^{ki}, \quad (\text{A.148})$$

$$I_{ij} I^{jk} = \delta_i^k, \quad (\text{A.149})$$

$$\begin{aligned} \mathbf{I} &= I^{ij} \bar{e}_i \otimes \bar{e}_j, \\ &= I_{ij} \bar{e}^i \otimes \bar{e}^j, \\ &= I_i^j \bar{e}^i \otimes \bar{e}_j, \\ &= I_j^i \bar{e}_i \otimes \bar{e}^j. \end{aligned} \quad (\text{A.150})$$

The scalar product can be written, as

$$\bar{u} \cdot \bar{v} = u^i v_j = u_i v^j = I_{ij} u^i v^j = I^{ij} u_i v_j. \quad (\text{A.151})$$

For the components of a matrix its found, that

$$\begin{aligned} \mathbf{T} &= T^{ij} \bar{e}_i \otimes \bar{e}_j = T_j^i \bar{e}_i \otimes \bar{e}^j \\ &= T_i^j \bar{e}^i \otimes \bar{e}_j = T_{ij} \bar{e}^i \otimes \bar{e}^j. \end{aligned} \quad (\text{A.152})$$

In eq. A.152  $T_j^i$  are the right covariant mixed components and  $T_i^j$  are the left covariant mixed components of the tensor  $\mathbf{T}$ .

# Appendix B

## Properties of the Fourier Transform

In the following the commonly used basic properties of the Fourier transform will be summarized as found in many textbooks.<sup>19,20,22,263</sup> For this the following nomenclature is introduced\*

$$\begin{aligned} f(t) &\leftrightarrow F(\omega), \\ g(t) &\leftrightarrow G(\omega) \text{ and} \\ a, b &\in \mathbb{R}. \end{aligned}$$

### Linearity

$$a \cdot f(t) + b \cdot g(t) \leftrightarrow a \cdot F(\omega) + b \cdot G(\omega). \quad (\text{B.1})$$

**Translation** A translation in the time domain will result in a modulation in the frequency domain,

$$f(a - t) \leftrightarrow F(\omega) e^{-i\omega a}. \quad (\text{B.2})$$

**Modulation** A modulation in time will cause a translation in the frequency,

$$f(t) e^{-i\omega_0 t} \leftrightarrow F(\omega - \omega_0). \quad (\text{B.3})$$

---

\* <time domain property>  $\leftrightarrow$  <frequency domain equivalent>

**Scaling** From a compression or stretching of the time axis it can be deduced, that

$$f(at) \leftrightarrow \frac{1}{|a|} F\left(\frac{\omega}{a}\right). \quad (\text{B.4})$$

**Parseval's theorem**

$$\int_{-\infty}^{+\infty} f_1(t) \cdot f_2^*(t) dt = \int_{-\infty}^{+\infty} F_1(\omega) \cdot F_2^*(\omega) d\omega. \quad (\text{B.5})$$

The symbol \* indicates the conjugated element of a complex variable. A special case of the Parseval's<sup>†</sup> theorem, which is important for the application, is the case  $f_1(t) \equiv f_2(t) = f(t)$ . Thus,

$$\int_{-\infty}^{+\infty} |f(t)|^2 dt = \int_{-\infty}^{+\infty} |F(\omega)|^2 d\omega. \quad (\text{B.6})$$

**FT of a derivative** For the temporal derivative of a function  $f(t)$  the FT leads to

$$FT(f'(t)) \leftrightarrow i\omega F(\omega). \quad (\text{B.7})$$

**Amplitude spectrum and the phase spectrum** For the analysis or visualization of the amplitude spectrum, also called the modular transform or magnitude spectrum, and the phase spectrum are commonly used in literature. The amplitude is defined as

$$A(\omega) = |F(\omega)| = \sqrt{\text{Re}\{F(\omega)\}^2 + \text{Im}\{F(\omega)\}^2} \quad (\text{B.8})$$

and is also called the frequency response. Related to the amplitude is the power spectrum, as defined as

$$P(\omega) = |F(\omega)|^2. \quad (\text{B.9})$$

The phase spectrum is given by

$$\varphi(\omega) = \arctan\left(\frac{\text{Im}\{F(\omega)\}}{\text{Re}\{F(\omega)\}}\right) \quad (\text{B.10})$$

and is also called phase response.

---

<sup>†</sup> Marc-Antoine Parseval de Chênes (★27. April 1755 in Rosières-aux-Salines, France; †16. August 1836 in Paris, France) was a French mathematician.<sup>5</sup>

## Appendix C

### The Maxwell Model under Oscillatory Shear

In chap. 3.2.1 the basic equation, eq. 3.20, is given for the linear rheological behaviour of a Maxwell body. In the following, the derivation of this equation from the basic model equation, eq. 2.42, will be shown.

First, the model equation has to be written in form of complex variables. For this the shear amplitude, the shear rate and the shear stress are given by eq. 3.3, eq. 3.4 and eq. 3.17 are restated to

$$\gamma(t) = \gamma_0 \cdot e^{i\omega t}, \quad (\text{C.1})$$

$$\tau(t) = \tau_0 \cdot e^{i(\omega t + \delta)}, \quad (\text{C.2})$$

$$\dot{\gamma}(t) = \gamma_0 i\omega \cdot e^{i\omega t}. \quad (\text{C.3})$$

Substituting the strain rate and the stress in eq. 2.42 by eq. C.3 and eq. C.2 results in

$$i\omega\eta\gamma_0 e^{i\omega t} = i\omega\lambda\tau_0 e^{i(\omega t + \delta)} + \tau_0 e^{i\omega t + \delta}. \quad (\text{C.4})$$

Eq. C.4 can be stepwise modified as

$$\begin{aligned} i\omega\eta\gamma_0 e^{i\omega t} &= \tau_0 e^{i(\omega t + \delta)} (i\omega\lambda + 1) \Big| \div \tau_0 \\ i\omega\eta \frac{\gamma_0}{\tau_0} e^{i\omega t} &= e^{i(\omega t + \delta)} (i\omega\lambda + 1) \Big| \cdot e^{-i\omega t}. \end{aligned} \quad (\text{C.5})$$

With eq. 2.24,  $\gamma_0/\tau_0 = 1/G$ , eq. C.5 becomes,

$$i\omega \frac{\eta}{G} = e^{i\delta} (i\omega\lambda + 1). \quad (\text{C.6})$$

With eq. 2.43 the ration of the shear viscosity and the shear modulus equals the relaxation time, thus

$$i\omega\lambda = e^{i\delta} (i\omega\lambda + 1). \quad (\text{C.7})$$

Reordering eq. C.7 results in

$$e^{i\delta} = \frac{i\omega\lambda}{(i\omega\lambda + 1)}. \quad (\text{C.8})$$

Multiplying eq. C.8 with the complex conjugate gives

$$e^{i\delta} = \frac{(\omega^2\lambda^2 + i\omega\lambda)}{\omega^2\lambda^2 + 1}. \quad (\text{C.9})$$

In eq. 3.18 the complex modulus is defined. In this formula the complex formulation of the shear amplitude and the shear stress have to be used, as given in eq. C.1 and eq. C.2.

$$\begin{aligned} G^*(\omega) &= \frac{\tau_0 \cdot e^{i(\omega t + \delta)}}{\gamma_0 \cdot e^{i\omega t}} \\ &= G e^{i\delta}. \end{aligned} \quad (\text{C.10})$$

The term  $e^{i\delta}$  of eq. C.10 can be substitute by the result from the Maxwell model in eq. C.9. Doing so, eq. 3.20 is obtained.

## Appendix D

### Derivation of the Fundamental Equation of the FT-Rheology

As described in chap. 3.3 the FT-spectra of oscillatory shear experiments have only odd multiples of the fundamental (excitation) frequency  $\omega_0$ . The explanation for this is given by Wilhelm et al.<sup>83,105</sup> and is in detail shown in the following.

The flow of a viscous fluid is sufficiently described with the Newtonian law for shear eq. 2.25

$$\sigma(\dot{\gamma}) = \eta \dot{\gamma}. \quad (\text{D.1})$$

To apply eq. D.1 also to viscoelastic fluids the viscosity is expanded via a Taylor<sup>18,126</sup> expansion

$$\eta(\dot{\gamma}) = \eta_0 + a \cdot \dot{\gamma}^2 + b \cdot \dot{\gamma}^4 + \dots \quad (\text{D.2})$$

For the oscillatory shear experiment the excitation of the sample is given by the time-dependent strain

$$\gamma(t) = \gamma_0 \cdot e^{i\omega_0 t}. \quad (\text{D.3})$$

Eq. D.3 uses the Euler\*-relation,<sup>†</sup> instead of the usual notation using trigonometric functions. The time derivative of eq. D.3 determines the applied

---

\* Leonard Euler (★15. April 1707 in Basel, Swiss; †18. September 1783 in St. Petersburg, Russia) was a Swiss mathematician.<sup>5</sup>

† Euler-relation:<sup>18</sup>  $e^{iy} = \cos(y) + i \sin(y)$ .

shear rate

$$\dot{\gamma}(t) = i\gamma_0\omega_0 \cdot e^{i\omega_0 t}. \quad (\text{D.4})$$

Using eq. D.2 in eq. D.1 the shear stress  $\sigma$  is given as a function of the shear rate  $\dot{\gamma}$ ,

$$\sigma(\dot{\gamma}) = \left( \eta_0 + a\dot{\gamma}^2 + b\dot{\gamma}^4 + \dots \right) \cdot \dot{\gamma}. \quad (\text{D.5})$$

Substituting  $\dot{\gamma}$  from eq. D.4 in eq. D.5 results in a the time-dependent shear stress,

$$\begin{aligned} \sigma(t) &= \left( \eta_0 + a \cdot i^2\gamma_0^2\omega_0^2 \cdot e^{i \cdot 2\omega_0 t} \right. \\ &+ \left. b \cdot i^4\gamma_0^4\omega_0^4 \cdot e^{i \cdot 4\omega_0 t} + \dots \right) \cdot i\gamma_0\omega_0 \cdot e^{i\omega_0 t} \\ &= \eta_0 \cdot i\gamma_0\omega_0 \cdot e^{i\omega_0 t} - a \cdot i\gamma_0^3\omega_0^3 \cdot e^{i \cdot 3\omega_0 t} + b \cdot i\gamma_0^5\omega_0^5 \cdot e^{i \cdot 5\omega_0 t} + \dots \\ &= I_1 e^{i\omega_0 t} - I_3 e^{i \cdot 3\omega_0 t} + I_5 e^{i \cdot 5\omega_0 t} + \dots \end{aligned} \quad (\text{D.6})$$

The similarity of eq. D.6 with the complex form of the Fouries series, as described in chap. 2.1.1, is obvious. Thus, eq. 2.8 is used, like

$$\begin{aligned} f(t) &= \mathfrak{C}_{F,1} e^{i\omega_0 t} + \mathfrak{C}_{F,2} e^{i \cdot 2\omega_0 t} + \mathfrak{C}_{F,3} e^{i \cdot 3\omega_0 t} \\ &+ \mathfrak{C}_{F,4} e^{i \cdot 4\omega_0 t} + \mathfrak{C}_{F,5} e^{i \cdot 5\omega_0 t} + \dots \end{aligned} \quad (\text{D.7})$$

By comparing the coefficients of the  $e^{i \cdot n\omega_0 t}$  from eq. D.6 and eq. D.7 it follows that all even  $\mathfrak{C}_{F,n}$  are zero, like

$$\mathfrak{C}_{F,2} = \mathfrak{C}_{F,4} = \mathfrak{C}_{F,n} = 0, \forall n = \{x \mid x, k \in \mathbb{N}^+, x = 2k\}. \quad (\text{D.8})$$

The odd coefficients of eq. D.7 are directly related to the  $I_n$  values of eq. D.6,

$$\begin{aligned} \mathfrak{C}_{F,1} &= I_1 = \eta_0 \cdot i\gamma_0\omega_0 \\ \mathfrak{C}_{F,3} &= I_3 = a \cdot i\gamma_0^3\omega_0^3 \\ \mathfrak{C}_{F,5} &= I_5 = b \cdot i\gamma_0^5\omega_0^5 \\ \mathfrak{C}_{F,n} &= I_n, \forall n = \{x \mid x, k \in \mathbb{N}^+, x = 2k - 1\}. \end{aligned} \quad (\text{D.9})$$

Eq. D.9 shows that the amplitudes or intensities of the decomposition of the stress are given by the  $I_n$  values and that only odd frequencies  $\omega_n$  are needed for the decomposition of the stress.

From this deduction the stress can be decomposed into a discrete spectrum of the odd multiples of the excitation frequency  $\omega_0$ ,

$$\sigma = \sum_{n=1}^N I_n e^{i \cdot n\omega_0 t}, \forall n = \{x \mid x, k \in \mathbb{N}^+, x = 2k - 1\}. \quad (\text{D.10})$$

# Appendix E

## Special Units for the Spatial Frequency

In this chapter the units of the optical analysis of the melt flow instabilities are explained. First the relations for the wavenumber  $k_w$ , wavelength  $\lambda_w$  and the spatial frequency  $\tilde{\nu}$  are given, as found in e.g. Hecht<sup>264</sup> or Wedler,<sup>265</sup>

$$\tilde{\nu} = \frac{2\pi}{k_w} = \frac{1}{\lambda_w} = \frac{q}{l}. \quad (\text{E.1})$$

Eq. E.1 uses  $q$ , the number of waves within the total length  $l$ . In chap. 4.4.6 the melt flow instabilities are characterized via two methods:

- 1. Manual read out:** The operator is manually counting the number of waves which he sees in an image.
- 2. FT-image analysis:** The images are analysed via a FT-algorithm by a computer resulting in a peak in the magnitude spectrum which indicates the number of lines in the image.

By both methods, a quantity with the units of waves per image is obtained. For the comparison of both methods for analysing the images of the melt flow instabilities neither the wavenumber  $k_w$  nor the wavelength  $\lambda_w$  nor the spatial frequency  $\tilde{\nu}$  are of primary interest.

The melt flow instabilities are characterized via a digital spatial frequency

$$\tilde{\nu}_{image} = \frac{q_{image}}{N_{image}}. \quad (\text{E.2})$$

In eq. E.2  $q_{image}$  is the number of waves found in  $N_{image}$  images\*. Thus, the unit of  $[\tilde{\nu}_{image}] = \frac{waves}{image}^\dagger$ . Eq. E.2 and eq. E.1 are related via

$$\tilde{\nu} \frac{L}{M} = \tilde{\nu}_{image}. \quad (E.3)$$

Eq. E.3 can be proofed as follows:

**Proof 1. Relation between length space and pixel space**

Starting with eq. E.1 a relation has to be found between the length scales and the pixel scales (fig. E.1). Thus, the length  $l$  is related to the pixel ratio  $m/M$  of the

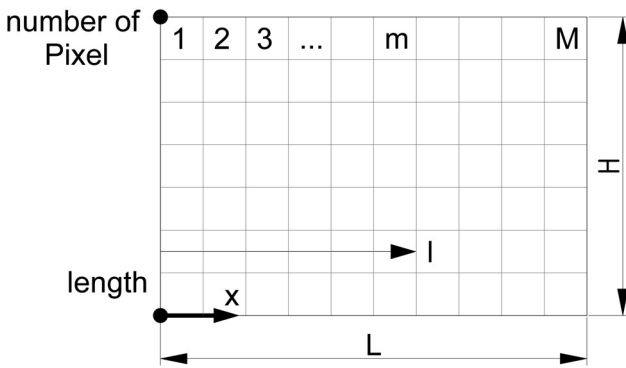


**Figure E.1.** – Relation between the length scale and the pixel scale of a digital image.

actual amount of pixels  $m$  relative to the total amount of pixels  $M$  in a row and the representative width  $L$  of the image in mm, as

$$l = \frac{m}{M} L. \quad (E.4)$$

Substituting  $l$  in eq. E.1 by eq. E.4 results in

$$\tilde{\nu} = \frac{q}{mL} M. \quad (E.5)$$

By multiplying eq. E.5 with  $L/M$ ,

$$\tilde{\nu} \frac{L}{M} = \frac{q}{m}. \quad (E.6)$$

\* Usually  $N_{image} = 1$ .

† The unit  $\frac{waves}{image}$  is abbreviated to  $image^{-1}$ .

---

The right side of eq. E.6 is related to the right side of eq. E.2 as follows. If  $l$  equals  $L$ , which is the width of the whole image of the size of  $M$  pixels, then  $q \equiv q_{image}$ . Thus,  $m = M$ . Using this, the right side of eq. E.6 is

$$\frac{q}{m} = \frac{q_{image}}{M}. \quad (E.7)$$

By allowing  $K$  images to be used for one analysis,

$$N_{image} = K \cdot M. \quad (E.8)$$

With rearranging eq. E.8 and using it to substitute  $M$  in eq. E.7 it follows, that

$$\frac{q}{m} = \frac{q_{image}}{N_{image}}. \quad (E.9)$$

The right side of eq. E.9 is identical with the right side of eq. E.2. Thus, it has been proven that

$$\tilde{v} \frac{L}{M} = \tilde{v}_{image}. \quad (E.10)$$

□



# Appendix F

## Tack: An Adhesive Material Property

A definition of tack is given by the ASTM as:

“ Tack is the property of a material which enables it to form a physical bond of a measurable strength upon contact with another surface.”<sup>266</sup>  
(ASTM D 1878-61T)

In daily life tack is known as stickiness, e.g. of adhesive tapes, adhesive notes etc., and is measured by the thumb test<sup>267,268</sup> The adhesive bonding is dependent on the combination of adhesive (e.g. glue) and adherent (e.g. substrate material).<sup>269</sup> The strength of the adhesive bonding can be measured either as the peak force or as the work of detachment, which is needed to remove the adhesive from the substrate, fig. F.1.<sup>247,259</sup> For measuring the adhesive strength different devices have been established,<sup>266</sup> e.g.:

1. The rolling ball tack test
2. The loop tack test
3. The peeling tack test
4. The probe tack test

The rolling ball tack test is used since the 1950's in industry.<sup>267</sup> A metal ball rolls down an inclined plane at the end of the inclined plane the adhesive material (mostly adhesive tapes) is put on a horizontal plane, see fig. F.2.

---

\* The thumb is pressed against the adhesive surface and then retracted. Thus, the adhesive force is felt.

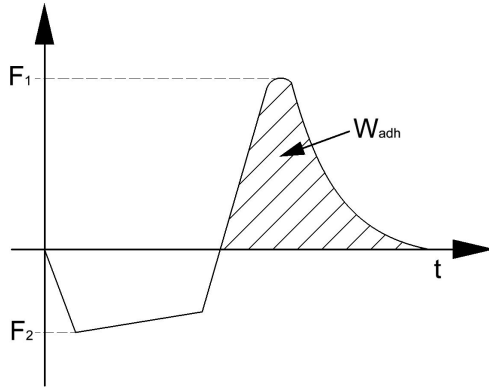


**Figure F.1.** – Peak force  $F_1$  and work of detachment  $W_{adh}$  of tack experiments.

The distance which the ball can travel on the adhesive gives a measure of the strength of the adhesive bonding.

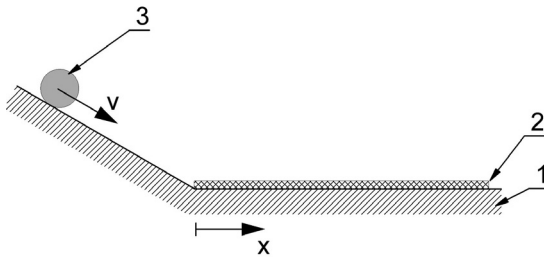


**Figure F.2.** – Rolling ball tack test. (1) substrate, (2) adhesive and (3) metal ball.

For the loop test, a loop is formed out of an adhesive tape, fig. F.3a. The loop is brought into contact with a defined surface for a defined time, but without any force, fig. F.3b. Then the loop is removed from the surface with a defined rate and the force is measured, fig. F.3c.

The peeling test<sup>270,271</sup> is similar to the loop test. A adhesive tape is brought into contact with surface. After a defined time the tape is peeled of the surface under a defined angle  $\alpha$ , fig. F.4.

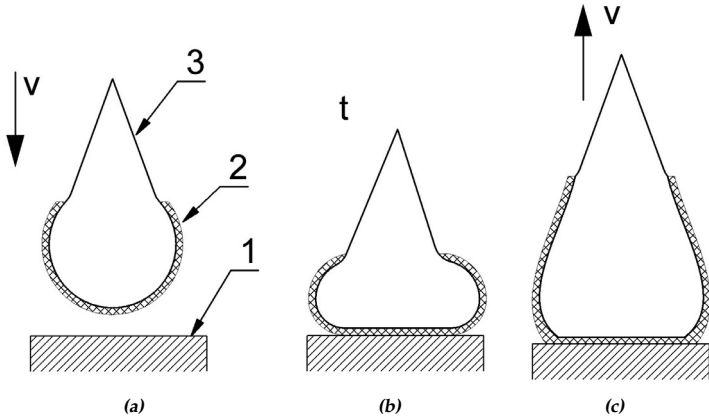


**Figure F.3.** – Loop tack test. (1) substrate, (2) adhesive and (3) tape. (a) a loop of an adhesive tape is brought into contact with the substrate. (b) the loop is kept for a time  $t$  in contact with the substrate. (c) afterwards it is removed with a defined rate.

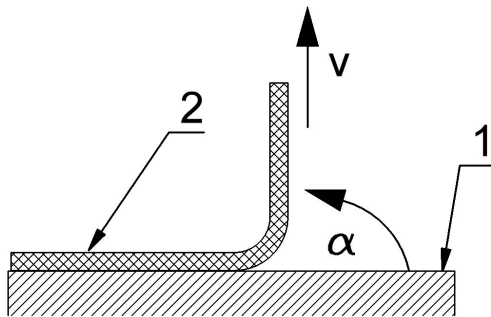


**Figure F.4.** – Peel tack test. (1) substrate and (2) adhesive tape.

For the probe tack test the adhesive is applied on a substrate plate, fig. F.5a. A cylindrical or spherical geometry is press on the adhesive for a defined time and with a defined force, fig. F.5b. Then the geometry and the adhesive are separated with a defined rate and the force is measured, fig. F.5a. While the probe moves upwards from the adhesive layer the formation of fibrils can be observed.<sup>250</sup> The formation of fibrils influence the strength of the adhesive. The success of the probe tack technique is based on the works of Zosel.<sup>247,272</sup>

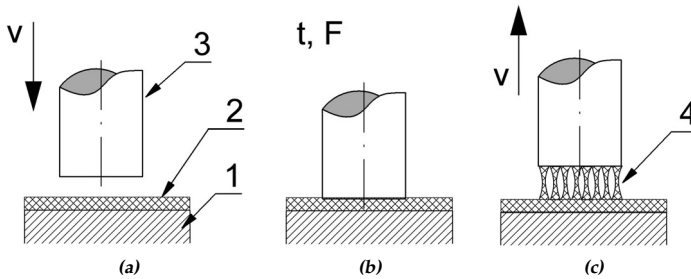


**Figure F.5.** – Probe tack test. (1) substrate, (2) adhesive, (3) probe geometry and (4) fibrils. (a) probe geometry is brought into contact with the adhesive. (b) the probe is kept for a time  $t$  with a force  $F$  in contact with the adhesive. (c) the probe is removed with a defined velocity  $v$ .

# Appendix G

## Mass and Conservation of Mass

The following summary of the deduction of the balance of mass equation can be found in a similar form in the textbook of e.g. Spurk,<sup>39</sup> to name only one of many.

The mass  $m$  of a mechanical body can be defined as the integral of all infinite small elements  $dm$  of a set  $\mathcal{M}$  of material points:

$$m = \int_{\mathcal{M}} dm \quad (\text{G.1})$$

The conservation of mass of a system is given by the following definition

**Definition 12. Conservation of mass**

*The mass of a closed physical system will be for all times a constant and thus has a vanishing time derivative,*

$$\frac{Dm}{Dt} = 0. \quad (\text{G.2})$$

□

The definition of the conservation of mass uses the material derivative  $D/Dt$  as explained in chap. H. In eq. G.1 the mass is substituted by the continuous density function  $\rho(x_i, t)$  by using

$$dm = \rho(x_i, t) dV. \quad (\text{G.3})$$

With eq. G.3 the eq. G.1 changes to

$$m = \iiint_{V(t)} \rho(x_i, t) dV. \quad (\text{G.4})$$

Similar statements can be made for an arbitrary continuous function  $f(x_i, t)$ .

$$\int_{\mathcal{M}} f(x_i, t) dm = \iiint_{V(t)} f(x_i, t) \rho(x_i, t) dV. \quad (G.5)$$

The material time derivative of eq. G.5 becomes

$$\frac{D}{Dt} \int_{\mathcal{M}} f(x_i, t) dm = \frac{D}{Dt} \iiint_{V(t)} f(x_i, t) \rho(x_i, t) dV. \quad (G.6)$$

For a continuous function the material derivative can be taken into the integral, as shown for the right side of eq. G.6

$$\frac{D}{Dt} \iiint_{V(t)} f(x_i, t) \rho(x_i, t) dV = \iiint_{V(t)} \frac{D}{Dt} f(x_i, t) \rho(x_i, t) dV. \quad (G.7)$$

For the problems which are discussed in this work the assumption is reasonable that the density is homogeneously distributed over the whole body and is not a function of time, so

$$\rho \neq \hat{\rho}(x_i, t) \text{ and } \rho = \text{const.} \quad (G.8)$$

Using eq. G.8 in eq. G.7, the integrand on the right side of eq. G.7 is changed to

$$\iiint_{V(t)} \frac{D}{Dt} f(x_i, t) \rho dV = \iiint_V \frac{Df(x_i, t) \rho}{Dt} dV + \iiint_V f(x_i, t) \rho \frac{DdV}{Dt}. \quad (G.9)$$

The right side of eq. G.9 possesses only integrals over fixed volumes. The further deductions are applied on a constant reference volume  $V_0$ , for which it is valid that

$$dV = JdV_0 \quad (G.10)$$

and the material time-derivative will be

$$\frac{DdV}{Dt} = \frac{DJ}{Dt} dV_0. \quad (G.11)$$

In both equations (eq. G.10 and eq. G.11) appears the functional determinant  $J = \frac{\partial x_i}{\partial \xi_j}$ . Introducing eq. G.10 and eq. G.11 into eq. G.9 leads to

$$\begin{aligned} \iiint_{V(t)} \frac{D}{Dt} f(x_i, t) \rho dV &= \iiint_V \frac{Df(x_i, t) \rho}{Dt} JdV_0 + \iiint_V f(x_i, t) \rho \frac{DJ}{Dt} dV_0 \\ &= \iiint_V \left( \frac{Df(x_i, t) \rho}{Dt} + f(x_i, t) \rho \frac{\partial u_i}{\partial x_i} \right) dV. \end{aligned} \quad (G.12)$$

---

The right side of eq. G.12 has to be equal to zero, according to eq. G.2. Further we are interested in the mass flow through a certain surface  $f(x_i, t) = A(x_i, t)$  and the density  $\rho$  can be taken in front of the integral in eq. G.12 and the whole equation can be divided by  $\rho$ , leaving

$$\begin{aligned}
 0 &= \iiint_x \left( \frac{DA(x_i, t)\rho}{Dt} + A(x_i, t)\rho \frac{\partial u_i}{\partial x_i} \right) dx \\
 &= \iiint_x \left( \frac{\partial A(x_i, t)\rho}{\partial t} + \frac{\partial A(x_i, t)\rho}{\partial x_i} u_i + A(x_i, t)\rho \frac{\partial u_i}{\partial x_i} \right) dx \quad (\text{G.13})
 \end{aligned}$$

or in the differential version of eq. G.13

$$0 = \frac{\partial A(x_i, t)\rho}{\partial t} + \frac{\partial A(x_i, t)\rho}{\partial x_i} u_i + A(x_i, t)\rho \frac{\partial u_i}{\partial x_i}. \quad (\text{G.14})$$



# Appendix H

## Material Derivative

The following relation can be found in books about fluid mechanics, i.e. the book of Hutter<sup>49</sup> or Spurk.<sup>39</sup> The material derivative is symbolically given by

$$\frac{D(f(x_i, t))}{Dt} \tag{H.1}$$

and represents the time derivative of a flow property  $f(x_i, t)$  in the material coordinates  $\zeta_i(x_i, t)$ . For the most fluid mechanical studies it is more convenient to use the field coordinates  $x_i(t)$ . With the field coordinates the material derivative is written as

$$\frac{D(f)}{Dt} = \frac{\partial f(x_i, t)}{\partial t} + \frac{\partial f(x_i, t)}{\partial x_i} u_i. \tag{H.2}$$



# Appendix I

## Improved Mass Balance

In the following section the newly stated mass balance is deduced. Starting with eq. G.14 under the assumption of the incompressibility (stated in chap. 5.2) eq. G.14 can be divided by the density  $\rho$ , thus

$$0 = \frac{\partial A(x_i, t)}{\partial t} + \frac{\partial A(x_i, t)}{\partial x_i} u_i + A(x_i, t) \frac{\partial u_i}{\partial x_i}. \quad (\text{I.1})$$

The next step is to describe the flow in the CaBER experiment in cylindrical coordinates  $x_i = [x, r, \varphi]$ , so eq. I.1 is rewritten into

$$\begin{aligned} 0 &= \frac{\partial A(x_i, t)}{\partial t} + u \frac{\partial A(x_i, t)}{\partial x} + \dot{r} \frac{\partial A(x_i, t)}{\partial r} + \frac{1}{r} \frac{\partial A(x_i, t)}{\partial \varphi} \\ &+ A(x_i, t) \frac{1}{r} \left( \frac{\partial(ur)}{\partial x} + \frac{\partial\dot{\varphi}}{\partial \varphi} + \frac{\partial(\dot{r}r)}{\partial r} \right). \end{aligned} \quad (\text{I.2})$$

As postulated in the assumption of the symmetry and assumption of the cylindrical shape in chap. 5.2, the filament should be strictly cylindrical. This assumption further reduces eq. I.2 to

$$\begin{aligned} 0 &= \frac{\partial A(x_i, t)}{\partial t} + u \frac{\partial A(x_i, t)}{\partial x} + \dot{r} \frac{\partial A(x_i, t)}{\partial r} \\ &+ A(x_i, t) \frac{1}{r} \left( \frac{\partial(ur)}{\partial x} + \frac{\partial(\dot{r}r)}{\partial r} \right). \end{aligned} \quad (\text{I.3})$$

Further the previous cited assumptions also require that the cylinder is not only rotational symmetric to the  $x$ -axis but also symmetric to the  $r - \varphi$ -plane in  $x = 0$ . This assumption reduces eq. I.3 to

$$0 = \frac{\partial A(x_i, t)}{\partial t} + \dot{r} \frac{\partial A(x_i, t)}{\partial r} + A(x_i, t) \frac{1}{r} \left( \frac{\partial(\dot{r}r)}{\partial r} \right). \quad (\text{I.4})$$

The last term of eq. I.4 is analysed by using the rules for partial differentiation and the equation for the cross-section area  $A(x_i, t)$  and its derivative\*:

$$\begin{aligned} \frac{\partial(\dot{r}r)}{\partial r} &= \frac{\partial \dot{r}}{\partial r} r + \underbrace{\frac{\partial r}{\partial r}}_{=1} \dot{r} \\ &= \underbrace{\frac{\partial \dot{r}}{\partial r}}_{=\dot{\epsilon}_2} r + \dot{r}. \end{aligned} \quad (\text{I.7})$$

Using eq. I.7, eq. I.6 and eq. I.5 in eq. I.4 it is obtained, that

$$0 = \frac{\partial A(x_i, t)}{\partial t} + 2\pi r \dot{r} + \pi r (r \dot{\epsilon}_2 + \dot{r}). \quad (\text{I.8})$$

As a final step to the solution of the eq. I.8 the focus lies on the time-derivative of  $A(x_i, t)$  which can be written as

$$\begin{aligned} \frac{\partial A(x_i, t)}{\partial t} &= \frac{\partial \pi r^2}{\partial t} \\ &= 2\pi r \dot{r}. \end{aligned} \quad (\text{I.9})$$

Substituting the first term on the right side of eq. I.8 by eq. I.9 leads to

$$\begin{aligned} 0 &= 2\pi r \dot{r} + 2\pi r \dot{r} + \pi r (r \dot{\epsilon}_2 + \dot{r}) \\ &= 5\pi r \dot{r} + \pi r^2 \dot{\epsilon}_2. \end{aligned} \quad (\text{I.10})$$

In eq. I.10 only the elongation rate in  $r$ -direction  $\dot{\epsilon}_2$  is unknown, because the radius  $r(t)$  is accessible via measurements and therefore its time-derivative  $\dot{r}$  is calculable. Based on this, a new equation is found determine  $\dot{\epsilon}_2$ , as

$$\dot{\epsilon}_2 = -5 \frac{\dot{r}}{r}. \quad (\text{I.11})$$

In chap. 5  $\dot{\epsilon}_2$  is named  $\dot{\epsilon}_{new}$ , in order to avoid confusion with the index for the coordinate direction and in order to highlight its new derivation within this thesis.

---

\* The cross-section area of a cylinder is found to be

$$A(x_i, t) = \pi r^2, \quad (\text{I.5})$$

$$\frac{\partial A(x_i, t)}{\partial r} = 2\pi r. \quad (\text{I.6})$$

# Appendix J

## Surface Tension

This section handles the definition of the surface tension in a similar way, as found in many textbooks.<sup>39,265,273,274</sup> One property of liquids is the possibility to form a free surface and in combination with this they exhibit the phenomenon of surface tension. From an atomistic point of view the

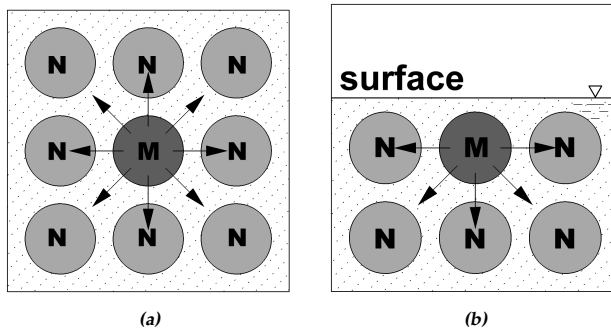


**Figure J.1.** – Intermolecular interaction of molecules of a liquid. If the molecule M is (a) in the bulk of the liquid and (b) if the molecule M is on the surface of the liquid.

creation of a free surface with an respective surface tension is based on intermolecular interactions. A single molecule, called M, located in the middle of a liquid is surrounded all around by similar neighbours N (see fig. J.1a). Thus, M has the same attracting forces  $F$  from all sides. If the

same molecule M is located on the surface of the liquid (see fig. J.1b) the interaction of forces is different, because towards the surface there are no molecules which can interact with M. Thus, M has a force which pulls it back to the bulk of the liquid. This introverted force is the reason why liquids tend to minimize their surface in order to minimize the amount of force.

In a macroscopic view the vector of surface tension  $\sigma_{\Gamma,i}$  can be described as the factor of proportionality between the capillary force  $F_{cap,i}$  and the according line element  $\Delta l$ ,

$$F_{cap,i} = \sigma_{\Gamma,i} \Delta l. \quad (J.1)$$

The vector of surface tension  $\sigma_{\Gamma,i}$  is defined by the capillary constant\*  $\Gamma$  which depends on the pair of the two fluids and the normal vector  $n_i$  of the line segment on the surface plane.

$$\sigma_{\Gamma,i} = \Gamma n_i. \quad (J.2)$$

If the surface is stationary then the tangential component is zero.

---

\* Also named surface tension.

## Appendix K

### The Young-Laplace Equation and its Application on a Cylindrical Body

Young and Laplace independently derived an equation for the balance between the surface tension and the inner stresses of a fluid droplet. This is in accordance to the surface tension which was explained in the previous chapter (chap. J).

For an ideal spherical droplet with the radius  $r$ , Young<sup>275</sup> and Laplace\* found that the inner stress  $\sigma_{11}$  is in balance with the surface tension  $\Gamma$ , as postulated via

$$\sigma_{11} = \frac{2\Gamma}{r}. \quad (\text{K.1})$$

This eq. K.1 is derived by balancing the energy which is needed to change the volume of the droplet  $dW_V$  and with the energy which is needed to change the surface  $dW_S$ . Both changes in energy are given by

$$dW_S = \Gamma dA \text{ and} \quad (\text{K.2})$$

$$dW_V = \sigma_{11} dV. \quad (\text{K.3})$$

---

\* Pierre Simon Marquis de Laplace (\*23. March 1749 in Beaumont-en-Auge, France; †5. March 1827 in Paris, France) was a French physicist and mathematician.<sup>5</sup>

The changes in surface and volume of a sphere is geometrically\* given by

$$dA = 8\pi r dr \text{ and} \quad (\text{K.6})$$

$$dV = 4\pi r^2 dr. \quad (\text{K.7})$$

By using eq. K.6 and eq. K.7 in eq. K.2 and eq. K.3 the Young-Laplace equation of eq. K.1 is obtained.

## K.1 Application of the Young-Laplace Equation on a Cylindrical Body

Chap. 5 explains the importance of the balance between inner stresses and the surface stresses during the CaBER experiment. An equation as formulated by Young and Laplace is needed. Only the constraints of the CaBER experiment have to be obeyed. This means that instead of an ideal spherical drop of a fluid, there is now a slender cylinder of a fluid under investigation.<sup>†</sup> In the following the complete derivation of the Young-Laplace equation for a cylindrical body<sup>‡</sup>, in the further called cylindrical Young-Laplace equation, is given. As for the ordinary Young-Laplace equation (eq. K.1) the energy of change of the surface  $W_{S,c}$  and the energy of change of the volume  $W_{V,c}$  have to be balanced.

For this the incremental change of the surface  $dA_{c,i}$  and the incremental change of the volume  $dV_{c,i}$  are used. To obtain the equations for the incremental changes the surface  $A_c$  and the volume  $V_c$  of the cylinder as given by eq. K.8 and eq. K.9, have to be differentiated in terms of all important

---

\* Formulate the derivatives of  $A$  and  $V$  of a sphere with respect to  $r$ .

$$A = 4\pi r^2 \text{ and} \quad (\text{K.4})$$

$$V = \frac{4}{3}\pi r^3. \quad (\text{K.5})$$

<sup>†</sup> To the author is no literature source known which states the Young-Laplace equation for a cylindrical body. However, by means of its simplicity there surely should be one.

<sup>‡</sup> An additional index  $c$  is added to the physical quantities, e.g.  $W_V \Rightarrow W_{V,c}$

coordinates  $i = [r, z]$ .\*

$$A_c = 2\pi r^2 + 2\pi rh \text{ and} \quad (\text{K.8})$$

$$V_c = \pi r^2 h. \quad (\text{K.9})$$

The incremental changes in  $r$ -direction are given by

$$dA_{c,r} = 4\pi r dr + 2\pi h dr \text{ and} \quad (\text{K.10})$$

$$dV_{c,r} = 2\pi r h dr. \quad (\text{K.11})$$

With the eq. K.10 and eq. K.11 the energies of change for the  $r$ -coordinate are given by

$$\begin{aligned} dW_{S,r} &= \Gamma dA \\ &= \Gamma (4\pi r dr + 2\pi h dr) \text{ and} \end{aligned} \quad (\text{K.12})$$

$$\begin{aligned} dW_{V,r} &= \sigma_{22} dV \\ &= \sigma_{22} 2\pi r h dr. \end{aligned} \quad (\text{K.13})$$

By setting eq. K.12 equal to eq. K.13 the first of the two equations of the balance of the forces for this problem is obtained

$$\begin{aligned} dW_{S,r} &= dW_{V,r} \\ \Gamma (4\pi r dr + 2\pi h dr) &= \sigma_{11} 2\pi r h dr \\ \Gamma \left( 2\frac{A}{h} + \pi r \right) &= \sigma_{22} A. \end{aligned} \quad (\text{K.14})$$

In eq. K.14 the cross-sectional area  $A = \pi r^2$  is used. Further simplifications of eq. K.14 are possible if the assumed slenderness of the cylinder, meaning  $r \ll h$ , is taken into account:

$$\Gamma (\pi r) = \sigma_{22} A. \quad (\text{K.15})$$

The second equation of the balance of the forces is derived by studying the changes in  $z$ -direction. The incremental changes in  $z$ -direction are given by

$$dA_{c,z} = 2\pi r dz \text{ and} \quad (\text{K.16})$$

$$dV_{c,z} = \pi r^2 dz. \quad (\text{K.17})$$

\* The angular coordinate  $\varphi$  can be neglected due to the rotational symmetry of the problem.

With the eq. K.16 and eq. K.17 the energies of change for the  $z$ -coordinate are given by

$$\begin{aligned}dW_{S,z} &= \Gamma dA \\ &= \Gamma 2\pi r dz \text{ and} \end{aligned} \tag{K.18}$$

$$\begin{aligned}dW_{V,z} &= \sigma_{11} dV \\ &= \sigma_{11} \pi r^2 dz. \end{aligned} \tag{K.19}$$

By setting eq. K.18 equal to eq. K.19 the second of the two equations of balance for this problem is obtained

$$\begin{aligned}dW_{S,z} &= dW_{V,z} \\ \Gamma 2\pi r dz &= \sigma_{11} \pi r^2 dz \\ \Gamma 2\pi r &= \sigma_{11} A. \end{aligned} \tag{K.20}$$

For the CaBER experiment with the added measurement of the axial force  $F$  the eq. K.20 has to be extended by an additional term. This is conducted by assuming that external axial force  $F$  is balanced by the inner stress and the surface tension, like

$$\sigma_{11} A - \Gamma 2\pi r = F. \tag{K.21}$$





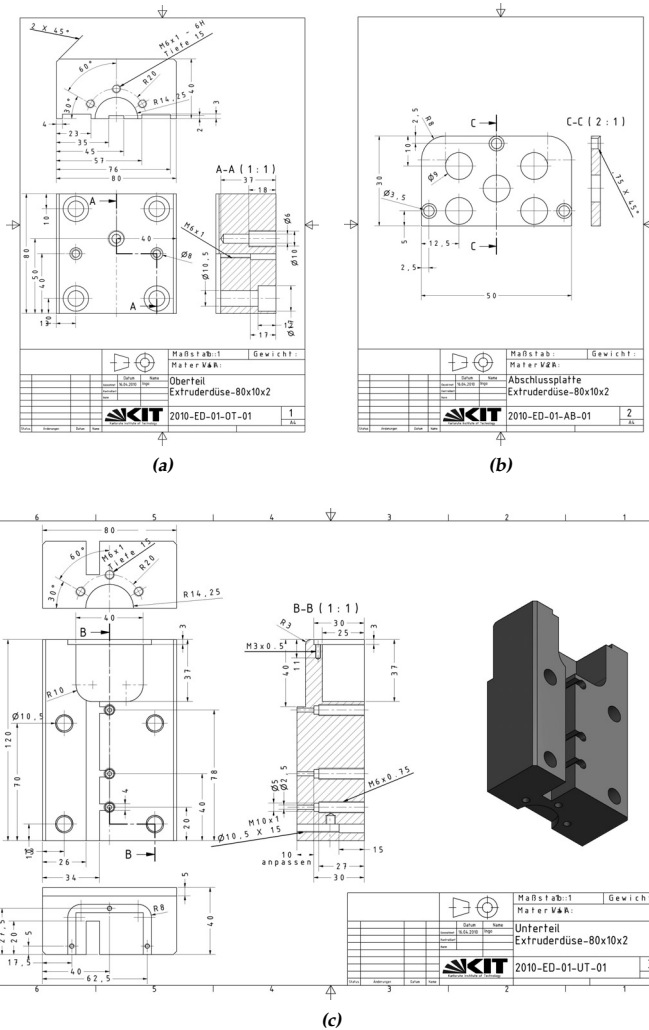


**Figure L.3.** – Technical drawings of the parts of the sharkskin die-2, fig. 4.7. (a) upper half die, (b) plug box plate and (c) lower half die.

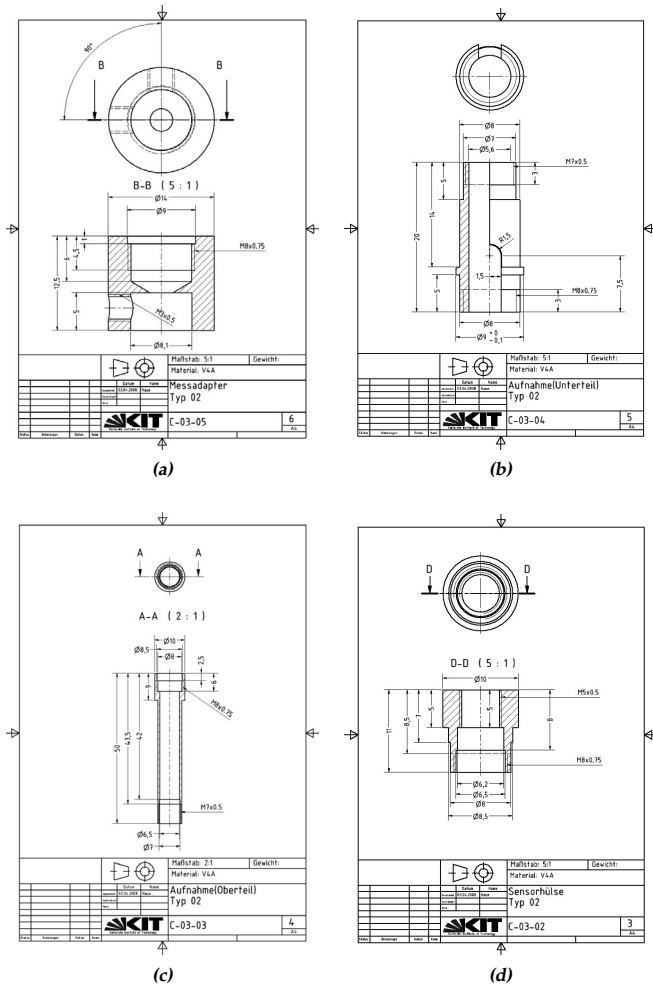


**Figure L.4.** – Technical drawings of the parts of the CaBER, fig. 5.7.  
 (a) adapter, (b) lower shaft, (c) upper shaft and (d) head of the shaft.

# **Appendix M**

## **A Short Genealogical Tree of this Work**

The science named rheology and the knowledge about polymers are rather young (less than 100 years), as written in chap. 1 and chap. 2.4. However, the fundamentals needed for the understanding of the rheology of polymer melts reach back to the 17th century, fig. M.1.

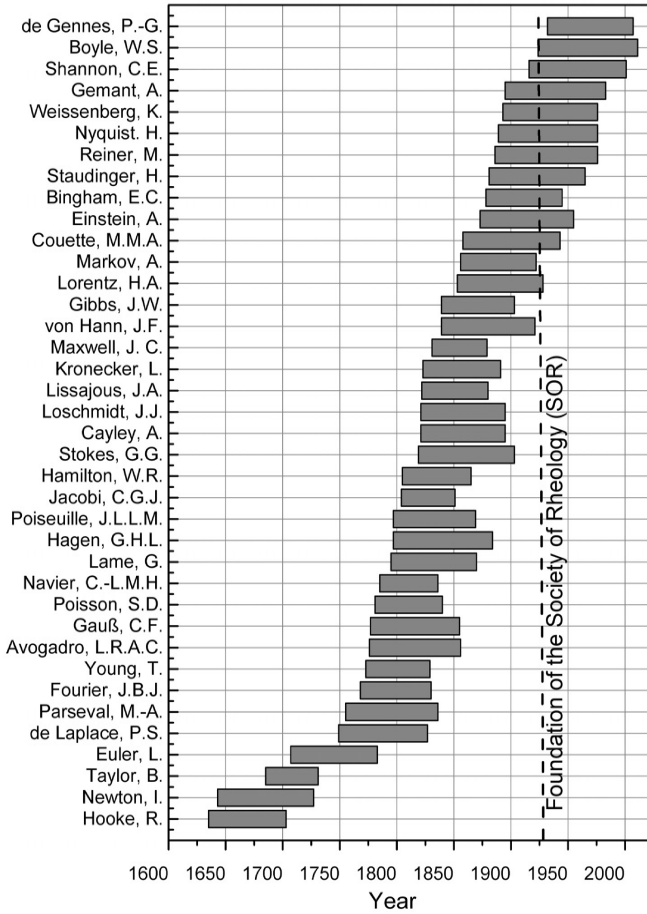


**Figure M.1.** – Time-line of famous scientist. The grey bars are indicating the lifetime of each scientist. The dashed line marks the year in which the Society of Rheology was founded (1929).

## References

- [1] A.C. Doyle. *The Adventures of Sherlock Holmes*. Strand Magazine, London, 1892.
- [2] A. Nadai. Eugene Cook Bingham. *J. Colloid Interface Sci.*, 2(1):1–5, 1947.
- [3] G.W. Scott-Blair. Markus Reiner 1886-1976. *Rheol. Acta*, 15(7):365–366, 1976.
- [4] D. Gross, W. Hauger, W. Schnell, and P. Wriggers. *Technische Mechanik 4*. Springer, Berlin, 2004.
- [5] C.C. Gillispie, editor. *Complete dictionary of scientific biography*. Scribners, Detroit, 2008.
- [6] J. Harris. Karl Weissenberg 1893-1976. *Rheol. Acta*, 15:281–282, 1976.
- [7] M.M.A. Couette. Etudes sur le frottement des liquides. *Ann. Chim. Phys.*, 21:433–510, 1891.
- [8] J.M. Piau, M. Bremond, J.M. Couette, and M. Piau. Maurice Couette, one of the founders of rheology. *Rheol. Acta*, 33(5):357–368, 1994.
- [9] M. Mooney and R.H. Ewart. The conicylindrical viscometer. *Physics*, 5(11):350–354, 1934.
- [10] S.M. Freeman and K. Weissenberg. Some new rheological phenomena and their significance for the constitution of materials. *Nature*, 162:320–323, 1948.
- [11] A.J. Giacomin, T. Samurkas, and J.M. Dealy. A novel sliding plate rheometer for molten plastics. *Polym. Eng. Sci.*, 29(8):499–504, 1989.
- [12] S.G. Hatzikiriakos and J.M. Dealy. Wall slip of molten high density polyethylene. i. sliding plate rheometer studies. *J. Rheol.*, 35(4):497–523, 1991.

- [13] G.W. Ehrenstein. *Polymer-Werkstoffe*. Hanser, München, 1999.
- [14] F.R. Schwarzl. *Polymermechanik: Struktur und mechanisches Verhalten von Polymeren*. Springer, Berlin, 1990.
- [15] K. Weissenberg. A continuum theory of rheological phenomena. *Nature*, 159:310–311, 1947.
- [16] M. Wilhelm, D. Maring, and H.-W. Spiess. Fourier-transform rheology. *Rheol. Acta*, 37(4):399–405, 1998.
- [17] J.S. Bendat and A.G. Piersol. *Random Data: Analysis and Measurement Procedures*. Wiley Interscience, New York, 2010.
- [18] I.N. Bronstein and K.A. Semendjajew. *Taschenbuch der Mathematik*. Harri Deutsch, Frankfurt a.M., 2001.
- [19] J.F. James. *A Student's Guide to Fourier Transform*. Cambridge University Press, Cambridge, 2002.
- [20] T. Butz. *Fouriertransformierte für Fußgänger*. B.G. Teubner, Stuttgart, 1998.
- [21] K. von Finkenstein, J. Lehn, H. Schellhaas, and H. Wegmann. *Arbeitsbuch der Mathematik für Ingenieure II*. B.G. Teubner, Stuttgart, 2000.
- [22] R.N. Bracewell. *The Fourier Transform and its Applications*. McGraw-Hill, New York, 1965.
- [23] K.K. Kammeyer and K. Kroschek. *Digitale Signalverarbeitung*. B.G. Teubner, Wiesbaden, 2006.
- [24] L.N. Trefethen. *Spectral methods in MATLAB*. SIAM, Philadelphia, 2000.
- [25] D.J. Higham and N.J. Higham. *MATLAB Guide*. SIAM, Philadelphia, 2005.
- [26] M. Frigo and S.G. Johnson. The design and implementation of FFTW3. *Proceedings of the IEEE*, 93(2):216–231, 2005.
- [27] J.E. Brittain. Electrical engineering hall of fame: Harry Nyquist. *Proc. IEEE*, 98(8):1535–1537, 2010.
- [28] C. Tropea, N. Damaschke, and H. Nobach. *Messtechnik I: Grundlagen der Messtechnik*. Shaker, Aachen, 2003.

- 
- [29] K. Schmidt-Rohr and H.W. Spiess. *Multidimensional Solid-State NMR and Polymers*. Academic Press, London, 1998.
- [30] J. Hohnerkamp. *Stochastic Dynamical Systems: Concepts, Numerical Methods, Data Analysis*. VCH Wiley, New York, 1994.
- [31] J.F. Böhme. *Stochastische Signale*. Teubner, Stuttgart, 1998.
- [32] E. Hänsler. *Statistische Signale*. Springer, Berlin, 1997.
- [33] L. Boltzmann. Einige allgemeine Sätze über das Wärmegleichgewicht. *Wien. Ber.*, 63:679–711, 1871.
- [34] J.H. Argyris, G. Faust, M. Haase, and R. Friedrich. *Die Erforschung des Chaos*. Springer, Heidelberg, 2010.
- [35] E.O. Doebelin and D.N. Manik. *Measurement Systems*. Tata McGraw-Hill, New Delhi, 2011.
- [36] D.A. Skoog, F.J. Holler, and S.R. Crouch. *Principles of instrumental analysis*. Thomson, Brooks/Cole, Belmont, 2007.
- [37] S. W. Golomb, E. Berlekamp, T.M. Cover, R.G. Gallager, J.L. Massey, and A.J. Viterbi. Claude Elwood Shannon (1916-2001). *Not. Amer. Math. Soc.*, 49(1):8–16, 2002.
- [38] T. Cawkell. Claude Elwood Shannon, 1916–2001. *J. Inf. Sci.*, 27:127–128, 2001.
- [39] J.H. Spurk. *Strömungslehre*. Springer, Berlin, 2004.
- [40] G. Böhme. *Strömungsmechanik nichtnewtonscher Fluide*. B.G.Teubner, Stuttgart, 2000.
- [41] R.G. Larson. *The Structure and Rheology of Complex Fluids*. Oxford, New York, 1999.
- [42] J.M. Dealy and R.G. Larson. *Structure and rheology of molten polymers: from structure to flow behavior and back again*. Hanser, München, 2006.
- [43] Y.P.A. Lovell and R.J. Young. *Introduction to Polymers*. CRC Press, Boca Raton, 1991.
- [44] C. Macosko. *Rheology, Principles, Measurements and Applications*. VCH Wiley, New York, 1994.
- [45] G. Schramm. *Einführung in die Rheologie und Rheometrie*. Gebrüder Haake GmbH, Karlsruhe, 2000.

- [46] T. Mezger. *Das Rheologie-Handbuch: für Anwender von Rotations- und Oszillations-Rheometern*. Vincentz, Hannover, 2006.
- [47] P.J. Carreau, D. De Kee, and R.P. Chabra. *Rheology of Polymeric Systems: Principle and Application*. Hanser, München, 1997.
- [48] M. Wilhelm. *Introduction to Rheology*. Karlsruhe Institute of Technology (KIT), Karlsruhe, 2008. lecture script Prof. Wilhelm.
- [49] K. Hutter. *Fluid- und Thermodynamik: Eine Einführung*. Springer, Berlin, 2003.
- [50] R. Hooke. *A description of helioscopes and some other instruments*. John Martyn, London, 1676.
- [51] R. Hooke. De potentia restitutiva or of spring: Explaining the power of springing bodies. In *Lectiones Cutlerinanae*. John Martyn, London, 1679.
- [52] I. Newton. *Philosophiae Naturalis Principia Mathematica*. Barrilott & filii, Genevae, 1739.
- [53] A. Einstein. *Die Grundlage der allgemeinen Relativitätstheorie*. Barth, Leipzig, 1929.
- [54] E. Klingbeil. *Tensorrechnung für Ingenieure*. BI-Wiss., Mannheim, 1989.
- [55] T. A. Osswald and G. Menges. *Material science of polymers for engineers*. Carl Hanser Verlag, München, 1995.
- [56] C. Truesdell and R.G. Muncaster. *Fundamentals of Maxwells kinetic theory of a simple monatomic gas: Treated as a branch of rational mechanics*. Academic Press, New York, 1980.
- [57] M.D. Lechner, K. Gehrke, E. Nordmeier, and R. Heering, editors. *Makromolekulare Chemie: Ein Lehrbuch für Chemiker, Physiker, Materialwissenschaftler und Verfahrenstechniker*. Birkhäuser, Basel, 2010.
- [58] D. Millar, editor. *The Cambridge dictionary of scientists*. Cambridge Univ. Pr., Cambridge, 2003.
- [59] G. Strobl. *The physics of polymers: concepts for understanding their structure and behaviour*. Springer, Berlin, 2007.
- [60] T.C.B. McLeish and R.G. Larson. Molecular constitutive equations for a class of branched polymers: The pom-pom polymer. *J. Rheol.*, 42(1):81–110, 1998.

- [61] T.I. Burghilea, H.J. Griess, and H. Münstedt. Comparative investigations of surface instabilities (sharkskin) of a linear and a long-chain branched polyethylene. *J. Non-Newtonian Fluid Mech.*, 165:1093–1104, 2010.
- [62] H. Palza, I.F.C. Naue, and M. Wilhelm. In situ pressure fluctuations of polymer melt flow instabilities: Experimental evidence about their origin and dynamics. *Macromol. Rapid Commun.*, 30(21):1799–1804, 2009.
- [63] M. Kempf. *Synthesis and rheology of model comb polymer architectures*. PhD thesis, Karlsruhe Institute of Technology (KIT), 2011.
- [64] M. Kempf, V.C. Barroso, and M. Wilhelm. Anionic synthesis and rheological characterization of poly(p-methylstyrene) model comb architectures with a defined and very low degree of long chain branching. *Macromol. Rapid Commun.*, 31(24):2140–2145, 2010.
- [65] C. Klein. *Rheology and fourier-transform rheology on water-based systems*. PhD thesis, Johannes Gutenberg University Mainz, 2005.
- [66] L. Hilliou and D. Vlassopoulos. Time-periodic structures and instabilities in shear-thickening polymer solutions. *Ind. Eng. Chem. Res.*, 41(25):6246–6255, 2002.
- [67] R. Schröder. *Neue Deutsche Biographie*, volume 7, chapter Hagen, Gotthilf Heinrich Ludwig, page 472. Bayerische Akademie der Wissenschaften, <http://www.deutschebiographie.de/pnd118719874.html>, 1966.
- [68] G. Hagen. Über die Bewegung des Wassers in engen cylindrischen Röhren. *Ann. Phys.*, 122(3):423–442, 1839.
- [69] S.P. Sutera and R. Skalak. The history of poiseuille’s law. *Ann. Rev. Fluid Mech.*, 25:1–20, 1993.
- [70] J.L.M. Poiseuille. Recherches experimentales sur le mouvement des liquides dans les tubes de tres-petits diametres. *Memoires presentes par divers savants a l’Academie Royale des Sciences de l’Institut de France*, IX:433–544, 1846.
- [71] M.H. Wagner, H. Bastian, A. Bernnat, S. Kurzbeck, and C.K. Chai. Determination of elongational viscosity of polymer melts by rme and rheotens experiments. *Rheol. Acta*, 41(4):316–325, 2002.

- [72] D.J. Lohse, S.T. Milner, L.J. Fetters, M. Xenidou, N. Hadjichristidis, R.A. Mendelson, C A. Garcia-Franco, and M.K. Lyon. Well-defined, model long chain branched polyethylene. 2. melt rheological behavior. *Macromolecules*, 35(8):3066–3075, 2002.
- [73] H.M. Laun. Description of the non-linear shear behaviour of a low density polyethylene melt by means of an experimentally determined strain dependent memory function. *Rheol. Acta*, 17(1):1–15, 1978.
- [74] H. Münstedt and H.M. Laun. Elongational behaviour of a low density polyethylene melt. *Rheol. Acta*, 18(4):492–504, 1979.
- [75] H. Münstedt and H.M. Laun. Elongational properties and molecular structure of polyethylene melts. *Rheol. Acta*, 20(3):211–221, 1981.
- [76] W. Gleissle and H. Reichert. Kurzzeit-Rotations-Rheometer zur Messung von hohen Schub- und Normalspannungen bei grossen Schergefällen. *Rheol. Acta*, 12(4):572–577, 1973.
- [77] W. Gleissle. Schub- und Normalspannungsmessungen an Silikonölen bei hohen Schergefällen mit einem neuen Kegel-Platte-Rheometer. *Colloid Polym. Sci.*, 252(10):848–853, 1974.
- [78] W. Gleissle and N. Ohl. On the relaxation of shear and normal stresses of viscoelastic fluids following constant shear rate experiments. *Rheol. Acta*, 29(4):261–280, 1990.
- [79] S.-G. Baek and J.J. Magda. Monolithic rheometer plate fabricated using silicon micromachining technology and containing miniature pressure sensors for  $n_1$  and  $n_2$  measurements. *J. Rheol.*, 47(5):1249–1260, 2003.
- [80] T. Schweizer. Measurement of the first and second normal stress differences in a polystyrene melt with a cone and partitioned plate tool. *Rheol. Acta*, 41(4):337–344, 2002.
- [81] T. Schweizer and A. Bardow. The role of instrument compliance in normal force measurements of polymer melts. *Rheol. Acta*, 45(4):393–402, 2006.
- [82] J.G. Nam, K. Hyun, K. H. Ahn, and S. J. Lee. Prediction of normal stresses under large amplitude oscillatory shear flow. *J. Non-Newtonian Fluid Mech.*, 150(1):1–10, 2008.

- 
- [83] M. Wilhelm. Fourier-transform rheology. *Macromol. Mater. Eng.*, 287(2):83–105, 2002.
- [84] M. Wilhelm, P. Reinheimer, and M. Ortseifer. High sensitivity fourier-transform rheology. *Rheol. Acta*, 38:349–356, 1999.
- [85] M. Wilhelm, P. Reinheimer, M. Ortseifer, T. Neidhöfer, and H.-W. Spiess. The crossover between linear and non-linear mechanical behaviour in polymer solutions as detected by fourier-transform rheology. *Rheol. Acta*, 39(3):241–246, 2000.
- [86] E.W. Weisstein. *CRC concise encyclopedia of mathematics*. Chapman & Hall/CRC, Boca Raton, 2003. 2. ed.
- [87] A. Gemant. Komplexe Viskosität. *Naturwissenschaften*, 23:406–407, 1935.
- [88] A. Gemant. The conception of a complexe viscosity and its application to dielectrics. *Trans. Faraday Soc.*, 175:1582–1590, 1935.
- [89] R.B. Bird and A.J. Giacomin. Who conceived the “complexe viscosity”? *Rheol. Acta*, 51:481–486, 2012.
- [90] M.L. Williams, R.F. Landel, and J.D. Ferry. The temperature dependence of relaxation mechanisms in amorphous polymers and other glass-forming liquids. *J. Am. Chem. Soc.*, 77(14):3701–3707, 1955.
- [91] G.S. Fulcher. Analysis of recent measurements of the viscosity of glasses. *J. Am. Ceram. Soc.*, 8(12):789–794, 1925.
- [92] J.-F. Joanny and P.A. Pincus. Biography of Pierre-Gilles de Gennes. *J. Phys. Chem. B*, 113(12):3593–3594, 2009.
- [93] S. B. Ranavavare, S.A. Safran, and F. Brochard-Wyart. In memory of Pierre-Gilles de Gennes. *J. Phys. Chem. B*, 113(12):3591–3592, 2009.
- [94] P.G. de Gennes. Reptation of a polymer chain in the presence of fixed obstacles. *J. Chem. Phys.*, 55:572, 1971.
- [95] T.-T. Tee and J.M. Dealy. Nonlinear viscoelasticity of polymer melts. *Trans. Soc. Rheol.*, 19(4):595–615, 1975.
- [96] H.D.I. Abarbanel. *Analysis of observed chaotic data*. Springer, Berlin, 1996.
- [97] S. Onogi, T. Masuda, and T. Matsumoto. Non-linear behavior of viscoelastic materials. i. disperse systems of polystyrene solution and carbon black. *Trans. Soc. Rheol.*, 14(2):275–294, 1970.

- [98] Y. Matsumoto, T. Segawa, Y. Warashina, and S. Onogi. Nonlinear behavior of viscoelastic materials. ii. the method of analysis and temperature dependence of nonlinear viscoelastic functions. *Trans. Soc. Rheol.*, 17(1):47–62, 1973.
- [99] H. Komatsu, T. Mitsui, and S. Onogi. Nonlinear viscoelastic properties of semisolid emulsions. *Trans. Soc. Rheol.*, 17(2):351–364, 1973.
- [100] J.S. Dodge and I.M. Krieger. Oscillatory shear of nonlinear fluids i. preliminary investigation. *Trans. Soc. Rheol.*, 15(4):589–601, 1971.
- [101] W. Philippoff. Vibrational measurements with large amplitudes. *J. Rheol.*, 10(1):317–334, 1966.
- [102] K.S. Cho and J.-E. Bae. Geometric insights on viscoelasticity: Symmetry, scaling and superposition of viscoelastic functions. *Korea-Australia Rheol. J.*, 23(1):49–58, 2011.
- [103] Y. Guo, W. Yu, Y. Xu, and C. Zhou. Correlations between local flow mechanism and macroscopic rheology in concentrated suspensions under oscillatory shear. *Soft Matter*, 7(6):2433–2443, 2011.
- [104] E. Guzman, L. Liggieri, E. Santini, Mi. Ferrari, and F. Ravera. Effect of hydrophilic and hydrophobic nanoparticles on the surface pressure response of dppc monolayers. *J. Phys. Chem. C*, 115(44):21715–21722, 2011.
- [105] K. Hyun, M. Wilhelm, C.O. Klein, K. S. Cho, J.G. Nam, K.H. Ahn, S.J. Lee, R.H. Ewoldt, and G.H. McKinley. A review of nonlinear oscillatory shear tests: Analysis and application of large amplitude oscillatory shear (LAOS). *Prog. Polym. Sci.*, 36(12):1697–1753, 2011.
- [106] K. Hyun and W. Kim. A new non-linear parameter  $q$  from ft-rheology under nonlinear dynamic oscillatory shear for polymer melts system. *Korea-Australia Rheol. J.*, 23(4):227–235, 2011.
- [107] S. Kollengodu-Subramanian, B. Srinivasan, J. Zhao, R. Rengaswamy, and G.B. McKenna. Application of empirical mode decomposition in the field of polymer physics. *J. Polym. Sci. Pol. Phys.*, 49(4):277–290, 2011.
- [108] J.L. Leblanc, J.-F. Pilard, E. Pianhanuruk, I. Campistron, and J.-Y. Buzare. Characterizing gum natural rubber samples through advanced techniques. *J. Appl. Polym. Sci.*, 119(5):3058–3071, 2011.

- [109] J.L. Leblanc, M. Putman, and E. Pianhanuruk. A thorough study on the relationships between dispersion quality and viscoelastic properties in carbon black filled sbr compounds. *J. Appl. Polym. Sci.*, 121(2):1096–1117, 2011.
- [110] T. Meins, K. Hyun, N. Dingenouts, M. Fotouhi Ardakani, B. Struth, and M. Wilhelm. New insight to the mechanism of the shear-induced macroscopic alignment of diblock copolymer melts by a unique and newly developed rheo-SAXS combination. *Macromolecules*, 45(1):455–472, 2012.
- [111] H.S. Melito and C.R. Daubert. Rheological innovations for characterizing food material properties. *Ann. Rev. Food Sci. Technol.*, 2:153–179, 2011.
- [112] C. Mendoza, N. Gindy, M. Wilhelm, and A. Fahmi. Linear and non-linear viscoelastic rheology of hybrid nanostructured materials from block copolymers with gold nanoparticles. *Rheol. Acta*, 50(3):257–275, 2011.
- [113] J.G Nam, K.H. Ahn, S.J. Lee, and K. Hyun. Strain stiffening of non-colloidal hard sphere suspensions dispersed in newtonian fluid near liquid-and-crystal coexistence region. *Rheol. Acta*, 50(11-12):925–936, 2011.
- [114] S. Ravindranath, S.-Q. Wang, M. Olechnowicz, V.S. Chavan, and R.P. Quirk. How polymeric solvents control shear inhomogeneity in large deformations of entangled polymer mixtures. *Rheol. Acta*, 50(2):97–105, 2011.
- [115] K. Reinheimer, M. Grosso, and M. Wilhelm. Fourier transform rheology as a universal non-linear mechanical characterization of droplet size and interfacial tension of dilute monodisperse emulsions. *J. Colloid Interface Sci.*, 360(2):818–825, 2011.
- [116] S.A. Rogers, B.M. Erwin, D. Vlassopoulos, and M. Cloitre. Oscillatory yielding of a colloidal star glass. *J. Rheol.*, 55(4):733–752, 2011.
- [117] S.A. Rogers, B.M. Erwin, D. Vlassopoulos, and M. Cloitre. A sequence of physical processes determined and quantified in laos: Application to a yield stress fluid. *J. Rheol.*, 55(2):435–458, 2011.
- [118] L.M.C. Sagis. Dynamic properties of interfaces in soft matter: Experiments and theory. *Rev. Mod. Phys.*, 83(4):1367–1403, 2011.

- [119] W. Sun, Y. Yang, T. Wang, X. Liu, C. Wang, and Z. Tong. Large amplitude oscillatory shear rheology for nonlinear viscoelasticity in hectorite suspensions containing poly(ethylene glycol). *Polymer*, 52(6):1402–1409, 2011.
- [120] A. Takeh, J. Worch, and S. Shanbhag. Analytical rheology of metallocene-catalyzed polyethylenes. *Macromolecules*, 44(9):3656–3665, 2011.
- [121] A. Vananroye, P. Leen, P. Van Puyvelde, and C. Clasen. TTS in LAOS: validation of time-temperature superposition under large amplitude oscillatory shear. *Rheol. Acta*, 50(9-10):795–807, 2011.
- [122] I. Vittorias, D. Lilge, V. Baroso, and M. Wilhelm. Linear and non-linear rheology of linear polydisperse polyethylene. *Rheol. Acta*, 50(7-8):691–700, 2011.
- [123] M.H. Wagner, V.H. Rolon-Garrido, K. Hyun, and M. Wilhelm. Analysis of medium amplitude oscillatory shear data of entangled linear and model comb polymers. *J. Rheol.*, 55(3):495–516, 2011.
- [124] P. Wang, J. Liu, W. Yu, and C. Zhou. Dynamic rheological properties of wood polymer composites: from linear to nonlinear behaviors. *Polym. Bull.*, 66(5):683–701, 2011.
- [125] M. Wilhelm. New methods for the rheological characterization of materials. *Chem. Eng. Process.*, 50(5-6):486–488, May 2011.
- [126] B. Taylor. *Methodus Incrementorum Directa & Inversa*. Impensis Gulielmi Innys, London, 1717.
- [127] R.W. Ramirez. *The FFT Fundamentals and Concepts*. Prentice-Hall, Engelwood Cliffs, 1985.
- [128] M.D. Graham. Wall slip and the nonlinear dynamics of large amplitude oscillatory shear flows. *J. Rheol.*, 39(4):697–712, 1995.
- [129] L. Heymann, S. Peukert, and N. Aksel. Investigation of the solid-liquid transition of highly concentrated suspensions in oscillatory amplitude sweeps. *J. Rheol.*, 46(1):93–112, 2002.
- [130] L.M.C. Sagis, M. Ramaekers, and E. van der Linden. Constitutive equations for an elastic material with anisotropic rigid particles. *Phys. Rev. E*, 63(5):051504, 2001.

- 
- [131] H.G. Sim, K.H. Ahn, and S.J. Lee. Three-dimensional dynamics simulation of electrorheological fluids under large amplitude oscillatory shear flow. *J. Rheol.*, 47(4):879–895, 2003.
- [132] I.A. Vittorias. *Fourier-transform rheology applied on homopolymer melts of different architectures- experiments and finite element simulation*. PhD thesis, TUD - Technical University Darmstadt, 2006.
- [133] K. Hyun and M. Wilhelm. Non-linear rheology of entangled linear and branched polymer melts under large amplitude oscillatory shear. *Kautsch. Gummi Kunstst.*, 4:123–129, 2010.
- [134] A.J. Giacomin, R.S. Jeyaseelan, T. Samurkas, and J.M. Dealy. Validity of separable bkz model for large-amplitude oscillatory shear. *J. Rheol.*, 37(5):811–826, 1993.
- [135] A.J. Giacomin and J.G. Oakley. Structural network models for molten plastics evaluated in large-amplitude oscillatory shear. *J. Rheol.*, 36(8):1529–1546, 1992.
- [136] R.S. Jeyaseelan and A.J. Giacomin. Best fit for differential constitutive model parameters to nonlinear oscillation data. *J. Non-Newtonian Fluid Mech.*, 47:267–280, 1993.
- [137] J.G. Oakley and A.J. Giacomin. A sliding plate normal thrust rheometer for molten plastics. *Polym. Eng. Sci.*, 34(7):580–584, 1994.
- [138] D. van Dusschoten and M. Wilhelm. Increased torque transducer sensitivity via oversampling. *Rheol. Acta*, 40(4):395–399, 2001.
- [139] T. Neidhöfer, M. Wilhelm, and B. Debbaut. Fourier-transform rheology experiments and finite-element simulations on linear polystyrene solutions. *J. Rheol.*, 47(6):1351–1371, 2003.
- [140] M. Wilhelm, M.A. Pollard, R. Graf, K. Klimke, H.-W. Spiess, O. Sperber, C. Piel, and W. Kaminsky. Topology in polyolefines as seen by solid-state NMR and FT-Rheology. *Abstr. Pap. Am. Chem. S.*, 226:U388, 2003.
- [141] M. Wilhelm. FT-Rheology: A very sensitive experimental technique to characterize the non-linear regime in materials. *Kautsch. Gummi Kunstst.*, 58(5):256–258, 2005.
- [142] P. R. Bevington and D. K. Robinson. *Data reduction and error analysis for the physical sciences*. McGraw-Hill, New York, 1992.

- [143] K. von Finkenstein, J. Lehn, H. Schellhaas, and H. Wegmann. *Arbeitsbuch der Mathematik für Ingenieure I*. B.G. Teubner, Stuttgart, 2000.
- [144] H. Benker. *Statistik mit MATHCAD und MATLAB*. Springer, Berlin, 2001.
- [145] I. Vittorias, M. Parkinson, K. Klimke, B. Debbaut, and M. Wilhelm. Detection and quantification of industrial polyethylene branching topologies via Fourier-transform rheology, NMR and simulation using the pom-pom model. *Rheol. Acta*, 46(3):321–340, 2007.
- [146] S. Filipe, I. Vittorias, and M. Wilhelm. Experimental correlation between mechanical non-linearity in laos flow and capillary flow instabilities for linear and branched commercial polyethylenes. *Macromol. Mater. Eng.*, 293(1):57–65, 2008.
- [147] J. Stoer. *Numerische Mathematik 1*. Springer, Berlin, 2005.
- [148] I.F.C. Naue. Kapillarrheologische Detektion von mechanischen Instabilitäten bei der Polymerverarbeitung. Master’s thesis, TUD - Technical University Darmstadt, 2007.
- [149] H. Palza, S. Filipe, I.F.C. Naue, and M. Wilhelm. Correlation between polyethylene topology and melt flow instabilities by determining in-situ pressure fluctuations and applying advanced data analysis. *Polymer*, 51(2):522–534, 2010.
- [150] H. Palza, I.F.C. Naue, M. Wilhelm, S. Filipe, A. Becker, J. Sunder, and A. Göttfert. On-line detection of polymer melt flow instabilities in a capillary rheometer. *Kautsch. Gummi Kunstst.*, 10:456–461, 2010.
- [151] I. F. C. Naue, S. Filipe, and M. Wilhelm. New detection of mechanical instabilities in the capillary rheometry of polymer melts. In *8th World Congress of Chemical Engineering*, Montreal, 2009.
- [152] J.P. Tordella. Fracture in the extrusion of amorphous polymers through capillaries. *J. Appl. Phys.*, 27(5):454–458, 1956.
- [153] J.P. Tordella. Unstable flow of molten polymers: A second site of melt fracture. *J. Appl. Polym. Sci.*, 7(1):215–229, 1963.
- [154] E.B. Bagley and A.M. Birks. Flow of polyethylene into a capillary. *J. Appl. Phys.*, 31(3):556–561, 1960.

- [155] T.F. Ballenger, I.-J. Chen, J.W. Crowder, G.E. Hagler, D.C. Bogue, and J.L. White. Polymer melt flow instabilities in extrusion: Investigation of the mechanism and material and geometric variables. *J. Rheol.*, 15(2):195–215, 1971.
- [156] E. Miller and J.P. Rothstein. Control of the sharkskin instability in the extrusion of polymer melts using induced temperature gradients. *Rheol. Acta*, 44(2):160–173, 2004.
- [157] H. Münstedt, M. Schmidt, and E. Wassner. Stick and slip phenomena during extrusion of polyethylene melts as investigated by laser-doppler velocimetry. *J. Rheol.*, 44(2):413–427, 2000.
- [158] E. Carreras, N. Kissi, J.-M. Piau, F. Toussaint, and S. Nigen. Pressure effects on viscosity and flow stability of polyethylene melts during extrusion. *Rheol. Acta*, 45(3):209–222, 2006.
- [159] C. Deeprasertkul, C. Rosenblatt, and S.-Q. Wang. Molecular character of sharkskin phenomenon in metallocene linear low density polyethylenes. *Macromol. Chem. Phys.*, 199(10):2113–2118, 1998.
- [160] P.J. Doerpinghaus and D.G. Baird. Comparison of the melt fracture behavior of metallocene and conventional polyethylenes. *Rheol. Acta*, 42(6):544–556, 2003.
- [161] M. Fernandez, J. Francisco-Vega, A. Santamaria, A. Muoz-Escalona, and P. Lafuente. The effect of chain architecture on sharkskin of metallocene polyethylenes. *Macromol. Rapid Commun.*, 21(14):973–978, 2000.
- [162] L. Robert, Y. Demay, and B. Vergnes. Stick-slip flow of high density polyethylene in a transparent slit die investigated by laser doppler velocimetry. *Rheol. Acta*, 43(1):89–98, 2004.
- [163] S.-Q. Wang. Molecular transitions and dynamics at polymer / wall interfaces: Origins of flow instabilities and wall slip. *Adv. Polym. Sci.*, pages 227–275, 1999.
- [164] S.C. Hatzikiriakos and K.B. Migler, editors. *Polymer Processing Instabilities: Control and Understanding*. Marcel Dekker, New York, 2005.
- [165] N. Nithi-Uthai and I. Manas-Zloczower. Numerical simulation of sharkskin phenomena in polymer melts. *Appl. Rheol.*, 13:79–86, 2003.

- [166] Y. M. Joshi. Studies on wall-slip in entangled polymeric liquids. *Appl. Rheol.*, 11:277–280, 2001.
- [167] R.G. Larson. Instabilities in viscoelastic flows. *Rheol. Acta*, 31(3):213–263, 1992.
- [168] M.M. Denn. Extrusion instabilities and wall slip. *Ann. Rev. Fluid Mech.*, 33(1):265–287, 2001.
- [169] F.N. Cogswell, J.R. Barone, N. Plucktaveesak, and S.-Q. Wang. Letter to the editor: The mystery of the mechanism of sharkskin. *J. Rheol.*, 43(1):245–252, 1999.
- [170] F.N. Cogswell. Stretching flow instabilities at the exits of extrusion dies. *J. Non-Newtonian Fluid Mech.*, 2(1):37–47, 1977.
- [171] Y.W. Inn, R.J. Fischer, and M.T. Shaw. Visual observation of development of sharkskin melt fracture in polybutadiene extrusion. *Rheol. Acta*, 37(6):573–582, 1998.
- [172] M.R. Mackley, R.P.G. Rutgers, and D.G. Gilbert. Surface instabilities during the extrusion of linear low density polyethylene. *J. Non-Newtonian Fluid Mech.*, 76(1-3):281–297, 1998.
- [173] R. Rutgers and M. Mackley. The correlation of experimental surface extrusion instabilities with numerically predicted exit surface stress concentrations and melt strength for linear low density polyethylene. *J. Rheol.*, 44(6):1319–1334, 2000.
- [174] R.P.G. Rutgers and M.R. Mackley. The effect of channel geometry and wall boundary conditions on the formation of extrusion surface instabilities for LLDPE. *J. Non-Newtonian Fluid Mech.*, 98(2-3):185–199, 2001.
- [175] K.B. Migler, Y. Son, F. Qiao, and K. Flynn. Extensional deformation, cohesive failure, and boundary conditions during sharkskin melt fracture. *J. Rheol.*, 46(2):383–400, 2002.
- [176] K.B. Migler, C. Lavallee, M.P. Dillon, S.S. Woods, and C.L. Gettinger. Visualizing the elimination of sharkskin through fluoropolymer additives: Coating and polymer–polymer slippage. *J. Rheol.*, 45(2):565–581, 2001.
- [177] S.-Q. Wang, P.A. Drda, and Y.-W. Inn. Exploring molecular origins of sharkskin, partial slip, and slope change in flow curves of linear low density polyethylene. *J. Rheol.*, 40(5):875–898, 1996.

- [178] J.R. Barone, N. Plucktaveesak, and S.-Q. Wang. Interfacial molecular instability mechanism for sharkskin phenomenon in capillary extrusion of linear polyethylenes. *J. Rheol.*, 42(4):813–832, 1998.
- [179] J. Barone and S.-Q. Wang. Flow birefringence study of sharkskin and stress relaxation in polybutadiene melts. *Rheol. Acta*, 38(5):404–414, 1999.
- [180] J.R. Barone and S.-Q. Wang. Rheo-optical observations of sharkskin formation in slit-die extrusion. *J. Rheol.*, 45(1):49–60, 2001.
- [181] N. El Kissi and J.M. Piau. Adhesion of linear low density polyethylene for flow regimes with sharkskin. *J. Rheol.*, 38(5):1447–1463, 1994.
- [182] J.-M. Piau, N. Kissi, F. Toussaint, and A. Mezghani. Distortions of polymer melt extrudates and their elimination using slippery surfaces. *Rheol. Acta*, 34(1):40–57, 1995.
- [183] E. Miller, S. Lee, and J. Rothstein. The effect of temperature gradients on the sharkskin surface instability in polymer extrusion through a slit die. *Rheol. Acta*, 45(6):943–950, 2006.
- [184] D.R. Arda and M.R. Mackley. The effect of die exit curvature, die surface roughness and a fluoropolymer additive on sharkskin extrusion instabilities in polyethylene processing. *J. Non-Newtonian Fluid Mech.*, 126(1):47–61, 2005.
- [185] D.R. Arda and M.R. Mackley. Sharkskin instabilities and the effect of slip from gas-assisted extrusion. *Rheol. Acta*, 44(4):352–359, 2005.
- [186] J.P. Tordella. Capillary flow of molten polyethylene—a photographic study of melt fracture. *Trans. Soc. Rheol.*, 1(1):203–212, 1957.
- [187] S.-Q. Wang and P.A. Drda. Stick-slip transition in capillary flow of polyethylene. 2. molecular weight dependence and low-temperature anomaly. *Macromolecules*, 29(11):4115–4119, 1996.
- [188] S.-Q. Wang and P.A. Drda. Superfluid-like stick-slip transition in capillary flow of linear polyethylene melts. 1. general features. *Macromolecules*, 29(7):2627–2632, 1996.
- [189] S.-Q. Wang and P.A. Drda. Stick-slip transition in capillary flow of linear polyethylene: 3. surface conditions. *Rheol. Acta*, 36(2):128–134, 1997.

- [190] S.-Q. Wang and N. Plucktaveesak. Self-oscillations in capillary flow of entangled polymers. *J. Rheol.*, 43(2):453–460, 1999.
- [191] A.V. Ramamurthy and J.C.H. McAdam. Velocity measurements in the die entry region of a capillary rheometer. *J. Rheol.*, 24(2):167–188, 1980.
- [192] Y. Yeh and H.Z. Cummins. Localized fluid flow measurements with an He-Ne laser spectrometer. *Appl. Phys. Lett.*, 4(10):176–178, 1964.
- [193] F. Durst, A. Melling, and J.H. Whitelaw. *Principles and practice of laser-doppler anemometry*. Academic Press, London, 1981.
- [194] M. Schmidt, E. Wassner, and H. Münstedt. Setup and test of a laser doppler velocimeter for investigations of flow behaviour of polymer melts. *Mech. Time-Dependent Mat.*, 3(4):371–393, 1999.
- [195] E. Wassner, M. Schmidt, and H. Münstedt. Entry flow of a low-density-polyethylene melt into a slit die: An experimental study by laser-doppler velocimetry. *J. Rheol.*, 43(6):1339–1353, 1999.
- [196] J. Molenaar and R.J. Koopmans. Modeling polymer melt-flow instabilities. *J. Rheol.*, 38(1):99–109, 1994.
- [197] C.F.J. Den Doelder, R.J. Koopmans, J. Molenaar, and A.A.F. Van de Ven. Comparing the wall slip and the constitutive approach for modelling spurt instabilities in polymer melt flows. *J. Non-Newtonian Fluid Mech.*, 75(1):25–41, 1998.
- [198] K.P. Adewale and A.I. Leonov. Modeling spurt and stress oscillations in flows of molten polymers. *Rheol. Acta*, 36(2):110–127, 1997.
- [199] A.V. Ramamurthy. Wall slip in viscous fluids and influence of materials of construction. *J. Rheol.*, 30(2):337–357, 1986.
- [200] E. Uhland. Das anomale Fließverhalten von Polyäthylen hoher Dichte. *Rheol. Acta*, 18(1):1–23, 1979.
- [201] J.M. Piau, N. El Kissi, and B. Tremblay. Influence of upstream instabilities and wall slip on melt fracture and sharkskin phenomena during silicones extrusion through orifice dies. *J. Non-Newtonian Fluid Mech.*, 34(2):145–180, 1990.
- [202] S. Kim and J.M. Dealy. Gross melt fracture of polyethylene. ii: Effects of molecular structure. *Polym. Eng. Sci.*, 42(3):495–503, 2002.

- [203] S. Kim and J.M. Dealy. Gross melt fracture of polyethylene. i: A criterion based on tensile stress. *Polym. Eng. Sci.*, 42(3):482–494, 2002.
- [204] M. Meller, A. Luciani, and J.A.E. Manson. Flow through a convergence. part 2: Mixing of high viscosity ratio polymer blends. *Polym. Eng. Sci.*, 42(3):634–653, 2002.
- [205] M. Meller, A. Luciani, A. Sarioglu, and J.-A.E. Manson. Flow through a convergence. part 1: Critical conditions for unstable flow. *Polym. Eng. Sci.*, 42(3):611–633, 2002.
- [206] H. Giesekus. Nicht-lineare Effekte beim Strömen viskoelastischer Flüssigkeiten durch Schlitz- und Lochdüsen. *Rheol. Acta*, 7(2):127–138, 1968.
- [207] H.-Y. Lee, D.H. Kim, and Y. Son. Anomalous rheological behavior of polyethylene melts in the gross melt fracture regime in the capillary extrusion. *Polymer*, 47(11):3929–3934, 2006.
- [208] O.L. Kulikov and K. Hornung. A simple geometrical solution to the surface fracturing problem in extrusion processes. *J. Non-Newtonian Fluid Mech.*, 98(2-3):107–115, 2001.
- [209] O.L. Kulikov and K. Hornung. Wall detachment and high rate surface defects during extrusion of clay. *J. Non-Newtonian Fluid Mech.*, 107(1-3):133–144, 2002.
- [210] O. Kulikov and K. Hornung. A simple way to suppress surface defects in the processing of polyethylene. *J. Non-Newtonian Fluid Mech.*, 124(1-3):103–114, 2004.
- [211] H.J. Larrazabal, A.N. Hrymak, and J. Vlachopoulos. On the relationship between the work of adhesion and the critical shear stress for the onset of flow instabilities. *Rheologica Acta*, 45(5):705–715, 2006.
- [212] R. Eisenschitz, B. Rabinowitsch, and K. Weissenberg. . *Mitt. deut. Materialp. Anst. Sonderh.*, 9:91, 1929.
- [213] E. B. Bagley. End corrections in the capillary flow of polyethylene. *J. Appl. Phys.*, 28(5):624–627, 1957.
- [214] W. Philippoff and F.H. Gaskins. The capillary experiment in rheology. *Trans. Soc. Rheol.*, 2:263–284, 1958.
- [215] S. Filipe. Non-linear rheology of polymer melts. *AIP Conf. Proc.*, 1152(1):168–174, 2009.

- [216] H. Palza, B. Reznik, M. Kappes, F. Hennrich, I.F.C. Naue, and M. Wilhelm. Characterization of melt flow instabilities in polyethylene/carbon nanotube composites. *Polymer*, 51(16):3753–3761, 2010.
- [217] B.T. Atwood and W.R. Schowalter. Measurements of slip at the wall during flow of high-density polyethylene through a rectangular conduit. *Rheol. Acta*, 28(2):134–146, 1989.
- [218] J.H. Giles, T.D. Ridder, R.H. Williams, D.A. Jones, and M.B. Denton. Product review: Selecting a ccd camera. *Anal. Chem.*, 70(19):663A–668A, 1998.
- [219] G. Smith. Willard Boyle (1924–2011). *Nature*, 474(7349):37–37, 2011.
- [220] R.N. Bracewell. *Fourier analysis and imaging*. Kluwer Academic/Plenum, New York, 2003.
- [221] R.C. Gonzales, R.E. Woods, and S.L. Eddins. *Digital Image Processing using MATLAB*. Prentice Hall, Upper Saddle River, 2004.
- [222] S.L. Anna, C. Rogers, and G.H. McKinley. On controlling the kinematics of a filament stretching rheometer using a real-time active control mechanism. *J. Non-Newtonian Fluid Mech.*, 87(2-3):307–335, 1999.
- [223] S.L. Anna and G.H. McKinley. Elasto-capillary thinning and breakup of model elastic liquids. *J. Rheol.*, 45(1):115–138, 2001.
- [224] S.L. Anna, G.H. McKinley, D.A. Nguyen, T. Sridhar, S.J. Muller, J. Huang, and D.F. James. An interlaboratory comparison of measurements from filament-stretching rheometers using common test fluids. *J. Rheol.*, 45(1):83–114, 2001.
- [225] J.P. Plog. Uniaxiale Dehnung. *Nachr. Chem.*, 57:155, 2009.
- [226] J. Meissner. Rheometer zur Untersuchung der deformationsmechanischen Eigenschaften von Kunststoff-Schmelzen unter definierter Zugbeanspruchung. *Rheol. Acta*, 8(1):78–88, 1969.
- [227] M. Sentmanat, B.N. Wang, and G.H. McKinley. Measuring the transient extensional rheology of polyethylene melts using the ser universal testing platform. *J. Rheol.*, 49(3):585–606, 2005.
- [228] D.M. Binding and K. Walters. On the use of flow through a contraction in estimating the extensional viscosity of mobile polymer solutions. *J. Non-Newtonian Fluid Mech.*, 30(2-3):233–250, 1988.

- [229] G.G. Fuller, C.A. Cathey, B. Hubbard, and B.E. Zebrowski. Extensional viscosity measurements for low-viscosity fluids. *J. Rheol.*, 31(3):235–249, 1987.
- [230] T. Sridhar. An overview of the project M1. *J. Non-Newtonian Fluid Mech.*, 35(2-3):85–92, 1990.
- [231] P. Dontula, M. Pasquali, L.E. Scriven, and C.W. Macosko. Can extensional viscosity be measured with opposed-nozzle devices? *Rheol. Acta*, 36(4):429–448, 1997.
- [232] J.E. Matta and R.P. Tytus. Liquid stretching using a falling cylinder. *J. Non-Newtonian Fluid Mech.*, 35(2-3):215–229, 1990.
- [233] V. Tirtaatmadja and T. Sridhar. A filament stretching device for measurement of extensional viscosity. *J. Rheol.*, 37(6):1081–1102, 1993.
- [234] S.H. Spiegelberg, D.C. Ables, and G.H. McKinley. The role of end-effects on measurements of extensional viscosity in filament stretching rheometers. *J. Non-Newtonian Fluid Mech.*, 64(2-3):229–267, 1996.
- [235] S. Gaudet, G.H. McKinley, and H.A. Stone. Extensional deformation of newtonian liquid bridges. *Phys. Fluids*, 8(10):2568–2579, 1996.
- [236] P. Szabo. Transient filament stretching rheometer I: Force balance analysis. *Rheol. Acta*, 36(3):277–284, 1997.
- [237] M.I. Kolte and O. Rasmussen, H.K. and Hassager. Transient filament stretching rheometer II: Numerical simulation. *Rheol. Acta*, 36(3):285–302, 1997.
- [238] A.V. Bazilevsky, V.M. Entov, and A.N. Rozhkov. Liquid filament microrheometer and some of its applications. In D.R. Oliver, editor, *Third European Rheology Conference and Golden Jubilee Meeting of the British Society of Rheology*, pages 41–43, 1990.
- [239] V.M. Entov and E.J. Hinch. Effect of a spectrum of relaxation times on the capillary thinning of a filament of elastic liquid. *J. Non-Newtonian Fluid Mech.*, 72(1):31–53, 1997.
- [240] M.I. Kolte and P. Szabo. Capillary thinning of polymeric filaments. *J. Rheol.*, 43(3):609–625, 1999.
- [241] G.H. McKinley and A. Tripathi. How to extract the Newtonian viscosity from capillary breakup measurements in a filament rheometer. *J. Rheol.*, 44(3):653–670, 2000.

- [242] K. Niedzwiedz, O. Arnolds, N. Willenbacher, and R. Brummer. Capillary breakup extensional rheometry of yield stress fluids. *Appl. Rheol.*, 19(4):41969, 2009.
- [243] O. Arnolds, H. Buggisch, D. Sachsenheimer, and N. Willenbacher. Capillary breakup extensional rheometry (CaBER) on semi-dilute and concentrated polyethyleneoxide (PEO) solutions. *Rheol. Acta*, 49(11):1207–1217, 2010.
- [244] O. Arnolds. *Dehnrheologie verdünnter, halbkonzentrierter und konzentrierter Polymerlösungen untersucht mit Capillary Breakup Extensional Rheometry (CaBER)*. PhD thesis, Karlsruhe Institute of Technology (KIT), 2011.
- [245] C. Klein, I. Naue, M. Wilhelm, R. Brummer, and J. Nijman. Extending the capabilities of the caber with highly sensitive force measurements. In *XVth International Congress On Rheology - The Society Of Rheology 80th Annual Meeting*, volume 1027, pages 1208–1210, Monterey, 2008. Amer. Inst. Physics.
- [246] C.O. Klein, I.F.C. Naue, J. Nijman, and M. Wilhelm. Addition of the force measurement capability to a commercially available extensional rheometer (caber). *Soft Materials*, 7(4):242–257, 2009.
- [247] A. Zosel. Adhesion and tack of polymers - influence of mechanical-properties and surface tensions. *Colloid Polym. Sci.*, 263(7):541–553, 1985.
- [248] A. Zosel. Effect of cross-linking on tack and peel strength of polymers. *J. Adhes.*, 34(1-4):201–209, 1991.
- [249] A. Zosel. The effect of bond formation on the tack of polymers. *J. Adhes. Sci. Technol.*, 11(11):1447–1457, 1997.
- [250] A. Zosel. The effect of fibrillation on the tack of pressure sensitive adhesives. *Int. J. Adhes. Adhes.*, 18(4):265–271, 1998.
- [251] A. Zosel. Built to last. *Adhes. Age*, 43(8):34, 2000.
- [252] E. Miller, C. Clasen, and J. Rothstein. The effect of step-stretch parameters on capillary breakup extensional rheology (CaBER) measurements. *Rheol. Acta*, 48(6):625–639, 2009.
- [253] K. Hutter and K. Jöhnk. *Continuum methods of physical modeling : mechanics of continua, dimensional analysis, turbulence*. Springer, Berlin, 2004.

- [254] C. Truesdell and K.R. Rajagopal. *An introduction to the mechanics of fluids*. Birkhäuser, Boston, 2009.
- [255] R.W. Ogden. *Non-linear elastic deformations*. Dover Publ., Mineola, 1997.
- [256] E.C. Bingham. *Fluidity and Plasticity*. McGraw-Hill, New York, 1922.
- [257] W. Ostwald. Über die Geschwindigkeitsfunktion der Viskosität disperser Systeme. I. *Kolloid Zeitschrift*, 36:99–117, 1925.
- [258] F.T. Trouton. On the coefficient of viscous traction and its relation to that of viscosity. *Proc. Roy. Soc.*, 77(519):426–440, 1906.
- [259] A. N. Gent and A. J. Kinloch. Adhesion of viscoelastic materials to rigid substrates. iii. energy criterion for failure. *J. Polym. Sci. A-2 Polym. Phys.*, 9(4):659–668, 1971.
- [260] C.J.S. Petrie. *Elongational Flows*. Pitman London, San Francisco, Melbourne, London, 1979.
- [261] P. Chadwick. *Continuum Mechanics*. Dover, Mineola, 1999.
- [262] H. Schade and K. Neemann. *Tensoranalysis*. de Gruyter, Berlin, 2009.
- [263] E.O. Brigham. *The Fast Fourier-Transform*. Prentice Hall, Englewood Cliffs, 1974.
- [264] Eugene Hecht. *Optik*. Oldenbourg, München, 2009.
- [265] G. Wedler. *Lehrbuch der physikalischen Chemie*. Wiley-VCH, Weinheim, 2004.
- [266] M. Gaborieau. *Solid-state NMR investigation of spatial and dynamic heterogeneity in acrylic pressure sensitive adhesives (PSAs) compared to model poly(n-alkyl acrylates) and poly(n-alkyl methacrylates)*. PhD thesis, Strasbourg University Louis Pasteur, 2005.
- [267] Y. Woo. *Inelastic analysis of the loop tack test for pressure sensitive adhesives*. PhD thesis, Virginia Polytechnic Institute and State University, 2002.
- [268] E. Maurer. *Strukturuntersuchungen an Haftklebstoffen beim mechanischen Tack-Test auf makroskopischer und mikroskopischer Längenskala*. PhD thesis, Technical University Munich, 2006.
- [269] M. Toyama, T. Ito, and H. Moriguchi. Studies on tack of pressure sensitive adhesive tapes. *J. Appl. Polym. Sci.*, 14(8):2039–2048, 1970.

- [270] D. H. Kaelble. Theory and analysis of peel adhesion: mechanisms and mechanics. *J. Rheol.*, 3:161–180, 1959.
- [271] A. N. Gent and C. W. Lin. Comparison of peel and lap shear bond strengths for elastic joints with and without residual stresses. *J. Adh.*, 30(1-4):1–11, 1989.
- [272] A. Zosel. Adhesive failure and deformation behaviour of polymers. *J. Adh.*, 30(1-4):135–149, 1989.
- [273] C. Gerthsen. *Gerthsen Physik*. Springer, Berlin, 2004.
- [274] H.-J. Butt and M. Kappl. *Surface and interfacial forces*. Wiley-VCH, Weinheim, 2010.
- [275] T. Young. An essay on the cohesion of fluids. *Philos. T. R. Soc. Lond.*, 95:65–87, 1805.

## Acknowledgement

During the last five years I had to interact with many people and scientists from different groups and universities. Here, I want to thank those people:

**Prof. M. Wilhelm** for providing me with lots of interesting tasks and opportunities during my PhD work in his group.

**Prof. P. Elsner** for supervising me as a professor from the mechanical engineering and for the helpful discussions.

**Prof. J.A. Kornfield** for the two months stay in her group at Caltech, Pasadena.

**Prof. Ibnelwaleed Hussein** (King Fahd University of Petroleum & Minerals, Dhahran) for the rare possibility to visit his university and for his interest in our research methods.

**Prof. H. Palza** (Universita di Chile, Santiago) for his collaboration, help, fruitful discussions about melt flow instabilities and for many nice evenings at the Vogelbräu, in Karlsruhe.

**Arrate Huegun Mutiloa, Ayuba Adegoke Adesina and Woojoo Han** for their interest in our work about melt flow instabilities, the work together and the discussions with them.

**Prof. H. Münstedt and H. Gries** for the interesting discussions about the origin of the melt flow instabilities and for donating the LLDPE and LDPE sample for studying the sharkskin meltflow instability.

**The workers of our mechanical workshop** at the institute, especially A. Jaks and A. Wagner, for their kind help and always well done work.

**The Göttfert company**, especial Dr. A. Göttfert, Dr. J. Sunder and U. Bäuerle, for their help, technical support and for commercial realisation of parts of my work.

**The group of Prof. Wilhelm** for their help and friendship, all the time.  
Also, thank you for enjoyable BBQ's, Christmas parties and so on.

**All the alumni of our group**, especially Dr. I. Vittorias, Dr. S. Filipe\*,  
Dr. V. Barroso, Dr. A. Calin and Dr. K. Hyun for introducing me  
to rheology and rheometry, for their help, their support and for all  
the enjoyable times with them.

**Daniel Zimmermann** for his help at certain measurements, industry pro-  
jects and all the logistical stuff.

**Sabine Weiland** for logistical help with all the administrative stuff at the  
KIT which crossed my path.

**Prof. H. Buggisch** (applied mechanics, Karlsruhe Institute of Technology)  
for the support in developing the theory for the CaBER, and to-  
gether with B. Hochstein and O. Arnolds for the discussions and the  
suggestions.

**Dr. B. Reznik** for borrowing me the copper mesh.

**J. Nijman and C. Küchenmeister** from Thermo scientific (Durlach, Ger-  
many) for making the improvement of the CaBER apparatus com-  
mercially available and for their support.

**Thomas Meins** for his friendship and challenging tasks in programming.

**Roland Kádár** for all the discussion about advanced data analysis of melt  
flow instabilities and their visualization. I also have to thank him  
for being finally a true fluid mechanic companion in a world of  
chemists.

**Christopher O. Klein** for his friendship all the time and for the many dis-  
cussions we had, which sometimes resulted in some new technical  
developments.

**Michael Kempf** for his friendship all the time since our diploma thesis (at  
the MPI-P in Mainz) and for the many discussions we had, which  
also resulted in some new developments. Special thanks to him for  
joining the strenuous hiking tours in the snow with me.

**Kathrin Reinheimer** for her friendship and lots of interesting tasks in MAT-  
LAB programming. These increased drastically my programming

---

\* Also thanks for the samples.

---

skills. Also thanks to Michael Schwall, her boyfriend, for some nice tricks in MATLAB which I could learn from him.

**Jane Mukha** for correcting the bad English of the first version of this thesis.

**Almut Dirks** for proofreading parts of my thesis.

**Jan Schulz** for helping me to find the right fluid for the illustration of the Weissenberg effect.

**My employees** at the NAUE GmbH, which worked hard and loyal, even without their boss being present.

**My whole family** and especially my parents which basically made all this work possible.

**My co-producer** at the *Poly-Entertainment* motion pictures Christopher "Kiki" Klein and Michael Kempf for four amazingly good Christmas movies, the evenings at the Vogelbräu and their friendship all way long.

The last but not least, many thanks to my beloved and worshipped wife Lucy who gave me time and space to do and finish my work. She never complained when I had to work all night and far away or when I had to go to a conference or visit an other university. Thus, I finish this work by saying: "AAABBCEEKLLMSTUYY,".